



Calhoun: The NPS Institutional Archive
DSpace Repository

Theses and Dissertations

1. Thesis and Dissertation Collection, all items

1992-03

A computational investigation of airfoil stall flutter

Clarkson, Jeffrey Dow

Monterey, California. Naval Postgraduate School

<http://hdl.handle.net/10945/23579>

This publication is a work of the U.S. Government as defined in Title 17, United States Code, Section 101. Copyright protection is not available for this work in the United States.

Downloaded from NPS Archive: Calhoun



<http://www.nps.edu/library>

Calhoun is the Naval Postgraduate School's public access digital repository for research materials and institutional publications created by the NPS community. Calhoun is named for Professor of Mathematics Guy K. Calhoun, NPS's first appointed -- and published -- scholarly author.

Dudley Knox Library / Naval Postgraduate School
411 Dyer Road / 1 University Circle
Monterey, California USA 93943

NAVAL POSTGRADUATE SCHOOL

Monterey, California



THESIS

A COMPUTATIONAL INVESTIGATION
OF AIRFOIL STALL FLUTTER

by

Lt. Jeffrey D. Clarkson
March 1992

Thesis Advisor
Thesis Co-Advisor

Dr. J. A. Ekaterinaris
Dr. M. F. Platzer

Approved for public release; distribution is unlimited.

T259845

REPORT DOCUMENTATION PAGE

1a. REPORT SECURITY CLASSIFICATION Unclassified		1b. RESTRICTIVE MARKINGS Unclassified		
2a. SECURITY CLASSIFICATION AUTHORITY		3. DISTRIBUTION/AVAILABILITY OF REPORT Approved for public release; distribution is unlimited.		
2b. DECLASSIFICATION/DOWNGRADING SCHEDULE				
4. PERFORMING ORGANIZATION REPORT NUMBER(S)		5. MONITORING ORGANIZATION REPORT NUMBER(S)		
6a. NAME OF PERFORMING ORGANIZATION Naval Postgraduate School	6b. OFFICE SYMBOL (If Applicable) 38	7a. NAME OF MONITORING ORGANIZATION Naval Postgraduate School		
6c. ADDRESS (city, state, and ZIP code) Monterey, CA 93943-5000		7b. ADDRESS (city, state, and ZIP code) Monterey, CA 93943-5000		
8a. NAME OF FUNDING/SPONSORING ORGANIZATION	8b. OFFICE SYMBOL (If Applicable)	9. PROCUREMENT INSTRUMENT IDENTIFICATION NUMBER		
8c. ADDRESS (city, state, and ZIP code)		10. SOURCE OF FUNDING NUMBERS		
		PROGRAM ELEMENT NO.	PROJECT NO.	
		TASK NO.	WORK UNIT ACCESSION NO.	
11. TITLE (Include Security Classification) A COMPUTATIONAL INVESTIGATION OF AIRFOIL STALL FLUTTER(U)				
12. PERSONAL AUTHOR(S) Clarkson, Jeffrey D.				
13a. TYPE OF REPORT Engineer's Thesis	13b. TIME COVERED FROM TO	14. DATE OF REPORT (year, month, day) March 1992	15. PAGE COUNT 191	
16. SUPPLEMENTARY NOTATION The views expressed in this thesis are those of the author and do not reflect the official policy or position of the Department of Defense or the U.S. Government.				
17. COSATI CODES		18. SUBJECT TERMS (continue on reverse if necessary and identify by block number) Stall Flutter, Oscillating Airfoil, Pitching Airfoil		
FIELD	GROUP			SUBGROUP
19. ABSTRACT (Continue on reverse if necessary and identify by block number) A fully factorized two-dimensional Navier-Stokes flow solver has been developed and applied to the problem of predicting subsonic airfoil flutter in the light stall regime. The inviscid fluxes are evaluated with a central difference ADI scheme and fourth and second order numerical dissipation is used to obtain oscillation-free solutions. The performance of algebraic and one-equation turbulence models in predicting separated flow is explored for computing high Reynolds number steady flow and unsteady flows over an oscillating NACA 0012 airfoil. Comparisons of the computed results with available experimental data indicate that even though the lift response is fairly well predicted, the computation of the pitching moment hysteresis loops is very sensitive to turbulence modeling. Results computed with several current models are in good agreement whenever the steady stall angle is exceeded only slightly. However, they fail to capture the vortex shedding process leading to the onset of stall flutter.				
20. DISTRIBUTION/AVAILABILITY OF ABSTRACT <input checked="" type="checkbox"/> UNCLASSIFIED/UNLIMITED <input type="checkbox"/> SAME AS RPT. <input type="checkbox"/> DTIC USERS		21. ABSTRACT SECURITY CLASSIFICATION Unclassified		
22a. NAME OF RESPONSIBLE INDIVIDUAL M. F. Platzner		22b. TELEPHONE (Include Area Code) (408) 646-2058	22c. OFFICE SYMBOL Code AAPL	

Approved for public release; distribution is unlimited.

**A COMPUTATIONAL INVESTIGATION OF AIRFOIL STALL
FLUTTER**

by

Jeffrey Dow Clarkson

Lieutenant , United States Navy
B.A.E, Georgia Institute of Technology, 1984

Submitted in partial fulfillment of the requirements
for the degree of

AERONAUTICAL ENGINEER

and

**MASTER OF SCIENCE IN AERONAUTICAL
ENGINEERING**

from the

NAVAL POSTGRADUATE SCHOOL

March 1992

ABSTRACT

A fully factorized two-dimensional Navier-Stokes flow solver has been developed and applied to the problem of predicting subsonic airfoil flutter in the light stall regime. The inviscid fluxes are evaluated with a central difference ADI scheme and fourth and second order numerical dissipation is used to obtain oscillation-free solutions. The performance of algebraic and one-equation turbulence models in predicting separated flow is explored for computing high Reynolds number steady flow and unsteady flows over an oscillating NACA 0012 airfoil. Comparisons of the computed results with available experimental data indicate that even though the lift response is fairly well predicted, the computation of the pitching moment hysteresis loops is very sensitive to turbulence modeling. Results computed with several current models are in good agreement whenever the steady stall angle is exceeded only slightly. However, they fail to capture the vortex shedding process leading to the onset of stall flutter.

TABLE OF CONTENTS

I.	INTRODUCTION	1
A.	BACKGROUND	1
B.	PURPOSE	2
II.	GOVERNING EQUATIONS	4
A.	CONTINUITY EQUATION	4
B.	MOMENTUM EQUATIONS	4
C.	ENERGY EQUATION	5
D.	CONSERVATION FORM OF GOVERNING EQUATIONS	6
III.	SOLUTION METHODS	8
A.	POTENTIAL FLOW METHOD (U2DIIF.F)	8
1.	Panel Method for Steady Airfoil Flows	8
2.	Unsteady Numerical Formulation	12
B.	VISCOUS/INVISCID INTERACTION METHOD (INCOMPBL.F)	14
1.	Interaction Method	15
2.	Interactive Model	17
3.	Turbulence Model	18
C.	EULER AND NAVIER-STOKES CODE (NS2.F)	19
1.	Numerical Grids	22
2.	The Numerical Scheme	26
3.	Boundary Conditions	28
4.	Turbulence Models	29
IV.	RESULTS AND DISCUSSION	35
A.	METHOD OF INVESTIGATION	35
1.	Steady-State	37
2.	Rapidly Pitching Airfoil	74

3. Harmonic Airfoil Oscillation Using the Baldwin-Lomax Turbulence Model.	90
4. Effect of Turbulence Modeling.....	128
V. CONCLUSIONS AND RECOMMENDATIONS.....	148
LIST OF REFERENCES.....	150
APPENDIX A - Flux Jacobian Matrix.....	152
APPENDIX B - Pitching Moment Derivation	153
APPENDIX C - Using the Programs	158
A. DIRECTIONS FOR THE EXECUTION OF NS2.F	158
1. Steady State Case.....	158
2. Unsteady Case.....	162
B. DIRECTIONS FOR THE EXECUTION OF U2DIIF.F.....	166
1. Unsteady Case.....	166
C. DIRECTIONS FOR THE EXECUTION OF INCOMPBL.F.....	172
1. Steady State Case.....	172
INITIAL DISTRIBUTION LIST.....	178

LIST OF FIGURES

Figure 1. NACA 0012 Inviscid 151x64 C-Grid.....	24
Figure 2. NACA 0012 Viscous 161x64 C-Grid.....	25
Figure 3. Pressure Distribution (Inviscid), $M=0.7$, $\alpha=1.4^\circ$, $Re=9 \times 10^6$	39
Figure 4. Convergence History, $M=0.7$, $\alpha=1.4^\circ$, $Re=9 \times 10^6$	40
Figure 5. Pressure Distribution , $M=0.7$, $\alpha=1.4^\circ$, $Re=9 \times 10^6$	41
Figure 6. Mach Contour, $M=0.7$, $\alpha=1.4^\circ$, $Re=3 \times 10^6$	42
Figure 7. Density Contour, $M=0.7$, $\alpha=1.4^\circ$, $Re=9 \times 10^6$	43
Figure 8. Velocity Field, $M=0.7$, $\alpha=1.4^\circ$, $Re=9 \times 10^6$	44
Figure 9. Pressure Distribution (Inviscid) , $M=0.799$, $\alpha=2.26^\circ$, $Re=9 \times 10^6$	47
Figure 10. Convergence History (Ns2.f), $M=0.799$, $\alpha=2.26^\circ$, $Re=9 \times 10^6$	48
Figure 11. Pressure Distribution, $M=0.799$, $\alpha=2.26^\circ$, $Re=9 \times 10^6$	49
Figure 12. Mach Contour, $M=0.799$, $\alpha=2.26^\circ$, $Re=9 \times 10^6$	50
Figure 13. Pressure Contour, $M=0.799$, $\alpha=2.26^\circ$, $Re=9 \times 10^6$	51
Figure 14. Density Contour, $M=0.799$, $\alpha=2.26^\circ$, $Re=9 \times 10^6$	52
Figure 15. Velocity Field, $M=0.799$, $\alpha=2.26^\circ$, $Re=9 \times 10^6$	53
Figure 16. Convergence History, $M=0.3$, $\alpha=4^\circ$, $Re=3 \times 10^6$	56
Figure 17. Pressure Distribution, $M=0.3$, $\alpha=4^\circ$, $Re=3 \times 10^6$	57
Figure 18. Skin Friction Distribution (Upper Surface), $M=0.3$, $\alpha=4^\circ$, $Re=3 \times 10^6$	58
Figure 19. Skin Friction Distribution (Lower Surface), $M=0.3$, $\alpha=4^\circ$, $Re=3 \times 10^6$	59
Figure 20. Mach Contour, $M=0.3$, $\alpha=4^\circ$, $Re=3 \times 10^6$	60
Figure 21. Density Contour, $M=0.3$, $\alpha=4^\circ$, $Re=3 \times 10^6$	61
Figure 22. Convergence History, $M=0.3$, $\alpha=11^\circ$, $Re=3 \times 10^6$	62
Figure 23. Pressure Distribution, $M=0.3$, $\alpha=11^\circ$, $Re=3 \times 10^6$	63
Figure 24. Skin Friction Distribution (Upper Surface), $M=0.3$, $\alpha=11^\circ$, $Re=3 \times 10^6$	64

Figure 25. Skin Friction Distribution (Lower Surface), $M=0.3$, $\alpha=11^\circ$, $Re=3 \times 10^6$	65
Figure 26. Mach Contour, $M=0.3$, $\alpha=11^\circ$, $Re=3 \times 10^6$	66
Figure 27. Density Contour, $M=0.3$, $\alpha=11^\circ$, $Re=3 \times 10^6$	67
Figure 28. Convergence History, $M=0.3$, $\alpha=14^\circ$, $Re=3 \times 10^6$	68
Figure 29. Pressure Distribution, $M=0.3$, $\alpha=14^\circ$, $Re=3 \times 10^6$	69
Figure 30. C_l vs α , $M=0.3$, $Re=3 \times 10^6$	70
Figure 31. C_m vs α , $M=0.3$, $Re=3 \times 10^6$	71
Figure 32. C_l vs. α and C_m vs. α , $M=0.3$, $Re=4 \times 10^6$	73
Figure 33. Rapidly Pitching Airfoil Motion	74
Figure 34. Pressure Distribution (Inviscid), Ramp Motion, $M=0.3$, $\alpha=4.87^\circ$, $k=0.01272$, $Re=2.7 \times 10^6$	76
Figure 35. Pressure Distribution, Ramp Motion, $M=0.3$, $\alpha=4.87^\circ$, $k=0.01272$, $Re=2.7 \times 10^6$	77
Figure 36. Pressure Distribution, Ramp Motion, $M=0.3$, $\alpha=6.72^\circ$, $k=0.01272$, $Re=2.7 \times 10^6$	78
Figure 37. Pressure Distribution, Ramp Motion, $M=0.3$, $\alpha=10.80^\circ$, $k=0.01272$, $Re=2.7 \times 10^6$	79
Figure 38. Pressure Distribution, Ramp Motion, $M=0.3$, $\alpha=12.83^\circ$, $k=0.01272$, $Re=2.7 \times 10^6$	80
Figure 39. Pressure Distribution, Ramp Motion, $M=0.3$, $\alpha=15.54^\circ$, $k=0.01272$, $Re=2.7 \times 10^6$	81
Figure 40. Mach Contour, Ramp Motion, $M=0.3$, $\alpha=10.8^\circ$, $k=0.01272$, $Re=2.7 \times 10^6$	82
Figure 41. Density Contour, Ramp Motion, $M=0.3$, $\alpha=10.8^\circ$, $k=0.01272$, $Re=2.7 \times 10^6$	83
Figure 42. Velocity Field, Ramp Motion, $M=0.3$, $\alpha=12.83^\circ$, $k=0.01272$, $Re=2.7 \times 10^6$	85
Figure 43. Velocity Field (Magnified), Ramp Motion, $M=0.3$, $\alpha=12.83^\circ$, $k=0.01272$, $Re=2.7 \times 10^6$	86
Figure 44. Velocity Field, Ramp Motion, $M=0.3$, $\alpha=15.54^\circ$, $k=0.01272$, $Re=2.7 \times 10^6$	87

Figure 45. C_l vs α , Ramp Motion, $M=0.3$, $k=0.01272$, $Re=2.7 \times 10^6$	88
Figure 46. C_m vs α , Ramp Motion, $M=0.3$, $k=0.01272$, $Re=2.7 \times 10^6$	89
Figure 47. Harmonically Oscillating Airfoil.....	90
Figure 48. Effect of Mach Number on Unsteady Motion, $\alpha(t)=12^\circ \pm 3^\circ \sin(\omega t)$, $k=0.10$, $Re=4 \times 10^6$	93
Figure 49. Effect of Mach Number on Unsteady Motion, $\alpha(t)=12^\circ \pm 3^\circ \sin(\omega t)$, $k=0.10$, $Re=4 \times 10^6$	94
Figure 50. Effect of Amplitude on Unsteady Motion, $M=0.3$, $\alpha(t)=12^\circ \pm A_1^\circ \sin(\omega t)$, $k=0.10$, $Re=4 \times 10^6$	95
Figure 51. Effect of Amplitude on Unsteady Motion, $M=0.3$, $\alpha(t)=12^\circ \pm A_1^\circ \sin(\omega t)$, $k=0.10$, $Re=4 \times 10^6$	96
Figure 52. Effect of Amplitude on Unsteady Motion, $M=0.3$, $\alpha(t)=14^\circ \pm A_1^\circ \sin(\omega t)$, $k=0.10$, $Re=4 \times 10^6$	97
Figure 53. Effect of Amplitude on Unsteady Motion, $M=0.3$, $\alpha(t)=14^\circ \pm A_1^\circ \sin(\omega t)$, $k=0.10$, $Re=4 \times 10^6$	98
Figure 54. Effect of 1 st and 2 nd Cycle on Unsteady Motion, $M=0.3$, $\alpha(t)=13^\circ \pm 2^\circ \sin(\omega t)$, $k=0.10$, $Re=4 \times 10^6$	99
Figure 55. Effect of 1 st and 2 nd Cycle on Unsteady Motion, $M=0.3$, $\alpha(t)=13^\circ \pm 2^\circ \sin(\omega t)$, $k=0.10$, $Re=4 \times 10^6$	100
Figure 56. Effect of Reduced Frequency on Unsteady Motion $M=0.3$, $\alpha(t)=13^\circ \pm 2.5^\circ \sin(\omega t)$, $Re=2 \times 10^6$	101
Figure 57. Instantaneous Particle Trace and Velocity Field, Oscillatory Motion, $M=0.3$, $\alpha=15.3^\circ$ (Downstroke), $\alpha(t)=13^\circ \pm 2.5^\circ \sin(\omega t)$, $k=0.20$, $Re=4 \times 10^6$	103
Figure 58. Instantaneous Particle Trace and Velocity Field, Oscillatory Motion, $M=0.3$, $\alpha=15.1^\circ$ (Downstroke), $\alpha(t)=13^\circ \pm 2.5^\circ \sin(\omega t)$, $k=0.20$, $Re=4 \times 10^6$	104
Figure 59. Instantaneous Particle Trace and Velocity Field, Oscillatory Motion, $M=0.3$, $\alpha=14.9^\circ$ (Downstroke), $\alpha(t)=13^\circ \pm 2.5^\circ \sin(\omega t)$, $k=0.20$, $Re=4 \times 10^6$	105
Figure 60. Instantaneous Particle Trace and Velocity Field, Oscillatory Motion, $M=0.3$, $\alpha=14.7^\circ$ (Downstroke), $\alpha(t)=13^\circ \pm 2.5^\circ \sin(\omega t)$, $k=0.20$, $Re=4 \times 10^6$	106

Figure 61. Instantaneous Particle Trace and Velocity Field, Oscillatory Motion, $M=0.3$, $\alpha=14.5^\circ$ (Downstroke), $\alpha(t)=13^\circ\pm 2.5^\circ\sin(\omega t)$, $k=0.20$, $Re=4\times 10^6$	107
Figure 62. Instantaneous Particle Trace and Velocity Field, Oscillatory Motion, $M=0.3$, $\alpha=12^\circ$ (Upstroke), $\alpha(t)=13^\circ\pm 2.5^\circ\sin(\omega t)$, $k=0.10$, $Re=2\times 10^6$	109
Figure 63. Instantaneous Particle Trace and Velocity Field, Oscillatory Motion, $M=0.3$, $\alpha=13^\circ$ (Upstroke), $\alpha(t)=13^\circ\pm 2.5^\circ\sin(\omega t)$, $k=0.10$, $Re=2\times 10^6$	110
Figure 64. Instantaneous Particle Trace and Velocity Field, Oscillatory Motion, $M=0.3$, $\alpha=13.5^\circ$ (Upstroke), $\alpha(t)=13^\circ\pm 2.5^\circ\sin(\omega t)$, $k=0.10$, $Re=2\times 10^6$	111
Figure 65. Instantaneous Particle Trace and Velocity Field, Oscillatory Motion, $M=0.3$, $\alpha=14^\circ$ (Upstroke), $\alpha(t)=13^\circ\pm 2.5^\circ\sin(\omega t)$, $k=0.10$, $Re=2\times 10^6$	112
Figure 66. Velocity Field, Oscillatory Motion, $M=0.3$, $\alpha=14.5^\circ$ (Upstroke), $\alpha(t)=13^\circ\pm 2.5^\circ\sin(\omega t)$, $k=0.10$, $Re=2\times 10^6$	113
Figure 67. Instantaneous Particle Trace and Velocity Field, Oscillatory Motion, $M=0.3$, $\alpha=14.7^\circ$ (Upstroke), $\alpha(t)=13^\circ\pm 2.5^\circ\sin(\omega t)$, $k=0.10$, $Re=2\times 10^6$	114
Figure 68. Instantaneous Particle Trace and Velocity Field, Oscillatory Motion, $M=0.3$, $\alpha=14.9^\circ$ (Upstroke), $\alpha(t)=13^\circ\pm 2.5^\circ\sin(\omega t)$, $k=0.10$, $Re=2\times 10^6$	115
Figure 69. Instantaneous Particle Trace and Velocity Field, Oscillatory Motion, $M=0.3$, $\alpha=15.1^\circ$ (Upstroke), $\alpha(t)=13^\circ\pm 2.5^\circ\sin(\omega t)$, $k=0.10$, $Re=2\times 10^6$	116
Figure 70. Instantaneous Particle Trace and Velocity Field, Oscillatory Motion, $M=0.3$, $\alpha=15.3^\circ$ (Upstroke), $\alpha(t)=13^\circ\pm 2.5^\circ\sin(\omega t)$, $k=0.10$, $Re=2\times 10^6$	117
Figure 71. Instantaneous Particle Trace and Velocity Field, Oscillatory Motion, $M=0.3$, $\alpha=15.5^\circ$ (Upstroke), $\alpha(t)=13^\circ\pm 2.5^\circ\sin(\omega t)$, $k=0.10$, $Re=2\times 10^6$	118
Figure 72. Instantaneous Particle Trace and Velocity Field, Oscillatory Motion, $M=0.3$, $\alpha=15.3^\circ$ (Downstroke), $\alpha(t)=13^\circ\pm 2.5^\circ\sin(\omega t)$, $k=0.10$, $Re=2\times 10^6$	119

Figure 73. Instantaneous Particle Trace and Velocity Field, Oscillatory Motion, $M=0.3$, $\alpha=15.1^\circ$ (Downstroke), $\alpha(t)=13^\circ\pm 2.5^\circ\sin(\omega t)$, $k=0.10$, $Re=2\times 10^6$	120
Figure 74. Instantaneous Particle Trace and Velocity Field, Oscillatory Motion, $M=0.3$, $\alpha=14.9^\circ$ (Downstroke), $\alpha(t)=13^\circ\pm 2.5^\circ\sin(\omega t)$, $k=0.10$, $Re=2\times 10^6$	121
Figure 75. Instantaneous Particle Trace and Velocity Field, Oscillatory Motion, $M=0.3$, $\alpha=14.7^\circ$ (Downstroke), $\alpha(t)=13^\circ\pm 2.5^\circ\sin(\omega t)$, $k=0.10$, $Re=2\times 10^6$	122
Figure 76. Instantaneous Particle Trace and Velocity Field, Oscillatory Motion, $M=0.3$, $\alpha=14.5^\circ$ (Downstroke), $\alpha(t)=13^\circ\pm 2.5^\circ\sin(\omega t)$, $k=0.10$, $Re=2\times 10^6$	123
Figure 77. Instantaneous Particle Trace and Velocity Field, Oscillatory Motion, $M=0.3$, $\alpha=14^\circ$ (Downstroke), $\alpha(t)=13^\circ\pm 2.5^\circ\sin(\omega t)$, $k=0.10$, $Re=2\times 10^6$	124
Figure 78. Velocity Field, Oscillatory Motion, $M=0.3$, $\alpha=13.5^\circ$ (Downstroke), $\alpha(t)=13^\circ\pm 2.5^\circ\sin(\omega t)$, $k=0.10$, $Re=2\times 10^6$	125
Figure 79. Instantaneous Particle Trace and Velocity Field, Oscillatory Motion, $M=0.3$, $\alpha=13^\circ$ (Downstroke), $\alpha(t)=13^\circ\pm 2.5^\circ\sin(\omega t)$, $k=0.10$, $Re=2\times 10^6$	126
Figure 80. Instantaneous Particle Trace and Velocity Field, Oscillatory Motion, $M=0.3$, $\alpha=12^\circ$ (Downstroke), $\alpha(t)=13^\circ\pm 2.5^\circ\sin(\omega t)$, $k=0.10$, $Re=2\times 10^6$	127
Figure 81. C_l vs α , Oscillatory Motion, $M=0.3$, $\alpha(t)=9^\circ\pm 5^\circ\sin(\omega t)$, $k=0.2$, $Re=4\times 10^6$	130
Figure 82. C_m vs α , Oscillatory Motion, $M=0.3$, $\alpha(t)=9^\circ\pm 5^\circ\sin(\omega t)$, $k=0.2$, $Re=4\times 10^6$	131
Figure 83. Pressure Distribution, Oscillatory Motion, $M=0.3$, $\alpha=11.9^\circ$ (Upstroke), $\alpha(t)=9^\circ\pm 5^\circ\sin(\omega t)$, $k=0.2$, $Re=4\times 10^6$	132
Figure 84. Pressure Distribution, Oscillatory Motion, $M=0.3$, $\alpha=13.7^\circ$ (Downstroke), $\alpha(t)=9^\circ\pm 5^\circ\sin(\omega t)$, $k=0.2$, $Re=4\times 10^6$	133
Figure 85. Pressure Distribution, Oscillatory Motion, $M=0.3$, $\alpha=13.0^\circ$ (Downstroke), $\alpha(t)=9^\circ\pm 5^\circ\sin(\omega t)$, $k=0.2$, $Re=4\times 10^6$	134
Figure 86. Pressure Distribution, Oscillatory Motion, $M=0.3$, $\alpha=10.5^\circ$ (Downstroke), $\alpha(t)=9^\circ\pm 5^\circ\sin(\omega t)$, $k=0.2$, $Re=4\times 10^6$	135

Figure 87. Pressure Distribution, Oscillatory Motion, $M=0.3$, $\alpha=8.9^\circ$ (Downstroke), $\alpha(t)=9^\circ\pm5^\circ\sin(\omega t)$, $k=0.2$, $Re=4\times10^6$	136
Figure 88. C_l vs α , Oscillatory Motion, $M=0.3$, $\alpha(t)=10^\circ\pm5.5^\circ\sin(\omega t)$, $k=0.10$, $Re=4\times10^6$	138
Figure 89. C_m vs α , Oscillatory Motion, $M=0.3$, $\alpha(t)=10^\circ\pm5.5^\circ\sin(\omega t)$, $k=0.10$, $Re=4\times10^6$	139
Figure 90. C_l vs α , Oscillatory Motion, $M=0.3$, $\alpha(t)=11^\circ\pm5^\circ\sin(\omega t)$, $k=0.10$, $Re=4\times10^6$	142
Figure 91. C_m vs α , Oscillatory Motion, $M=0.3$, $\alpha(t)=11^\circ\pm5^\circ\sin(\omega t)$, $k=0.10$, $Re=4\times10^6$	143
Figure 92. Instantaneous Particle Trace, Oscillatory Motion, $M=0.3$, $\alpha=15^\circ$ (Downstroke), $\alpha(t)=11^\circ\pm5^\circ\sin(\omega t)$, $k=0.10$, $Re=4\times10^6$	144
Figure 93. Velocity Field, Oscillatory Motion, $M=0.3$, $\alpha=15^\circ$ (Downstroke), $\alpha(t)=11^\circ\pm5^\circ\sin(\omega t)$, $k=0.10$, $Re=4\times10^6$	145
Figure 94. Instantaneous Particle Trace, Oscillatory Motion, $M=0.3$, $\alpha=14^\circ$ (Downstroke), $\alpha(t)=11^\circ\pm5^\circ\sin(\omega t)$, $k=0.10$, $Re=4\times10^6$	146
Figure 95. Velocity Field, Oscillatory Motion, $M=0.3$, $\alpha=14^\circ$ (Downstroke), $\alpha(t)=11^\circ\pm5^\circ\sin(\omega t)$, $k=0.10$, $Re=4\times10^6$	147
Figure 96. Pitching Moment Derivation	153

ACKNOWLEDGEMENTS

My sincere appreciation goes to Professor Ekaterinaris, for with out his vast knowledge of CFD, patience, and insightful guidance, I would not have been able to complete this thesis.

I would also like to acknowledge Professor M. Platzer, who during the course of my studies has offered me a great deal more than just an understanding of Computational Fluid Dynamics. During the many hours spent discussing aerodynamics, science, and education my respect and admiration for Professor Platzer has only deepened.

Finally, I would like to thank Tony Cricelli for sharing his seemingly unlimited knowledge of computers, operations systems and programming languages.

I. INTRODUCTION

A. BACKGROUND

The development of numerical solution methods for two-dimensional Navier-Stokes equations during the past few years provides new tools for the investigation and prediction of airfoil flows. Of great interest is the study of flow separation on airfoils in unsteady motion which is usually referred to as the dynamic stall phenomenon. McCroskey et al [Ref. 1] performed a series of careful experiments which serve as valuable benchmark data. More recently, Lorber and Carta [Ref. 2] contributed important additional experimental dynamic stall information for a Sikorsky airfoil. They also investigated incipient torsional stall flutter [Ref. 3] and found that small-amplitude airfoil oscillations near static stall may be unstable.

For a pitching airfoil the instantaneous work done on the fluid by the airfoil due to its motion is the product of the pitching moment about the axis of rotation and the differential change in angle of attack. This product usually is a positive quantity. However, if the net work per cycle of oscillation were to become negative then the fluid would be doing work on the airfoil. Once the airfoil begins to extract energy from the freestream, the amplitude of the oscillation will grow and finally diverge. This condition is known as stall flutter. Normally, flutter of an airfoil is due to a combination of torsion and bending. However, in this case flutter is caused by a single degree of freedom oscillatory motion. During a cycle of oscillation the lift coefficient and the pitching moment coefficient plotted versus angle of attack produce a hysteresis loop. It is the

pitching moment hysteresis loop that provides an indication of incipient stall flutter. As shown by Carta and Niebanck [Ref. 4], clockwise pitching moment loops represent negative aerodynamic damping and therefore cause oscillations of a free airfoil to grow in amplitude, while counterclockwise loops cause such oscillations to decay. Hence torsional flutter will occur as soon as the area of the clockwise loop exceeds that of the counterclockwise loop. The aerodynamics of small-amplitude airfoil torsional oscillations near stall need to be investigated experimentally and computationally in order to examine the stall flutter mechanism.

B. PURPOSE

The first objective of this investigation is to test an unsteady, compressible Navier-Stokes code (Ns2.f) using an Alternating-Direction-Implicit (ADI) scheme based on the the Beam-Warming [Ref. 5] approximate factorization method to determine its ability to obtain realistic airfoil flow solutions for a variety of flow regimes is examined. The accuracy of the numerical solution is investigated by comparing the computed solutions with available experimental data. Test cases include steady-state flow solutions at various flow speeds and angles of attack, as well as, unsteady flow solutions over rapidly pitching and harmonically oscillating airfoils. In addition, the accuracy of the Navier-Stokes solutions are further explored by comparing each case with an unsteady, inviscid, incompressible, panel code (U2diif.f), and with a steady, incompressible, viscous/inviscid interaction code (Incompbl.f). The final and principal objective of this study is to determine the influence of mildly separated flow during part of a harmonic oscillation cycle on blade stability. Results are presented for NACA 0012 airfoils showing the influence of various parameters.

Flow field details are also included in order to provide a better understanding of certain flow features that may lead to stall flutter.

II. GOVERNING EQUATIONS

The continuity equation, the momentum equation, and the energy equation must be solved simultaneously in order to obtain a flow solution of a compressible viscous fluid about a body. A complete derivation of these equation can be found in various texts, eg., Anderson [Ref. 6]. However, main steps of the derivations are presented in the following sections.

A. CONTINUITY EQUATION

The continuity equation is the result of applying the physical principle of the conservation of mass to a finite control volume fixed in space. Simply stated the net flow out of a control volume through its bounding surface must be equal to the time rate of change of the mass inside the control volume. For any arbitrary control volume, the continuity equation can be expressed as

$$\frac{\partial \rho}{\partial t} + \nabla(\rho \vec{V}) = 0 \quad (1)$$

which for a two-dimension Cartesian Coordinate system becomes

$$\frac{\partial \rho}{\partial t} + \frac{\partial(\rho u)}{\partial x} + \frac{\partial(\rho w)}{\partial z} = 0 \quad (2)$$

B. MOMENTUM EQUATIONS

The equation for the conservation of momentum is obtained by applying Newton's second law, which state that the net force acting on a fluid particle is equal to the time rate of change of linear momentum of the fluid particle. In

Cartesian coordinates the momentum equations can be expressed as follows

$$\frac{\partial(\rho u)}{\partial t} + \frac{\partial(\rho u^2 + p)}{\partial x} + \frac{\partial(\rho u w)}{\partial z} = \frac{\partial \tau_{xx}}{\partial x} + \frac{\partial \tau_{xz}}{\partial z} \quad (3)$$

and in the y-direction.

$$\frac{\partial(\rho w)}{\partial t} + \frac{\partial(\rho u w)}{\partial x} + \frac{\partial(\rho w^2 + p)}{\partial z} = \frac{\partial \tau_{xz}}{\partial x} + \frac{\partial \tau_{zz}}{\partial z} \quad (4)$$

Stress terms are as follows

$$\begin{aligned} \tau_{xx} &= \frac{2}{3}\mu \left(2\frac{\partial u}{\partial x} - \frac{\partial w}{\partial z} \right) \\ \tau_{zz} &= \frac{2}{3}\mu \left(2\frac{\partial w}{\partial z} - \frac{\partial u}{\partial x} \right) \\ \tau_{xz} &= \mu \left(\frac{\partial w}{\partial x} + \frac{\partial u}{\partial z} \right) \end{aligned} \quad (5)$$

C. ENERGY EQUATION

The conservation law form of the energy equation is derived by applying the first law of thermodynamics ($dE=dQ+dW$) to a fluid particle. This leads to

$$\begin{aligned} \frac{\partial E}{\partial t} + \frac{\partial}{\partial x}[(E+p)u] + \frac{\partial}{\partial z}[(E+p)w] = \\ \frac{\partial}{\partial x}(\mu \tau_{xx} + w \tau_{xz} - \dot{q}_x) + \frac{\partial}{\partial z}(\mu \tau_{xz} + w \tau_{zz} - \dot{q}_z) \end{aligned} \quad (6)$$

where the total energy per unit volume and the heat flux are given by

$$E = (e + 1/2 V^2)\rho, \quad \dot{q}_i = -k \partial T / \partial x_i \quad (7)$$

Here k is the thermal conductivity.

D. CONSERVATION FORM OF GOVERNING EQUATIONS

The starting point for the numerical algorithm which is presented in the next section is the strong conservation law form of the two-dimensional Navier-Stokes equations. The non-dimensionalized vector form of the governing equations in conservation law form for a Cartesian coordinate system is:

$$\frac{\partial \mathbf{q}}{\partial t} + \frac{\partial \mathbf{F}}{\partial x} + \frac{\partial \mathbf{G}}{\partial z} = \frac{1}{\text{Re}} \left(\frac{\partial \mathbf{F}_v}{\partial x} + \frac{\partial \mathbf{G}_v}{\partial z} \right) \quad (8)$$

where,

$$\mathbf{q} = \begin{bmatrix} \rho \\ \rho u \\ \rho w \\ e \end{bmatrix}, \quad \mathbf{F} = \begin{bmatrix} \rho u \\ \rho u^2 + p \\ \rho u w \\ (e + p)u \end{bmatrix}, \quad \mathbf{G} = \begin{bmatrix} \rho w \\ \rho w u \\ \rho w^2 + p \\ (e + p)w \end{bmatrix}, \quad \mathbf{F}_v = \begin{bmatrix} 0 \\ \tau_{xx} \\ \tau_{xz} \\ f_4 \end{bmatrix}, \quad \mathbf{G}_v = \begin{bmatrix} 0 \\ \tau_{xz} \\ \tau_{zz} \\ g_4 \end{bmatrix} \quad (9)$$

with,

$$\begin{aligned} \tau_{xx} &= \frac{4}{3} \mu \left(u_x - \frac{1}{2} w_z \right) \\ \tau_{xz} &= \mu (u_z - w_x) \\ \tau_{zz} &= \frac{4}{3} \mu \left(w_z - \frac{1}{2} u_x \right) \\ f_4 &= u \tau_{xx} + w \tau_{xz} + \frac{\mu}{\text{Pr}(\gamma - 1)} a_x^2 \\ g_4 &= u \tau_{xz} + w \tau_{zz} + \frac{\mu}{\text{Pr}(\gamma - 1)} a_z^2 \end{aligned} \quad (10)$$

Here the pressure is related to the conservation variables of \mathbf{q} by the equation

$$p = (\gamma - 1) \left[e - 0.5 \rho (u^2 + v^2) \right] \quad (11)$$

where $\gamma = 1.4$ is the ratio of specific heats, and a is the local speed of sound given by, $a^2 = \gamma p / \rho$.

The density and the velocities are non-dimensionalized with the freestream density ρ_∞ and the free stream speed of sound a_∞ , respectively. The total energy is normalized by $a_\infty^2 \rho_\infty$. The time (t) scales as $t^* = t a_\infty / c$, where (c) is a characteristic length, such as the chord length. The Euler equations are obtained from Equation (8) by dropping the viscous terms. The strong form is chosen because it enables shock capturing.

III. SOLUTION METHODS

A. POTENTIAL FLOW METHOD (U2DIIIF.F)

For inviscid incompressible flow the conservation equations reduce to the Laplace equation which can be solved in a number of ways. We present here a brief outline of the widely used panel method for both steady and unsteady airfoil flow.

1. Panel Method for Steady Airfoil Flows

The frame of reference for the formulation of the steady flow problem is a fixed (x,y) coordinate system located at the leading edge of the airfoil. The freestream velocity is represented by $+V_\infty$ and the x-axis passes from the leading edge through the trailing edge of the airfoil.

In order to formulate a method for computing the flow around an airfoil, the airfoil surface is divided into (n) straight line segments or panels. The end points of the panels are called nodes, and since there are (n) panels there are then (n+1) nodes. Complex airfoil geometries can therefore be modeled with a greater number of nodes and panels. The trailing edge panel is the first panel, and the next panel continues on the lower surface in a clockwise manner until the n^{th} panel is reached at the trailing edge of the upper surface.

Now that the frame of reference has been specified, two additional vectors must be defined, the unit normal vector \mathbf{n}_i , which is always perpendicular to the (i^{th}) panel and directed outward from the airfoil surface and the unit tangential vector \mathbf{t}_i , which is parallel to the (i^{th}) panel and is directed from the (n) node to the (n+1) node.

Two types of singularities are sufficient to model lifting airfoil flows. U2diif.f places uniform source distributions q_j and a uniform vorticity distribution γ on each of the j -panels. Both singularities satisfy Laplace's equation, a linear homogeneous second order partial differential equation. Since the solutions to linear PDE's can be superimposed on each other, a simple flow can be added to another simple flow and so on, until a very complicated flow field is created.

The flow field around an airfoil, represented by the velocity potential, can be constructed from the potential of the freestream flow added to the velocity potential of source and vorticity distributions, hence

$$\Phi = \varphi_{\infty} + \varphi_s + \varphi_v \quad (12)$$

where,

$$\varphi_{\infty} = V_{\infty} (x \cos \alpha + y \sin \alpha) \quad (13)$$

$$\varphi_s = \int \frac{q(s)}{2\pi} \ln r \, ds \quad (14)$$

$$\varphi_v = - \int \frac{\gamma(s)}{2\pi} \theta \, ds \quad (15)$$

summation of the three potentials yields

$$\Phi = V_{\infty} (x \cos \alpha + y \sin \alpha) + \int \frac{q(s)}{2\pi} \ln r \, ds - \int \frac{\gamma(s)}{2\pi} \theta \, ds \quad (16)$$

Equation (16) can now be evaluated at any point in the flow field by evaluating the integrals along the airfoil contour (s), where the flow field point is located at

a distance (r) at an angle (θ) measured from a point on the airfoil. Introducing n panels and then summing the contributions of each panel yields

$$\Phi = V_{\infty} + (x \cos \alpha + y \sin \alpha) + \sum_{j=1}^n \int_{j^{\text{th}} \text{ panel}} \left(\frac{q_j}{2\pi} \ln r + \frac{\gamma}{2\pi} \theta \right) ds \quad (17)$$

Once the boundary conditions are defined the system of (n) equations can be solved for ($n+1$) unknowns.

Next, it is useful to introduce the concept of influence coefficients. An influence coefficient is the velocity induced at a point in the flow field (field point) by a unit strength singularity, source or vorticity, placed anywhere within this field. U2diif.f places these points on each panel. A detailed description of the use of influence coefficients is found in Teng [Ref. 7].

For the steady flow problem the influence coefficients are given in Table 1.

TABLE 1. INFLUENCE COEFFICIENTS

A_{ij}^n	Normal component induced at i^{th} control point by unit source distribution on j^{th} panel.
A_{ij}^t	Tangential component induced at i^{th} control point by unit source distribution on j^{th} panel.
B_{ij}^n	Normal component induced at i^{th} control point by unit vorticity distribution on j^{th} panel.
B_{ij}^t	Tangential component induced at i^{th} control point by unit vorticity distribution on j^{th} panel.
θ_{ij}	Angle of control point (i) and panel (j) measured from x-axis.

There are only two boundary conditions that must be satisfied in order to solve the lifting airfoil flow problem. The first boundary condition is the condition that the flow remains tangent to the airfoil surface and the second condition is that the pressures on the upper and lower trailing edge panels must be equal. This condition is known as the Kutta condition. Pressure is related to velocity through Bernoulli's equation for steady potential flow, which allows the Kutta condition to be expressed as

$$\left(V^{\text{tangent}}\right)_{\text{lower}} = -\left(V^{\text{tangent}}\right)_{\text{upper}} \quad (18)$$

The flow tangency condition is expressed as

$$\left(V^{\text{normal}}\right)_i = 0, \quad i = 1, 2, \dots, n \quad (19)$$

Equation (18), the Kutta condition, using the influence coefficient concept is expressed as follows

$$\begin{aligned} -\sum_{j=1}^n [A_{1j}^t q_j] - \gamma \sum_{j=1}^n [B_{1j}^t] - V_{\infty} \cos(\alpha - \theta_1) = \\ \sum_{j=1}^n [A_{nj}^t q_j] + \gamma \sum_{j=1}^n [B_{nj}^t] + V_{\infty} \cos(\alpha - \theta_n) \end{aligned} \quad (20)$$

Equation (19) the flow tangency condition, becomes, using the influence coefficient form

$$\sum_{j=1}^n [A_{1j}^n q_j] + \gamma \sum_{j=1}^n [B_{1j}^n] + V_{\infty} \sin(\alpha - \theta_1) = 0, \quad i = 1, 2, \dots, n \quad (21)$$

These equations can then be written in the following matrix form

$$\begin{bmatrix} a_{1,1} & . & . & . & a_{1,n+1} \\ . & . & . & . & . \\ . & . & . & . & . \\ . & . & . & . & . \\ a_{n+1,1} & . & . & . & a_{n+1,n+1} \end{bmatrix} \begin{bmatrix} q_1 \\ q_2 \\ . \\ q_n \\ \gamma \end{bmatrix} = \begin{bmatrix} b_1 \\ b_2 \\ . \\ b_n \\ b_{n+1} \end{bmatrix} \quad (22)$$

and solved with the method of Gauss Elimination with Partial Pivoting.

2. Unsteady Numerical Formulation

A brief and concise description of the unsteady numerical formulation is found in Krainer [Ref. 8]. To model unsteady flow around an airfoil using the panel method, N unknown source strengths and one unknown vorticity strength are located along the airfoil, a wake panel of unknown vorticity strength, length and orientation is attached to the trailing edge of the airfoil. This makes a total of $N+4$ unknowns. The flow tangency requirement at each of the N panels represents a system of N equations. Using influence coefficients and using the subscript k to count time, the tangential flow condition of the i^{th} element is written as follows

$$\begin{aligned} & \sum_{j=1}^n \left[A_{ij}^n (q_j)_k \right] + \gamma_k \sum_{j=1}^n B_{ij}^n + \left[\left(\mathbf{V}_\infty + (U(t)\mathbf{i} + V(t)\mathbf{j}) + \Omega(t)(x\mathbf{i} - y\mathbf{j}) \right)_i n_i \right]_k \\ & + (\gamma_w)_k (B_{i,n+1}^n)_k + \sum_{m=1}^{k-1} \left[(C_{im}^n) (\Gamma_{m-1} - \Gamma_m)_k \right] = 0 \quad i = 1, 2, \dots, n \end{aligned} \quad (23)$$

where V_∞ is the mean velocity, $(U(t)\mathbf{i} + V(t)\mathbf{j})$ is a time dependent translational velocity and $\Omega(t)$ is a rotational velocity. The vectors \mathbf{i} and \mathbf{j} are in the airfoil fixed coordinate system.

The Kutta condition is a single equation that determines the circulation around the airfoil. In this case the pressures at the upper and lower surface are equated at the midpoints of panels adjacent to the trailing edge (i.e., the first and last panel)

$$\left[(v_l^t)_k \right]^2 + \left[(v_N^t)_k \right]^2 = 2 \left[\frac{\partial(\phi_n - \phi_l)}{\partial t} \right]_k = 2 \left[\frac{\partial \Gamma}{\partial t} \right]_k = 2 l \frac{\gamma_k - \gamma_{k-1}}{t_k - t_{k-1}} \quad (24)$$

The Helmholtz theorem is another single equation that provides a relation for the strength of the vorticity distribution along the wake element. The Helmholtz theorem states that any change in circulation around an airfoil must be countered by a change in vorticity in the wake of equal magnitude but of opposite sign. This theorem can be written as follows

$$\Delta_k (\gamma_w)_k = l (\gamma_{k-1} - \gamma_k) \quad (25)$$

where l is the length of each individual wake element and γ its vorticity strength. Therefore, the vorticity in the wake element is equal to the negative change in circulation around the airfoil with respect to the $k-1$ timestep.

To acquire the two additional equations required to solve for the $N+4$ unknowns, assumptions about the geometry of the wake panel are made. First, the wake panel is oriented in the direction of the local resultant velocity at its midpoint, as viewed in the (moving) airfoil frame of reference.

$$\tan \Theta_k = \frac{(v_w^y)_k}{(v_w^x)_k} \quad (26)$$

$(v^y_w)_k$ and $(v^x_w)_k$ are the x- and y-velocity components at the midpoint of each wake panel. Second, the length of the wake panel is assumed proportional to the magnitude of the local resultant velocity at its midpoint and to the timestep.

$$\Delta_k = \sqrt{[(v^x_w)_k]^2 + [(v^y_w)_k]^2} (t_k - t_{k-1}) \quad (27)$$

The nonlinearities in the Kutta condition and in the wake panel assumptions necessitate an iterative solution procedure.

B. VISCOUS/INVISCID INTERACTION METHOD (INCOMPBL.F)

The theory and numerical methods presented in this section are taken from the work of Cebeci and Bradshaw [Ref. 9] and the investigations performed by Krainer [Ref. 8] and Snir [Ref. 10]. As stated in the introduction the results from the Navier-Stokes code (Ns2.f) were compared with a viscous/inviscid interaction method code (Incompbl.f) made available by Cebeci. An abbreviated description of this method is given in this section. For a complete description see the original publications, References 8 and 9.

The governing principle behind the viscous/inviscid interaction method is an approximation to the Navier-Stokes equation that allows a flowfield to be divided into an inner viscous region and an outer inviscid region when the Reynolds number is sufficiently large. This concept of a thin viscous layer near the surface of a body and an outer region where these viscous effects are small compared to the inertial effects is known as the boundary layer theory. Unlike the Laplace equation, which is the governing equation for potential flow, the

thin shear layer equations are nonlinear

$$\begin{aligned}\frac{\partial u}{\partial x} + \frac{\partial v}{\partial y} &= 0 \\ u \frac{\partial u}{\partial x} + v \frac{\partial v}{\partial y} &= u_e \frac{du_e}{dx} + v \frac{\partial}{\partial y} \left[\left(1 + \frac{v_t}{v} \right) \frac{\partial u}{\partial y} \right]\end{aligned}\tag{28}$$

with the boundary conditions

$$\begin{aligned}y=0, & \quad u=v=0, \\ y=\infty, & \quad u=u_e(x)\end{aligned}\tag{29}$$

The direct boundary layer method solution to the boundary layer equations by the Keller Box Method involves four steps. First the boundary layer equations are transformed into a system of first order differential equations. Next the Keller box method is used to approximate the first order differential equations by simple centered differences and two-point averages, using values at the corners of one difference molecule only. Newton's method is used to linearize the resulting algebraic equation. The Keller block elimination method is then used to solve the resulting block tridiagonal system. The procedure described above does not provide solutions to flows that are separated or have regions of reverse flow.

1. Interaction Method

The interactive boundary layer method provides a special coupling between the inner viscous flow and the outer inviscid flow, which enables reverse and separated flows to be calculated. In such areas, the external

velocity is substantially changed by the viscous effects and can no longer be considered as a known boundary condition for the boundary layer flow.

The general approach to the solution is the same as for the direct method with modifications. Since the outer flow is unknown, the velocity at the edge of the boundary layer is given by the interaction law and is written as

$$u(x, y_e) = u_{el} + \frac{1}{\pi} \int \frac{d}{d\xi} (u_e \delta^*) \frac{d\xi}{x - \xi} \quad (30)$$

where $u_e(x, y_e)$ is the total velocity at the edge of the boundary layer, $u_{el}(x)$ is the velocity computed by the inviscid panel method, δ^* is the displacement thickness, and the integral term is known as the Hilbert integral.

The following transformations are used to transform the boundary layer equation into a system of first order differential equations

$$\begin{aligned} \xi &= \frac{x}{L}, \quad \eta = \sqrt{R_L} \frac{y}{L}, \quad R_L = \frac{u_o L}{\nu} \\ f(x, \eta) &= \frac{1}{\sqrt{u_o \nu x}} \psi(x, y), \quad w = \frac{u_e(x, y)}{u_o} \end{aligned} \quad (31)$$

The boundary layer equation takes the form

$$\begin{aligned} f' &= U, \quad U' = V, \quad W' = 0, \\ (bV)' + \frac{1}{2} x W \frac{\partial W}{\partial x} &= x \left(U \frac{\partial U}{\partial x} - V \frac{\partial f}{\partial x} \right) \end{aligned} \quad (32)$$

with boundary conditions:

$$\begin{aligned} \eta=0, \quad U(x,0)=0, \quad f(x,0)=0, \\ \eta=\eta_e, \quad U(x,\eta_e)=W(x,\eta_e) \end{aligned} \quad (33)$$

The velocity at the edge of the boundary layer now becomes

$$w(x, \eta_e) = \frac{u_{el}(x)}{u_o} + \frac{1}{\pi} \int \frac{d}{d\xi} \left(\sqrt{\frac{v\xi}{u_o}} [W(\xi, \eta_e)\eta_e - f(\xi, \eta_e)] \right) \frac{d\xi}{x - \xi} \quad (34)$$

The finite difference box method is used to solve the equations, in the same way it was used for the direct case, but with two additions. First in areas of flow reversal the $u\partial u/\partial x$ is omitted to assure stable integration. And second, the edge velocity is approximated by the relation presented in the next section.

By using central differencing to approximate the differential equations, a system of nonlinear algebraic equations is obtained for the unknown variables (which are f , U , V , and W). To solve the system of equations, the system is linearized by the Newton iterative procedure, and the resulting linear system is solved for the new unknown variables which are the increments δf , δU , δV , and δW .

The solution procedure is repeated until the change in the increments is negligible compared to the preceding iteration. The iterative process is performed again at the next downstream station.

2. Interactive Model

The interactive model is used to couple the boundary layer to the external flow. It is needed in areas where strong interaction occurs, and both the boundary layer and the outer flow must be solved simultaneously. The external velocity is assumed to consist of a potential flow term and a correction term due to viscous effects. $[u_e(x) = u_{el}(x) + u_e\delta(x)]$

The normal velocities at the surface of the airfoil, induced by sources distributed on the surface, displace the streamlines from the surface in the same way that the actual boundary layer displaces them.

Several assumptions are made in order to express the correction term in the form of the Hilbert integral. First, the surface is approximated to be a flat plate, and the normal velocity is then half the local source strength $\sigma(x)$. Second, the inviscid velocity does not change across the boundary layer: Therefore, the local horizontal velocity induced by the source distribution, is the correction term to the inviscid velocity, and can be represented by the Hilbert integral

$$\frac{1}{\pi} \int \frac{\sigma(\xi)}{x - \xi} d\xi = \frac{1}{\pi} \int \frac{d}{d\xi} (u_e \delta^*) \frac{d\xi}{x - \xi} \quad (35)$$

The integration is carried out on all the sources on the surface. The Hilbert integral is then approximated by a finite series

$$\frac{1}{\pi} \int \frac{d}{d\xi} (u_e \delta^*) \frac{d\xi}{x - \xi} = \sum_{k=1}^K c_{ik} (u_e \delta^*)^k \quad (36)$$

where c_{ik} is a matrix of interaction coefficients which are functions of the geometry only.

Since the computation of $u_e \delta$ involves values of δ^* downstream of the current x location, which are not known yet, these terms are taken from the previous iteration using a relaxation formula.

3. Turbulence Model

The turbulence model used in the code is the Cebeci-Smith model [Ref. 11] and Michel's method is used to predict the transition from laminar to turbulent flow.

C. EULER AND NAVIER-STOKES CODE (NS2.F)

In order to facilitate the numerical implementation for arbitrary complex flow domains, the Navier-Stokes equations are transformed to a generalized coordinate system, (ξ, ζ) , using the transformations

$$\begin{aligned}\xi &= \xi(x, z) \\ \zeta &= \zeta(x, z)\end{aligned}\tag{37}$$

The grid spacing in the curvilinear space is uniform and of unit length so that unweighted differencing schemes can be employed for the numerical implementation. The grid points in the Cartesian system, referred to as the physical domain, correspond via a one to one relationship to the points of the curvilinear transformed system, referred to as the computational domain. Singularities of the transformation may occur on the computational boundaries. Such singularities occur for grids with multiple connected regions. The transformation of the governing equations from the physical domain to the computational domain is obtained in most cases by numerically evaluating the metrics and the Jacobian of the transformation. The derivatives with respect to the x, y variables can be expressed in terms of the new variables by the chain rule.

$$\begin{aligned}\frac{\partial}{\partial x} &= \xi_x \frac{\partial}{\partial \xi} + \zeta_x \frac{\partial}{\partial \zeta} \\ \frac{\partial}{\partial z} &= \xi_z \frac{\partial}{\partial \xi} + \zeta_z \frac{\partial}{\partial \zeta}\end{aligned}\tag{38}$$

The metrics and the Jacobian of the transformation are given by

$$\xi_x = J z_\zeta, \quad \zeta_x = -J z_\xi, \quad (39)$$

$$\xi_z = -J x_\zeta, \quad \zeta_z = J x_\xi, \quad (40)$$

$$J = \frac{1}{(x_\xi z_\zeta - x_\zeta z_\xi)} \quad (41)$$

The Navier-Stokes equations written in generalized curvilinear coordinates retain the strong conservation law form expressed by Equation (8). The governing equation for generalized curvilinear coordinates is

$$\frac{\partial \hat{\mathbf{q}}}{\partial t} + \frac{\partial \hat{\mathbf{F}}}{\partial \xi} + \frac{\partial \hat{\mathbf{G}}}{\partial \zeta} = \frac{1}{\text{Re}} \left[\frac{\partial \hat{\mathbf{F}}_v}{\partial \xi} + \frac{\partial \hat{\mathbf{G}}_v}{\partial \zeta} \right] \quad (42)$$

The conservation variable vector $\hat{\mathbf{q}}$ and the inviscid fluxes $\hat{\mathbf{F}}$ and $\hat{\mathbf{G}}$ in the transformed space are given by

$$\hat{\mathbf{q}} = \frac{1}{J} \begin{bmatrix} \rho \\ \rho u \\ \rho w \\ e \end{bmatrix}, \quad \hat{\mathbf{F}} = \frac{1}{J} \begin{bmatrix} \rho U \\ \rho u U + \xi_x p \\ \rho w U + \xi_z p \\ (e + p)U - \xi_x p \end{bmatrix}, \quad \hat{\mathbf{G}} = \frac{1}{J} \begin{bmatrix} \rho W \\ \rho W u + \zeta_x p \\ \rho w W + \zeta_z p \\ (e + p)W - \zeta_x p \end{bmatrix} \quad (43)$$

where U and W are the contravariant velocity components along the ξ and ζ directions respectively, given by:

$$U = \xi_t + \xi_x u + \xi_z w, \quad W = \zeta_t + \zeta_x u + \zeta_z w \quad (44)$$

The viscous flux terms are transformed as

$$\hat{\mathbf{F}}_v = \frac{1}{J} (\xi_x \mathbf{F}_v + \xi_z \mathbf{G}_v), \quad \hat{\mathbf{G}}_v = \frac{1}{J} (\zeta_x \mathbf{F}_v + \zeta_z \mathbf{G}_v) \quad (45)$$

with the stress terms from Equation (10) expressed in terms of the transformed variables ξ, ζ as

$$\begin{aligned}
\tau_{xx} &= \frac{4}{3}\mu \left[(\xi_x u_\xi + \zeta_x u_\zeta) - \frac{1}{2}(\xi_z w_\xi + \zeta_z w_\zeta) \right] \\
\tau_{xz} &= \mu \left[(\xi_z u_\xi + \zeta_z u_\zeta) + (\xi_x w_\xi + \zeta_x w_\zeta) \right] \\
\tau_{zz} &= \frac{4}{3}\mu \left[(\xi_z w_\xi + \zeta_z w_\zeta) - \frac{1}{2}(\xi_x u_\xi + \zeta_x u_\zeta) \right] \\
f_4 &= u\tau_{xx} + w\tau_{xz} + \frac{\mu}{\text{Pr}(\gamma-1)} \left[\xi_x \frac{\partial a^2}{\partial \xi} + \zeta_x \frac{\partial a^2}{\partial \zeta} \right] \\
g_4 &= u\tau_{xz} + w\tau_{zz} + \frac{\mu}{\text{Pr}(\gamma-1)} \left[\xi_z \frac{\partial a^2}{\partial \xi} + \zeta_z \frac{\partial a^2}{\partial \zeta} \right]
\end{aligned} \tag{46}$$

When the thin layer approximation [Ref. 12] to the two-dimensional conservation law form of the governing equations is applied, they take the following form

$$\frac{\partial \hat{\mathbf{q}}}{\partial t} + \frac{\partial \hat{\mathbf{F}}}{\partial \xi} + \frac{\partial \hat{\mathbf{G}}}{\partial \zeta} = \frac{1}{\text{Re}} \left[\frac{\partial \hat{\mathbf{G}}_v}{\partial \zeta} \right] \tag{47}$$

where,

$$\hat{\mathbf{q}} = \frac{1}{J} \begin{bmatrix} \rho \\ \rho u \\ \rho w \\ e \end{bmatrix}, \quad \hat{\mathbf{F}} = \frac{1}{J} \begin{bmatrix} \rho U \\ \rho u U + \xi_x p \\ \rho w U + \xi_z p \\ (e+p)U - \xi_x p \end{bmatrix}, \quad \hat{\mathbf{G}} = \frac{1}{J} \begin{bmatrix} \rho W \\ \rho W u + \zeta_x p \\ \rho W w + \zeta_z p \\ (e+p)W - \zeta_x p \end{bmatrix} \tag{48}$$

The viscous flux term is transformed as

$$\hat{\mathbf{G}}_v = \frac{1}{J} \begin{pmatrix} 0 \\ \mu m_1 u_\zeta + (\mu/3)m_2 \zeta_x \\ \mu m_1 w_\zeta + (\mu/3)m_2 \zeta_x \\ \mu m_1 m_3 + (\mu/3)m_2 m_4 \end{pmatrix} \quad (49)$$

Here,

$$\begin{aligned} m_1 &= \zeta_x^2 + \zeta_z^2 \\ m_2 &= \zeta_x u_\zeta + \zeta_z w_\zeta \\ m_3 &= \frac{1}{2} \frac{\partial}{\partial \zeta} (u^2 + w^2) / 2 + \frac{1}{\text{Pr}(\gamma - 1)} \left[\frac{\partial a^2}{\partial \zeta} \right] \\ m_4 &= \zeta_x u + \zeta_z w \end{aligned} \quad (50)$$

1. Numerical Grids

In order to compute flow solutions of partial differential equations (such as the Navier-Stokes Equations) with finite differences, a discretized version of the physical domain must be generated. During the course of this investigation, several different NACA 0012 airfoil C-type grids were generated using two different grid generation methods. A grid generation code call GRAPE that uses the Poisson differential equation was used in the early stages of investigation. The inviscid and viscous grids shown in Figures 1 and 2 were generated from an algebraic grid generation code. Note the finer resolution of the viscous grid near the airfoil surface. This resolution is required to accurately represent the boundary layer. The flow solutions presented in Chapter IV were computed by using the grids shown in Figures 1 and 2. The

advantage to using an algebraic grid , vice a PDE method or a conformal mapping method, is that it is computationally efficient.

A simple description of the algebraic grid generation method is offered. First the airfoil surface coordinates are unwrapped to form a simple curve, by separating the lower trailing edge from the upper trailing edge. This curve is the starting point for the generation of the computational domain. Lines are drawn normal to the curve and grid points are then located at intervals on these lines. Lines may be clustered near the leading or trailing edge of the airfoil; or at some other area of interest, eg., a shock location. The resolution of the points normal to the surface is achieved by the use of an algebraic function that provides uniform stretching normal to the body surface. Once the grid is created in the computation domain it is then transformed back into the physical domain using inverse transformations.

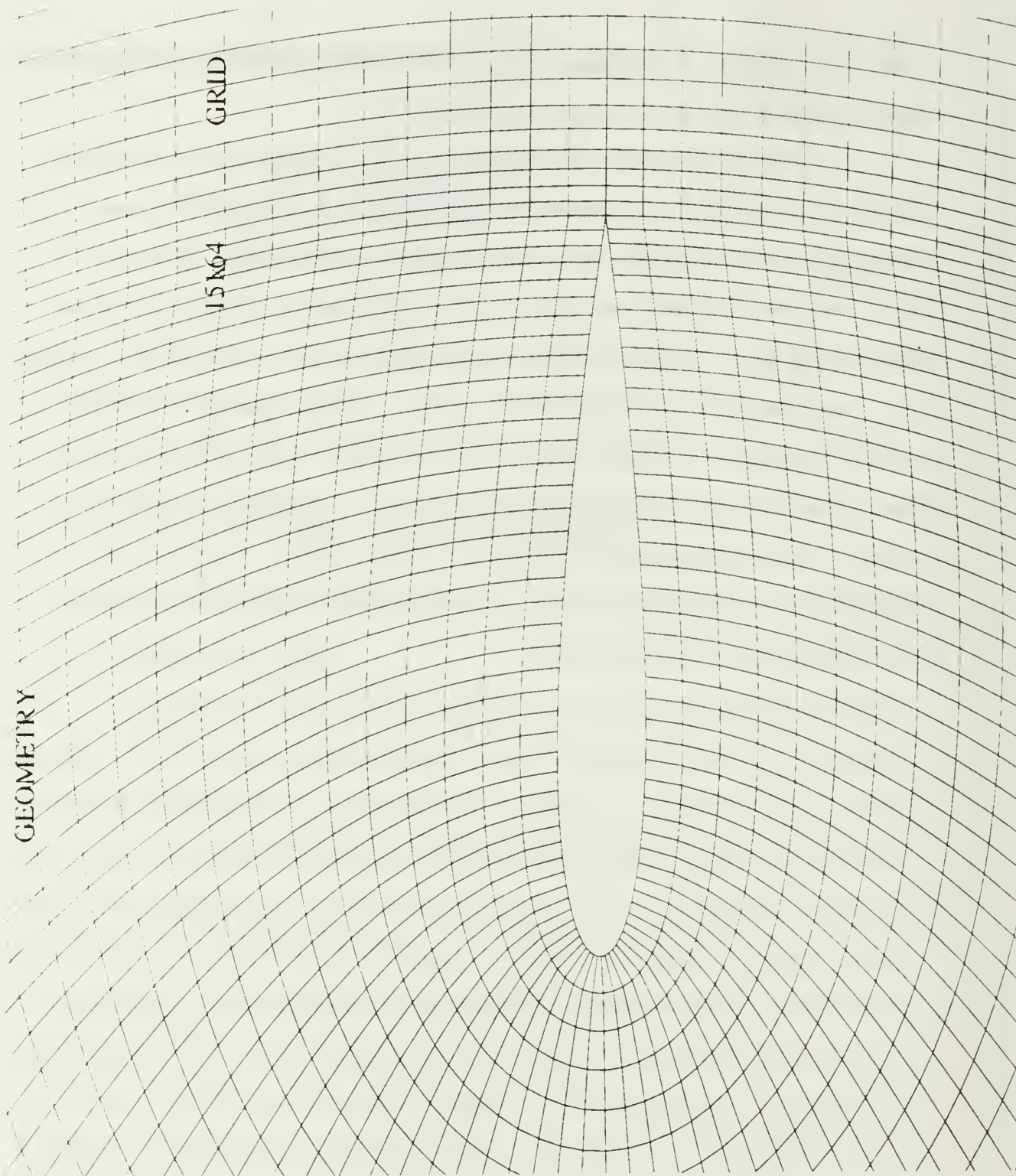


Figure 1. NACA 0012 Inviscid 151x64 C-Grid

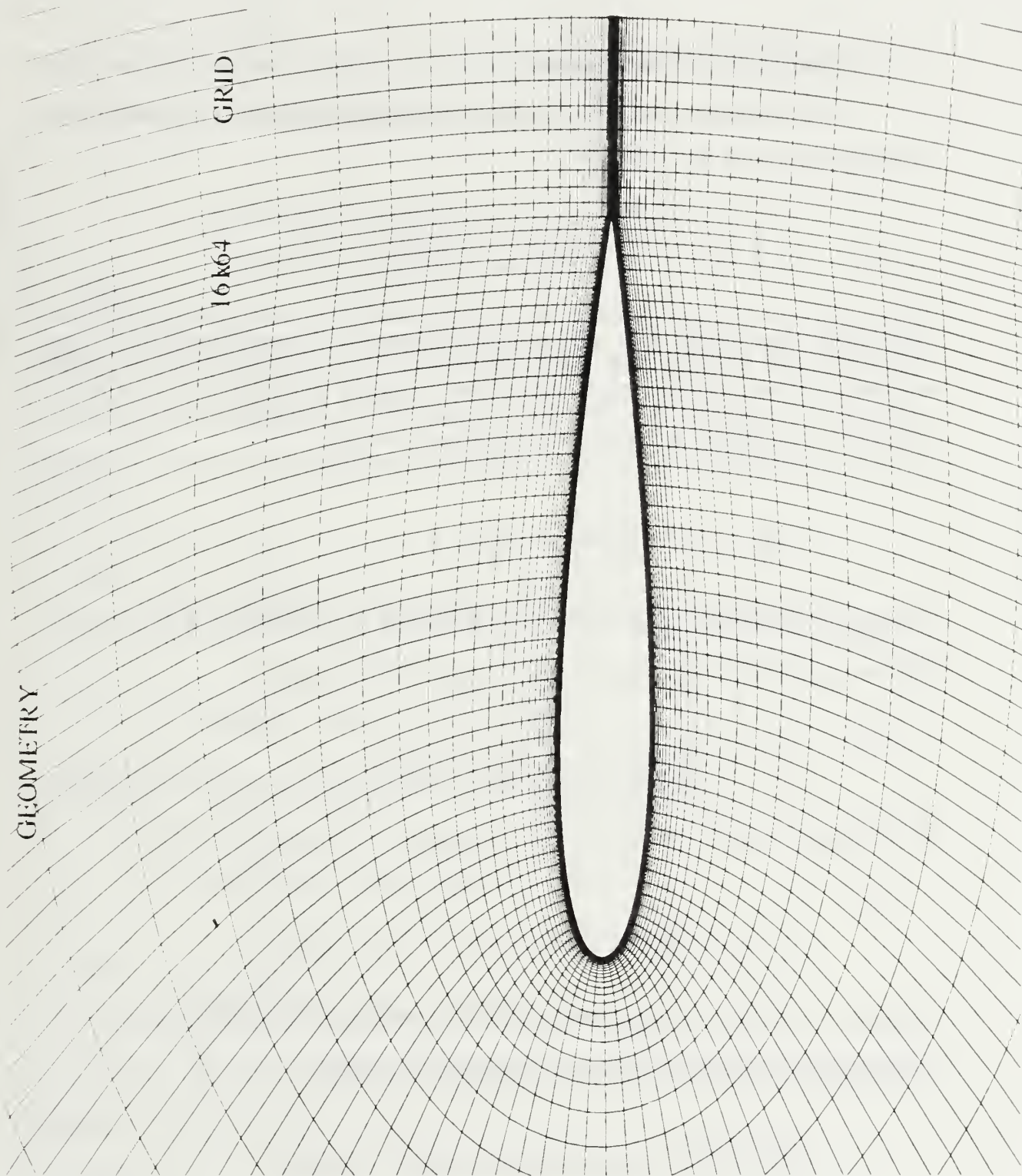


Figure 2. NACA 0012 Viscous 161x64 C-Grid

2. The Numerical Scheme

The integration in time is performed implicitly with a second order accurate scheme of the form

$$\Delta q^n = q^{n+1} - q^n = \frac{\Delta t}{2} \frac{\partial}{\partial t} (\Delta q^n) + \frac{\Delta t}{2} \frac{\partial q^n}{\partial t} + O\left(\frac{\Delta t^2}{2} + \Delta t^3\right) \quad (51)$$

Using this trapezoidal rule differencing scheme to approximate the time derivative of the conservative dependent variable q vector, the unknown conservative variables at the $n+1$ timestep are given by

$$\Delta q^n = q^{n+1} + \frac{\Delta t}{2} \left\{ \left(\frac{\partial q}{\partial t} \right)^n + \left(\frac{\partial q}{\partial t} \right)^{n+1} \right\} \quad (52)$$

The spatial derivatives of the governing equations are discretized using central differences, and the right hand side of Equation (52) becomes

$$\Delta q^n = -\frac{\Delta t}{2} \left\{ (\delta_\xi \hat{F} + \delta_\zeta \hat{G})^n + (\delta_\xi \hat{F} + \delta_\zeta \hat{G})^{n+1} \right\} \quad (53)$$

The nonlinear terms \hat{F} and \hat{G} at the $n+1$ timestep are linearized as follows

$$\hat{F}^{n+1} = \hat{F}^n + \frac{\partial \hat{F}^n}{\partial q} \Delta q^{n+1} + O(\Delta t^2) = \hat{F}^n + \hat{A}^n \Delta q^{n+1} + O(\Delta t^2) \quad (54)$$

where \hat{A}^n is the flux Jacobian matrix given in Appendix A. Substitution of the linearized form of the flux vectors in Equation (54) yields

$$\left\{ [I] + \frac{\Delta t}{2} (\delta_\xi \hat{A}_{i,k}^n + \delta_\zeta \hat{B}_{i,k}^n) \right\} \Delta q_{i,k}^{n+1} = \Delta t \{ \delta_\xi \hat{F}_{i,k}^n - \delta_\zeta \hat{G}_{i,k}^n \} \quad (55)$$

The two-dimensional operator on the left hand side of Equation (55) is approximately factorized as follows:

$$\left\{ [I] + \frac{\Delta t}{2} \delta_{\xi} \hat{A}_{i,k}^n \right\} \left\{ [I] + \frac{\Delta t}{2} \delta_{\zeta} \hat{B}_{i,k}^n \right\} \Delta q_{i,k}^{n+1} = \Delta t \{ \delta_{\xi} \hat{F}_{i,k}^n - \delta_{\zeta} \hat{G}_{i,k}^n \} \quad (56)$$

On the right hand side of Equation (56) an explicit dissipation term D_{expl} , is added for numerical stability. In order to obtain an oscillation free solution a second order dissipation term D_{impl} is added to the left hand side spatial operators. Thus, the complete discretized form of the governing equations becomes

$$\left\{ [I] + \frac{\Delta t}{2} \left(\delta_{\xi} \hat{A}_{i,k}^n + (D_{\text{impl}})_{\xi} \right) \right\} \left\{ [I] + \frac{\Delta t}{2} \left(\delta_{\zeta} \hat{B}_{i,k}^n + (D_{\text{impl}})_{\zeta} \right) \right\} \Delta q_{i,k}^{n+1} = \quad (57)$$

$$\left\{ -\Delta \left[\delta_{\xi} \hat{F}_{i,k}^n - \delta_{\zeta} \hat{G}_{i,k}^n \right] - \epsilon_{\text{expl}} D_{i,k}^n \right\} = (\text{RHS})^n \quad (58)$$

This equation is solved by performing two sweeps as follows:

$$\left\{ [I] + \frac{\Delta t}{2} \left(\delta_{\xi} \hat{A}_{i,k}^n + (D_{\text{impl}})_{\xi} \right) \right\} \Delta q_{i,k}^{*n+1} = (\text{RHS})^n \quad (59)$$

$$\left\{ [I] + \frac{\Delta t}{2} \left(\delta_{\zeta} \hat{B}_{i,k}^n + (D_{\text{impl}})_{\zeta} \right) \right\} \Delta q_{i,k}^{*n+1} = \Delta q_{i,k}^{*n+1} \quad (60)$$

During each sweep the following linear block tridiagonal system of equations is solved

$$a_{i-1,k} \Delta \bar{q}_{i-1,k} + b_{i,k} \Delta \bar{q}_{i,k} + c_{i+1,k} \Delta \bar{q}_{i+1,k} = f_{i,k}^n \quad (61)$$

where $\Delta_q = \Delta_q^{*n+1}$ and $f = (\text{RHS})^n$ when the ξ direction sweep is performed, and $\Delta_q = \Delta_q^{n+1}$ and $f = (\text{RHS})^{*n}$ when the ζ direction sweep is performed. The block matrices have the form

$$a_{i,k} = \frac{\Delta t}{2} \hat{A}_{i,k} - \varepsilon_{\text{impl}} \Delta t \frac{J_{i,k}}{J_{i+1,k}} \quad (62)$$

$$b_{i,k} = (1 + 2\varepsilon_{\text{impl}} \Delta t) [I] \quad (63)$$

$$c_{i,k} = \frac{\Delta t}{2} \hat{A}_{i,k} - \varepsilon_{\text{impl}} \Delta t \frac{J_{i,k}}{J_{i-1,k}} \quad (64)$$

3. Boundary Conditions

All flows were computed at subsonic free stream speeds. For subsonic inflow and outflow boundaries the flow variables are evaluated using zero order Riemann invariant extrapolation. At the inflow boundary there is one incoming and three outgoing characteristics, therefore, three variables, density (ρ), normal velocity (w_1), and pressure (p) are specified and the fourth variable axial velocity (u_1), is extrapolated from the interior. The inflow boundary conditions are given by

$$\begin{aligned} \rho_1 &= \left(\frac{a_1}{\gamma s_1} \right)^{1/(\gamma-1)}, \quad s_1 = (p_\infty / \rho_\infty)^\gamma, \quad a_1 = \frac{(\gamma-1)}{4} (R_1^+ - R_2^-) \\ u_1 &= (R_1^+ + R_2^-) / 2 \\ w_1 &= w_\infty \\ p_1 &= \left(\frac{\rho_1 a_1^2}{\gamma} \right) \end{aligned} \quad (65)$$

where R^+_1 , R^-_2 are the incoming and outgoing Riemann invariants given by

$$R^+_1 = u_\infty + 2a_\infty/(\gamma - 1), \quad R^-_2 = u_2 - 2a_2/(\gamma - 1) \quad (66)$$

At the outflow boundary there is one incoming and three outgoing characteristics and only one quantity, pressure, is specified while the others are extrapolated from the interior. For the density and the normal velocity, simple first-order extrapolation is used, and the axial outflow velocity is obtained from the zero order outgoing Riemann invariant. The outflow boundary conditions are given by

$$\begin{aligned} \rho_1 &= \rho_2 \\ u_1 &= R^+_1 - 2a_1/(\gamma - 1), \quad a_1 = \sqrt{\mathcal{P}_1/\rho_1} \\ w_1 &= w_2 \\ p_1 &= p_2 \end{aligned} \quad (67)$$

On the body surface the nonslip condition is applied for the velocities. The density and pressure are obtained from the interior by extrapolation. For the C-type grids used in this study averaging of the flow variable at the wake cut is used.

4. Turbulence Models

a. Baldwin-Lomax Turbulence Model

The Baldwin-Lomax model [Ref. 12] is a two-layer, inner and outer eddy viscosity model for the computation of two- and three-dimensional flows. Patterned after the Cebeci-Smith model [Ref. 11], it incorporates a modification that bypasses the need for finding the edge of the boundary layer. This is achieved by introducing the vorticity in place of the boundary layer

thickness. The turbulent effect is simulated by an inner eddy viscosity, given by:

$$(\mu_t)_{\text{inner}} = \rho l^2 |\omega| \quad y \leq y_{\text{crossover}} \quad (68)$$

where $y_{\text{crossover}}$ is the smallest value of y at which the values of the inner and outer eddy viscosities are the same and the Prandtl mixing length l is

$$l = ky \left[1 - \exp\left(\frac{-y^+}{A^+}\right) \right] \quad (69)$$

The magnitude of the vorticity in two-dimensions $|\omega|$ and y^+ are defined as follows

$$|\omega| = \left(\frac{\partial u}{\partial y} - \frac{\partial v}{\partial x} \right) \quad \text{and} \quad y^+ = \frac{\rho_w u_\tau y}{\mu_w} = \frac{\sqrt{\rho_w u_w} y}{\mu_w} \quad (70)$$

where A^+ is a constant. The subscript w denotes values at the wall or airfoil surface in this case.

The outer eddy viscosity is given by the following expression

$$(\mu_t)_{\text{outer}} = \kappa C_{CP} \rho F(y)_{\text{WAKE}} F(y)_{\text{KLEB}} \quad y_{\text{crossover}} \leq y \quad (71)$$

where κ and C_{CP} are constants and $F(y)_{\text{wake}} = y_{\text{max}} F_{\text{max}}$ for boundary layers and $F(y)_{\text{wake}} = C_{wk} y_{\text{max}} (U_{DIF}^2 / F_{\text{max}})$ for wakes and separated boundary layers. The quantities y_{max} and F_{max} are determined from the expression

$$F(y) = y |\omega| \left[1 - \exp\left(\frac{-y^+}{A^+}\right) \right] \quad (72)$$

The exponential term of Equation (72) is set to zero for wakes. F_{\max} is the maximum value of $F(y)$ that occurs in a profile and y_{\max} is the value of y at which it occurs. $F(y)_{\text{KLEB}}$ is the Klebanoff intermittency factor given by

$$F(y)_{\text{KLEB}} = \left[1 + 5.5 \left(\frac{C_{\text{KLEB}} y}{y_{\max}} \right)^6 \right]^{-1} \quad (73)$$

The quantity U_{DIF} is the difference between $U_{\max} = U_{y=y_{\max}}$ and the minimum total velocity in the profile

$$U_{\text{DIF}} = \left(\sqrt{u^2 + v^2} \right)_{y=y_{\max}} - \left(\sqrt{u^2 + v^2} \right)_{y=y_{\min}} \quad (74)$$

The second term in U_{DIF} is taken to be zero except in the case of wakes.

The constants were determined to achieve agreement with Reference 11 and can be found in the original document. This model completely models turbulent flow over an airfoil, it is relatively easy to code, it does not degrade the solution convergence, and it is computationally efficient.

b. Johnson-King Turbulence Model

The Johnson-King model [Ref. 13] takes into account the convective and diffusive effects on the Reynolds shear stress $-u'w'$ in the streamwise direction. The eddy viscosity is given by

$$\nu_t = \nu_{t_0} \left[1 - \exp \left(- \frac{\nu_{t_i}}{\nu_{t_0}} \right) \right] \quad (75)$$

where ν_t , ν_{t_0} describe the eddy viscosity variation in the inner and outer part of the boundary layer. The inner eddy viscosity is computed as

$v_{t_1} = D^2 \kappa y \sqrt{(-\bar{u}'\bar{w}')_{\max}}$, where $D^2 = 1 - e^{-(y/A^+)}$, where the constant $A^+=15$. The outer viscosity is given by

$$v_{t0} = \sigma(x) [0.168 U_t \delta^x \gamma] \quad (76)$$

where γ is the Klebanoff intermittency function $\gamma = [1 + 5.5(y/\delta)^6]^{-1}$ and $\sigma(x)$ is the solution of the ordinary differential equation which describes the development of $-u'w'_{l_{\max}}$ along the path of maximum shear stress. This model accounts for the effects of convection and diffusion on the Reynolds stress development through the solution of the following ODE

$$\frac{\partial g}{\partial x} = \frac{a_1}{2\bar{u}_m L_m} \left\{ \left(1 - \frac{g}{g_{eq}} \right) + \frac{C_{dif} L_m}{a_1 \delta \left[0.7 - \left(\frac{y}{\delta} \right) \right]} \left| 1 - \sqrt{\frac{v_{t_0}}{v_{t_0,eq}}} \right| \right\} \quad (77)$$

here C_{dif} and a_1 are modeling constants, u_m is the maximum average mean velocity and $g = [-u'w'_{l_{\max}}]^{-1/2}$, $g_{eq} = [-u'w'_{l_{\max,eq}}]^{-1/2}$ where L_m is the dissipation length evaluated as

$$\begin{aligned} L_m &= 0.40y & y_m / \delta \leq 0.225 \\ L_m &= 0.09y & y_m / \delta \geq 0.225 \end{aligned} \quad (78)$$

The equilibrium shear stress g_{eq} in Equation (77) is determined from the following equilibrium eddy viscosity distribution

$$\begin{aligned} v_{t,eq} &= v_{t_0,eq} \left[1 - \exp\left(-\frac{v_{t,eq}}{v_{t_0,eq}}\right) \right] \\ v_{t,eq} &= D^2 \kappa \gamma \sqrt{(-\bar{u}'\bar{w}')_{m,eq}} \\ v_{t_0,eq} &= \sigma(x) [0.168 U_e \delta^* \gamma] \end{aligned} \quad (79)$$

An implicit Euler method is used for the numerical solution of Equation (77), and the maximum shear stress at each iteration level is updated as follows

$$\sigma(x)^{n+1} = \sigma(x)^n \frac{v_{t_0}^{n+1}}{v_{t_0}^n} \quad (80)$$

Solutions with the Johnson-King turbulence model were obtained as follows. First a convergent solution using the Baldwin-Lomax turbulence model for the entire flow field was computed. Then the Johnson-King model was applied only to the upper part of the airfoil. To initiate the solution $\sigma(x)$ in Equation (76) is set equal to unity and it is allowed to change according to Equation (80) until the final solution is obtained.

c. Algebraic RNG-based Turbulence Model

Recently an algebraic eddy viscosity, as well as a two-equation κ - ϵ model based on Renormalization Group (RNG) Theory of turbulence [Ref. 14] were proposed for the closure of the Reynolds-averaged Navier-Stokes equations. The algebraic model, although free from uncertainties related to the experimental determination of empirical modeling constants, still requires specifications at an integral length-scale of turbulence which reduces the

generalities of the model. Here the integral scale is assumed proportional to the distance from the wall and the eddy viscosity for the RNG-based algebraic turbulence model is obtained as in Martinelli [Ref. 15] from the following formula

$$\nu = \nu_1 \left[1 + H \left\{ \frac{\hat{a}}{\nu_1^3} \phi \left(\frac{1}{y} + \frac{1}{0.225\delta} \right)^{-4} - C_c \right\} \right]^{\frac{1}{3}} \quad (81)$$

where $\nu = \nu_t + \nu_l$, H is the Heavyside step function and ϕ is the dissipation function $\phi = \tau_{ij} (\partial u_i / \partial x_j)$. The RNG-based turbulence model is applied only for the suction surface separated flow region while the pressure side and the wake regions are computed with the Baldwin-Lomax model.

IV. RESULTS AND DISCUSSION

A. METHOD OF INVESTIGATION

As stated in the introduction this investigation is divided into three parts; validation of the Navier-Stokes code (Ns2.f) through comparison with experimental data and a well tested inviscid unsteady Panel method code as well as a steady viscous/inviscid code. Finally evaluation of the effects of reduced frequency, mean angle, amplitude, Mach number, and Reynolds number on unsteady flow behavior are examined. Also, during the course of this study it became necessary to investigate the effects of several turbulence models on the results computed for the harmonically oscillating cases.

The following table lists the cases studied during the course of this investigation:

TABLE 2. TEST CASES

Case	Type of Motion	Parameters
1	Steady State (Transonic)	$M=0.7, \alpha=1.4^\circ, Re=9 \times 10^6$
2	Steady State (Transonic)	$M=0.799, \alpha=2.26^\circ, Re=9 \times 10^6$
3	Steady State	$M=0.3, Re=3 \times 10^6$
4	Steady State	$M=0.3, Re=4 \times 10^6$
5	Rapidly Pitching Airfoil (Ramp)	$M=0.3, k=0.01272, Re=2.7 \times 10^6$
6	Harmonically Oscillating (Multiple Parameters)	$\alpha(t)=A_0^\circ \pm A_1^\circ \sin(\omega t)$
7	Harmonically Oscillating (Small Amplitude)	$\alpha(t)=13^\circ \pm 2.5^\circ \sin(\omega t), k=0.2, Re=4 \times 10^6$
8	Harmonically Oscillating (Small Amplitude)	$\alpha(t)=13^\circ \pm 2.5^\circ \sin(\omega t), k=0.1, Re=2 \times 10^6$
9	Harmonically Oscillating	$\alpha(t)=9^\circ \pm 5^\circ \sin(\omega t), k=0.2, Re=4 \times 10^6$
10	Harmonically Oscillating	$\alpha(t)=10^\circ \pm 5.5^\circ \sin(\omega t), k=0.1, Re=4 \times 10^6$
11	Harmonically Oscillating	$\alpha(t)=11^\circ \pm 5^\circ \sin(\omega t), k=0.1, Re=4 \times 10^6$

1. Steady-State

Flow solutions can be obtained either by rotating the grid or by rotating the flow. Cases 1 and 2 solutions were obtained by rotating the grid.

First the procedure was used for the computation of steady flow over the NACA 0012 airfoil. Steady-state solutions were obtained for subsonic and transonic flow regime. Flow solutions for Case 1 and 2 (Table 2) were computed by rotating the direction of the flow relative to the stationary grid. However, in Cases 3 and 4 the grid was rotated to the desired angle using a simple Fortran code called `rotgr.f` and the free stream flow remained parallel to the x-axis. The program also translates the grid to a desired pivot point. In this thesis the pivot point was always chosen to be the quarter chord point. Either method produced the same solution. The steady-state solutions tested the accuracy of `Ns2.f` and provided initial solutions for the unsteady cases. `Ns2.f` was also compared to an existing steady, incompressible, viscous/inviscid method (`Incompbl.f`) obtained from Dr. T. Cebeci, California State University at Long Beach.

a. Case 1. $M=0.7$, $\alpha=1.4^\circ$, $Re=9 \times 10^6$

The flow conditions for the first test case are $M_\infty=0.7$, at an angle of attack of 1.4 degrees, and a Reynolds number of nine million. Explicit boundary conditions were used and the Baldwin-Lomax turbulence model was selected. The solution was obtained on a 161x64 point grid. This case was chosen because the solution converged rapidly. Figure 3 shows good agreement between the inviscid (Euler) pressure distribution and the measured values of Harris [Ref. 16]. Next, a Navier-Stokes solution was obtained whose convergence history is given in Figure 4. The solution was carried out to 2500

iteration at a timestep of approximately 0.08. The pressure distribution computed by Ns2.f (Figure 5) is also in good agreement with the measured values. However, the suction peak is more accurately predicted by the inviscid solution. For a free stream Mach number (M_∞) of 0.7 a maximum Mach number of 1.1 (Figure 6) is obtained on the upper surface near the leading edge. The density contour plot, Figure 7, shows the smooth contours indicative of a fully converged solution. The velocity field, Figure 8, shows the boundary layer thickness, represented by the thick dark line. The sonic line is represented by the line extending from 7% chord to 20% chord.

Cp plot for 0012 M=0.7 $\alpha=1.4$

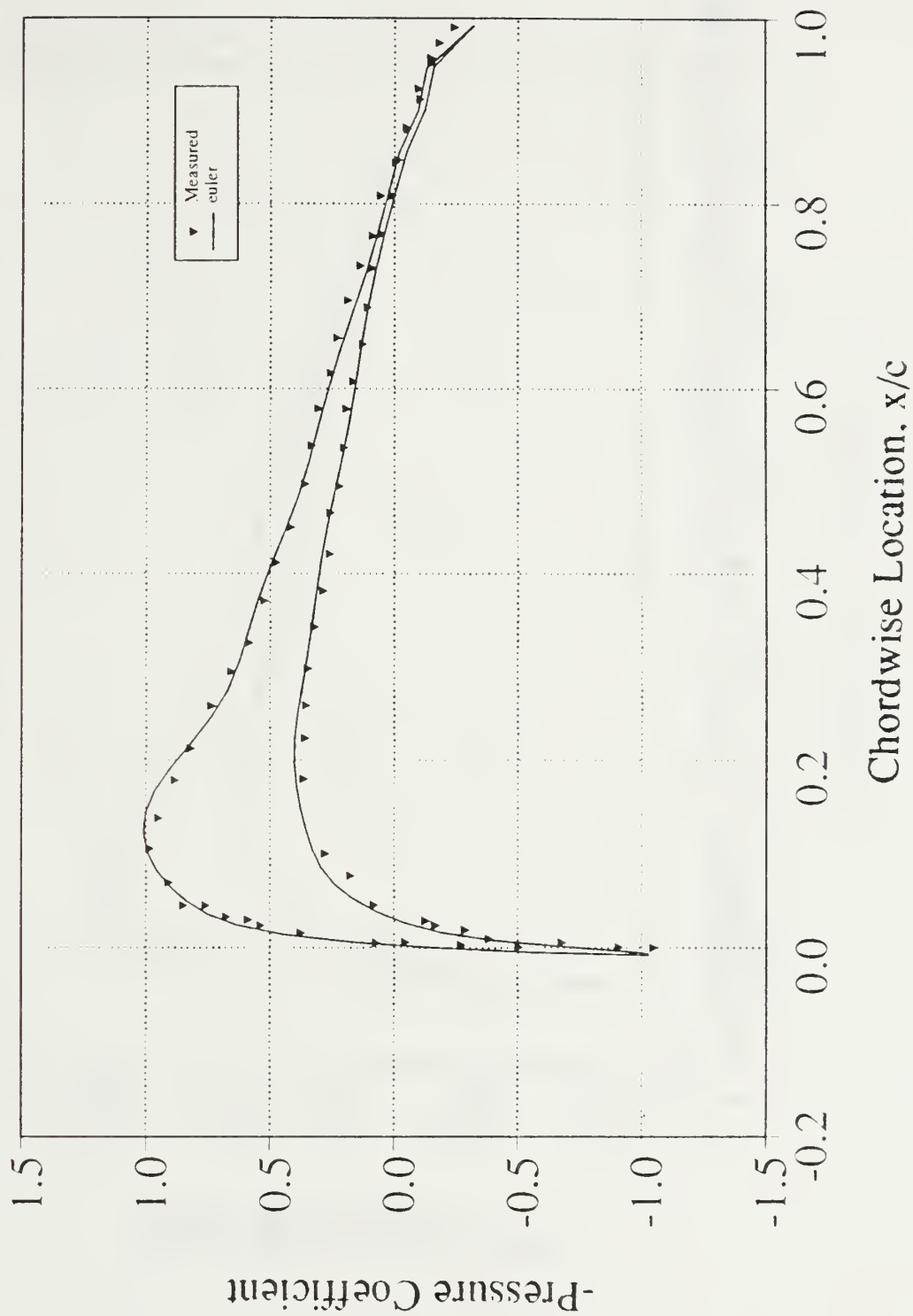


Figure 3. Pressure Distribution (Inviscid), $M=0.7$, $\alpha=1.4^\circ$, $Re=9 \times 10^6$

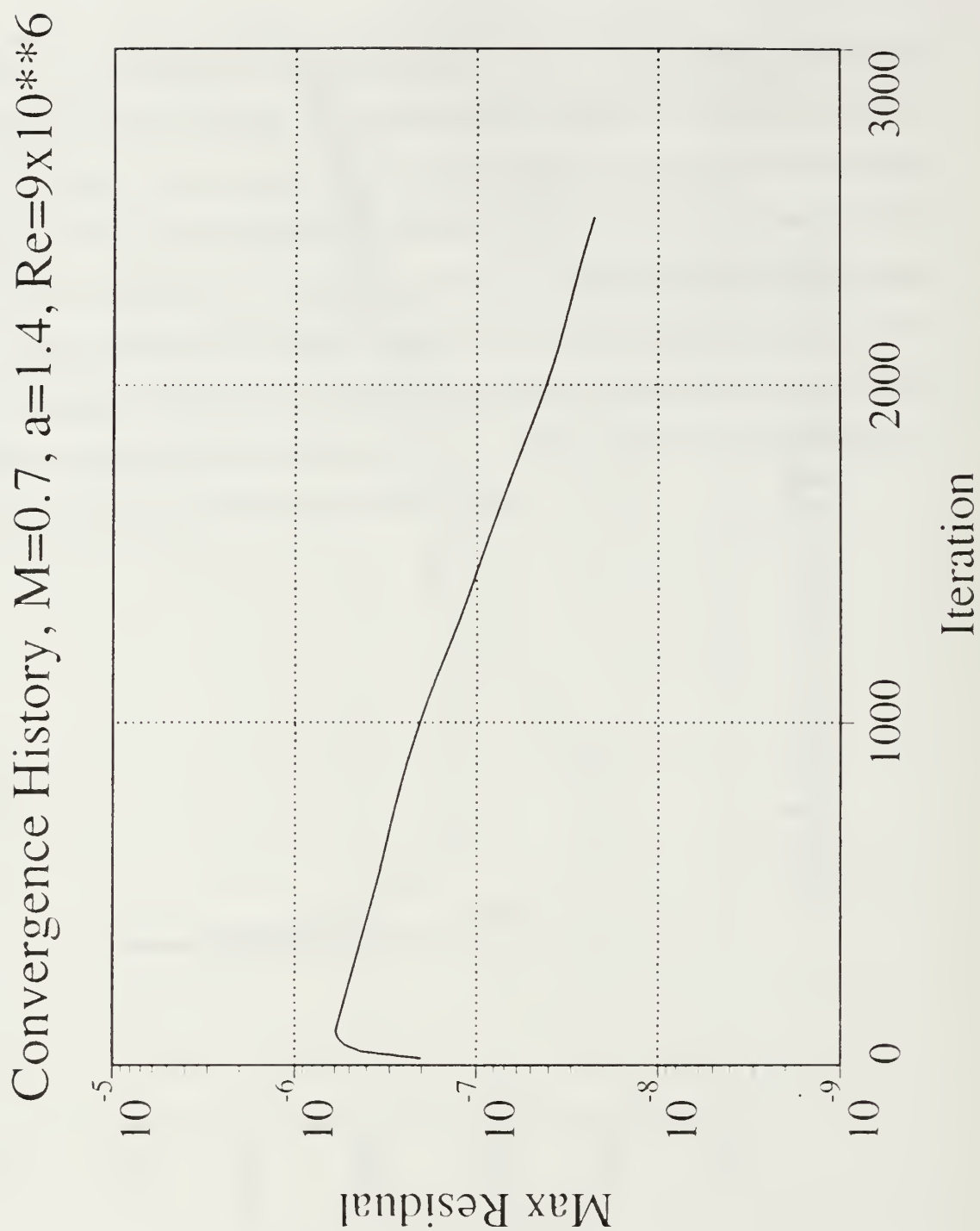


Figure 4. Convergence History, $M=0.7$, $\alpha=1.4^\circ$, $Re=9 \times 10^6$

$M=0.7$, $\alpha=1.4$ deg, $Re=9 \times 10^6$

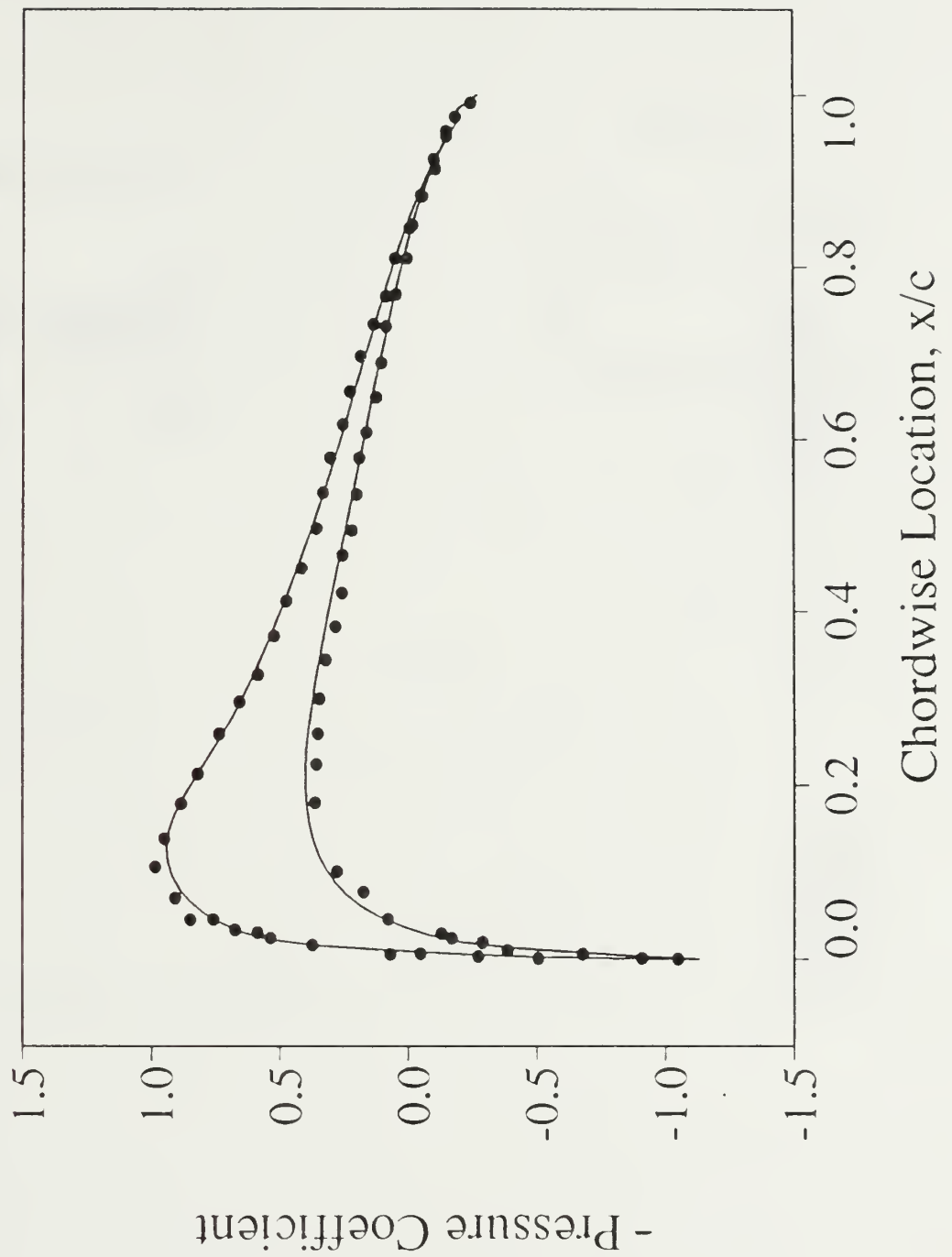


Figure 5. Pressure Distribution , $M=0.7$, $\alpha=1.4^\circ$, $Re=9 \times 10^6$

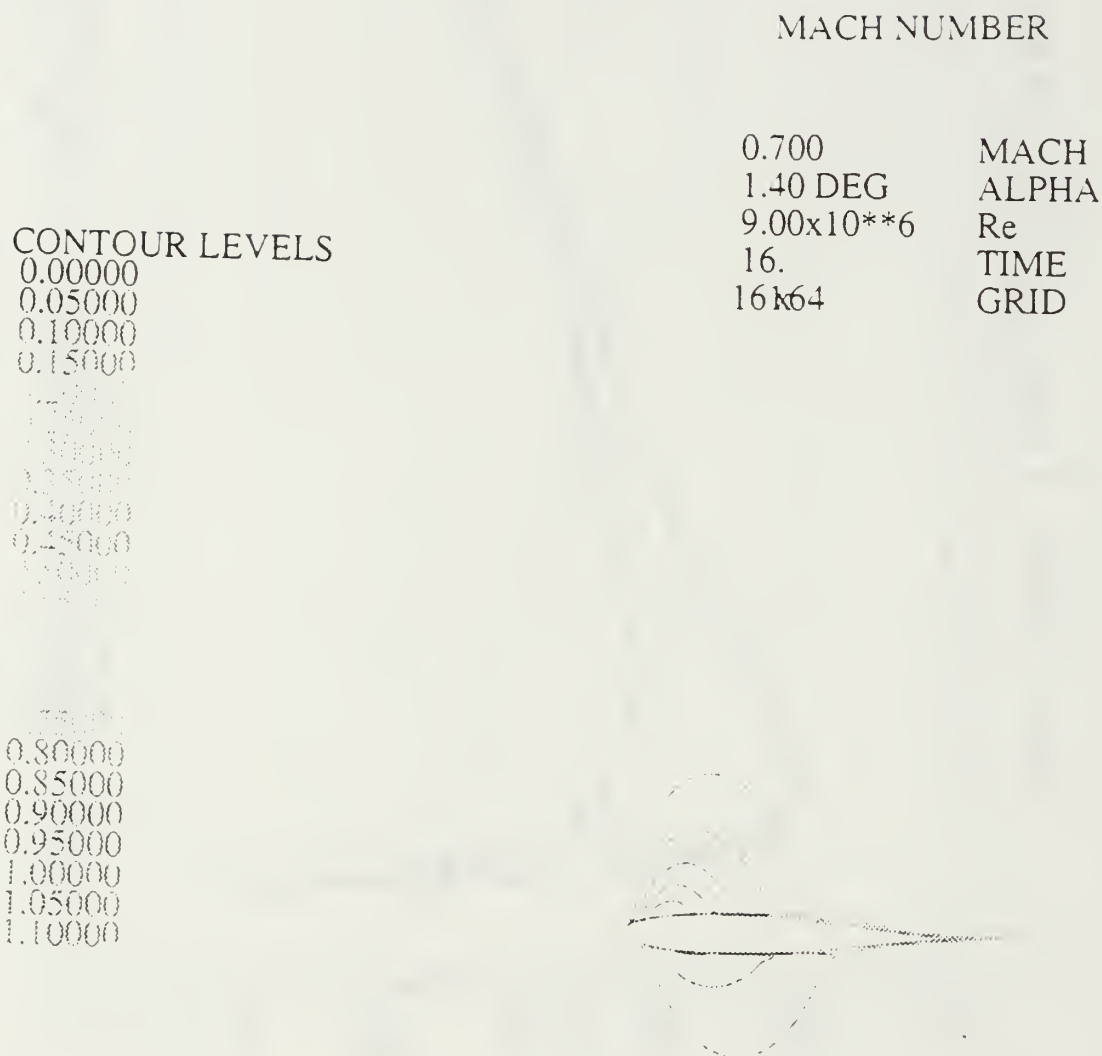


Figure 6. Mach Contour, $M=0.7$, $\alpha=1.4^\circ$, $Re=3 \times 10^6$

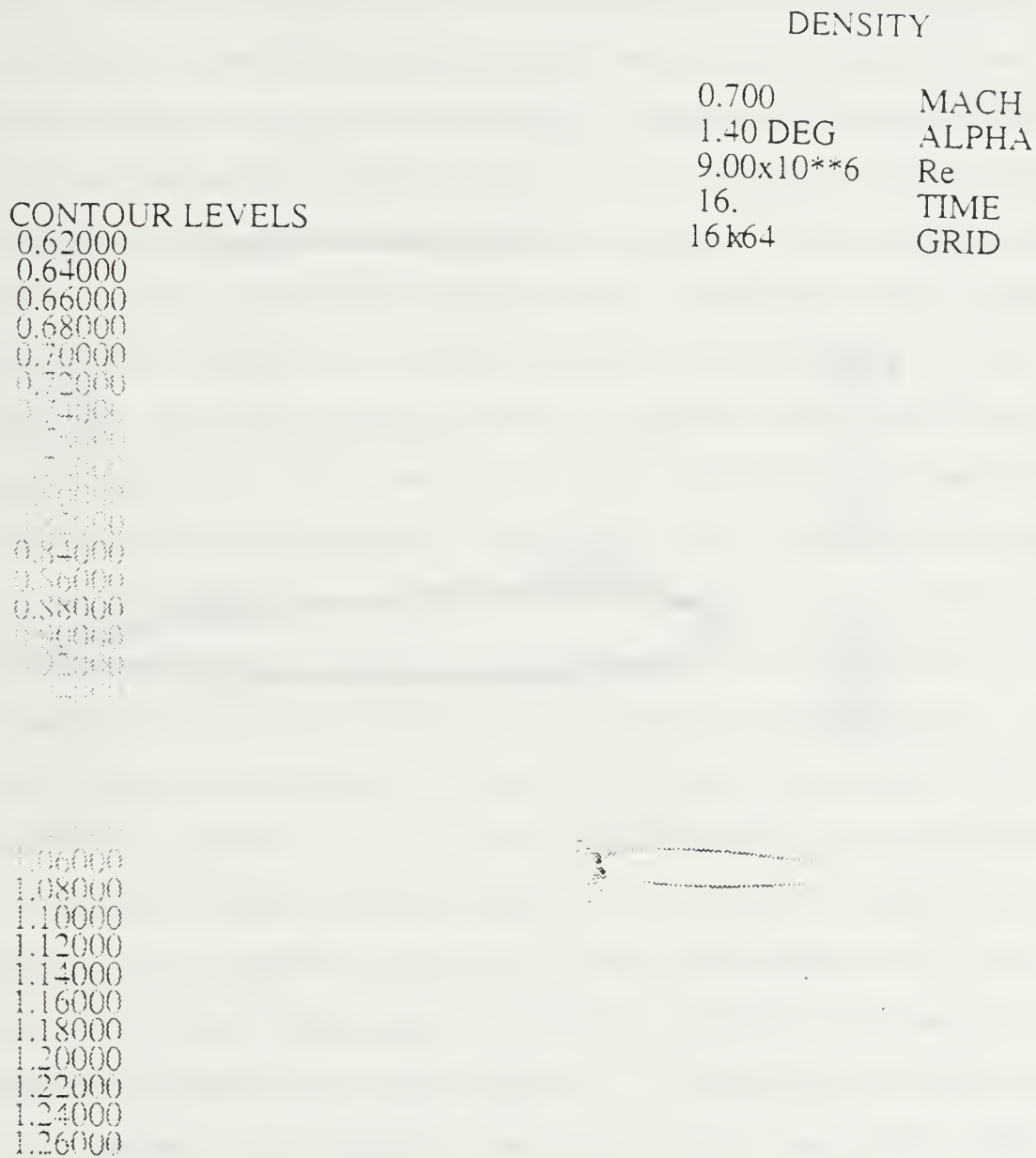


Figure 7. Density Contour, $M=0.7$, $\alpha=1.4^\circ$, $Re=9 \times 10^6$

WIND TUNNEL PHOTOGRAPH OF PRESSURE

CONTOUR LEVELS

0.88000
0.50000
0.52000
0.54000
0.56000
0.58000
0.60000
0.62000
0.64000
0.66000
0.68000
0.70000
0.72000
0.74000

0.84000
0.86000
0.88000
0.90000
0.92000
0.94000
0.96000
0.98000
1.00000

0.700 TACH
1.400 EG ALPHA
9.00x10⁶ Re
16. TIME
16.64 GRID

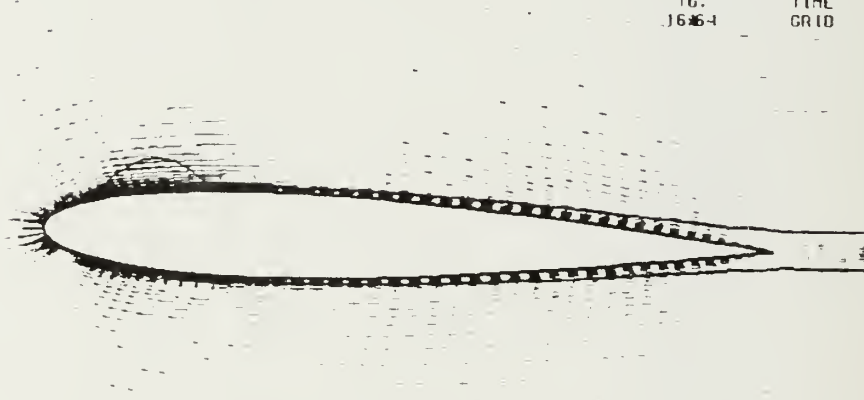


Figure 8. Velocity Field, $M=0.7$, $\alpha=1.4^\circ$, $Re=9 \times 10^6$

b. Case 2. $M=0.799$, $\alpha=2.26^\circ$, $Re=9 \times 10^6$

The next steady-state case investigated was at a Mach number equal to 0.799, at an angle of attack of 2.26 degrees and a Reynolds number of nine million. As in Case 1, an Euler solution was first obtained and compared to measured data as well as to a viscous solution obtained with an upwind scheme using the Johnson-King turbulence model. As seen in Figure 9, the pressure distribution for the inviscid solution is in fair agreement with the measured data until the shock is reached at the 50% chord point. After this point the computed solution fails to predict the pressure jump due to the presence of a shock at mid-chord. Note that the upwind scheme in combination with the Johnson-King turbulence model accurately predicts the location of the shock, even though the magnitude of the pressure gradient is off slightly. Next, a viscous solution was computed by Ns2.f with the Baldwin-Lomax turbulence model. Fourth order dissipation was added to produce a smooth flow solution across the weak shock located at mid chord. The solution was continued for 6000 iterations. The spike in the convergence history (Figure 10) was due to the addition of more fourth order dissipation. It is seen that the shock location was not predicted. At this angle of attack and Mach number the flow starts to separate and the Baldwin-Lomax turbulence model fails to model this separated flow region. Figure 11 shows the viscous pressure distribution comparison. The sonic line is shown on the Mach contour plot of Figure 12. A maximum Mach Number of 1.45 is reached in this supersonic flow region. Note the steep Mach gradient (Figure 12) at approximately 60% chord. Figures 13 and 14 show the pressure contour and density contour, respectively. Again the steep density gradient indicates the shock location at approximately 60% chord vice the measured

location at 50% chord. Finally, the velocity field and sonic line are shown in Figure 15.

NACA0012 $M=0.799$ at $\alpha=2.3$ deg

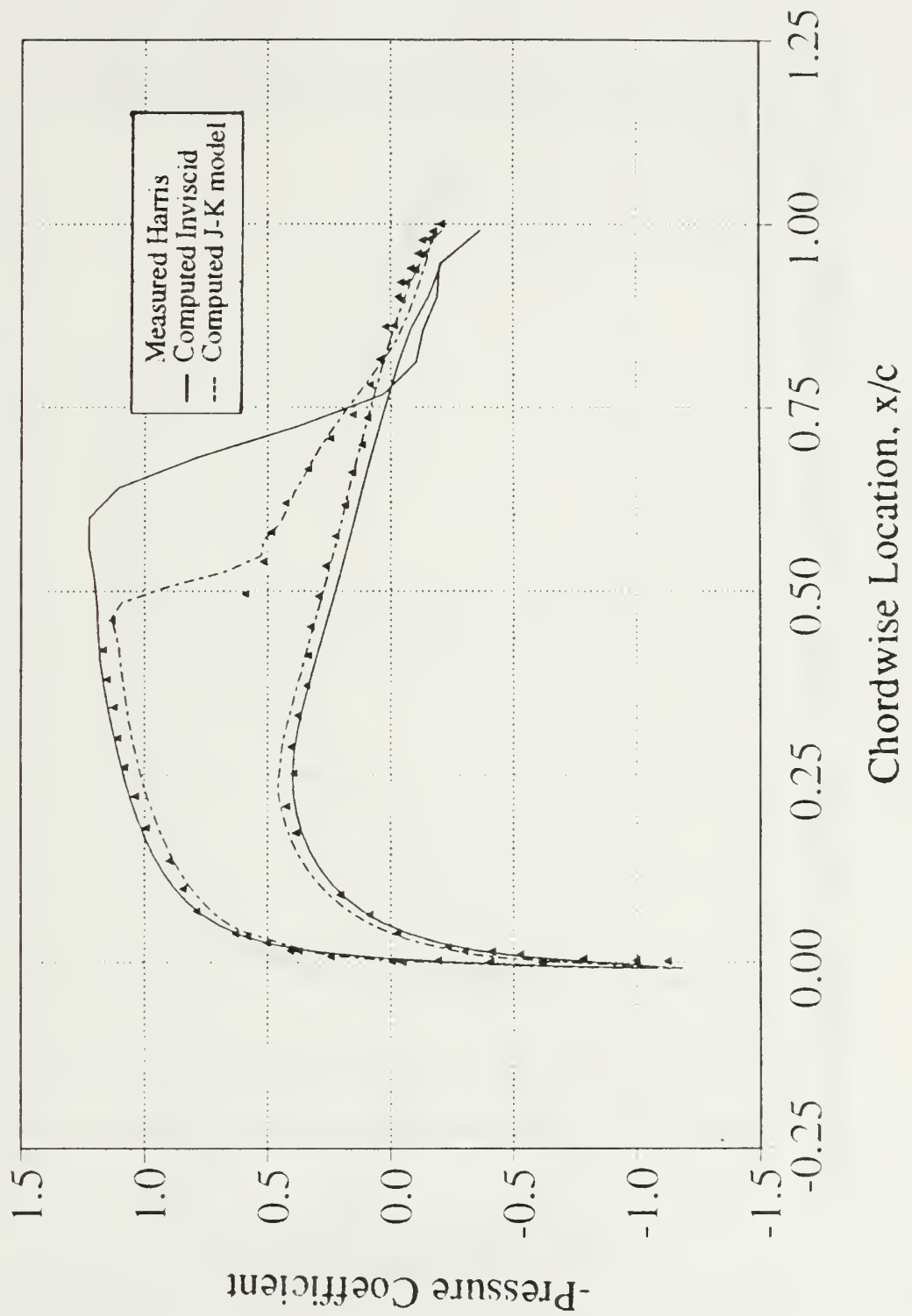


Figure 9. Pressure Distribution (Inviscid) , $M=0.799$, $\alpha=2.26^\circ$, $Re=9 \times 10^6$

Convergence History, $M=0.799$, $\alpha=2.26^\circ$, $Re=9 \times 10^6$

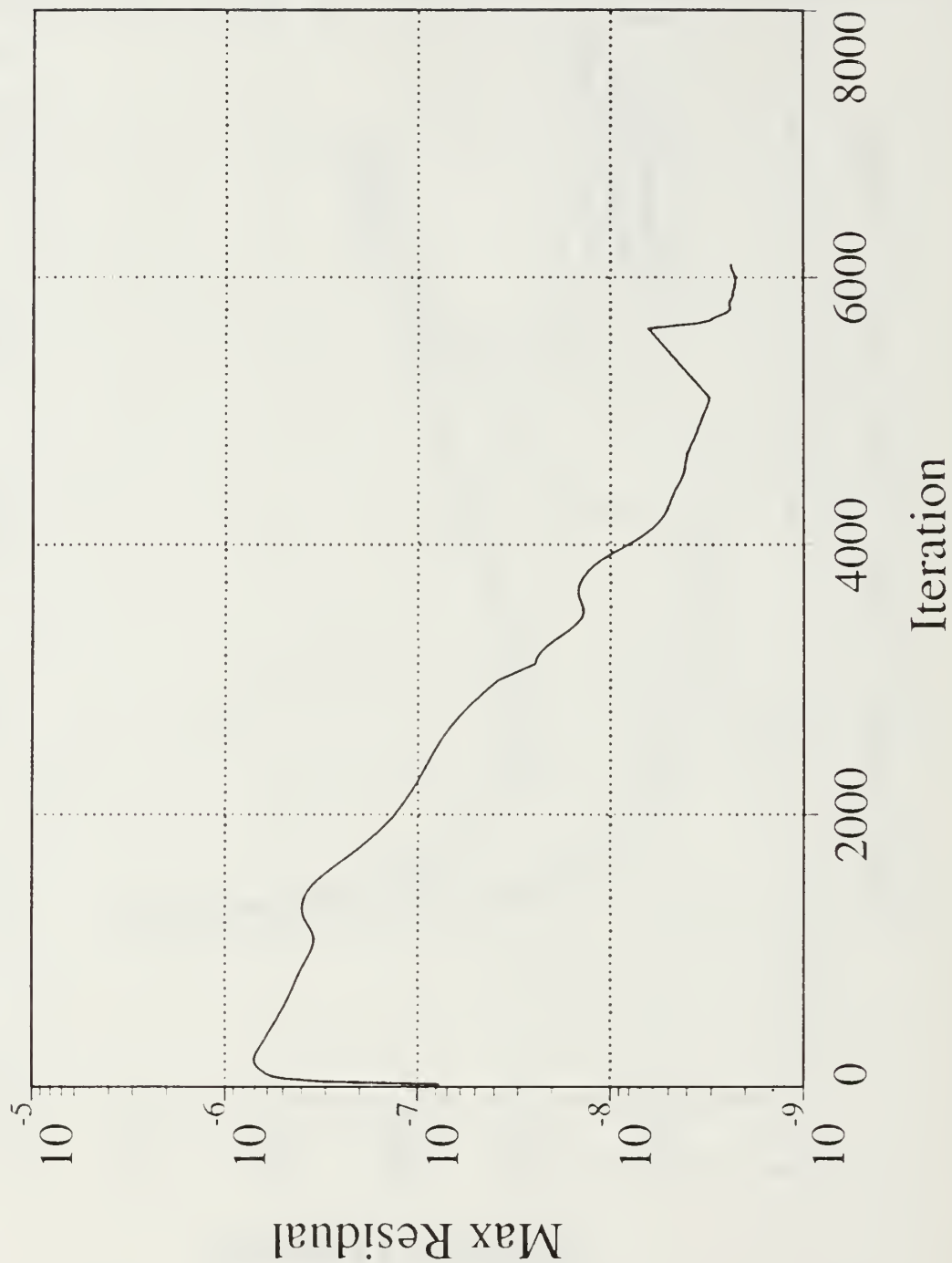


Figure 10. Convergence History (Ns2.f), $M=0.799$, $\alpha=2.26^\circ$, $Re=9 \times 10^6$

$M=7.99$, $\alpha=2.26^\circ$, $Re=9 \times 10^6$

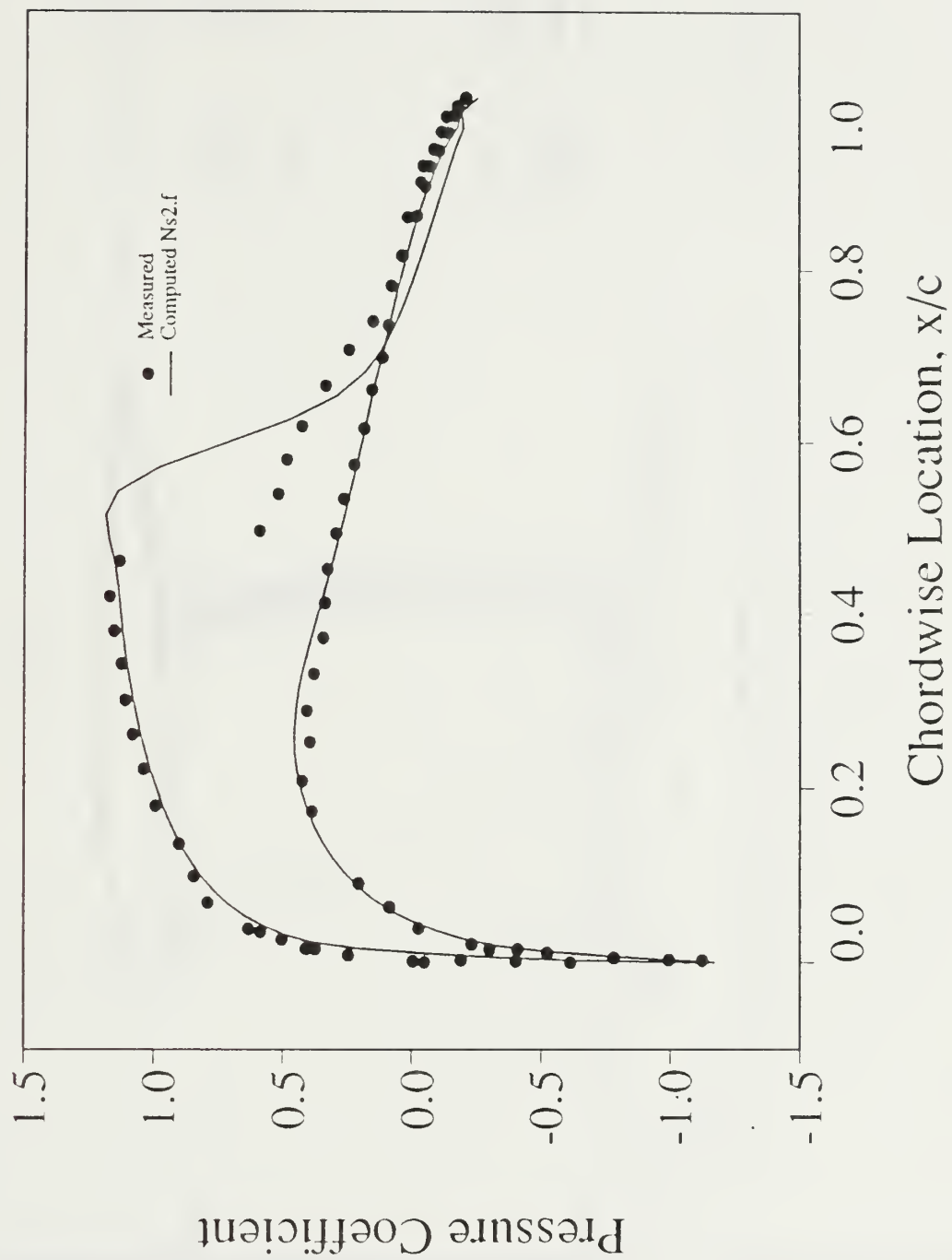
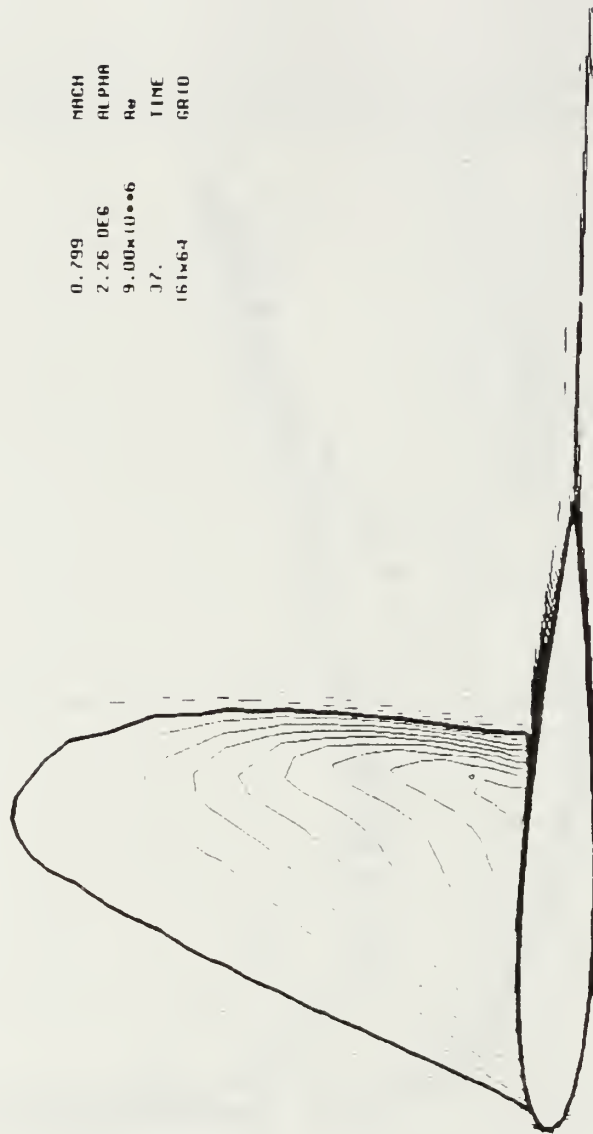


Figure 11. Pressure Distribution, $M=0.799$, $\alpha=2.26^\circ$, $Re=9 \times 10^6$

MACH NUMBER



CONTOUR LEVELS

0.00000
0.05000
0.10000
0.15000
0.20000
0.25000
0.30000
0.35000
0.40000
0.45000
0.50000
0.55000
0.60000
0.65000
0.70000
0.75000
0.80000
0.85000
0.90000
0.95000
1.00000
1.05000
1.10000
1.15000
1.20000
1.25000
1.30000
1.35000
1.40000
1.45000

MACH
ALPHA
Re
TIME
GRID

0.799
2.26 DEG
9.00e+06
37.
161x64

Figure 12. Mach Contour, $M=0.799$, $\alpha=2.26^\circ$, $Re=9 \times 10^6$

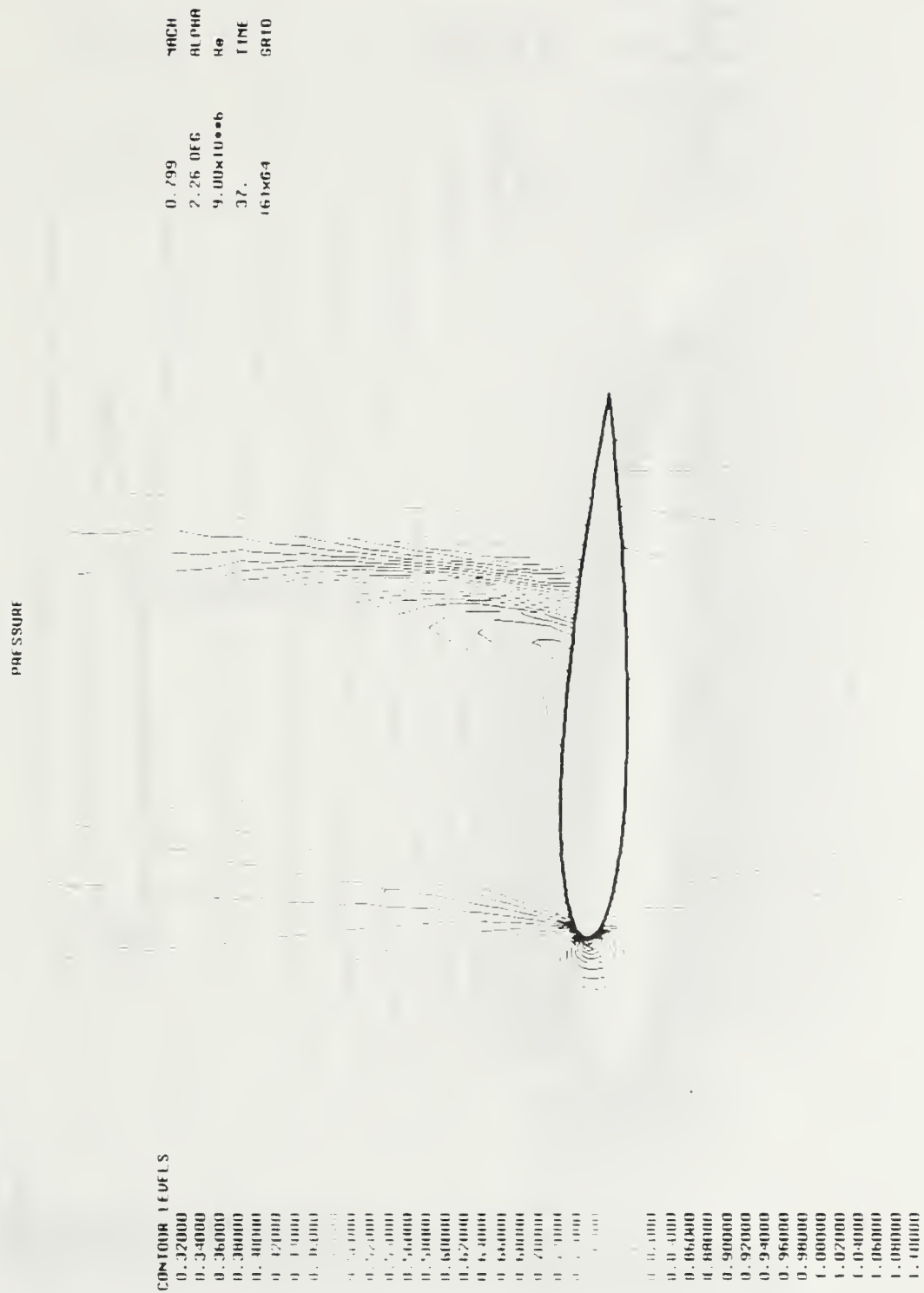


Figure 13. Pressure Contour, $M=0.799$, $\alpha=2.26^\circ$, $Re=9 \times 10^6$

DENSITY

MACH 0.799
 RI PHA 2.26 DEG
 Re 9.00×10^6
 TIME 37.
 CR10 161464

CONTOUR LEVELS

0.42500
 0.45000
 0.47500
 0.50000
 0.52500
 0.55000
 0.57500
 0.60000
 0.62500
 0.65000
 0.67500
 0.70000
 0.72500
 0.75000
 0.77500
 0.80000
 0.82500
 0.85000
 0.87500
 0.90000
 0.92500
 0.95000
 0.97500
 1.00000
 1.02500
 1.05000
 1.07500
 1.10000
 1.12500
 1.15000
 1.17500
 1.20000
 1.22500
 1.25000
 1.27500
 1.30000
 1.32500
 1.35000

Figure 14. Density Contour, $M=0.799$, $\alpha=2.26^\circ$, $Re=9 \times 10^6$

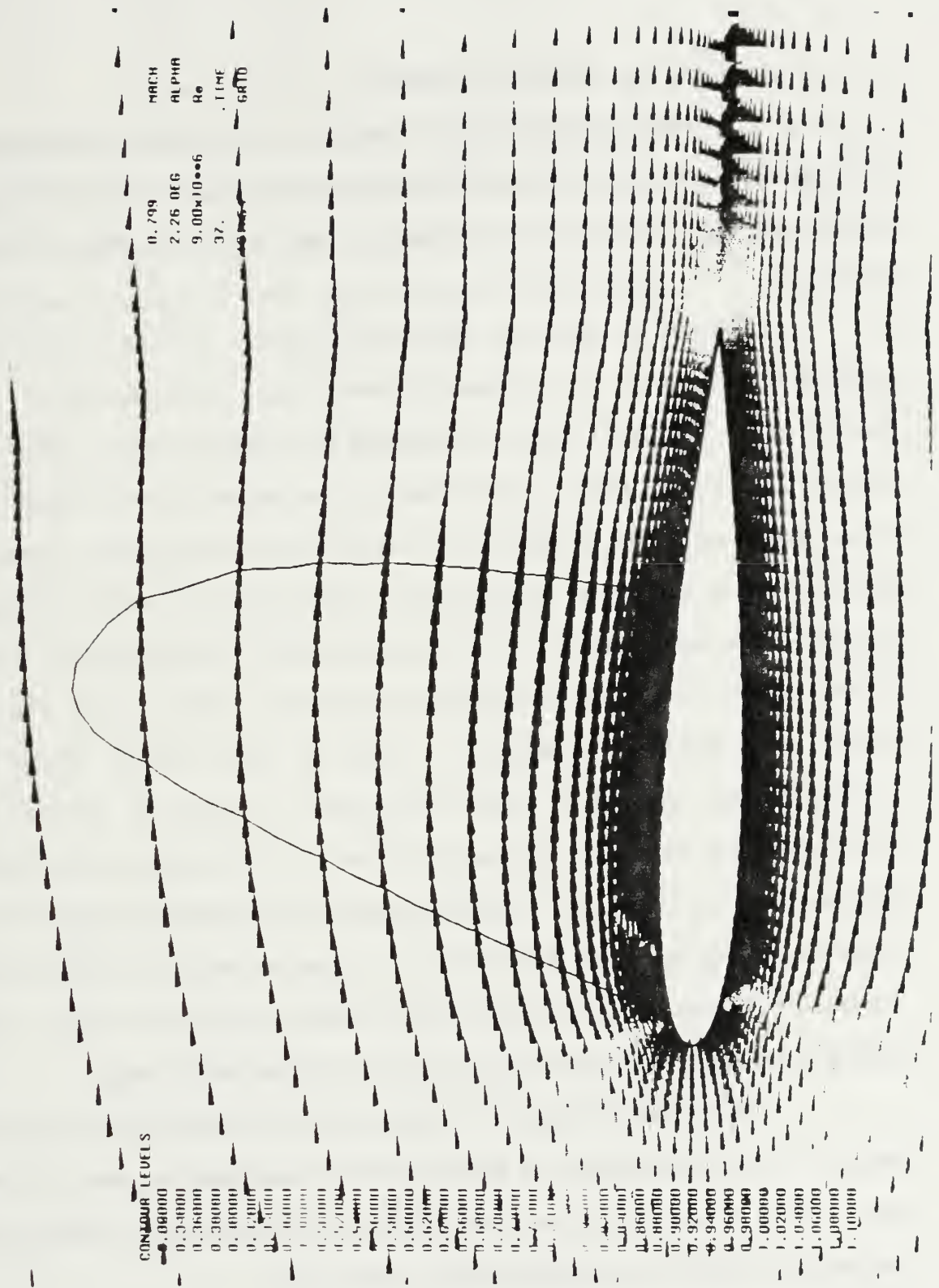


Figure 15. Velocity Field, $M=0.799$, $\alpha=2.26^\circ$, $Re=9 \times 10^6$

c. Case 3. $M=0.3$, $Re=3 \times 10^6$

In order to produce C_l vs α and C_m vs α curves, solutions were computed for $\alpha=2^\circ$, $\alpha=4^\circ$, $\alpha=6^\circ$, $\alpha=8^\circ$, $\alpha=9^\circ$, $\alpha=10^\circ$, $\alpha=12^\circ$, $\alpha=13^\circ$, $\alpha=13.5^\circ$, $\alpha=14^\circ$, and $\alpha=15^\circ$. However, only results for $\alpha=4^\circ$, $\alpha=11^\circ$, and $\alpha=14^\circ$, are presented.

Figure 16 shows the convergence history of $Ns2.f$ for a 161×64 algebraic C-type grid. The Courant-Friedrichs-Levy (CFL) condition was approximately 2000-2500 which corresponded to a timestep between 0.005 and 0.01. A comparison of the computed pressure distributions at $\alpha=4^\circ$ (Figure 17) shows good agreement between the Navier-Stokes calculations using the Baldwin-Lomax turbulence model and the viscous/inviscid code predictions. The measured suction peak is somewhat higher than predicted by the codes. Figures 18 and 19 show fair skin friction agreement. Note that the Navier-Stokes code assumes turbulent flow over the entire airfoil, while the viscous/inviscid interaction code uses Michel's method to predict the laminar/turbulent transition. As seen in Figure 18, the transition point for the upper surface is at 10% chord. A Mach contour plot is shown in Figure 20 and a density contour plot with the normalized stagnation pressure (0.98) contour overlayed in Figure 21. A maximum Mach number of 0.48 was attained. The density contours are smooth with steep gradients at the leading edge.

In Figures 22 through 29 similar results are presented for angles of attack of 11 and 14 degrees. It is seen that the agreement between the two codes and the measured pressure distributions is quite satisfactory, although the suction peak tends to be underpredicted by both codes.

Figures 30 and 31 show the C_l vs α and C_m vs α curves, respectively. Stall is seen to occur at approximately $\alpha=13.5^\circ$. The Navier-Stokes code reproduces the experimental lift and moment values up to the maximum lift value quite well, whereas the viscous/inviscid code shows greater deviation for angles of attack exceeding about eight degrees.

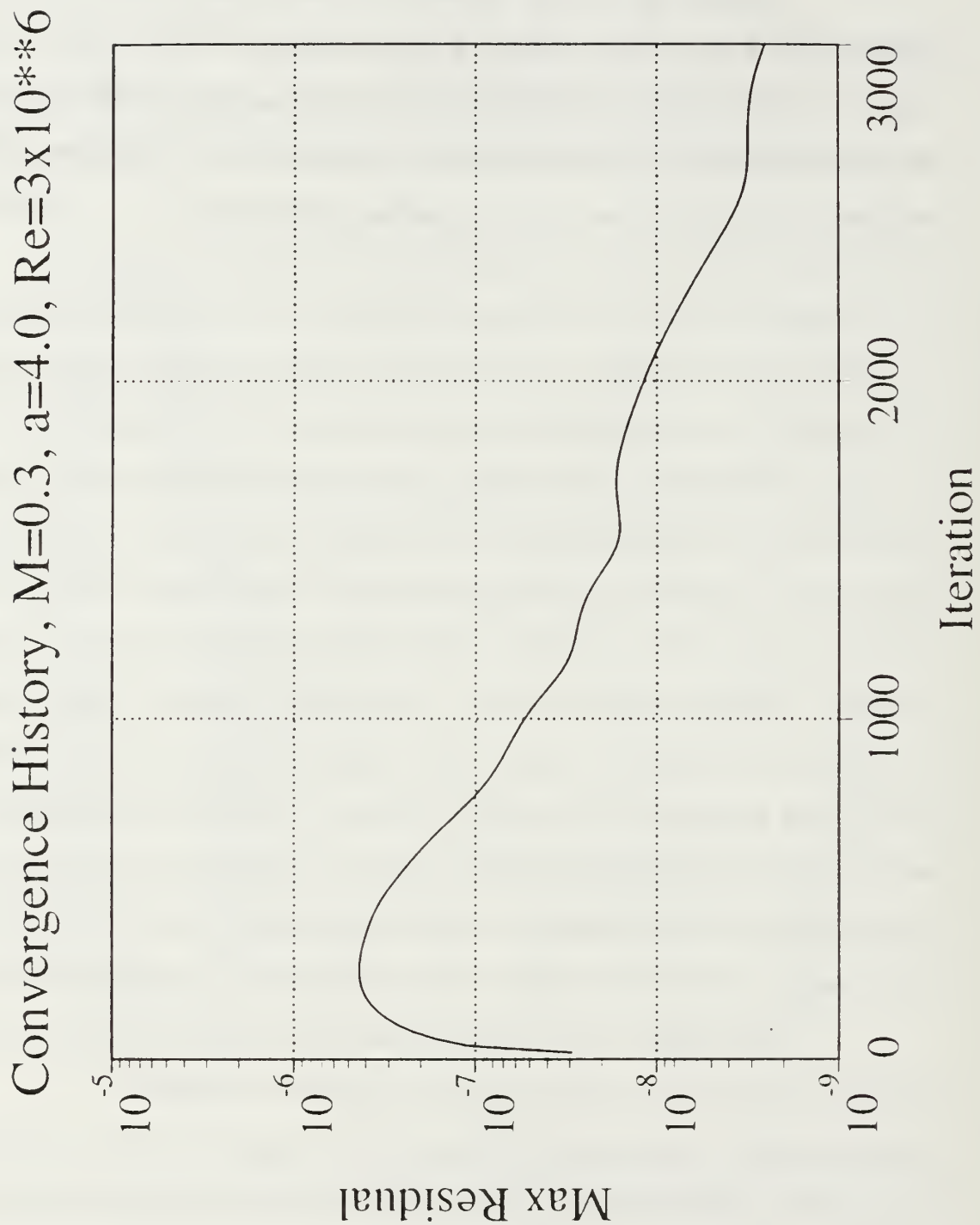


Figure 16. Convergence History, $M=0.3$, $\alpha=4^\circ$, $Re=3 \times 10^6$

Steady State: $M=0.3$, $Re=3 \times 10^6$

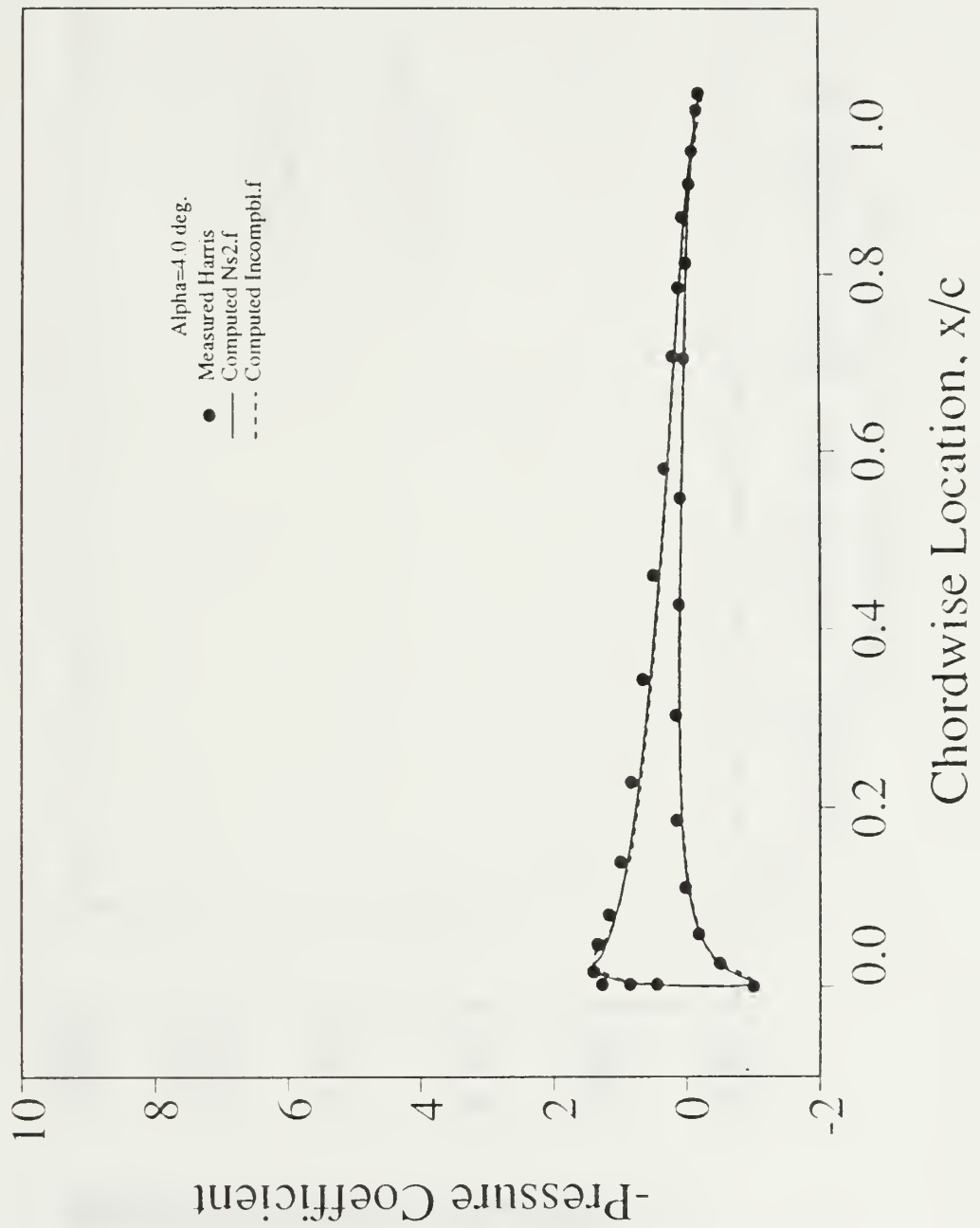


Figure 17. Pressure Distribution, $M=0.3$, $\alpha=4^\circ$, $Re=3 \times 10^6$

$M=0.3$, $\alpha=4.0$ deg, $Re=3 \times 10^6$

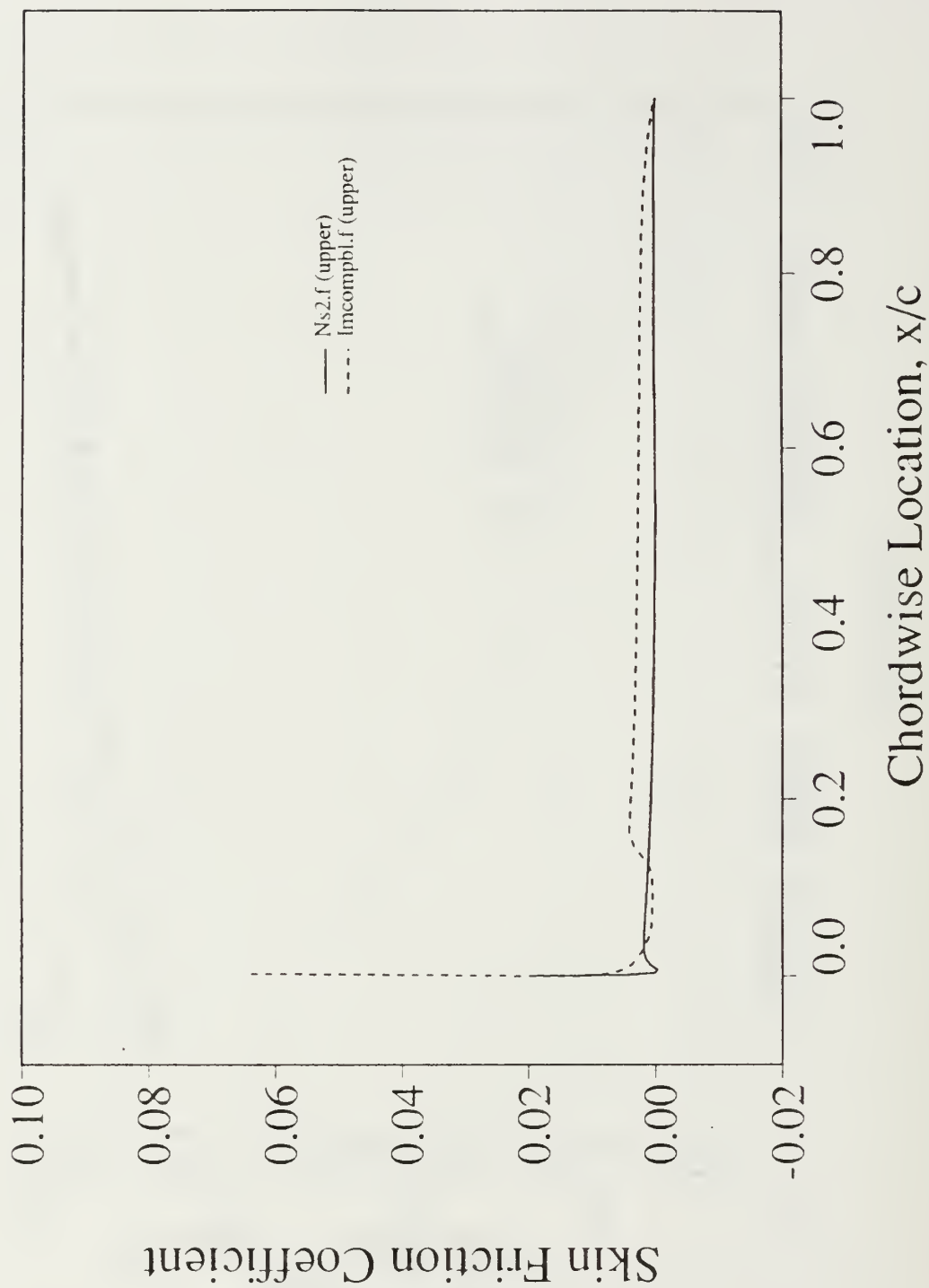


Figure 18. Skin Friction Distribution (Upper Surface), $M=0.3$, $\alpha=4^\circ$, $Re=3 \times 10^6$

$M=0.3$, $\alpha=4.0^\circ$, $Re=3 \times 10^6$

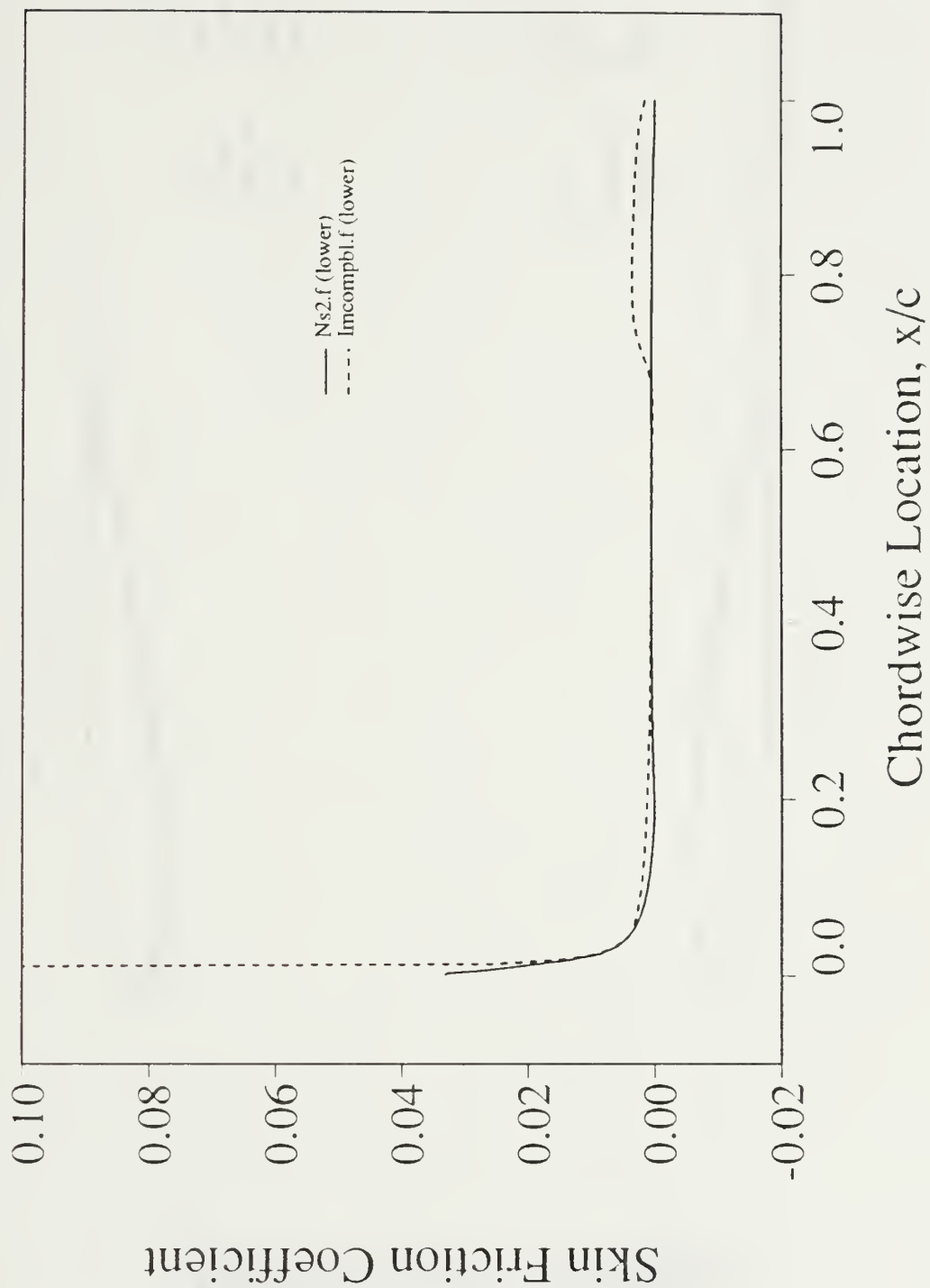


Figure 19. Skin Friction Distribution (Lower Surface), $M=0.3$, $\alpha=4^\circ$, $Re=3 \times 10^6$

TACH NUMBER

MACH
0.300
ALPHA
4.00 DEG
Re
3.00x10⁶
TIME
26.
GR10
161x64

CONTOUR LEVELS

0.00000
0.02000
0.04000
0.06000
0.08000
0.10000
0.12000
0.14000
0.16000
0.18000
0.20000
0.22000
0.24000
0.26000
0.28000
0.30000
0.32000
0.34000
0.36000
0.38000
0.40000
0.42000
0.44000
0.46000
0.48000



Figure 20. Mach Contour, $M=0.3$, $\alpha=4^\circ$, $Re=3 \times 10^6$

NORMALIZED DENSITY CONTOUR PRESSURE

CONTOUR LEVELS

0.90000
0.90500
0.91000
0.91500
0.92000
0.92500
0.93000
0.93500
0.94000
0.94500
0.95000
0.95500
0.96000
0.96500
0.97000
0.97500
0.98000
0.98500
0.99000
0.99500
1.00000
1.00500
1.01000
1.01500
1.02000
1.02500
1.03000
1.03500
1.04000
1.04500

0.300
4.00 DEG
3.00x10⁶
26.
161x6.4

TIME
GRI



Figure 21. Density Contour, $M=0.3$, $\alpha=4^\circ$, $Re=3 \times 10^6$

Convergence History, $M=0.3$, $\alpha=11.0$, $Re=3 \times 10^6$

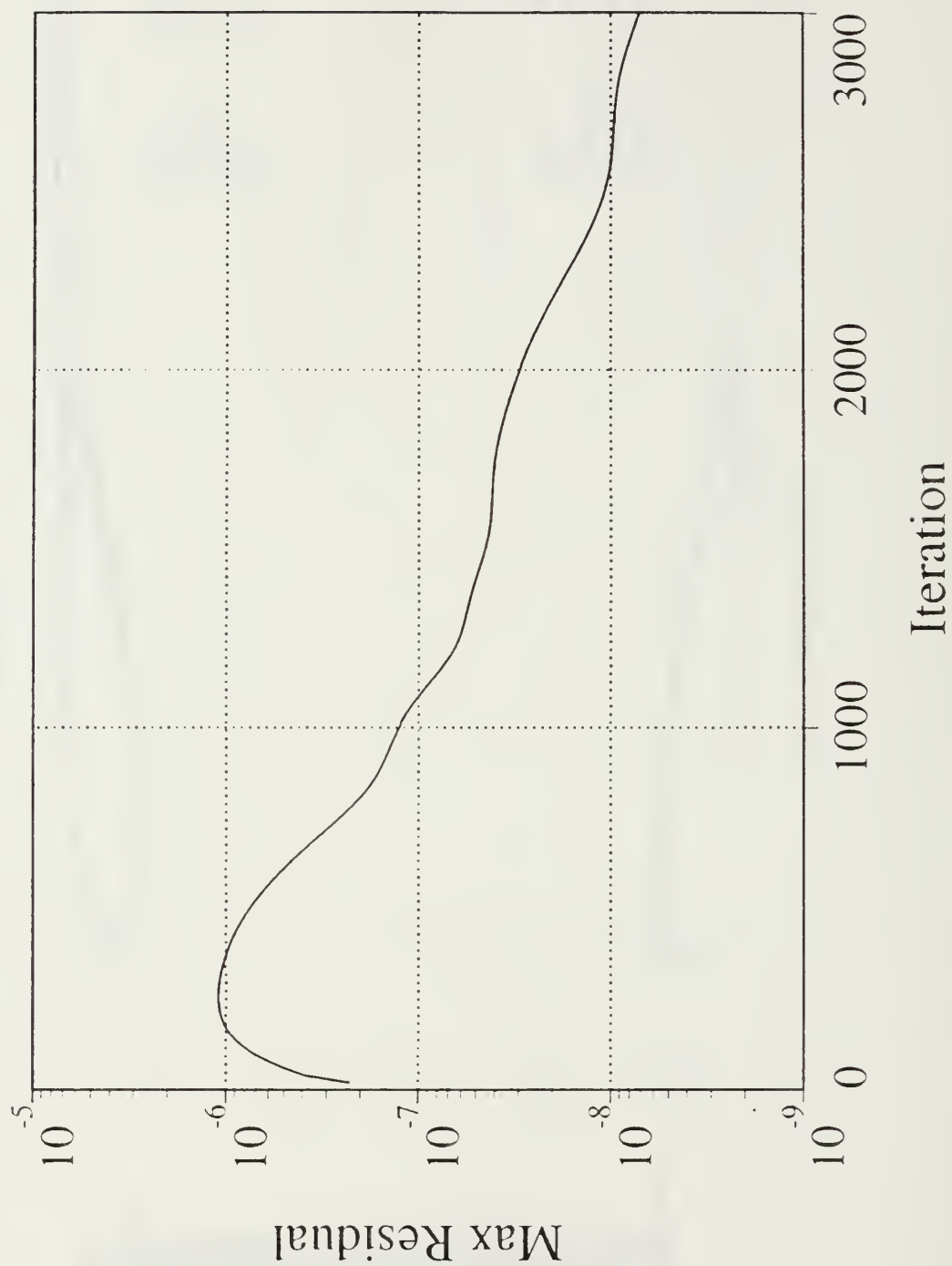


Figure 22. Convergence History, $M=0.3$, $\alpha=11^\circ$, $Re=3 \times 10^6$

$M=0.3$, $\alpha=11.0^\circ$, $Re=3 \times 10^6$

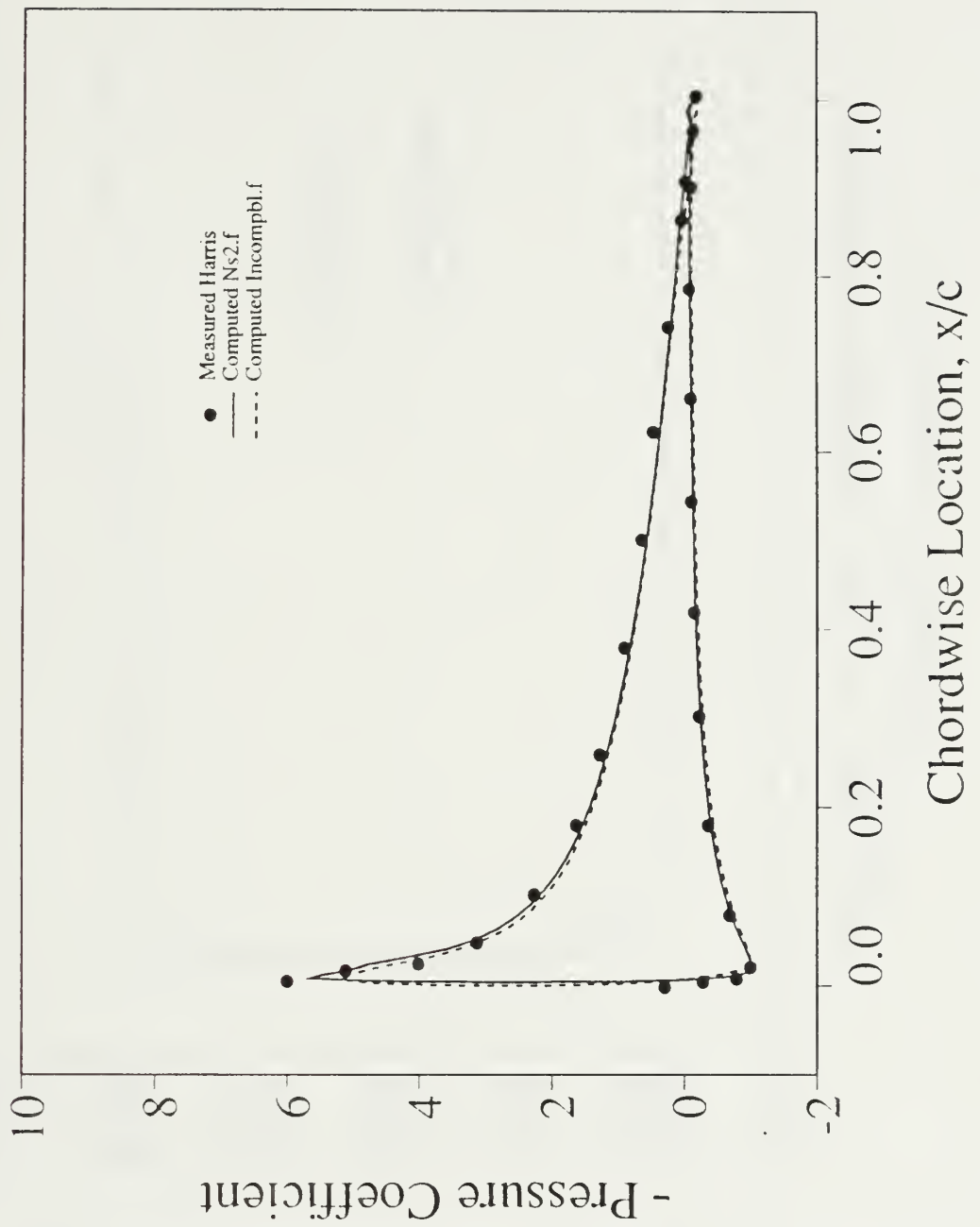


Figure 23. Pressure Distribution, $M=0.3$, $\alpha=11^\circ$, $Re=3 \times 10^6$

$M=0.3$, $\alpha=11.0$ deg, $Re=3 \times 10^6$

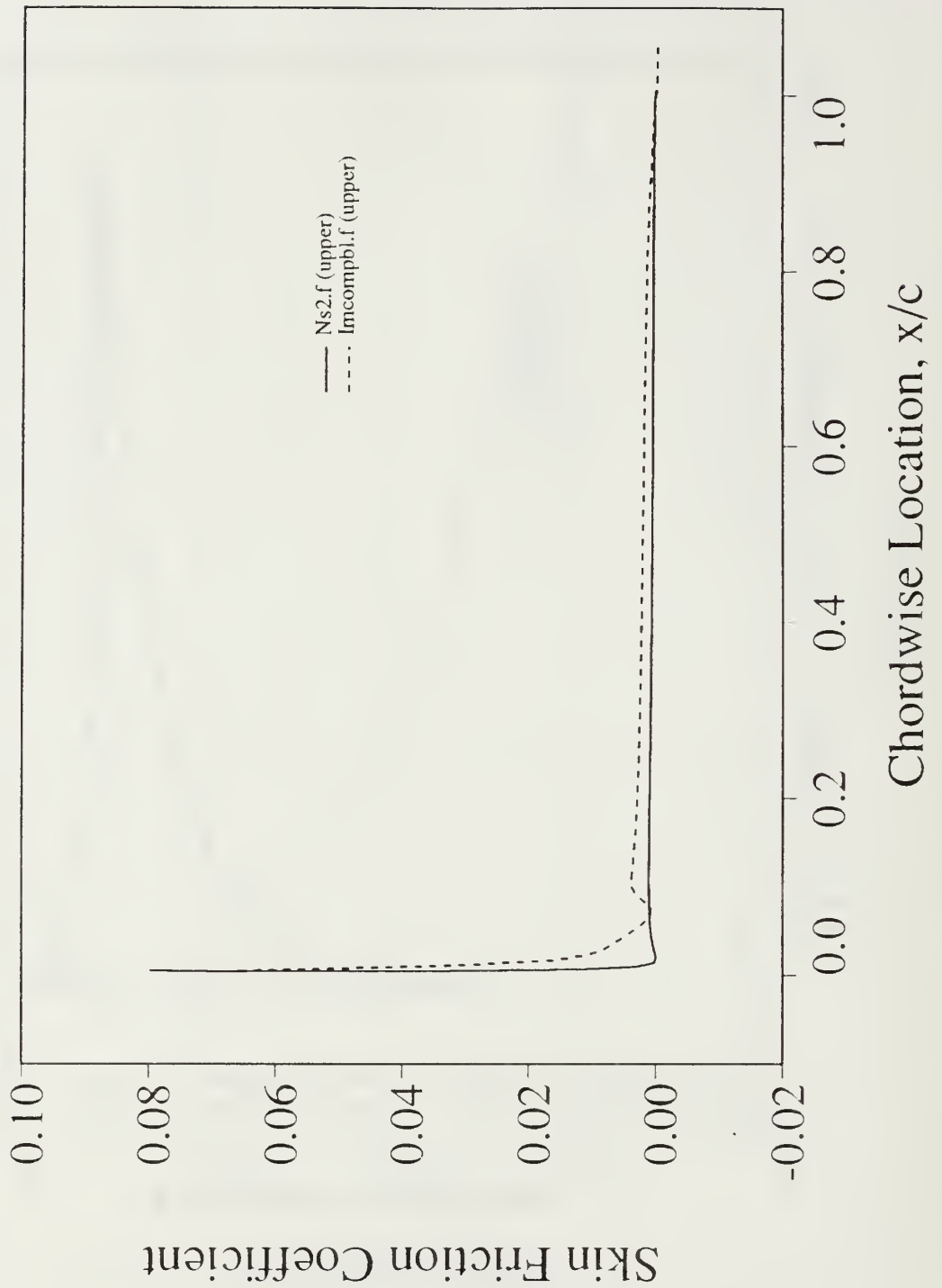


Figure 24. Skin Friction Distribution (Upper Surface), $M=0.3$, $\alpha=11^\circ$, $Re=3 \times 10^6$

$M=0.3$, $\alpha=11.0^\circ$, $Re=3 \times 10^6$

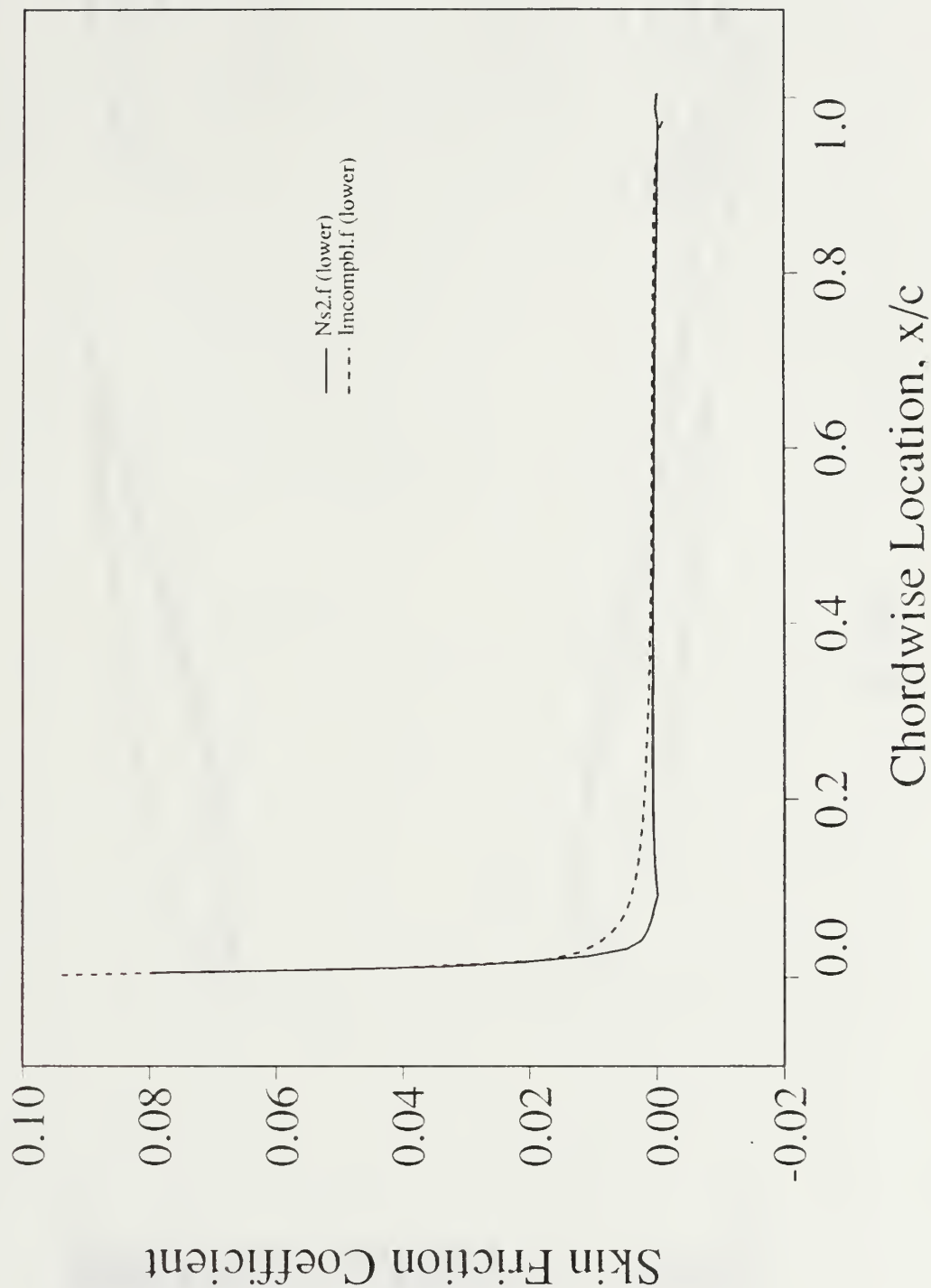


Figure 25. Skin Friction Distribution (Lower Surface), $M=0.3$, $\alpha=11^\circ$, $Re=3 \times 10^6$

MACH NUMBER

MACH 0.300
 ALPHA 11.00 DEG
 Re 3.00×10^6
 TIME 25.
 GRID 161x63

CONTOUR LEVELS

0.00000
 0.02500
 0.05000
 0.07500
 0.10000
 0.12500
 0.15000
 0.17500
 0.20000
 0.22500
 0.25000
 0.27500
 0.30000
 0.32500
 0.35000
 0.37500
 0.40000
 0.42500
 0.45000
 0.47500
 0.50000
 0.52500
 0.55000
 0.57500
 0.60000
 0.62500
 0.65000
 0.67500
 0.70000
 0.72500
 0.75000
 0.77500
 0.80000
 0.82500
 0.85000



Figure 26. Mach Contour, $M=0.3$, $\alpha=11^\circ$, $Re=3 \times 10^6$

CONTOUR LEVELS

0.840000
0.660000
0.680000
0.700000
0.720000
0.740000
0.760000
0.780000
0.800000
0.820000
0.840000
0.860000
0.880000
0.900000
0.920000
0.940000
0.960000
0.980000
1.000000
1.020000
1.040000
1.060000

MACH 0.300
ALPHA 11.00 DEG
Re 3.00x10+6
TIME 25.
GRID 161x64



Figure 27. Density Contour, $M=0.3$, $\alpha=11^\circ$, $Re=3 \times 10^6$

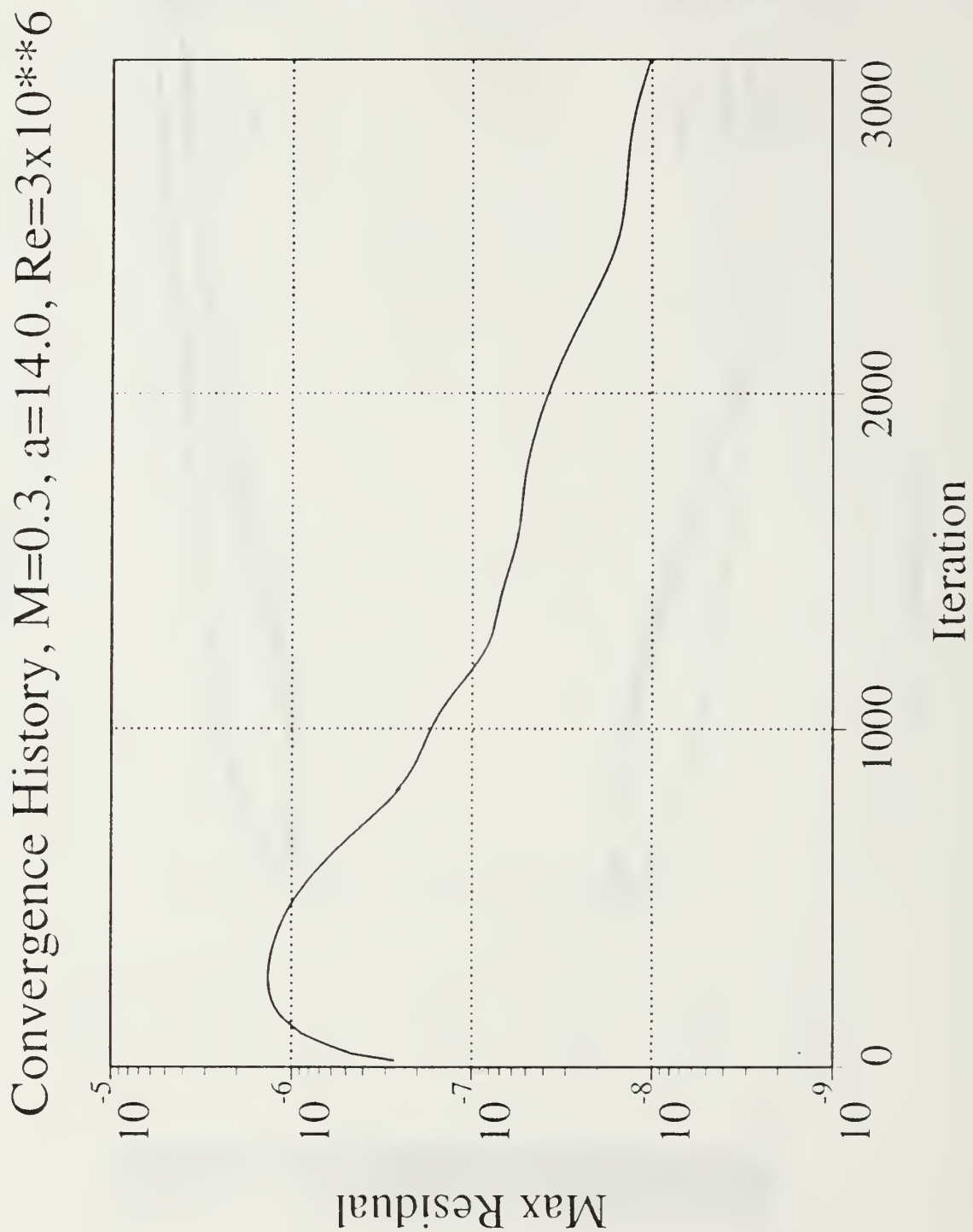


Figure 28. Convergence History, $M=0.3$, $\alpha=14^\circ$, $Re=3 \times 10^6$

Steady State: $M=0.3$, $Re=3 \times 10^6$

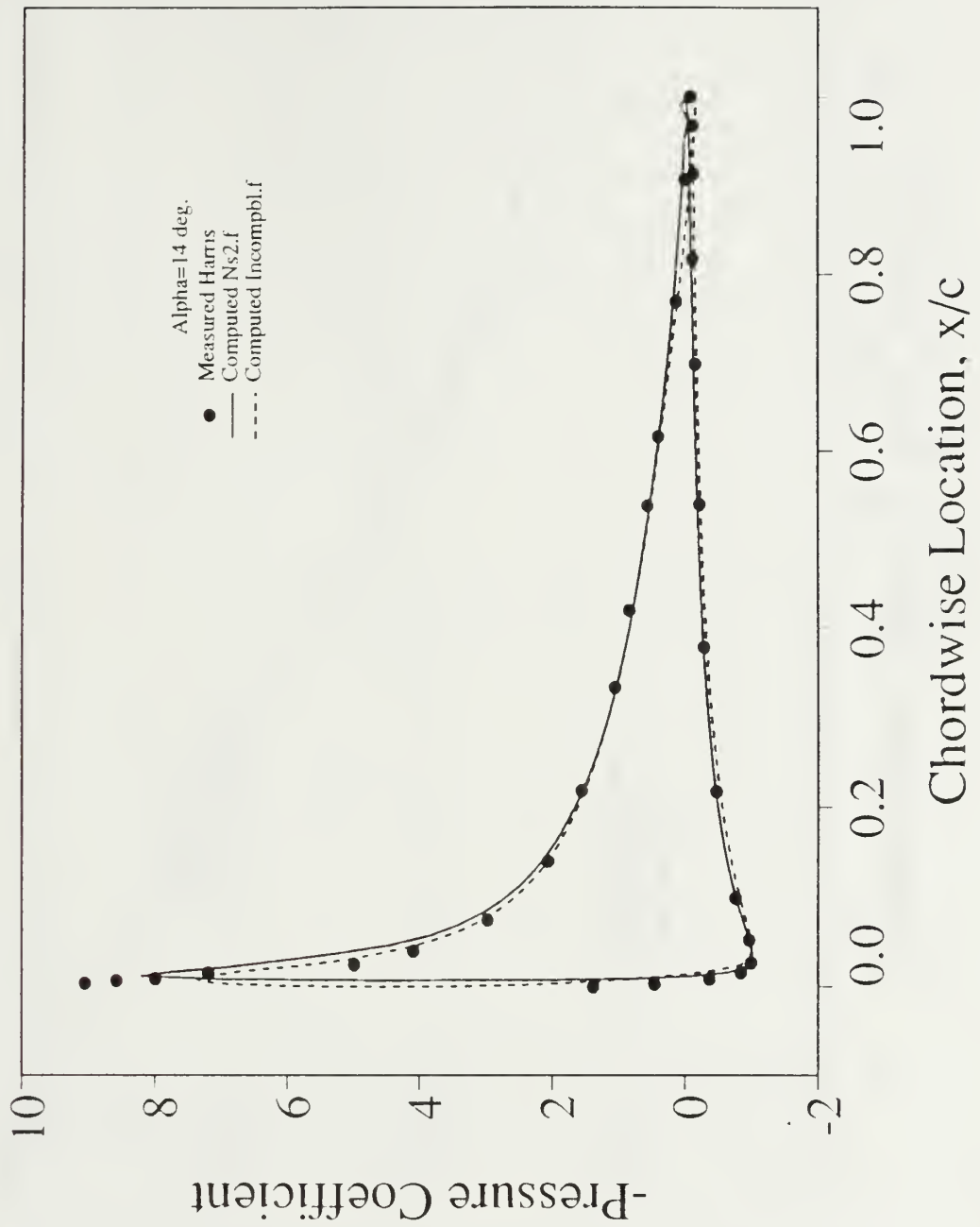


Figure 29. Pressure Distribution, $M=0.3$, $\alpha=14^\circ$, $Re=3 \times 10^6$

Steady State: $M=0.3$, $Re=3 \times 10^6$

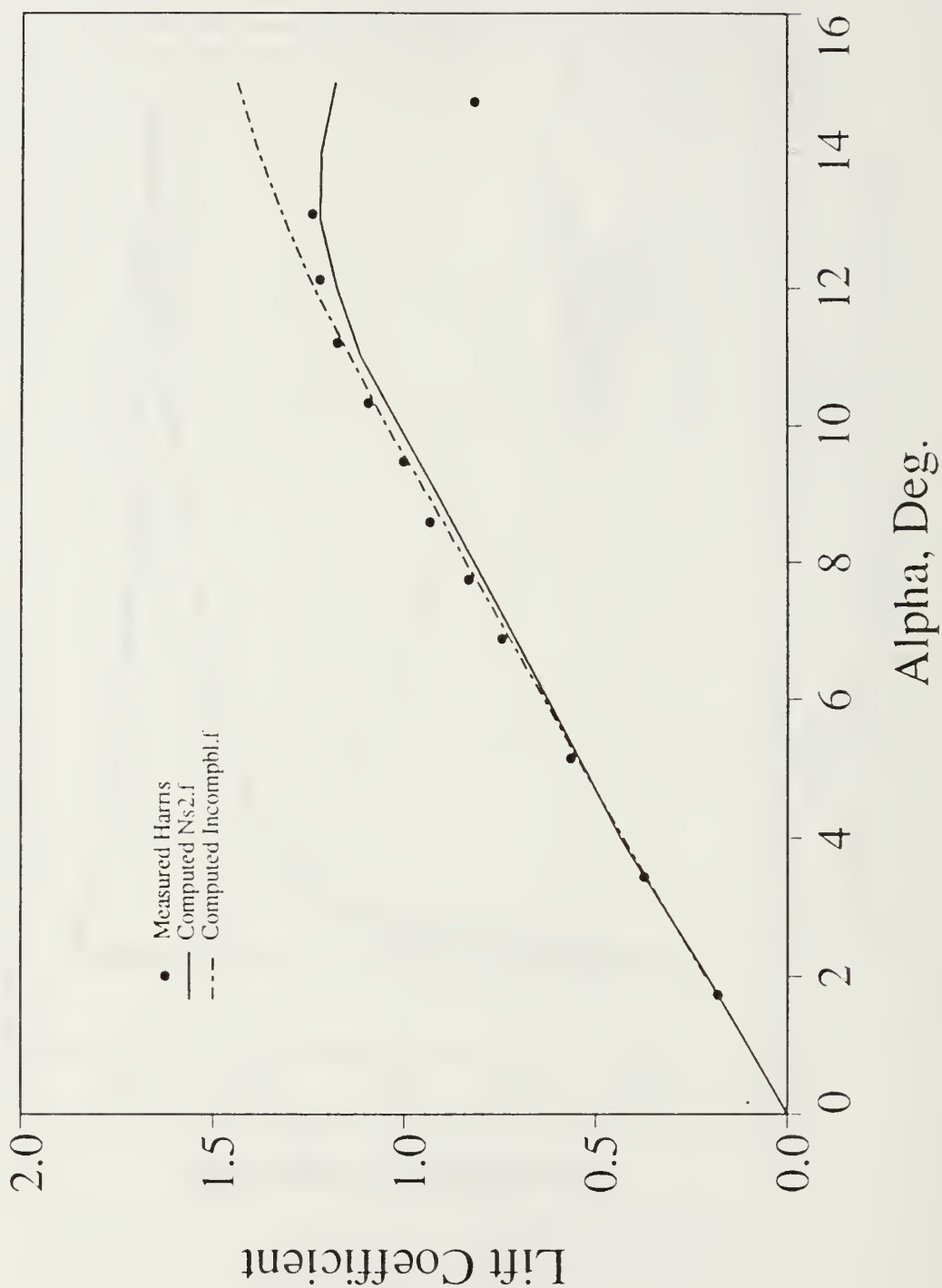


Figure 30. C_L vs α , $M=0.3$, $Re=3 \times 10^6$

Steady State: $M=0.3$, $Re=3 \times 10^6$

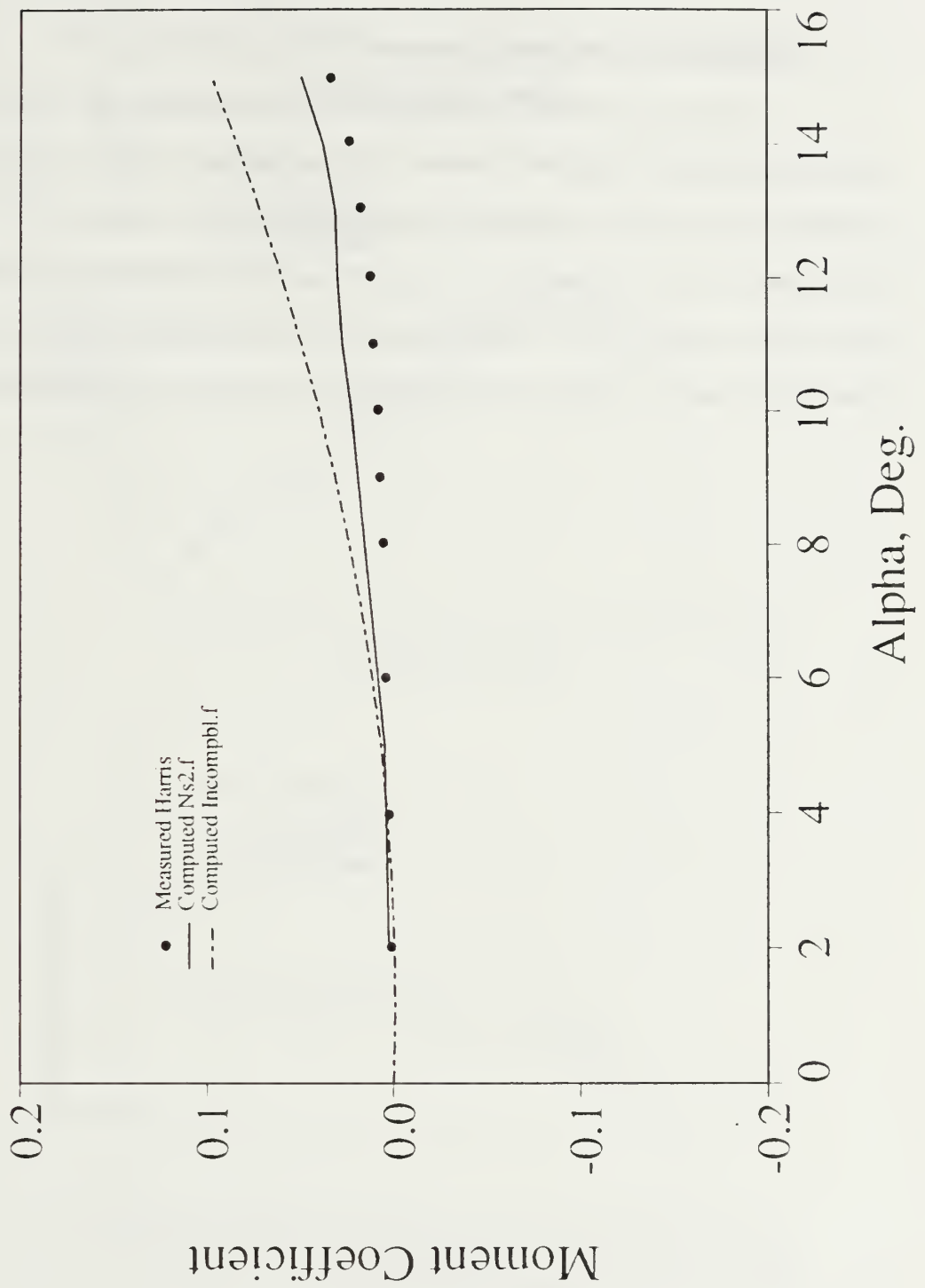


Figure 31. C_m vs α , $M=0.3$, $Re=3 \times 10^6$

d. Case 4. $M=0.3$, $Re=4 \times 10^6$

Figure 32 shows a comparison of the computed lift curve with the experimental data at a Reynolds number of four million. It can be seen that the computed maximum lift angle and hence the static stall angle is 13.5° degrees. This agrees quite well with the experimentally measured stall angle of McCroskey et al [Ref. 17]. The computed lift and pitching moment are in fair agreement for small angles of attack, but start to deviate at larger angles.

$M = 0.3$, $Re = 4 \times 10^6$ Baldwin-Lomax Turbulence Model

Experiment: McCroskey

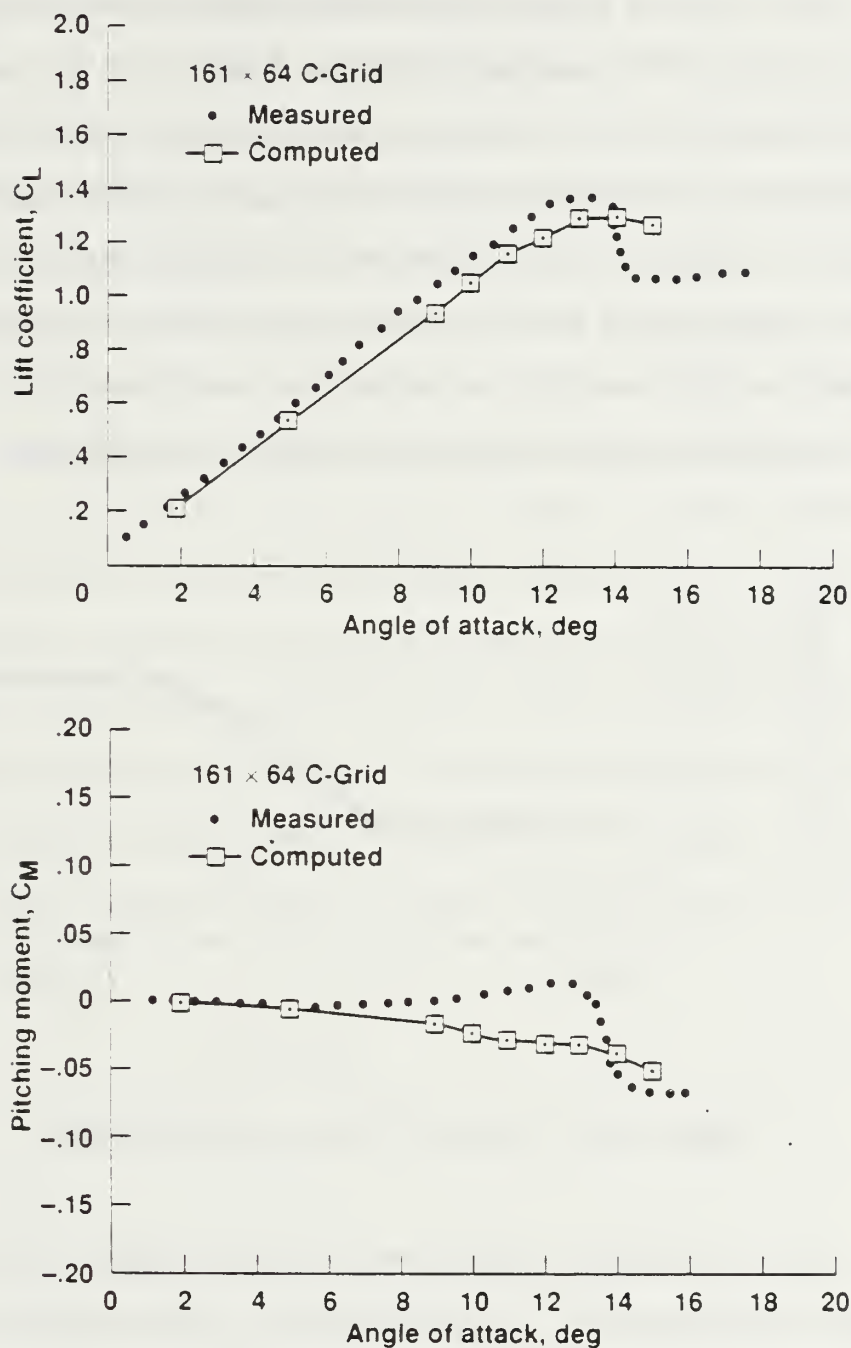


Figure 32. C_L vs. α and C_M vs. α , $M=0.3$, $Re=4 \times 10^6$

2. Rapidly Pitching Airfoil

Next, AGARD Case 6 from Landon [Ref. 18] was investigated using Ns2.f and U2diif.f. The computed results are compared to the measured data. The flow condition for this case corresponds to a freestream Mach number equal to 0.3 at a non-dimensional pitch rate equal to 0.01272 and a Reynolds number of 2.7 million. Flow solutions for a rapidly pitching airfoil were computed by pitching the airfoil about the quarter chord at a constant rate from zero degrees angle of attack to a final angle of attack of 15.54° . Figure 33 shows a sketch of the motion produced by a rapidly pitching airfoil.

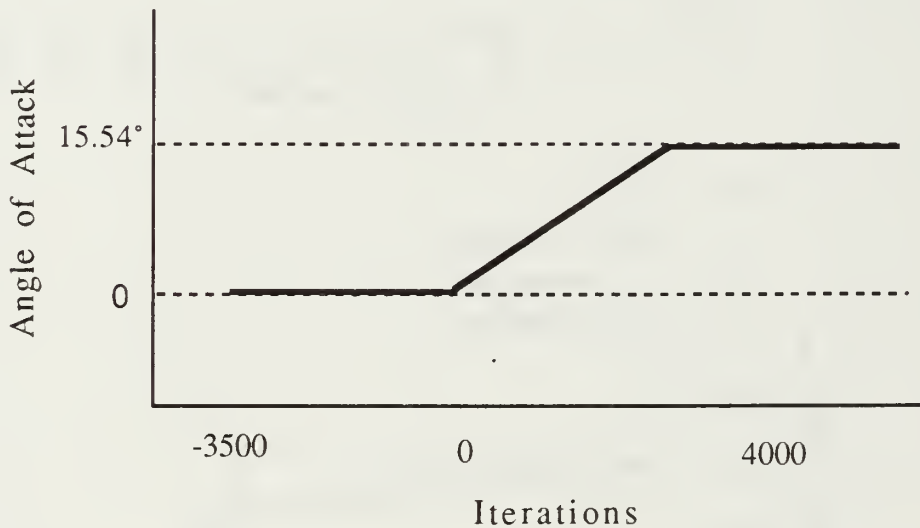


Figure 33. Rapidly Pitching Airfoil Motion

First a steady-state solution at zero degrees angle of attack was well converged to 3800 iterations. Then the iteration counter was reset to zero and the airfoil was rapidly pitched up to the final angle. The reduced frequency k is given by $k = \alpha c / 2 U_\infty$, where α is the pitch rate. In terms of non-dimensional quantities $\alpha(t) = 2M_\infty k$ and $\alpha(t) = \alpha_0 + \alpha_1(t/T)$, where α_0 (A_0), is the initial angle

of attack $\alpha=0^\circ$, α_1 (A_1), is the final angle of attack $\alpha=15.54^\circ$, and T is the time required for the airfoil to complete the pitching motion.

a. Case 5. $M=0.3$, $k=0.01272$, $Re=2.7 \times 10^6$

Figure 34 shows the comparison of the computed pressure distribution for the ramp-type unsteady motion at $\alpha=4.84^\circ$, for an inviscid Euler calculation. This Euler solution uses a 121×35 C-grid for the computation. Similar results were produced for ensuing angles of attack. Figures 35 through 39 show pressure distributions at $\alpha=4.84^\circ$, $\alpha=6.72^\circ$, $\alpha=10.80^\circ$, $\alpha=12.83^\circ$, and $\alpha=15.54^\circ$. Surprisingly, the inviscid code predicted the suction peak more accurately than the N-S code for all angles of attack. Several explanations are offered to account for this unexpected result. First the 161×65 C-grid may not be fine enough to predict the magnitude of the suction peak and the N-S code may have too much numerical viscosity, thus in effect performing calculation at a lower Reynolds number. The flow at the leading edge may in fact be laminar, while the computed solution assumed turbulent flow everywhere. Figure 40 shows the Mach contour and Figure 41 shows the density contour at $\alpha=10.8^\circ$.

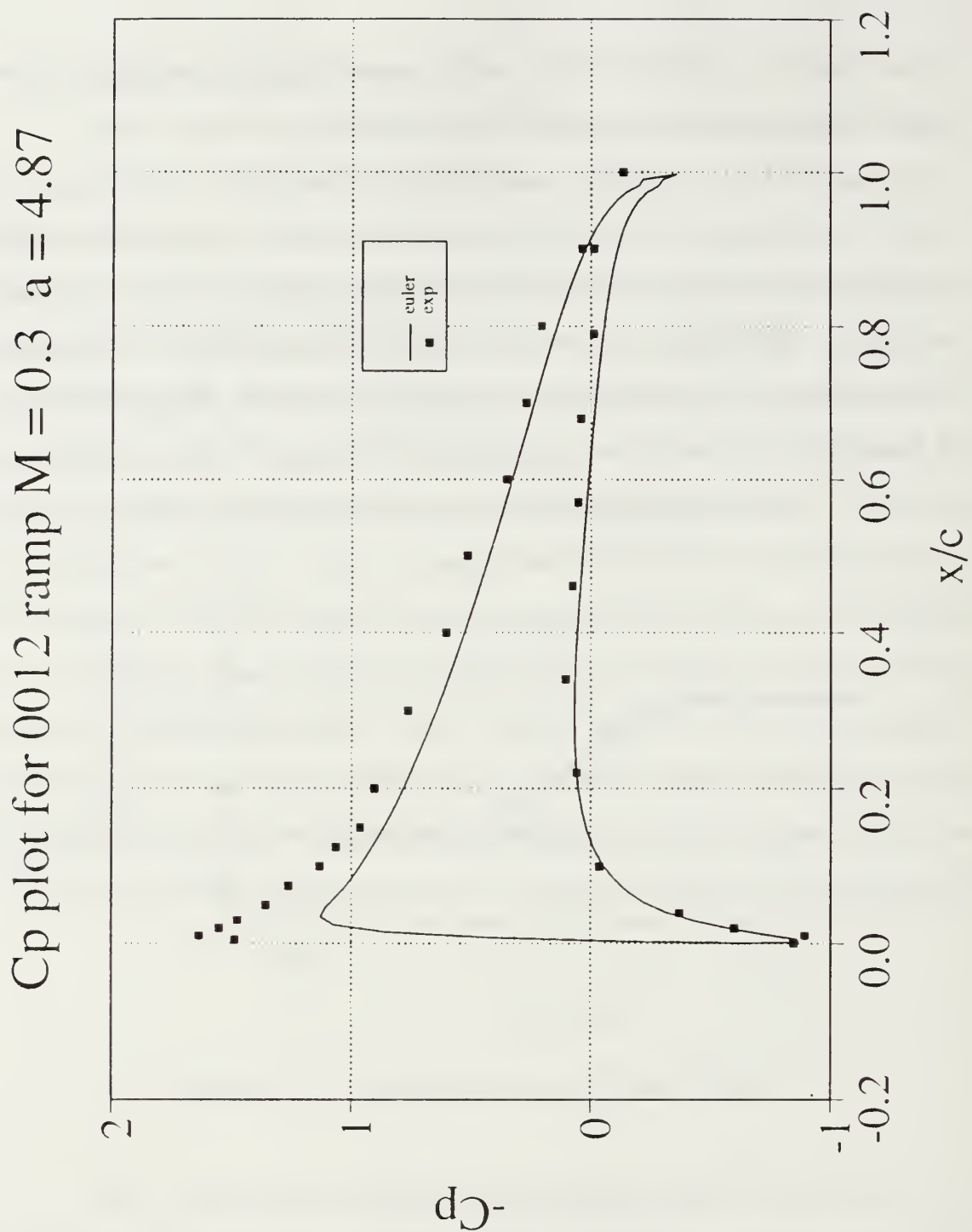


Figure 34. Pressure Distribution (Inviscid), Ramp Motion, $M=0.3$, $\alpha=4.87^\circ$, $k=0.01272$, $Re=2.7 \times 10^6$

Ramp Motion: $M=0.3$, $K=0.01272$, $Re=2.7 \times 10^6$

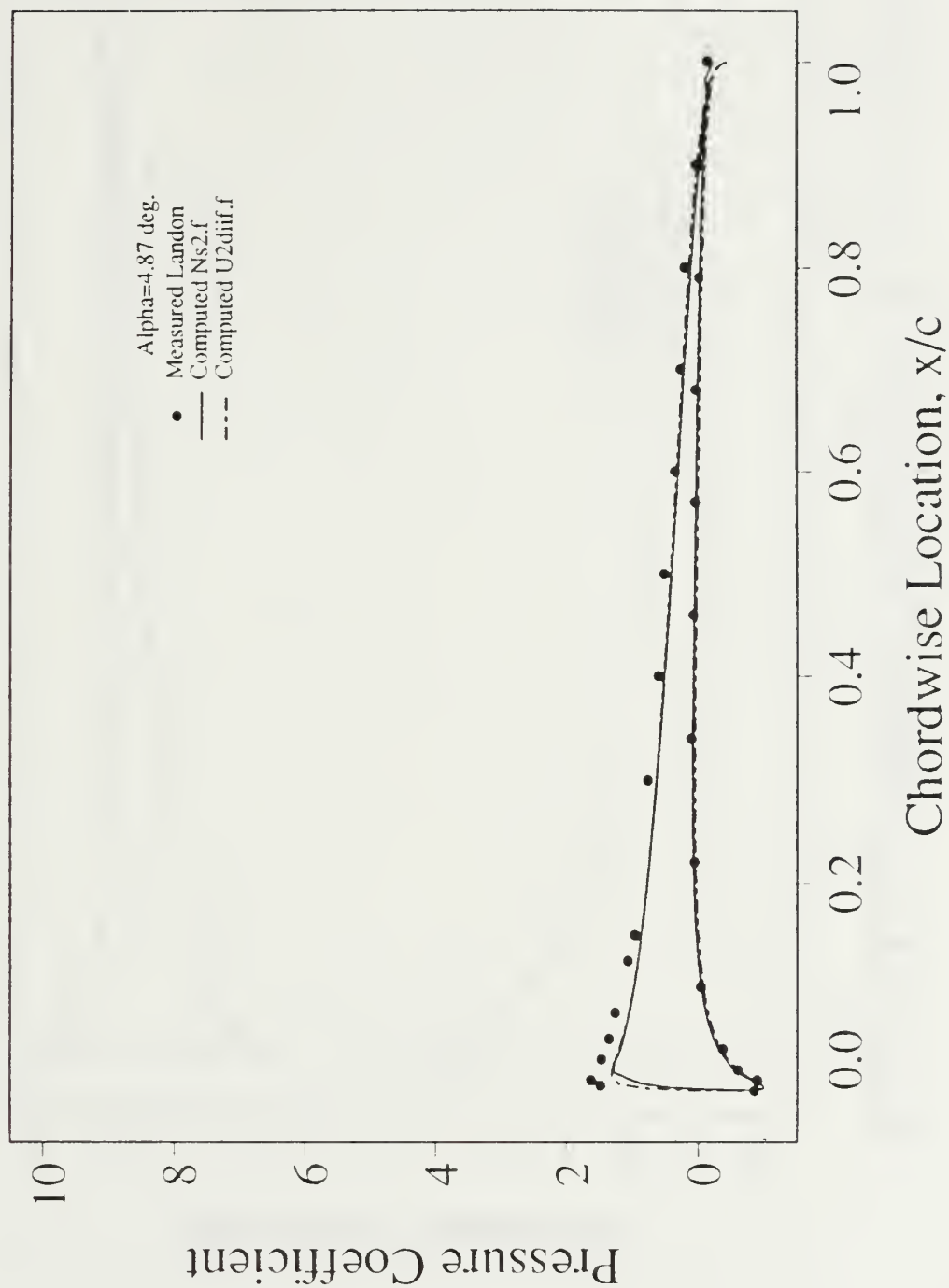


Figure 35. Pressure Distribution, Ramp Motion, $M=0.3$, $\alpha=4.87^\circ$, $k=0.01272$, $Re=2.7 \times 10^6$

Ramp Motion: $M=0.3$, $K=0.01272$, $Re=2.7 \times 10^6$

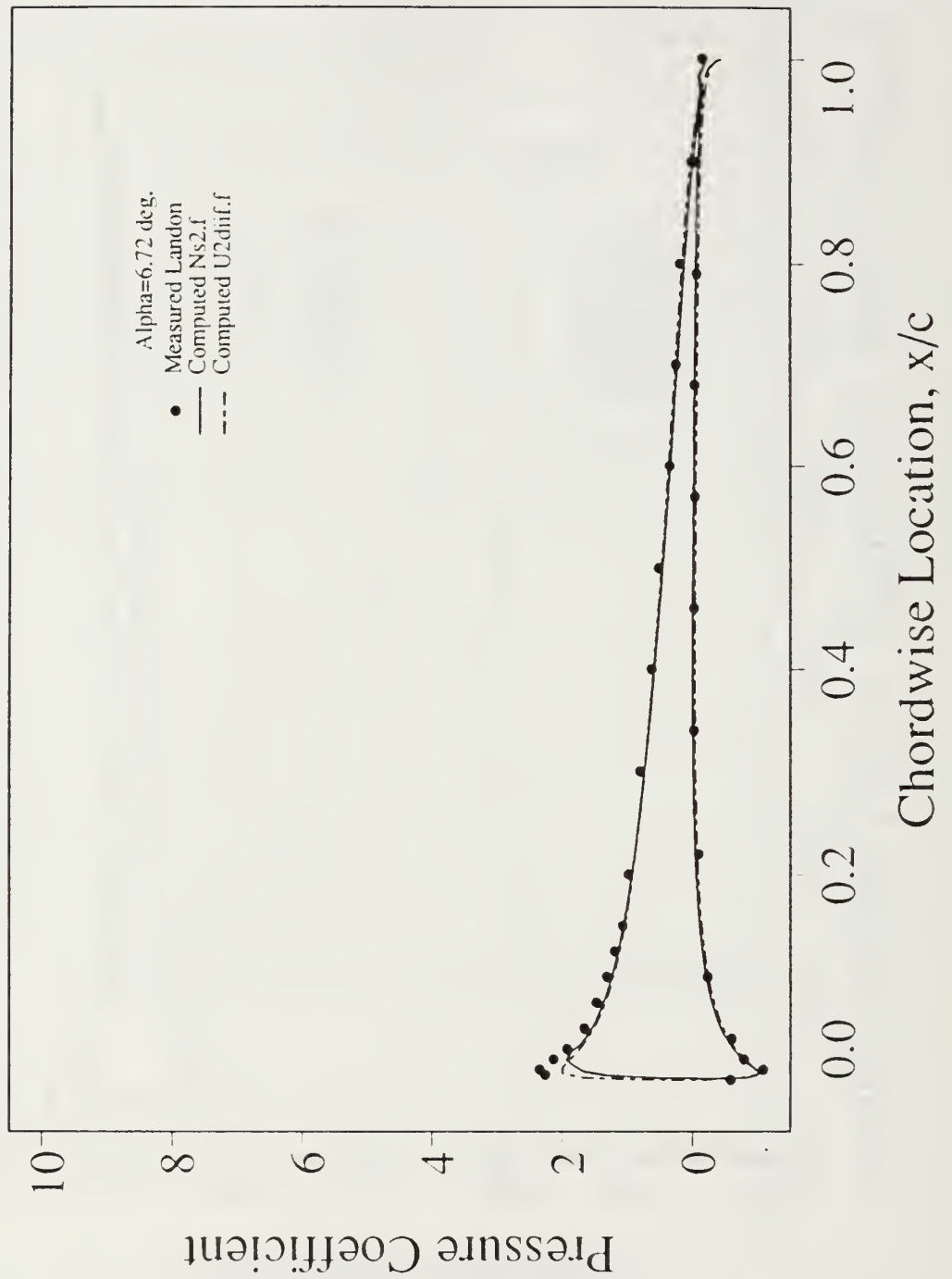


Figure 36. Pressure Distribution, Ramp Motion, $M=0.3$, $\alpha=6.72^\circ$, $k=0.01272$, $Re=2.7 \times 10^6$

Ramp Motion: $M=0.3$, $K=0.01272$, $Re=2.7 \times 10^6$

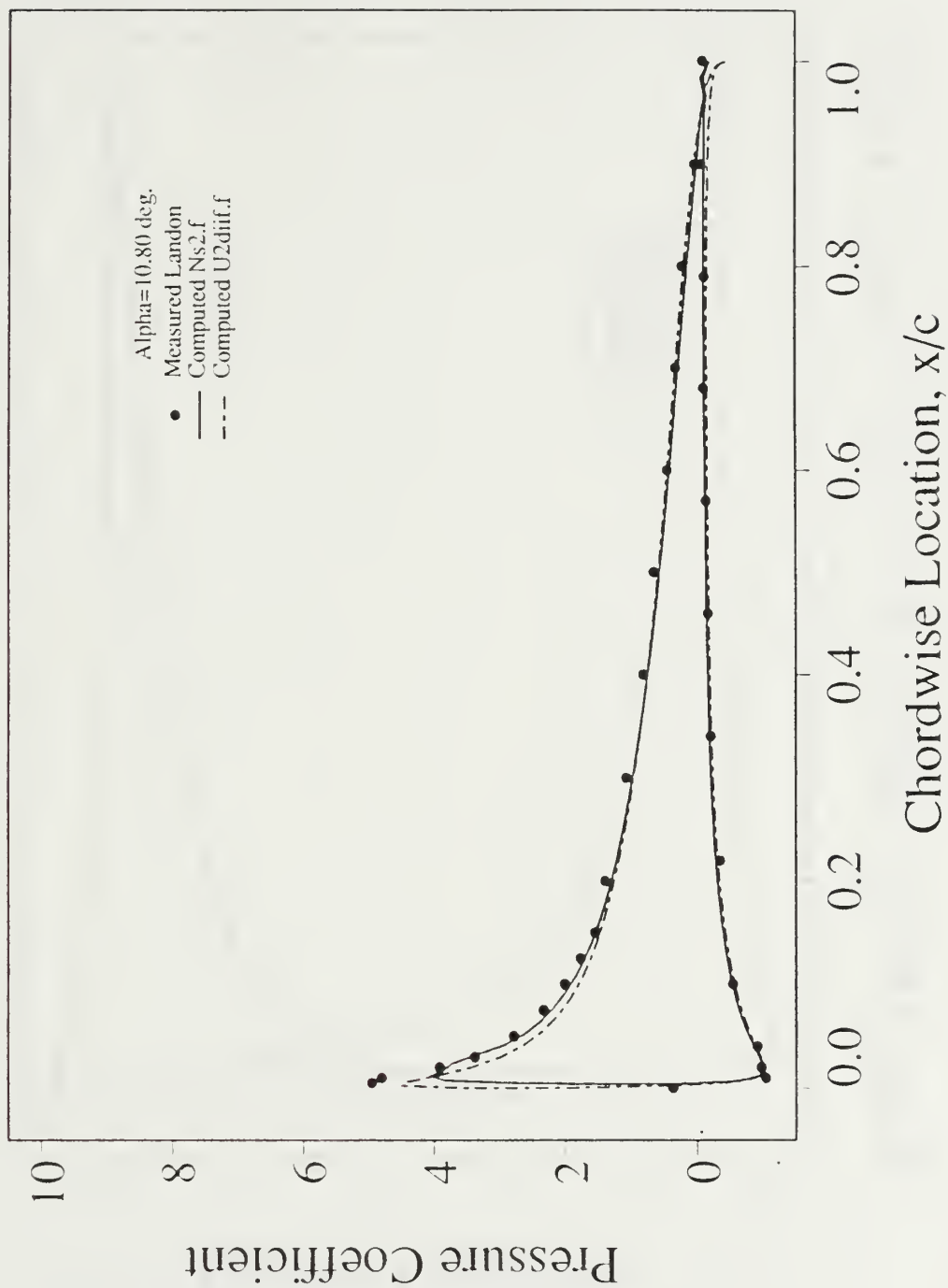


Figure 37. Pressure Distribution, Ramp Motion, $M=0.3$, $\alpha=10.80^\circ$, $k=0.01272$, $Re=2.7 \times 10^6$

Ramp Motion: $M=0.3$, $K=0.01272$, $Re=2.7 \times 10^6$

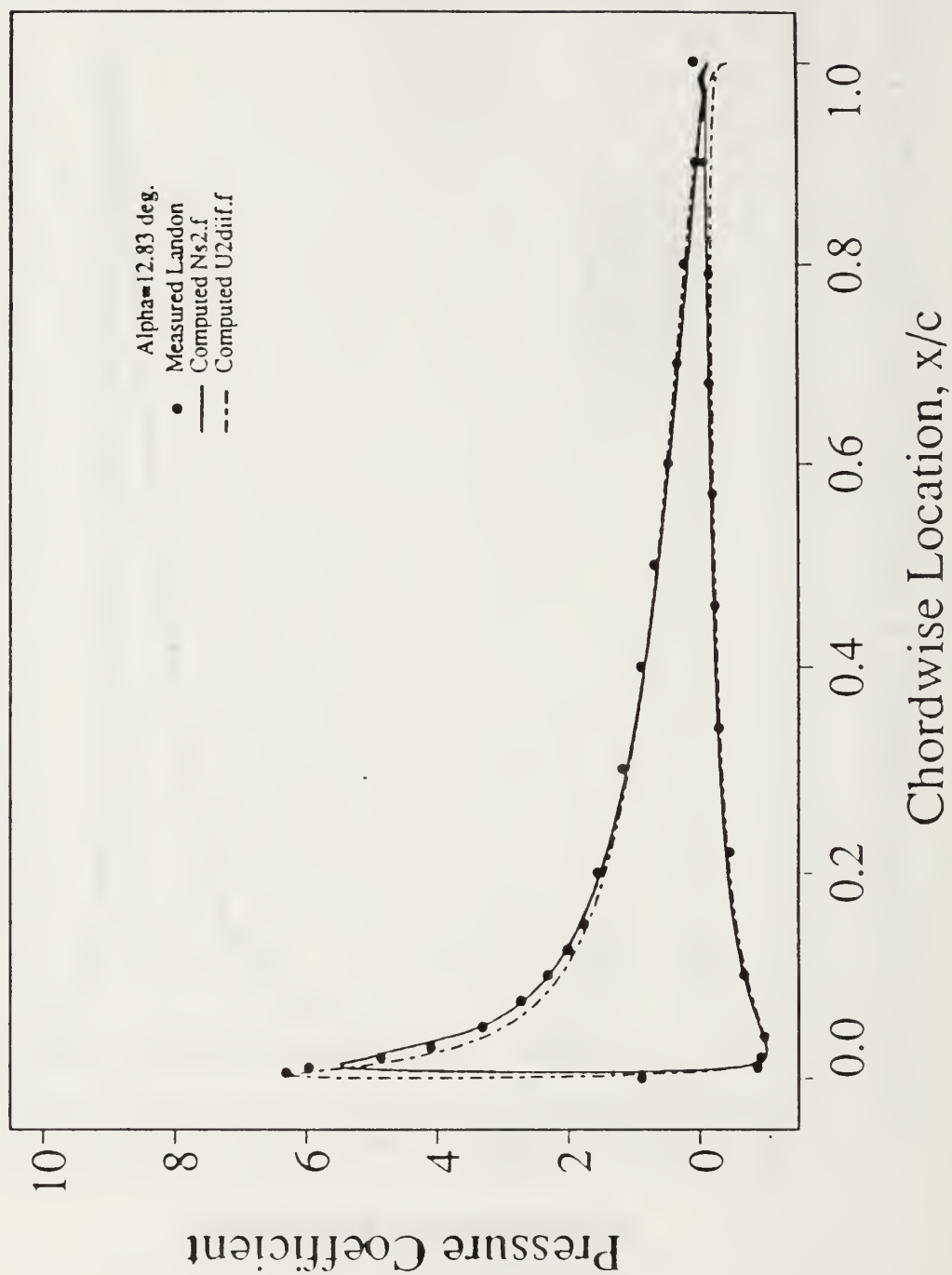


Figure 38. Pressure Distribution, Ramp Motion, $M=0.3$, $\alpha=12.83^\circ$, $k=0.01272$, $Re=2.7 \times 10^6$

Ramp Motion: $M=0.3$, $K=0.01272$, $Re=2.7 \times 10^6$

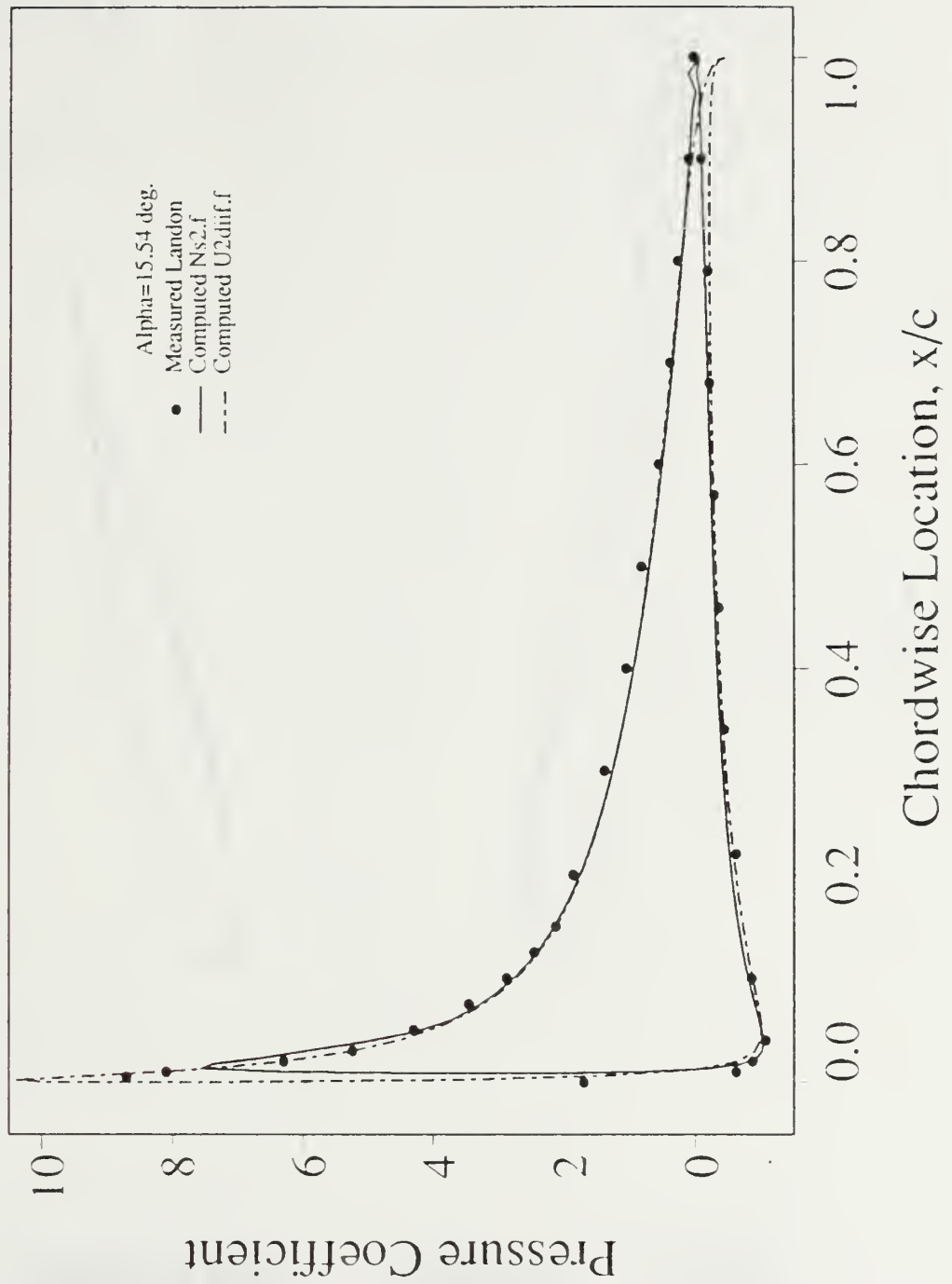


Figure 39. Pressure Distribution, Ramp Motion, $M=0.3$, $\alpha=15.54^\circ$, $k=0.01272$, $Re=2.7 \times 10^6$

MACH NUMBER

0.300
10.81 DEG
2.70E+06
25.
6010

CONTOUR LEVELS

0.00000
0.02000
0.04000
0.06000
0.08000
0.10000

0.12000
0.14000
0.16000
0.18000
0.20000
0.22000

0.24000
0.26000
0.28000
0.30000
0.32000
0.34000
0.36000
0.38000
0.40000
0.42000
0.44000
0.46000
0.48000
0.50000
0.52000
0.54000
0.56000
0.58000
0.60000
0.62000
0.64000
0.66000
0.68000
0.70000
0.72000
0.74000
0.76000
0.78000
0.80000
0.82000
0.84000
0.86000
0.88000
0.90000
0.92000
0.94000
0.96000
0.98000
1.00000



Figure 40. Mach Contour, Ramp Motion, $M=0.3$, $\alpha=10.8^\circ$, $k=0.01272$, $Re=2.7 \times 10^6$



00000000
00000000
00000000
00000000
00000000

Year	1990	1991	1992	1993
1990	100	100	100	100
1991	100	100	100	100
1992	100	100	100	100
1993	100	100	100	100

1,984,000
1,967,000
0,980,000
0,990,000
1,000,000
1,010,000
1,020,000
1,030,000
1,040,000
1,050,000



83

A detail of the flow field generated by Ns2.f at $\alpha=12.83^\circ$ is shown in Figure 42. The flow appears to be smooth and attached (the dark line shows the boundary layer edge). However, magnification, as shown in Figure 43, reveals the start of a slight reverse flow region at approximately 10% chord. At $\alpha=15.54^\circ$, Figure 44, the boundary layer is much thicker with reverse flow profiles from approximately 10% chord to the trailing edge.

Figures 45 and 46 present the computed C_l vs α and C_m vs α curves, respectively. The Navier-Stokes code underpredicts lift and pitching moment coefficients whereas the inviscid panel method gives significantly better lift predictions. However, it fails to predict the pitching moment coefficient for angles greater than 10° . A more comprehensive investigation of the dynamics of a rapidly pitching airfoil can be found in Grohsmeyer [Ref. 19].



85



Figure 43. Velocity Field (Magnified), Ramp Motion, $M=0.3$, $\alpha=12.83^\circ$, $k=0.01272$, $Re=2.7 \times 10^6$

Ramp Motion: $M=0.3$, $K=0.01272$, $Re=2.7 \times 10^6$

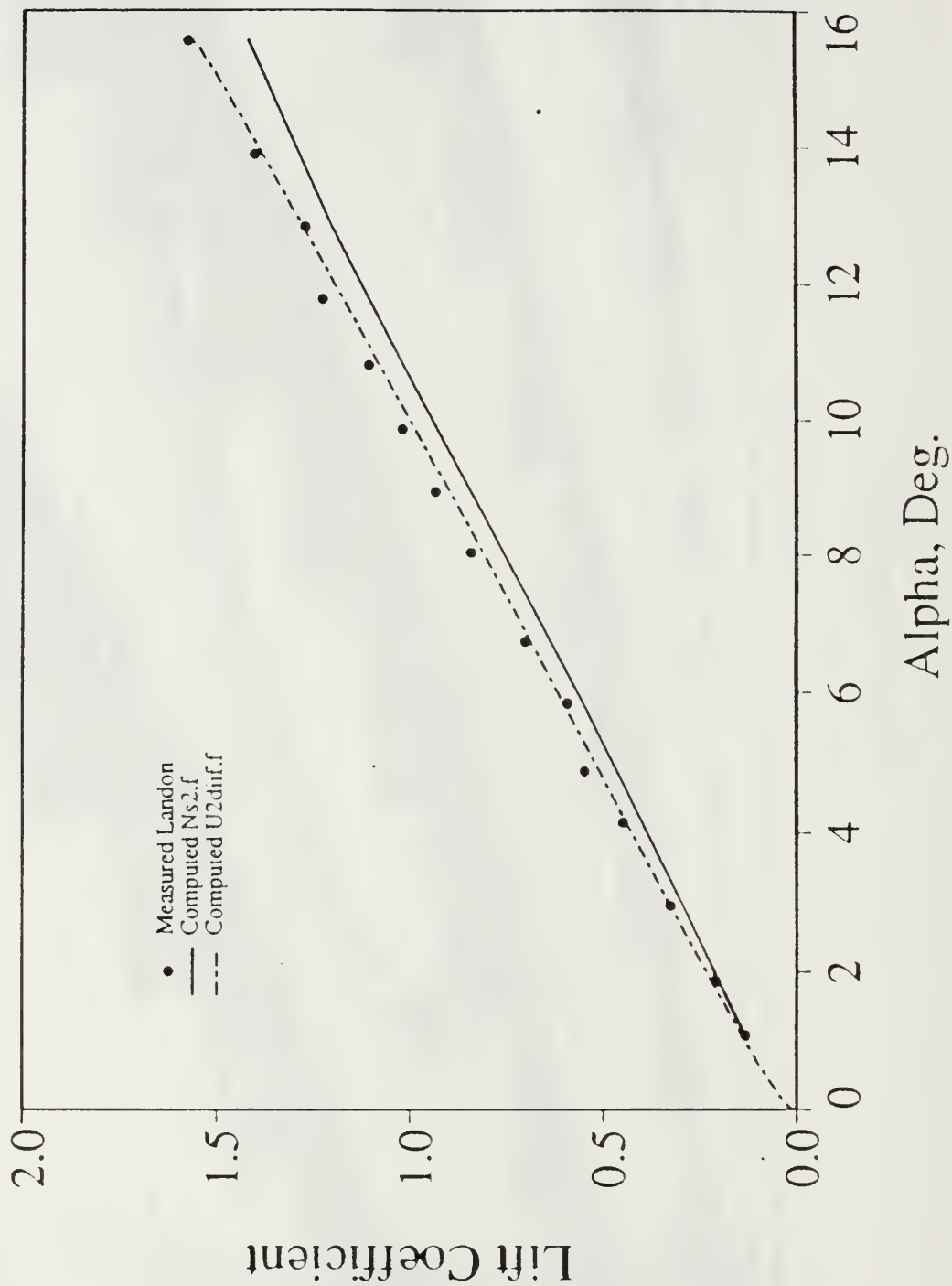


Figure 45. C_l vs α , Ramp Motion, $M=0.3$, $k=0.01272$, $Re=2.7 \times 10^6$

Ramp Motion: $M=0.3$, $K=0.01272$, $Re=2.7 \times 10^6$

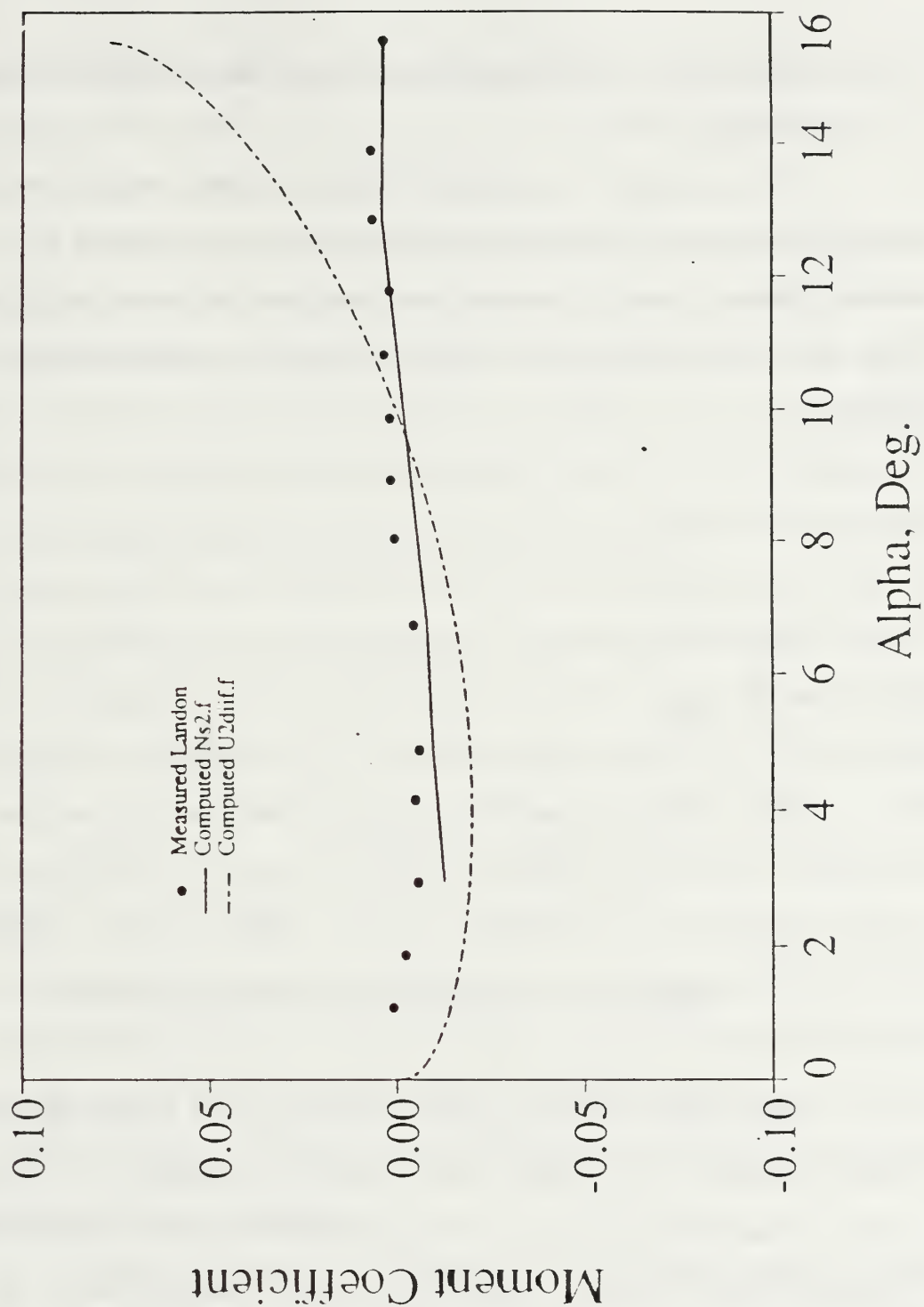


Figure 46. C_m vs α , Ramp Motion, $M=0.3$, $k=0.01272$, $Re=2.7 \times 10^6$

3. Harmonic Airfoil Oscillation Using the Baldwin-Lomax Turbulence Model

Next, the code was applied to sinusoidal airfoil oscillations about the quarter chord point. These time periodic solutions were obtained for the second cycle because the results obtained for the third cycle were indistinguishable from ones of the second cycle. Figure 47 shows the computed angle of attack history.

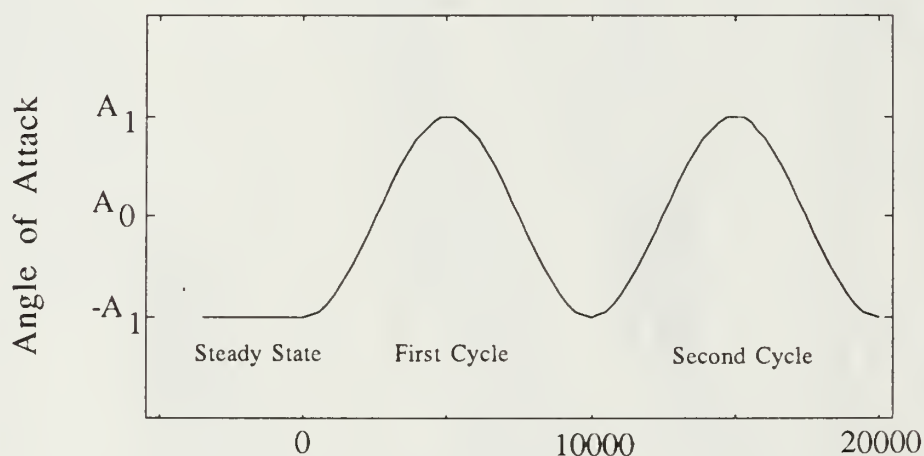


Figure 47. Harmonically Oscillating Airfoil

Here, A_0 is the mean angle of attack, and A_1 is the amplitude. For each oscillatory case a steady-state solution was obtained for the minimum angle of attack during the cycle. The iteration counter was set to zero as the sinusoidal motion was time shifted half a cycle so that the start of the motion begins at the minimum angle of attack. This ensures a smooth transition for the converged steady state solution to the start of the oscillatory motion. Ten

thousand (10,000) iterations were computed per cycle, with a timestep equal to approximately 0.05 to 0.01.

a. Case 6. $\alpha(t)=A_0 \pm A_1 \sin(\omega t)$

All the computations presented in this section are computed with Ns2.f using the Baldwin-Lomax turbulence model. Figures 48 and 49 show the effect of Mach number on the lift and moment hysteresis loops for small amplitude oscillations about a mean angle of 12 degrees with an amplitude of 3.0 degrees, at a Reynolds number of four million and at a reduced frequency of 0.1. Note that the hysteresis loops for $M_\infty=0.4$ oscillate wildly and third cycle computations do not coincide with results from previous cycles. For the $M_\infty=0.3$ computation the moment hysteresis loop indicates a stable condition. The effect of amplitude is shown in Figures 50 and 51. Figures 52 and 53 also show the effect of amplitude for a larger mean angle of attack, $A_0=14.0^\circ$, at the same Mach number, reduced frequency, and Reynolds number, as before. Both solutions oscillate in a manner that is not repeatable if the motion is allowed to continue for additional cycles. For this comparison the maximum angle of attack attained during a cycle exceeded 16.5° . A comparison of the first and second cycle lift and moment coefficient loops is shown in Figures 54 and 55. Note that the second cycle lift curve starts at a slightly greater lift coefficient than in the first cycle. Aside from this anomaly, the loops are in good agreement but exhibit no instability.

Figure 56 shows the computed lift and moment loops for small amplitude oscillations about a mean angle of 13 degrees with an amplitude of 2.5 degrees, at a Reynolds number of two million, for three values of reduced

frequency. It can be seen that all the moment loops computed in this section using the Baldwin-Lomax turbulence model indicate torsional stability.

Oscil. Motion:

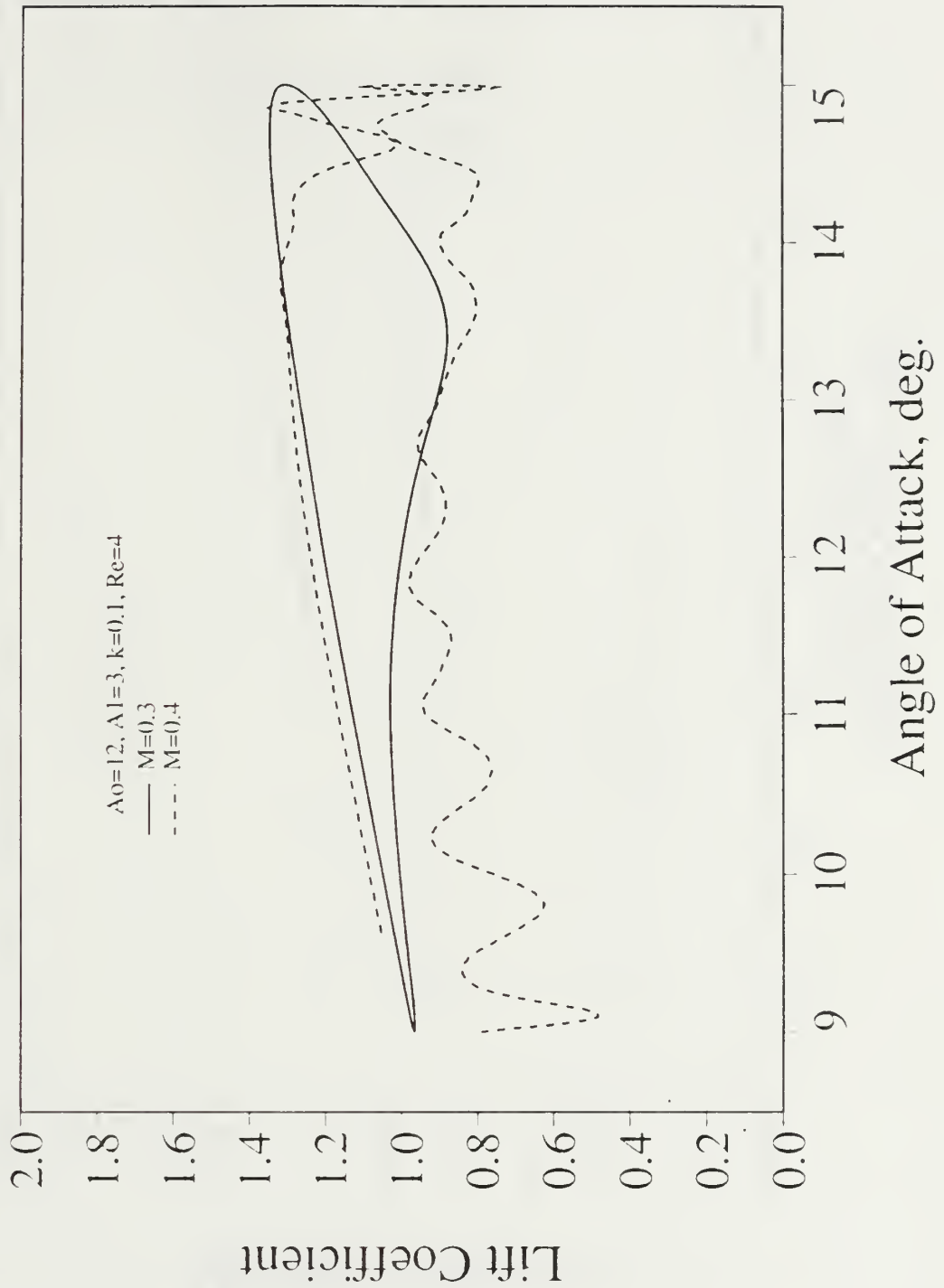


Figure 48. Effect of Mach Number on Unsteady Motion, $\alpha(t)=12^\circ \pm 3^\circ \sin(\omega t)$, $k=0.10$, $Re=4 \times 10^6$

Oscil. Motion:

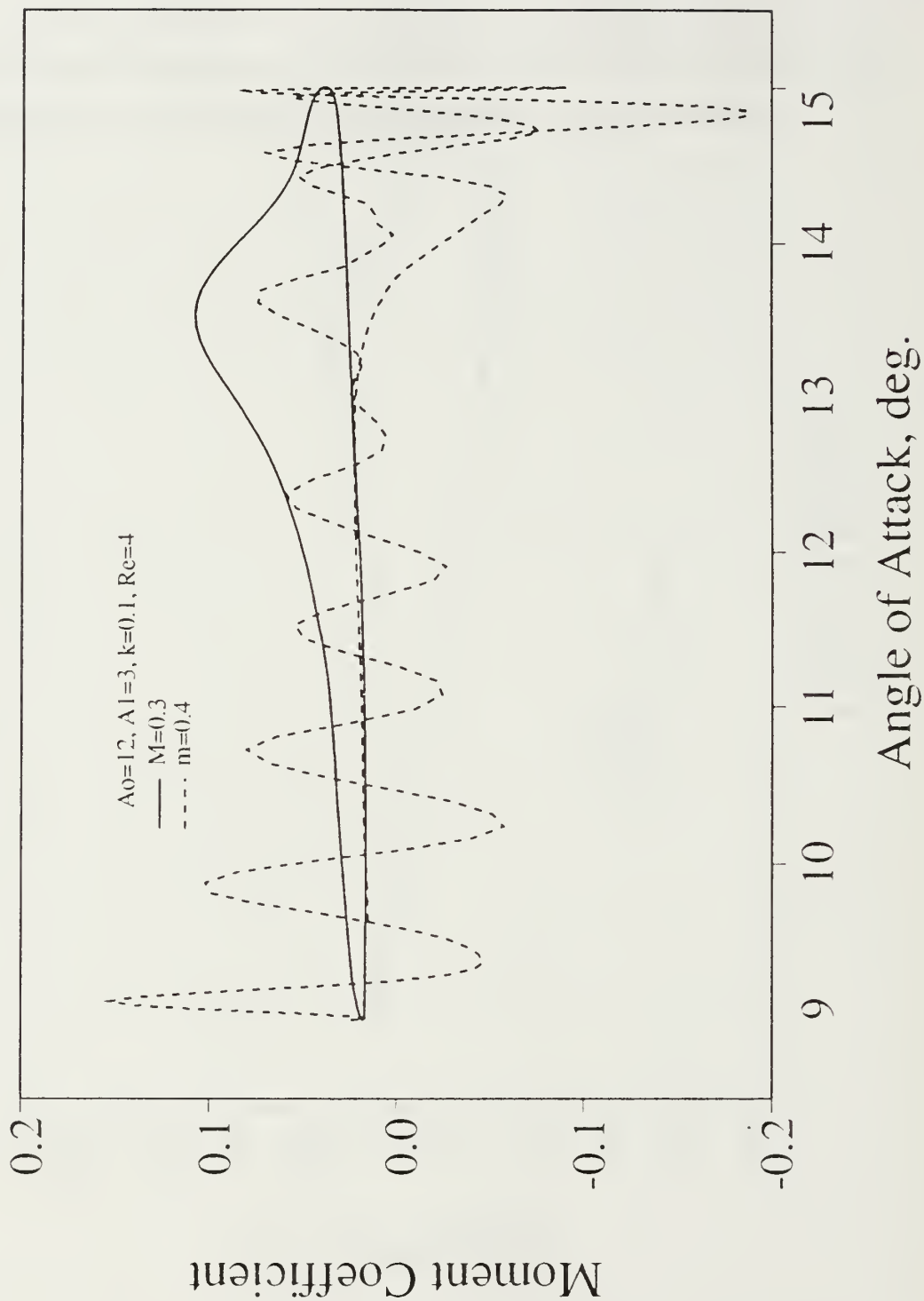


Figure 49. Effect of Mach Number on Unsteady Motion,
 $\alpha(t)=12^\circ \pm 3^\circ \sin(\omega t)$, $k=0.10$, $Re=4 \times 10^6$

Oscil. Motion:

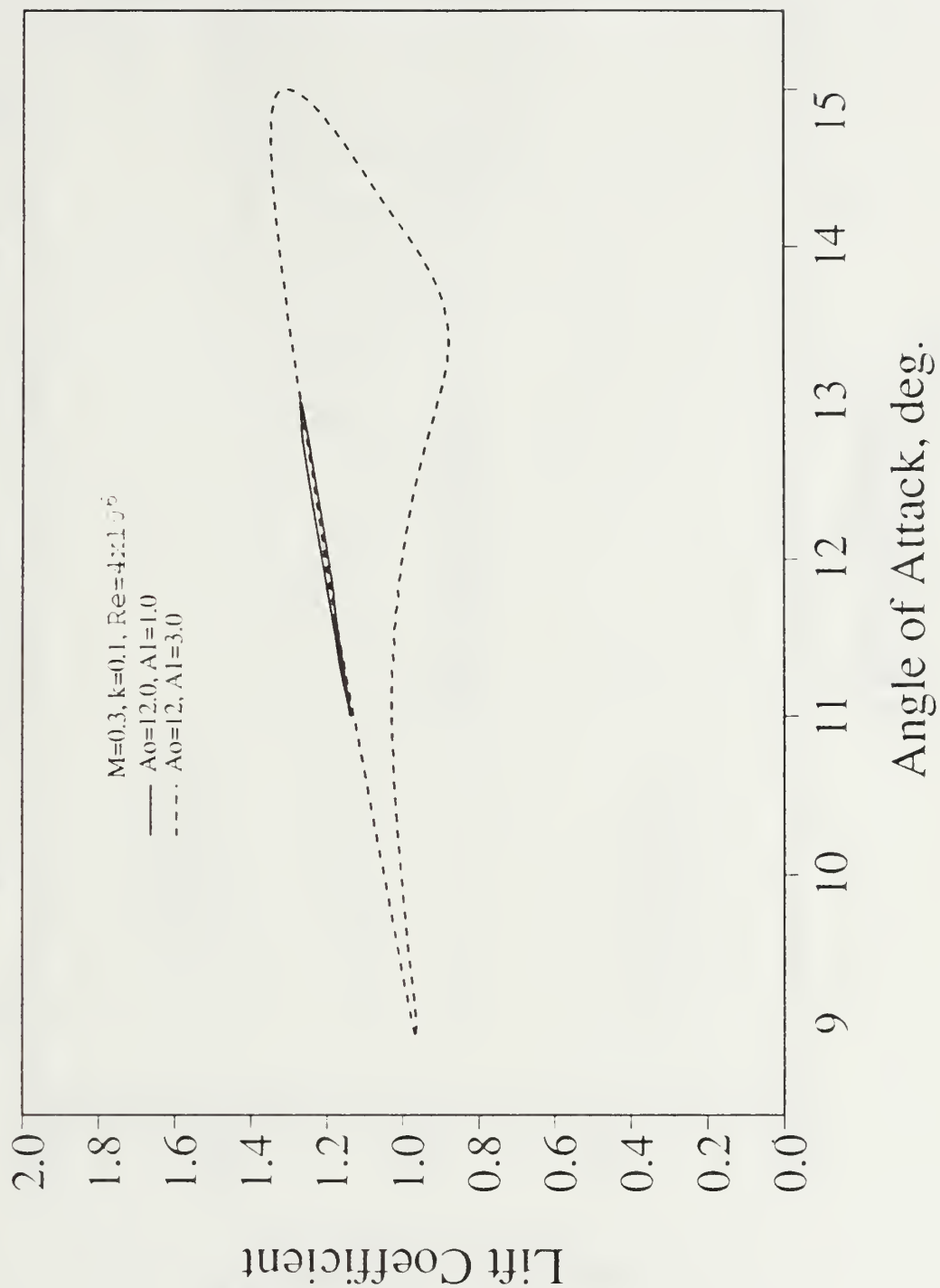


Figure 50. Effect of Amplitude on Unsteady Motion, $M=0.3$, $\alpha(t)=12^\circ \pm A_1^\circ \sin(\omega t)$, $k=0.10$, $Re=4 \times 10^6$

Oscil. Motion:

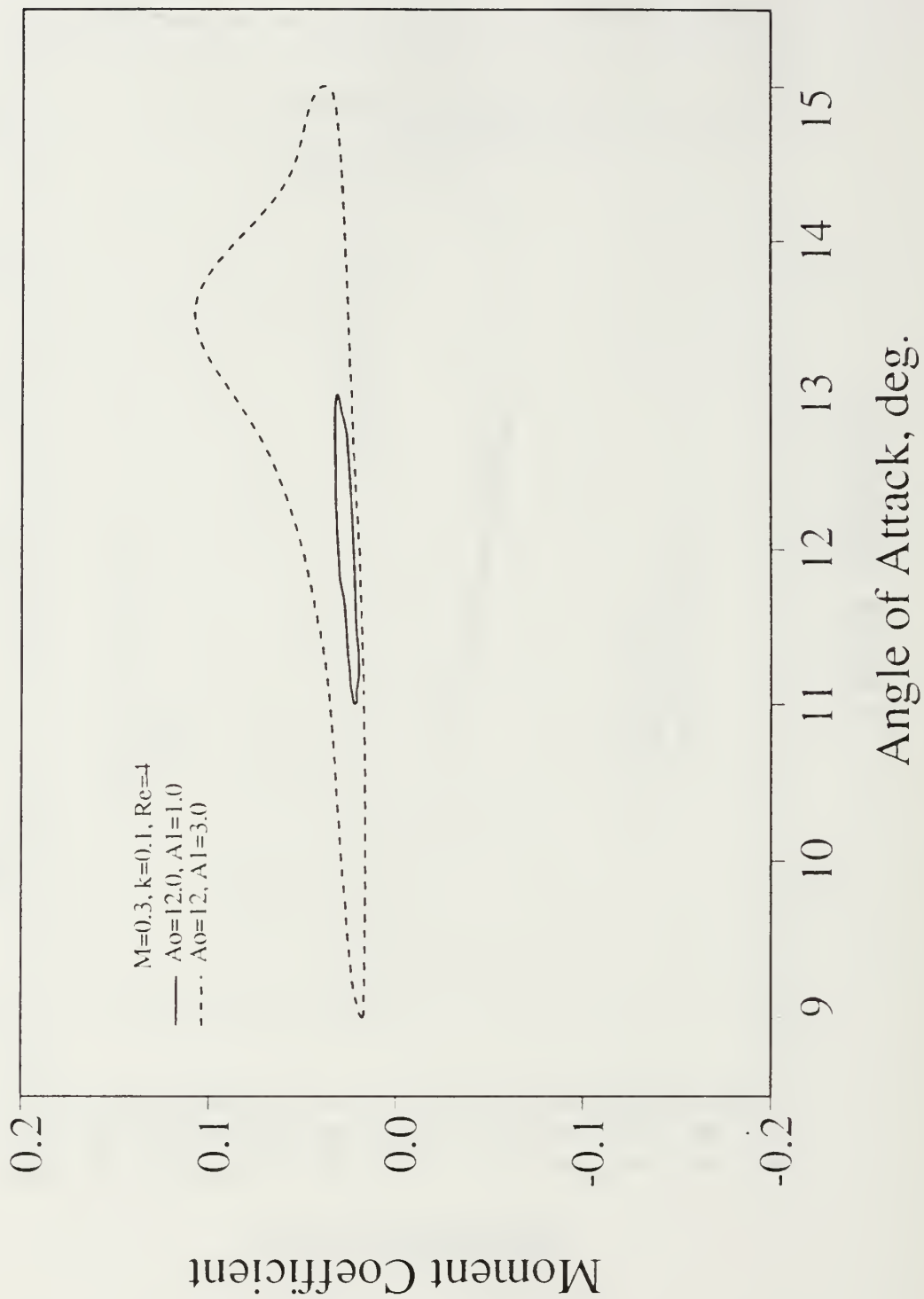


Figure 51. Effect of Amplitude on Unsteady Motion, $M=0.3$, $\alpha(t)=12^\circ \pm A_1^\circ \sin(\omega t)$, $k=0.10$, $Re=4 \times 10^6$

Oscil. Motion:

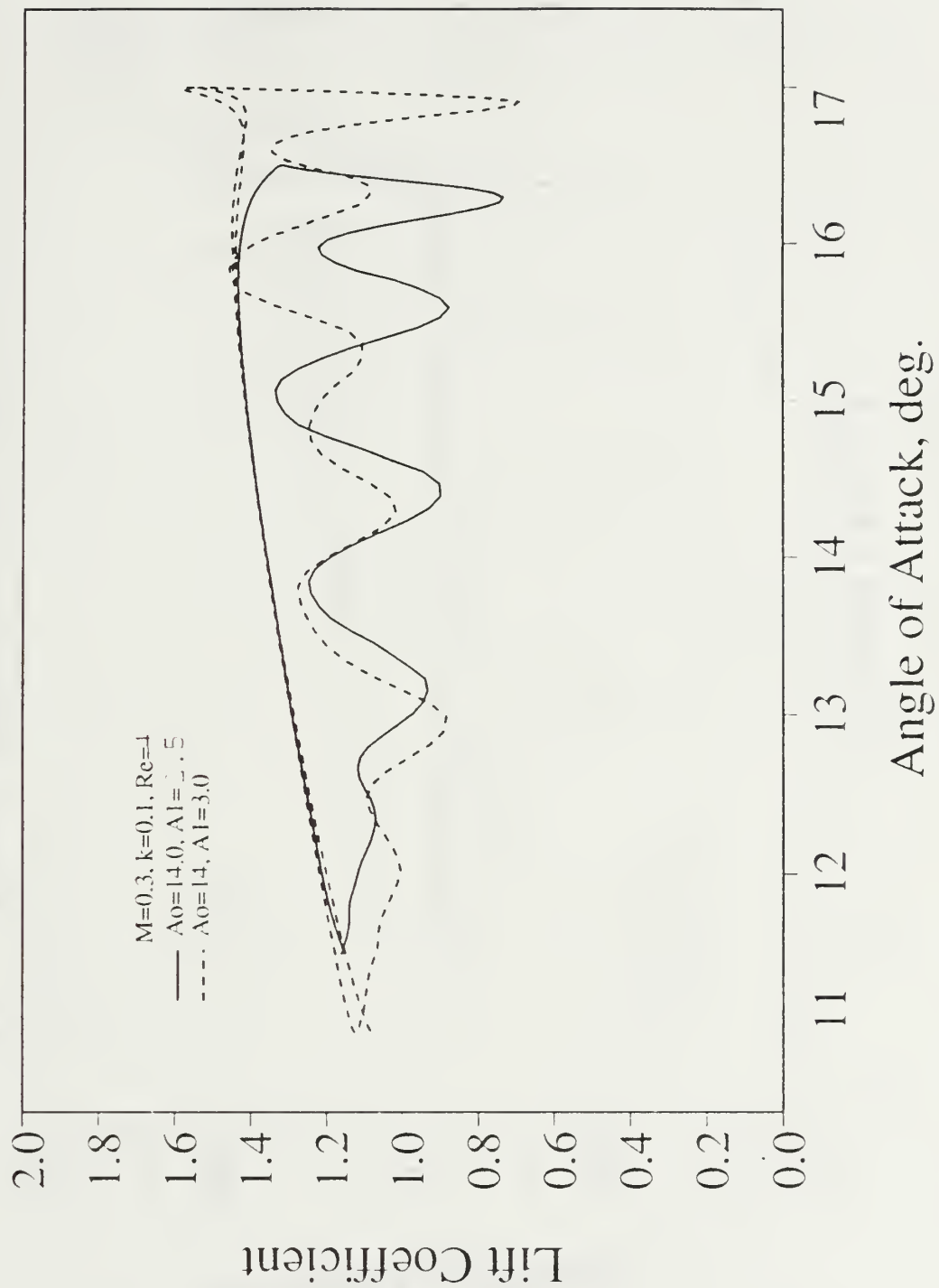


Figure 52. Effect of Amplitude on Unsteady Motion, $M=0.3$, $\alpha(t)=14^\circ \pm A_1 \sin(\omega t)$, $k=0.10$, $Re=4 \times 10^6$

Oscil. Motion:

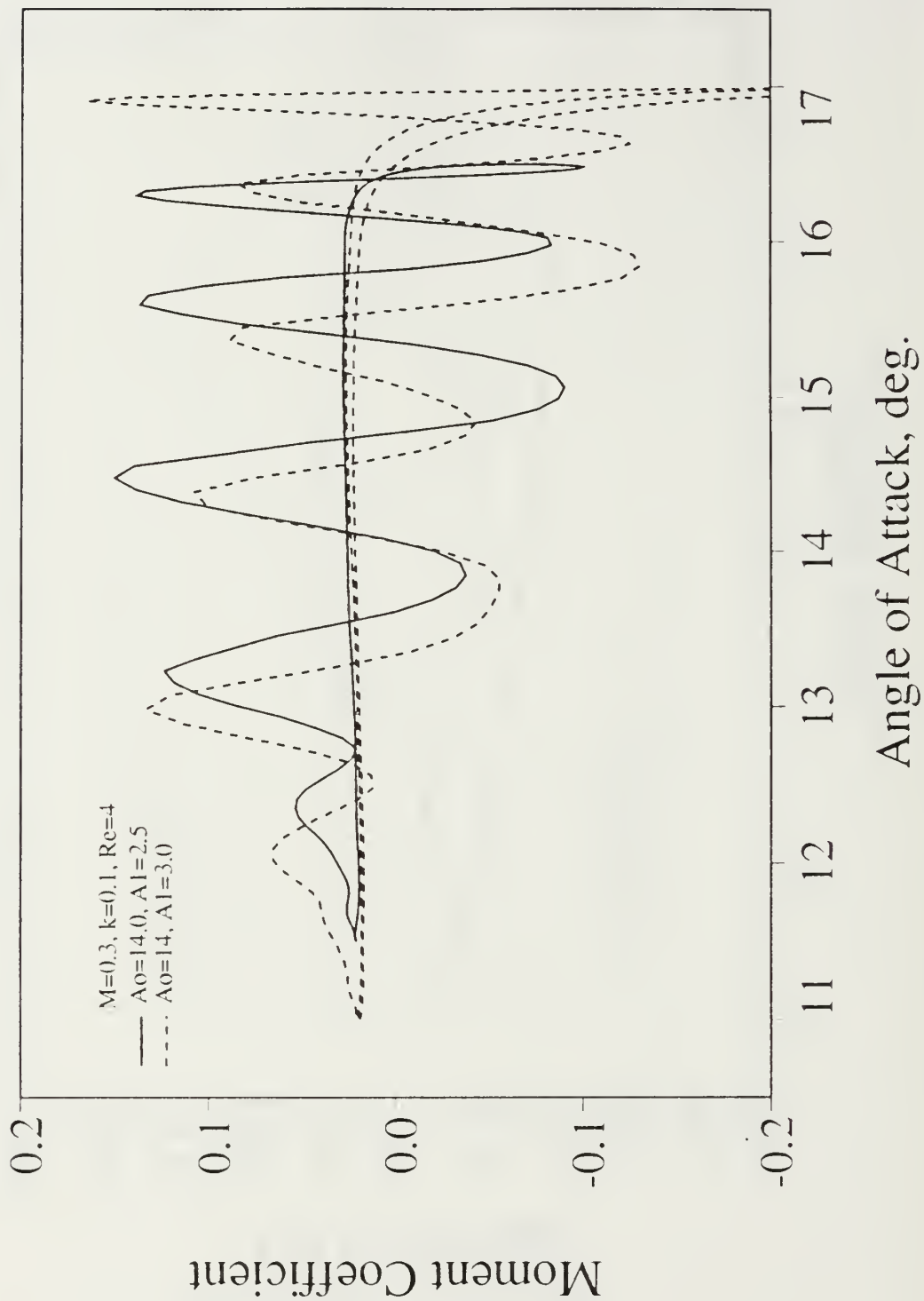


Figure 53. Effect of Amplitude on Unsteady Motion, $M=0.3$, $\alpha(t)=14^\circ \pm A_1^\circ \sin(\omega t)$, $k=0.10$, $Re=4 \times 10^6$

Oscil. Motion: $A_0=13$, $A_1=2$

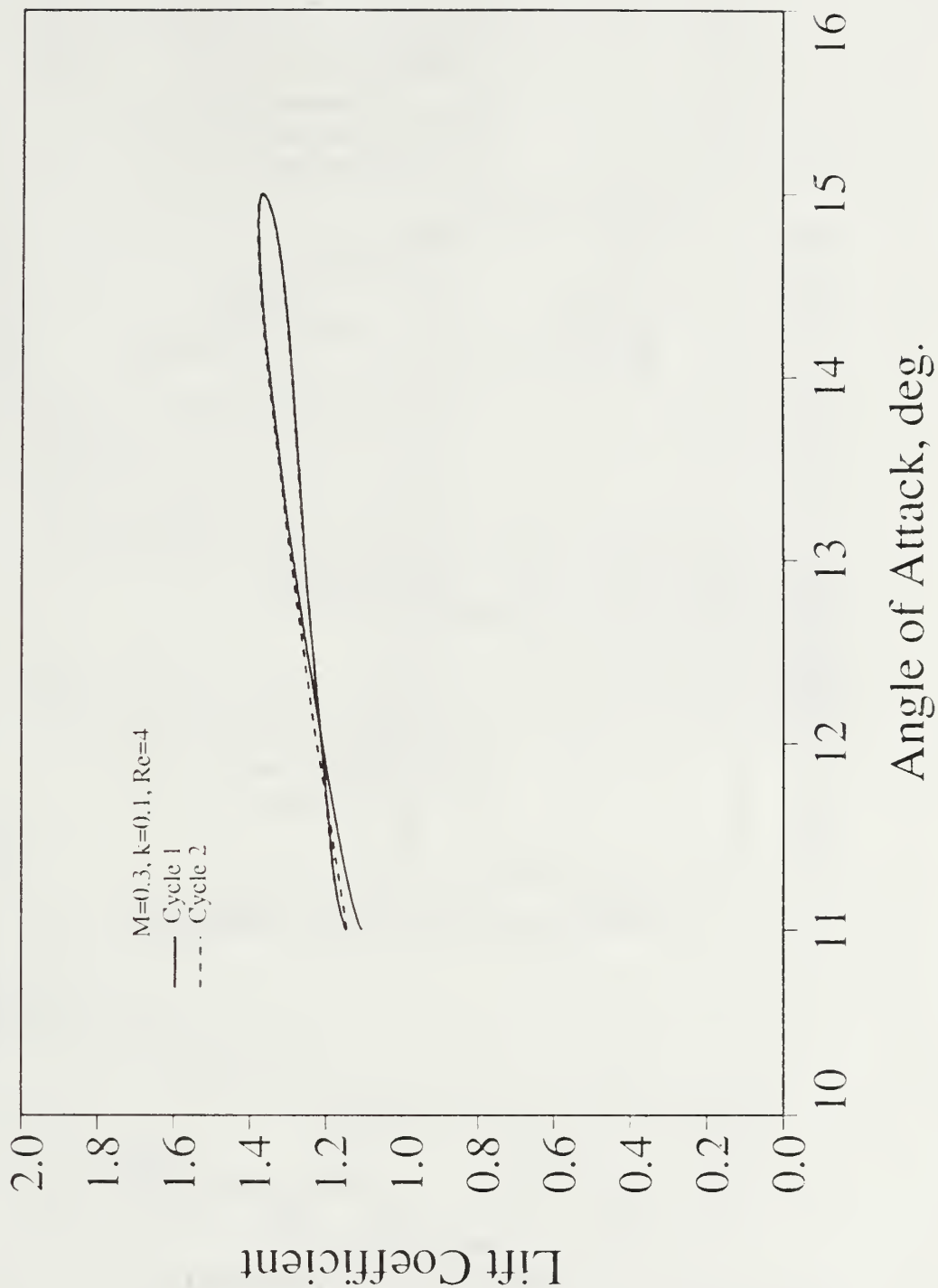


Figure 54. Effect of 1st and 2nd Cycle on Unsteady Motion, $M=0.3$, $\alpha(t)=13^\circ \pm 2^\circ \sin(\omega t)$, $k=0.10$, $Re=4 \times 10^6$

Oscil Motion: $A_0=13$, $A_1=2$

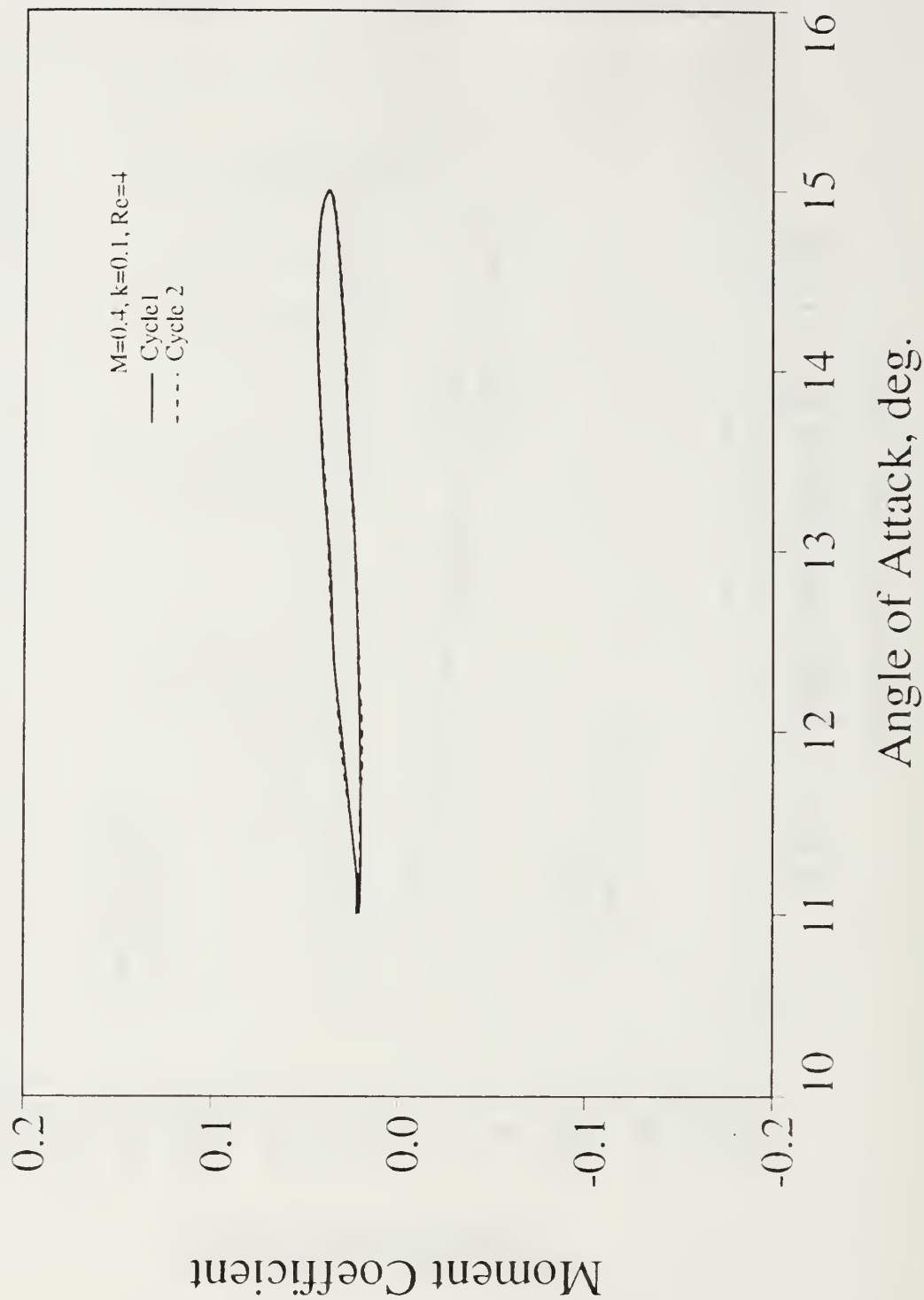


Figure 55. Effect of 1st and 2nd Cycle on Unsteady Motion, $M=0.3$, $\alpha(t)=13\pm 2^\circ \sin(\omega t)$, $k=0.10$, $Re=4 \times 10^6$

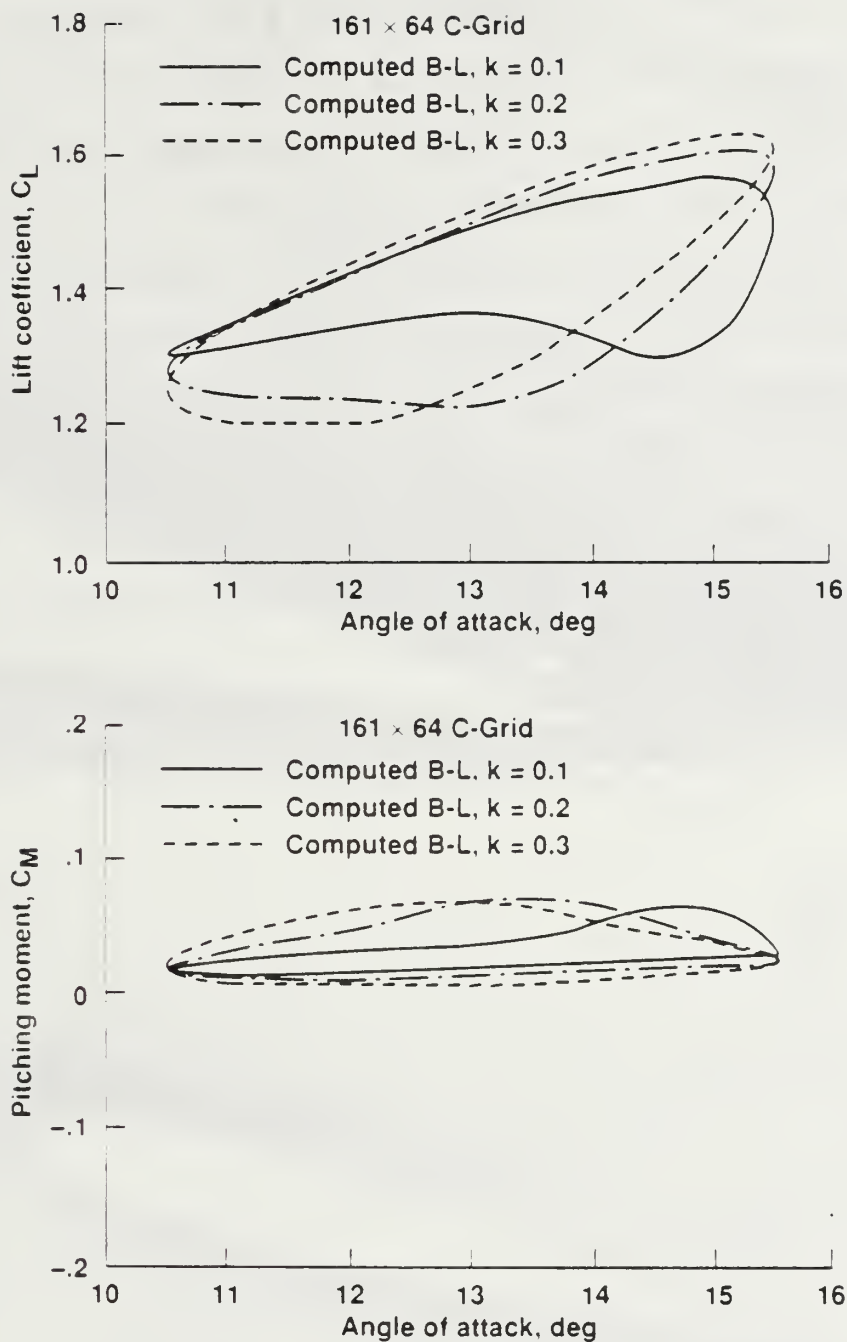


Figure 56. Effect of Reduced Frequency on Unsteady Motion
 $M=0.3$, $\alpha(t)=13\pm 2.5^\circ \sin(\omega t)$, $Re=2 \times 10^6$

b. Case 7. $\alpha(t)=13^\circ\pm2.5^\circ\sin(\omega t)$, $k=0.2$, $Re=4\times10^6$

In an effort to determine if the flow field was in fact predicting a trailing edge vortex that would shed during the oscillation cycle as seen in the experimental results, instantaneous particle traces and the corresponding velocity fields were plotted for the downstroke at a Mach number of 0.3, a mean angle of attack of 13 degrees, an amplitude of 2.5 degrees, a reduced frequency of 0.1 and a Reynolds number of four million. Figures 57 through 61 show the downstroke portion of the cycle beginning at $\alpha=15.3^\circ$ and ending at $\alpha=14.5^\circ$. A recirculatory region is seen in Figure 57 which grows slightly, as seen in Figure 58. This region then appears to diminish in size and intensity.

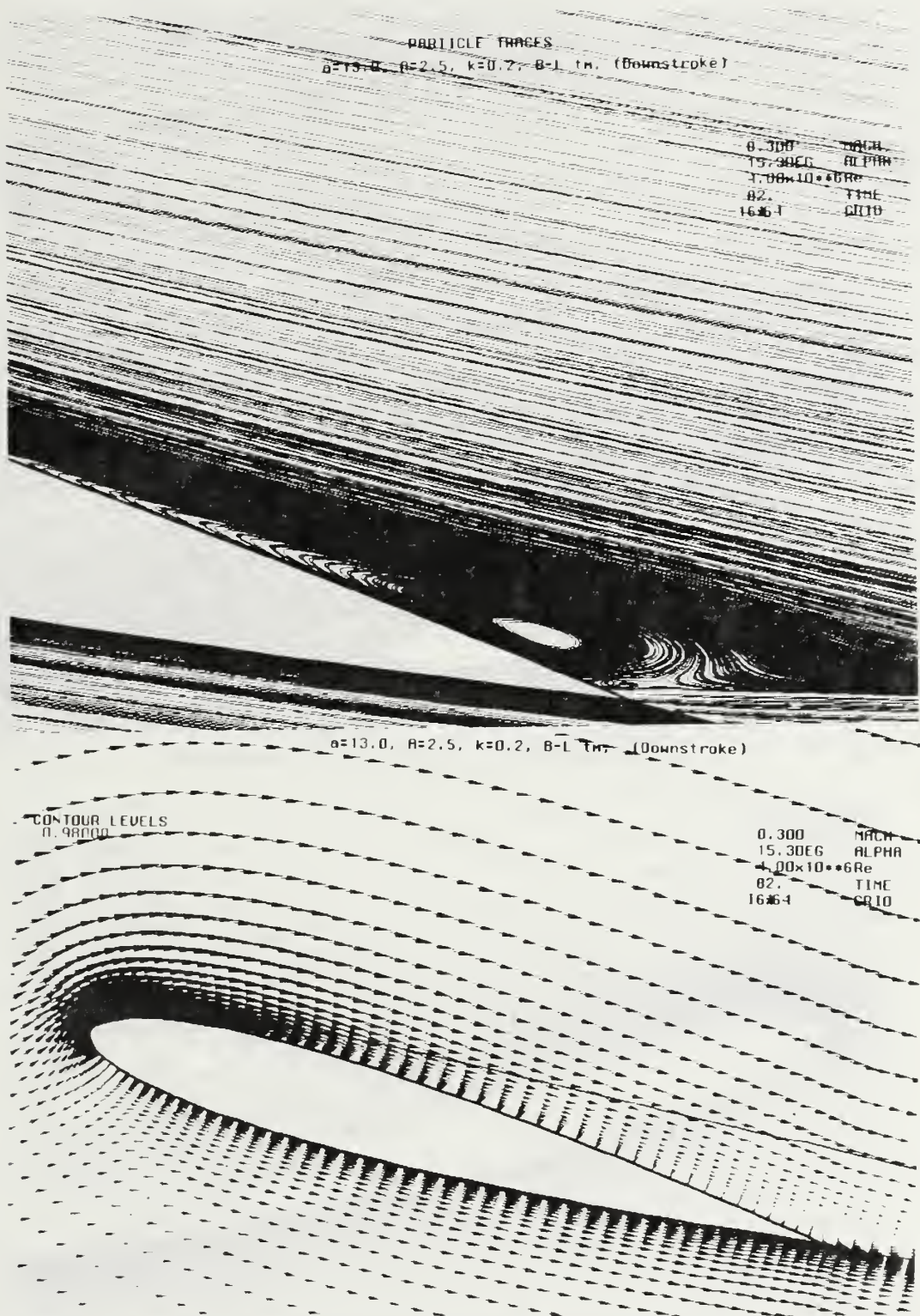


Figure 57. Instantaneous Particle Trace and Velocity Field, Oscillatory Motion, $M=0.3$, $\alpha=15.3^\circ$ (Downstroke), $\alpha(t)=13^\circ \pm 2.5^\circ \sin(\omega t)$, $k=0.20$, $Re=4 \times 10^6$

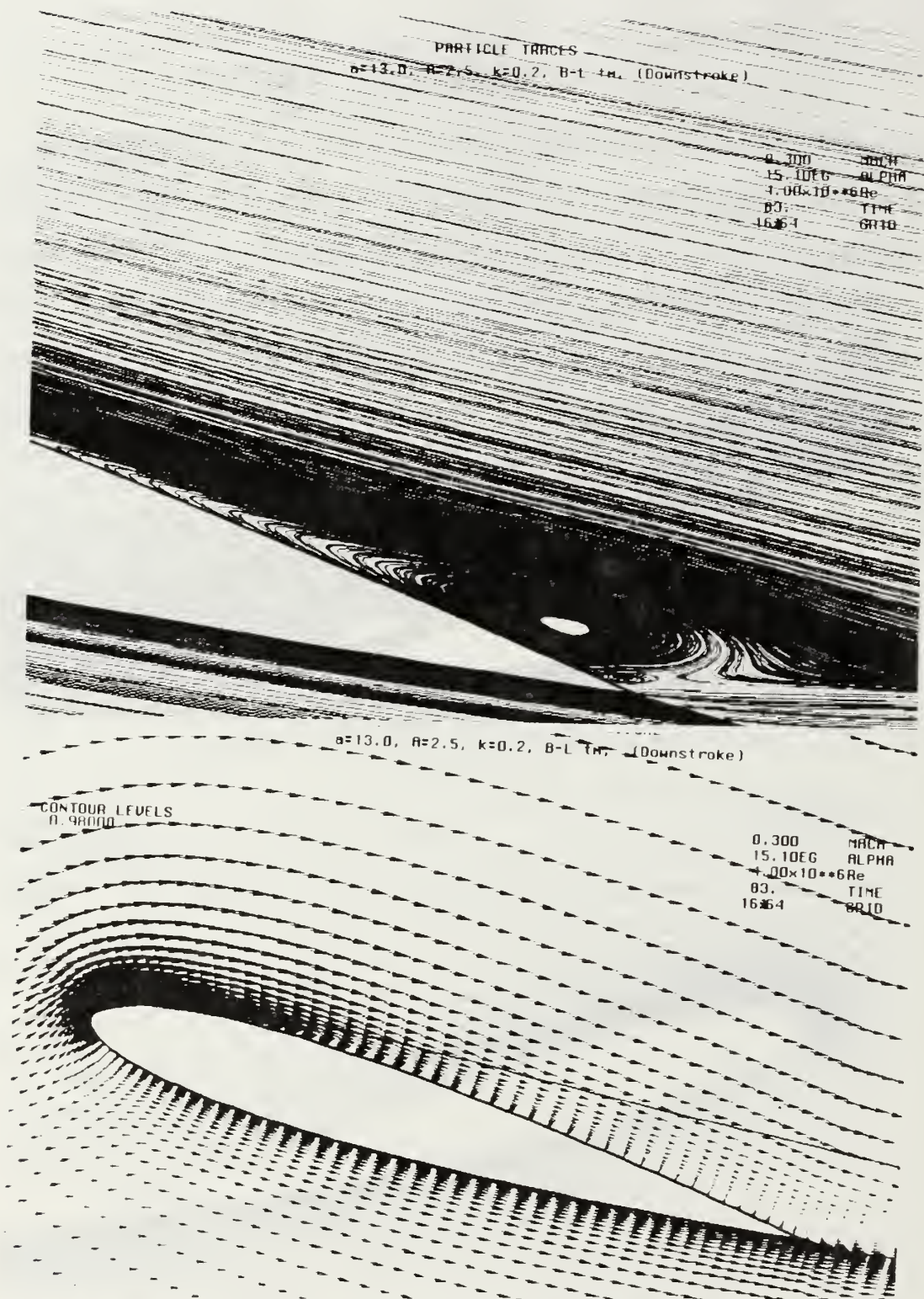


Figure 58. Instantaneous Particle Trace and Velocity Field, Oscillatory Motion, $M=0.3$, $\alpha=15.1^\circ$ (Downstroke), $\alpha(t)=13^\circ \pm 2.5^\circ \sin(\omega t)$, $k=0.20$, $Re=4 \times 10^6$

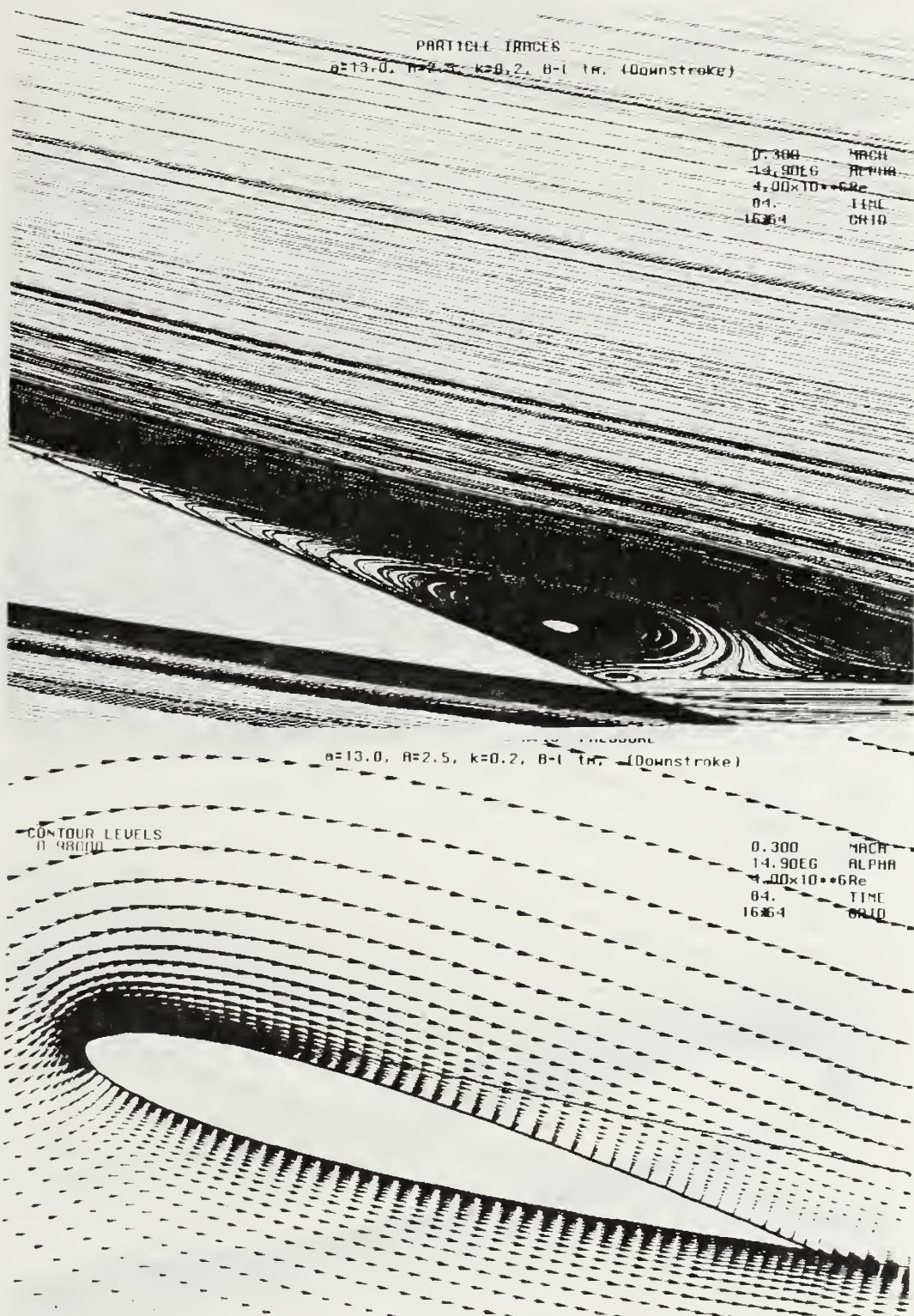


Figure 59. Instantaneous Particle Trace and Velocity Field, Oscillatory Motion, $M=0.3$, $\alpha=14.9^\circ$ (Downstroke), $\alpha(t)=13^\circ \pm 2.5^\circ \sin(\omega t)$, $k=0.20$, $Re=4 \times 10^6$

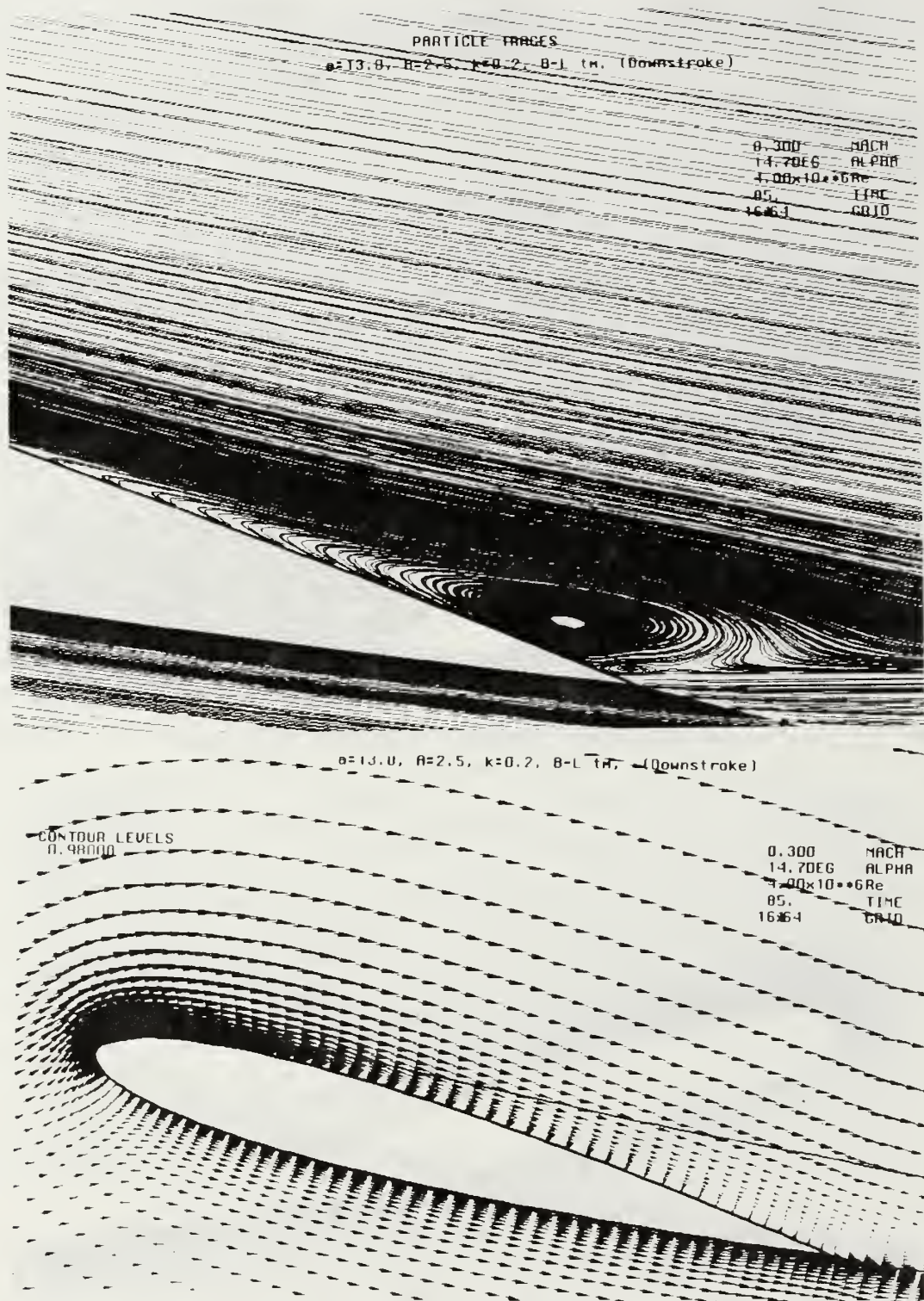


Figure 60. Instantaneous Particle Trace and Velocity Field, Oscillatory Motion, $M=0.3$, $\alpha=14.7^\circ$ (Downstroke), $\alpha(t)=13^\circ \pm 2.5^\circ \sin(\omega t)$, $k=0.20$, $Re=4 \times 10^6$

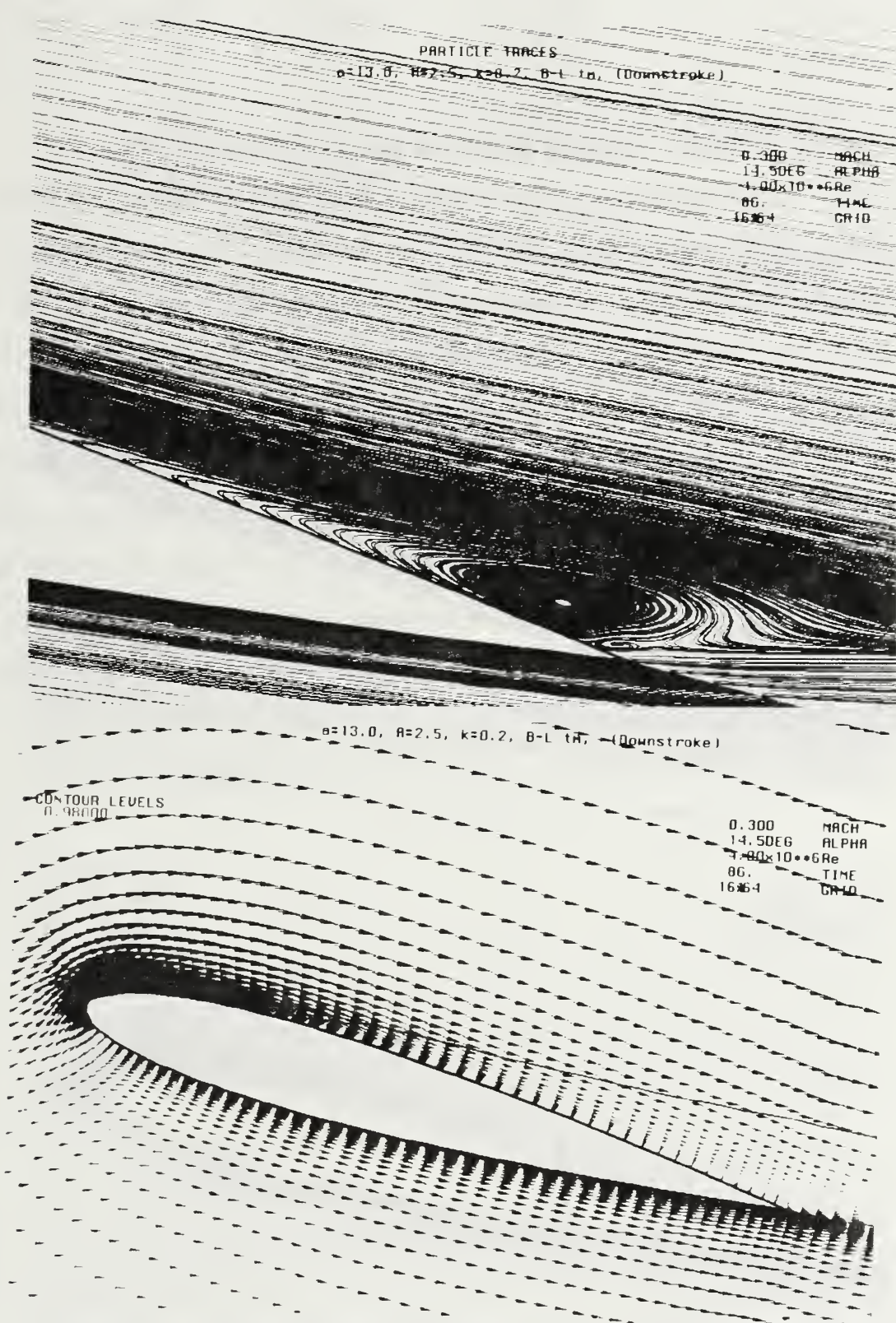


Figure 61. Instantaneous Particle Trace and Velocity Field, Oscillatory Motion, $M=0.3$, $\alpha=14.5^\circ$ (Downstroke), $\alpha(t)=13^\circ \pm 2.5^\circ \sin(\omega t)$, $k=0.20$, $Re=4 \times 10^6$

c. Case 8. $\alpha(t)=13^\circ\pm2.5^\circ\sin(\omega t)$, $k=0.1$, $Re=2\times10^6$

The plots generated for Case 7 did show a recirculatory region, but a full understanding of its development and structure could not be gained from only a portion of the oscillatory cycle. Therefore in Figures 62 through 80 a complete cycle is shown for the same flow condition as in Case 7 with only the reduced frequency being increased from 0.1 to 0.2 and Reynolds Number decreased from four million to two million. A recirculatory region is seen to form at $\alpha=14.9^\circ$ on the upstroke, which continues to grow and intensify. This recirculatory region reaches its largest value at $\alpha=15.3^\circ$ on the downstroke and then diminishes and finally the flow becomes completely reattached. It is important to note that even for this relatively fast oscillation the recirculatory region did not shed into the wake.

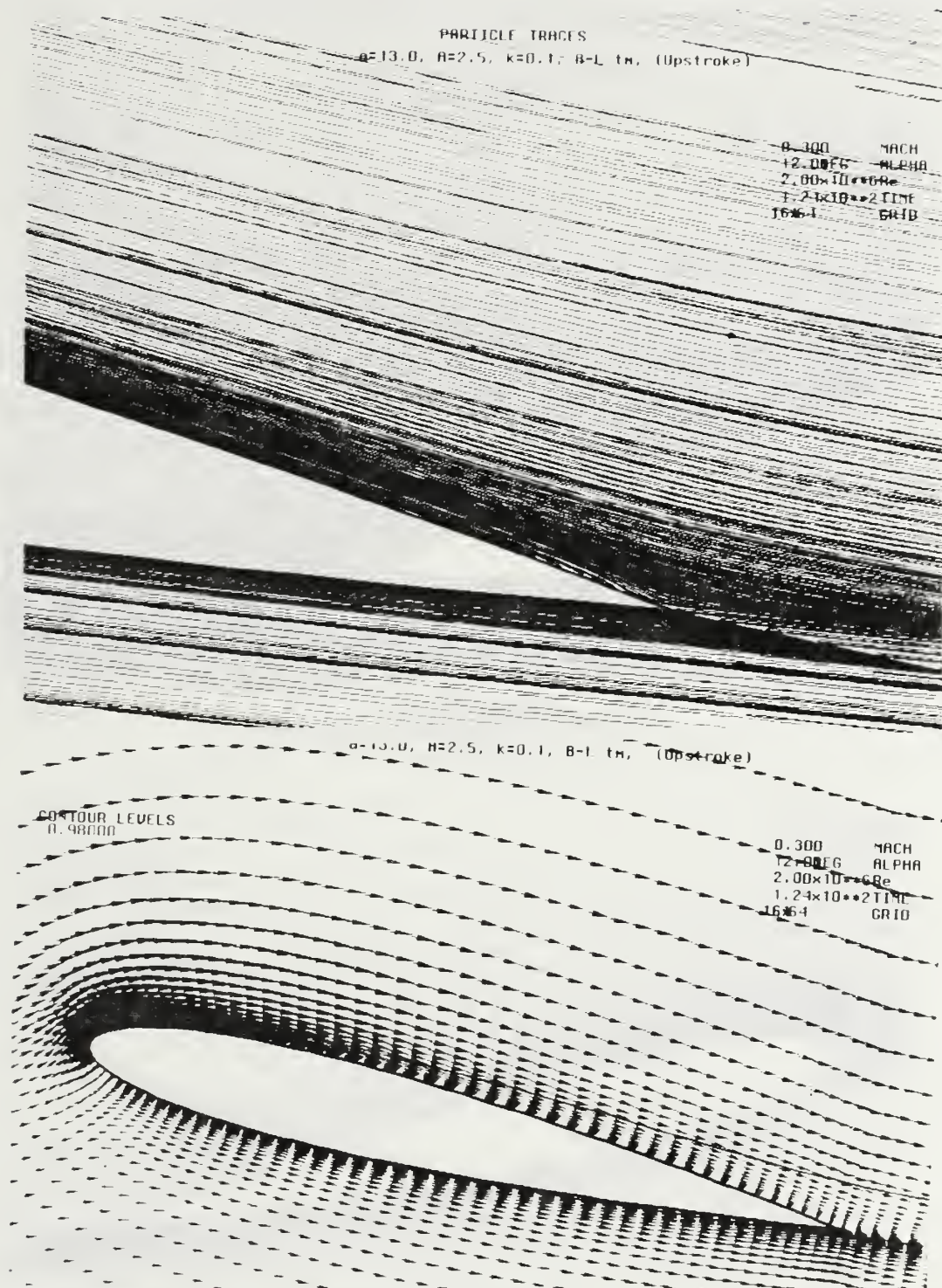


Figure 62. Instantaneous Particle Trace and Velocity Field, Oscillatory Motion, $M=0.3$, $\alpha=12^\circ$ (Upstroke), $\alpha(t)=13^\circ \pm 2.5^\circ \sin(\omega t)$, $k=0.10$, $Re=2 \times 10^6$

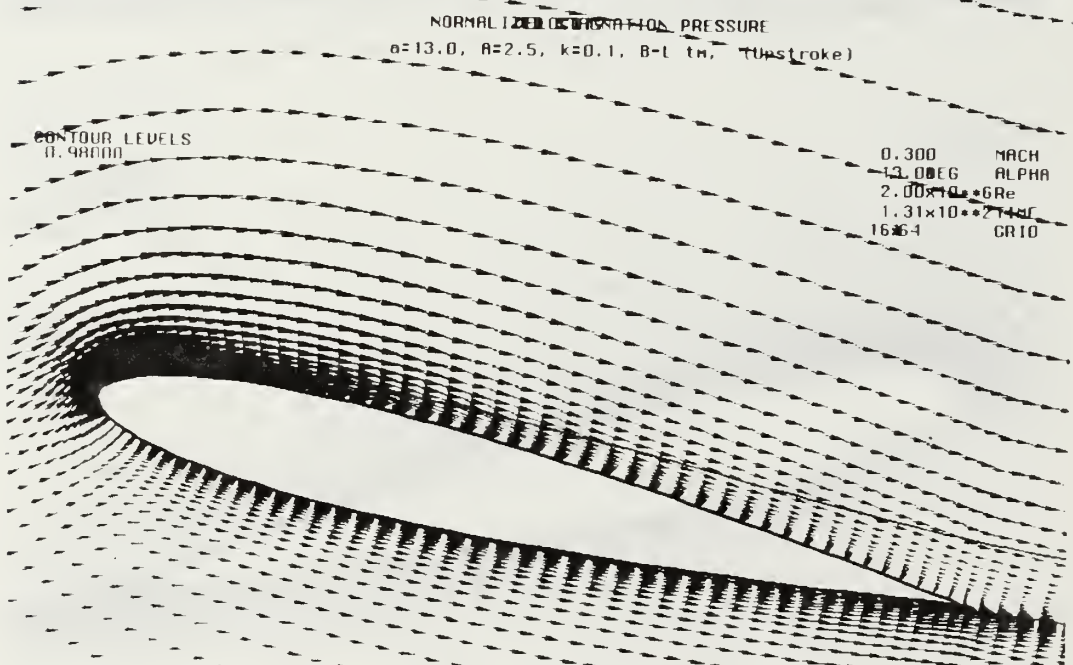
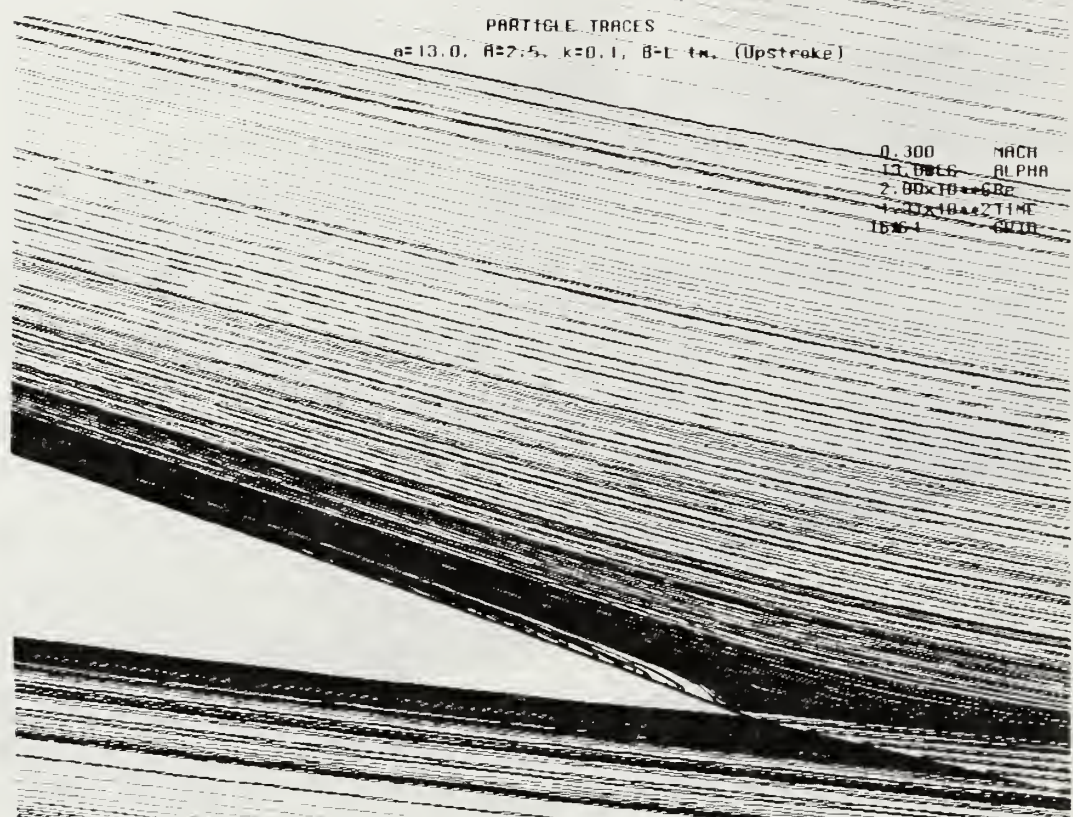


Figure 63. Instantaneous Particle Trace and Velocity Field, Oscillatory Motion, $M=0.3$, $\alpha=13^\circ$ (Upstroke), $\alpha(t)=13^\circ \pm 2.5^\circ \sin(\omega t)$, $k=0.10$, $Re=2 \times 10^6$

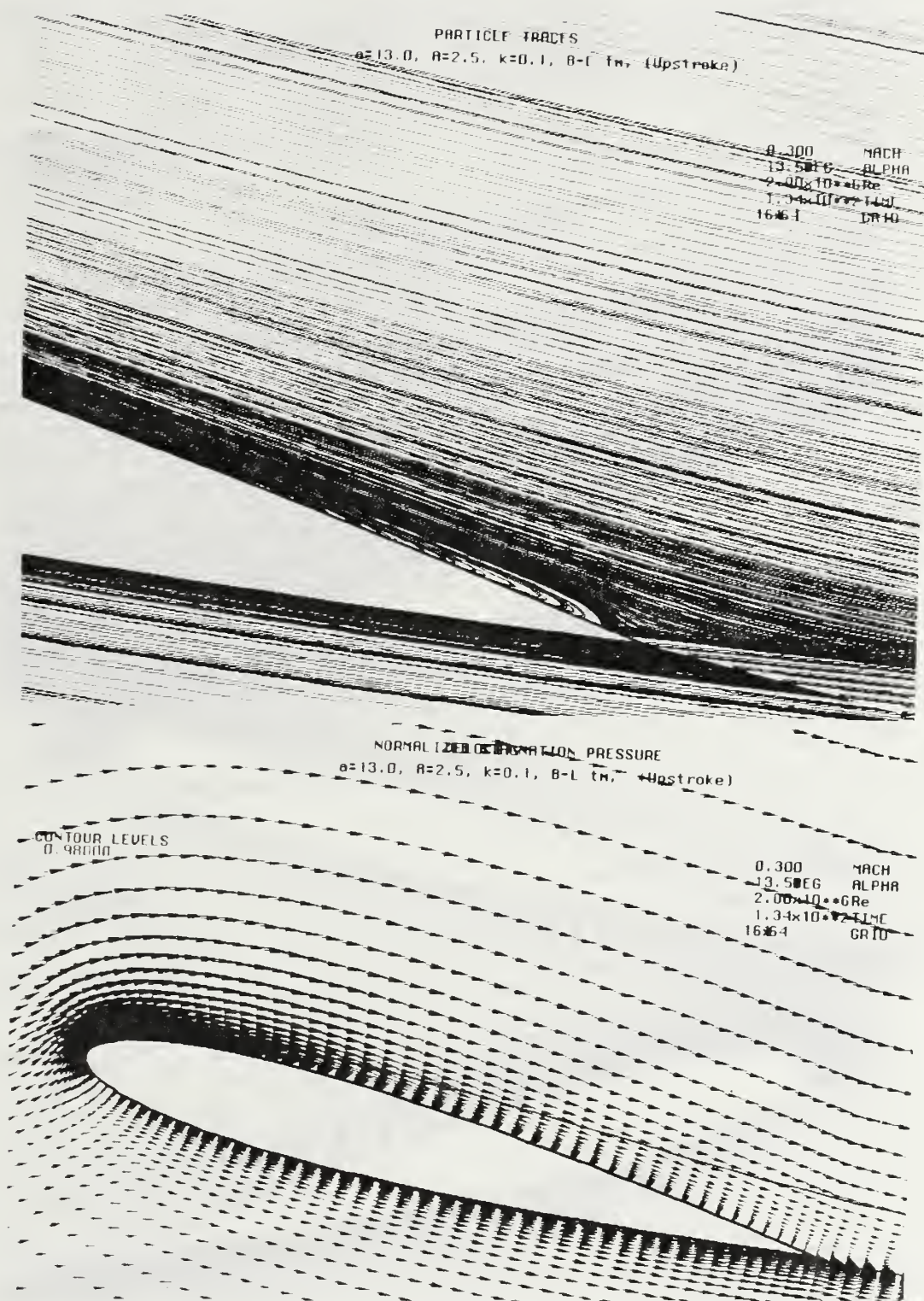


Figure 64. Instantaneous Particle Trace and Velocity Field, Oscillatory Motion, $M=0.3$, $\alpha=13.5^\circ$ (Upstroke), $\alpha(t)=13^\circ \pm 2.5^\circ \sin(\omega t)$, $k=0.10$, $Re=2 \times 10^6$

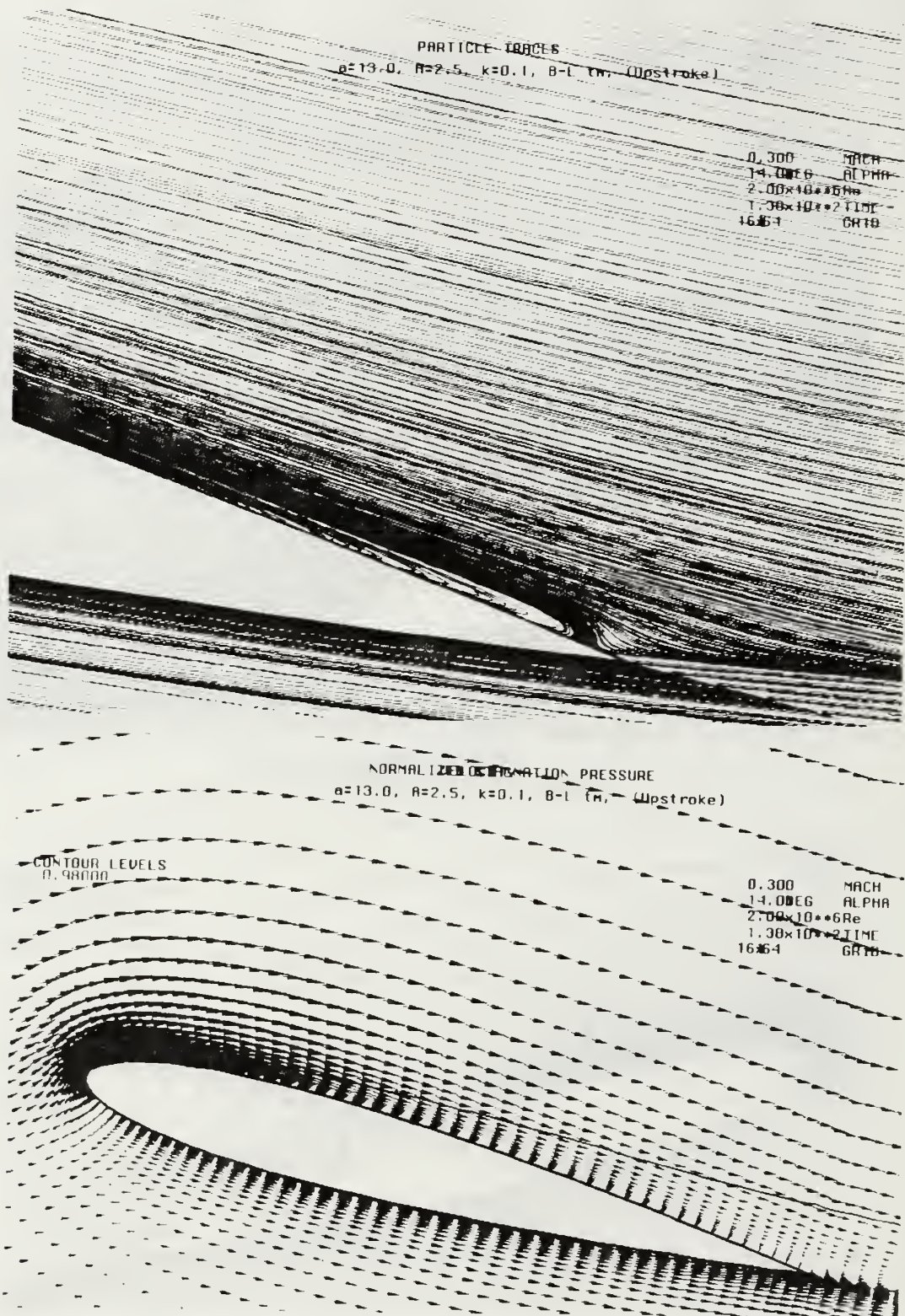


Figure 65. Instantaneous Particle Trace and Velocity Field, Oscillatory Motion, $M=0.3$, $\alpha=14^\circ$ (Upstroke), $\alpha(t)=13^\circ \pm 2.5^\circ \sin(\omega t)$, $k=0.10$, $Re=2 \times 10^6$

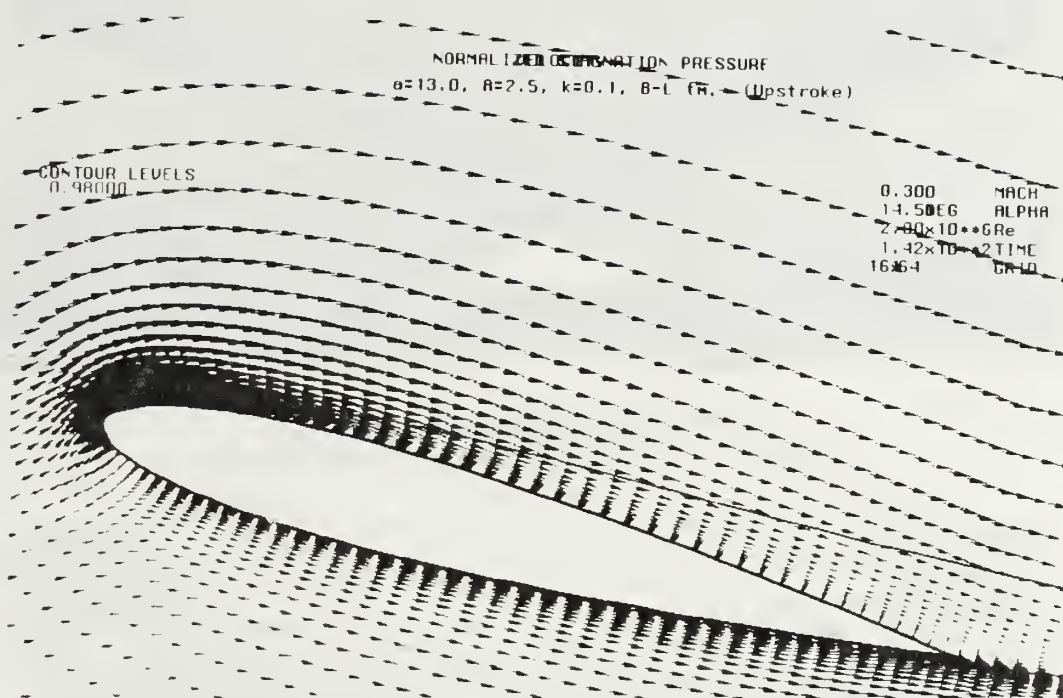


Figure 66. Velocity Field, Oscillatory Motion, $M=0.3$, $\alpha=14.5^\circ$ (Upstroke), $\alpha(t)=13^\circ \pm 2.5^\circ \sin(\omega t)$, $k=0.10$, $Re=2 \times 10^6$

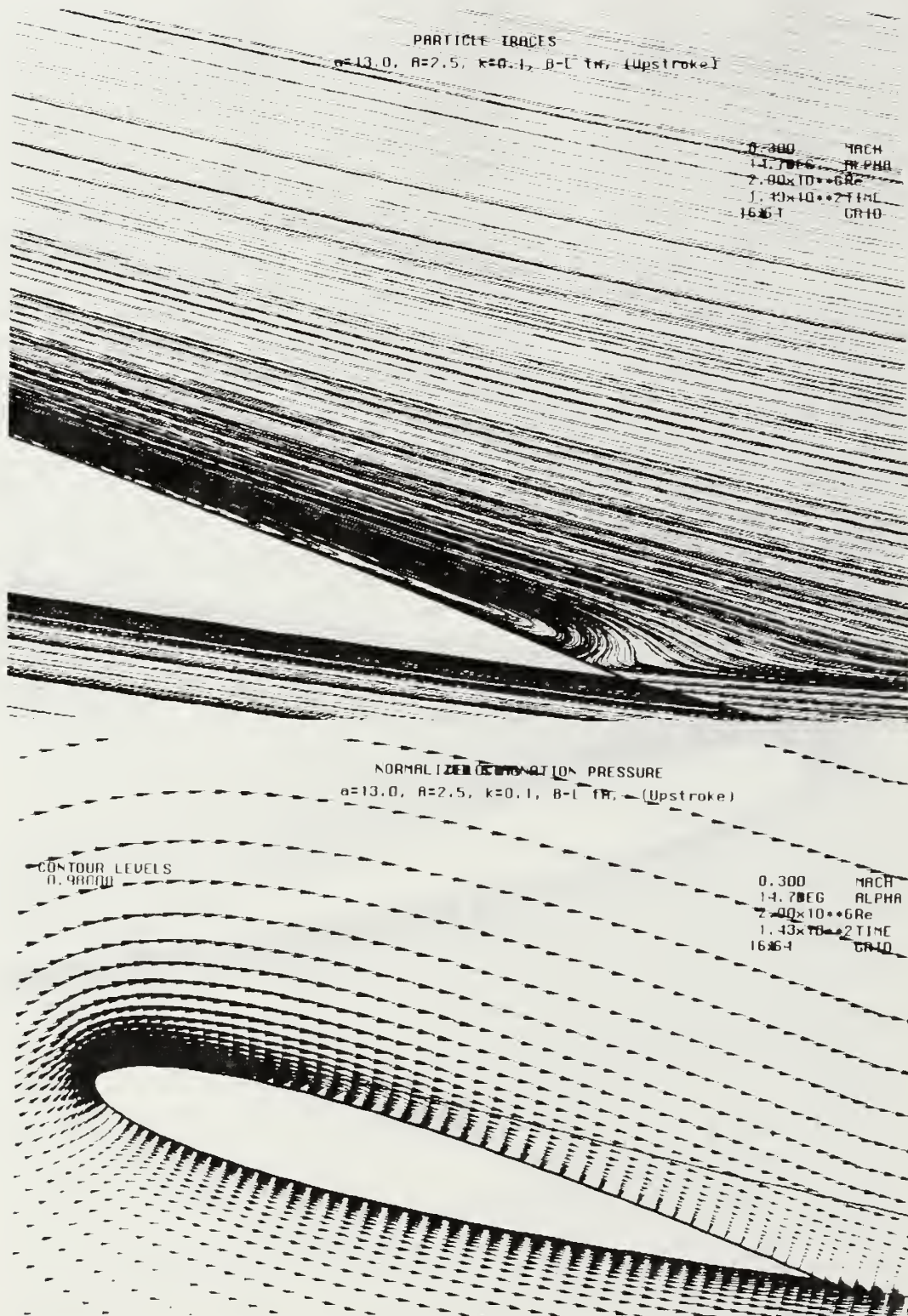


Figure 67. Instantaneous Particle Trace and Velocity Field, Oscillatory Motion, $M=0.3$, $\alpha=14.7^\circ$ (Upstroke), $\alpha(t)=13^\circ \pm 2.5^\circ \sin(\omega t)$, $k=0.10$, $Re=2 \times 10^6$

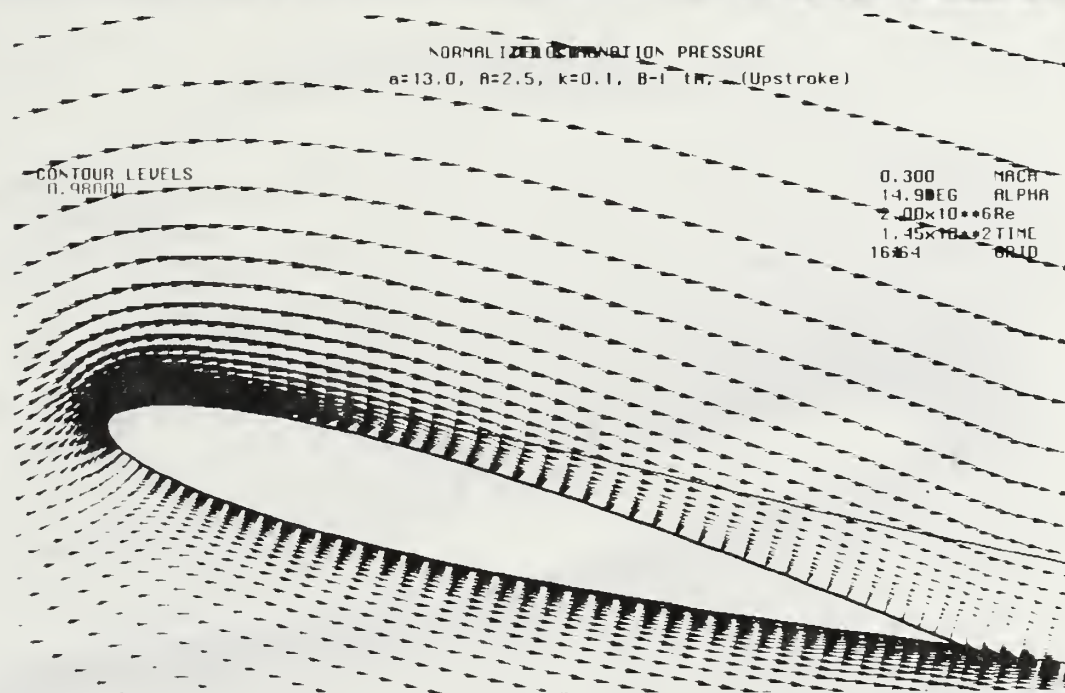
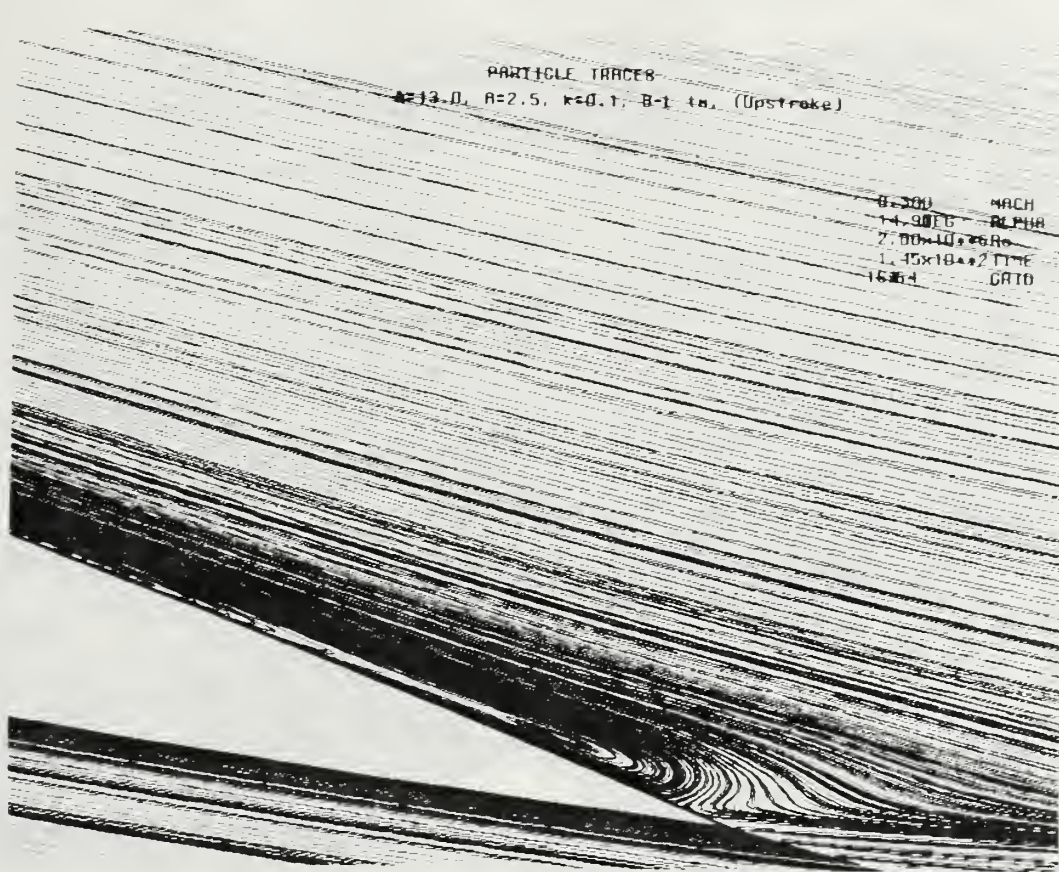


Figure 68. Instantaneous Particle Trace and Velocity Field, Oscillatory Motion, $M=0.3$, $\alpha=14.9^\circ$ (Upstroke), $\alpha(t)=13^\circ \pm 2.5^\circ \sin(\omega t)$, $k=0.10$, $Re=2 \times 10^6$

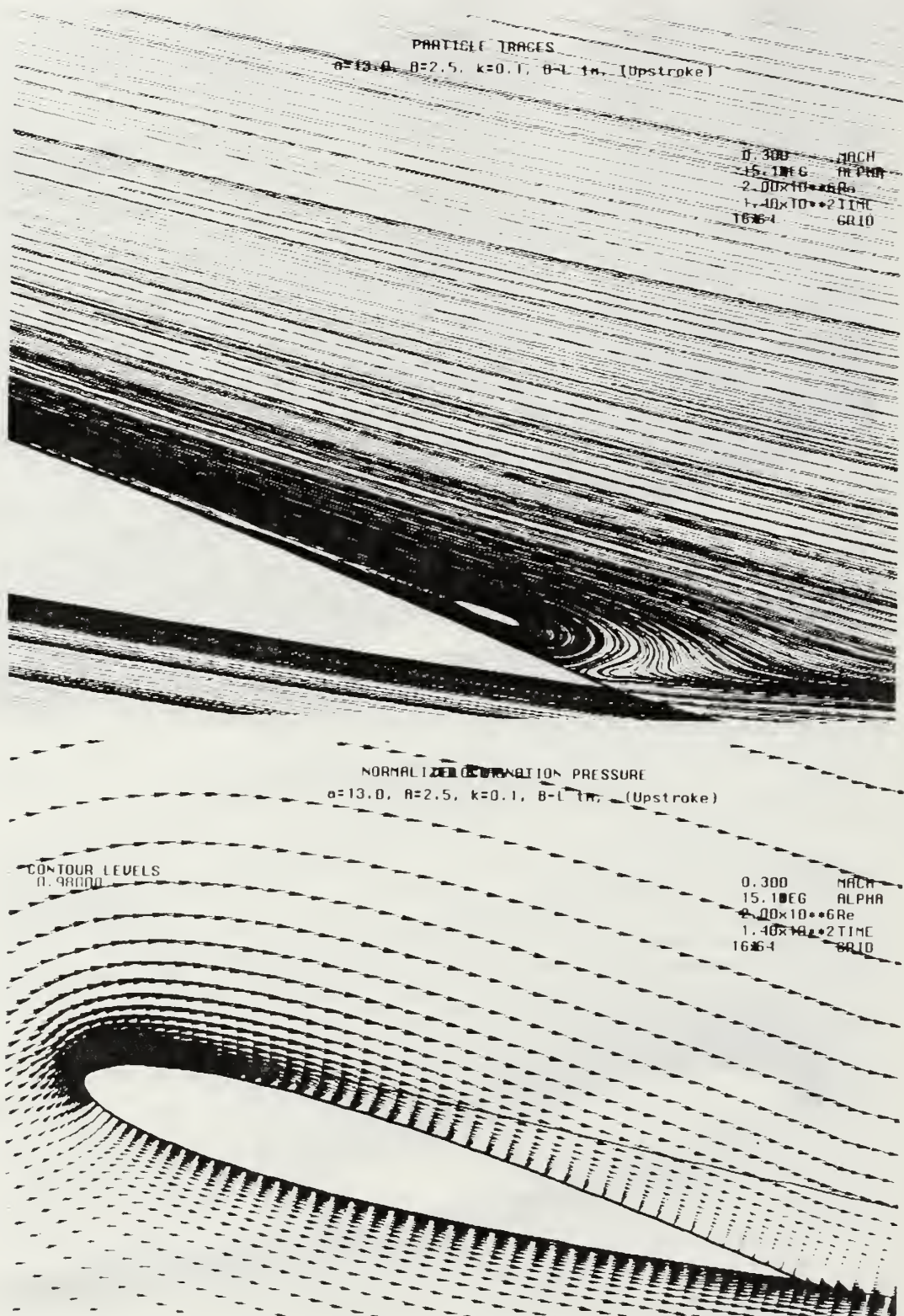


Figure 69. Instantaneous Particle Trace and Velocity Field, Oscillatory Motion, $M=0.3$, $\alpha=15.1^\circ$ (Upstroke), $\alpha(t)=13^\circ \pm 2.5^\circ \sin(\omega t)$, $k=0.10$, $Re=2 \times 10^6$

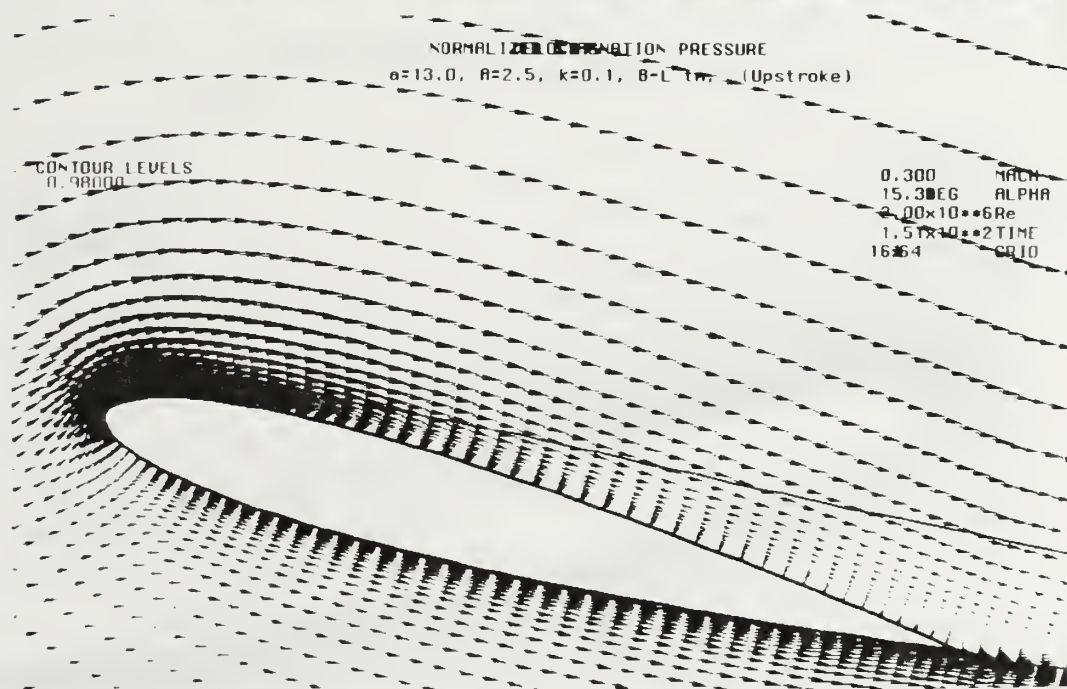
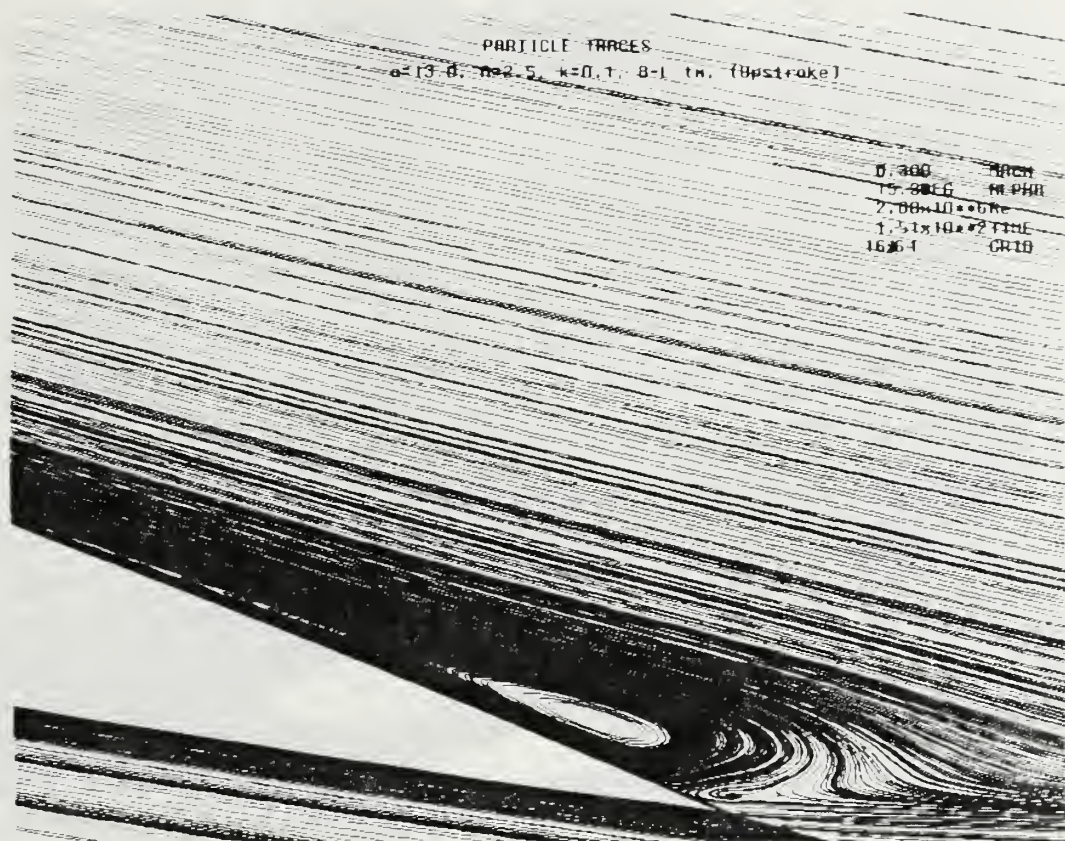


Figure 70. Instantaneous Particle Trace and Velocity Field, Oscillatory Motion, $M=0.3$, $\alpha=15.3^\circ$ (Upstroke), $\alpha(t)=13^\circ \pm 2.5^\circ \sin(\omega t)$, $k=0.10$, $Re=2 \times 10^6$

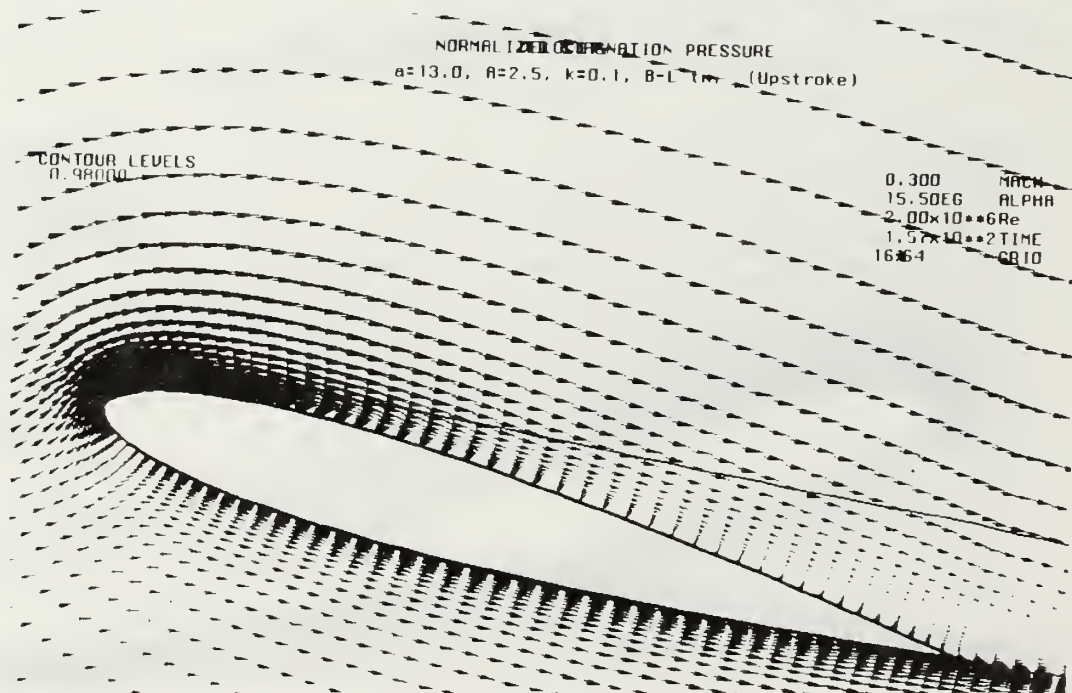


Figure 71. Instantaneous Particle Trace and Velocity Field,
 Oscillatory Motion, $M=0.3$, $\alpha=15.5^\circ$ (Upstroke), $\alpha(t)=13^\circ \pm 2.5^\circ \sin(\omega t)$,
 $k=0.10$, $Re=2 \times 10^6$

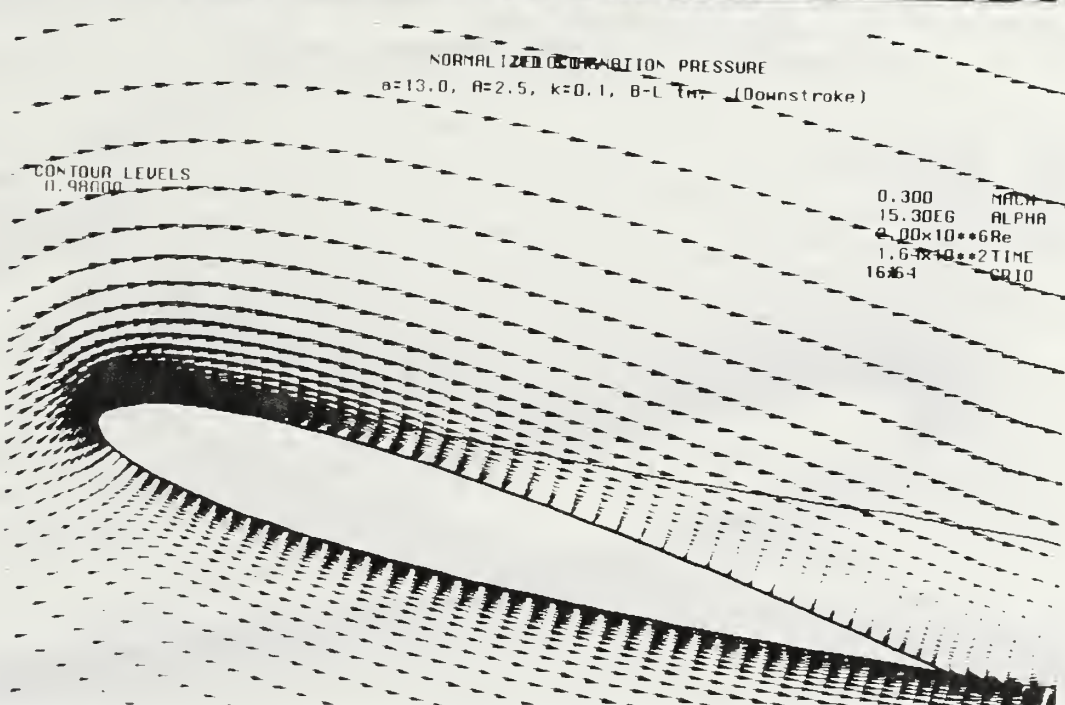
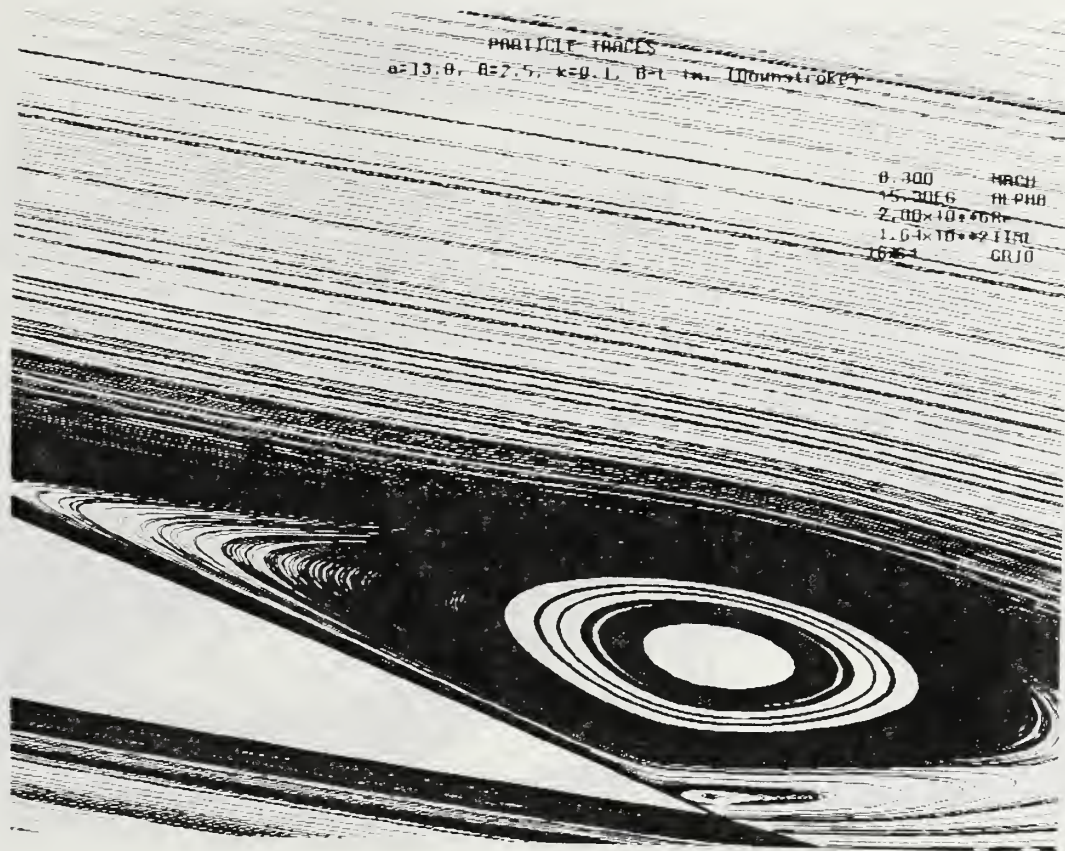


Figure 72. Instantaneous Particle Trace and Velocity Field, Oscillatory Motion, $M=0.3$, $\alpha=15.3^\circ$ (Downstroke), $\alpha(t)=13^\circ \pm 2.5^\circ \sin(\omega t)$, $k=0.10$, $Re=2 \times 10^6$

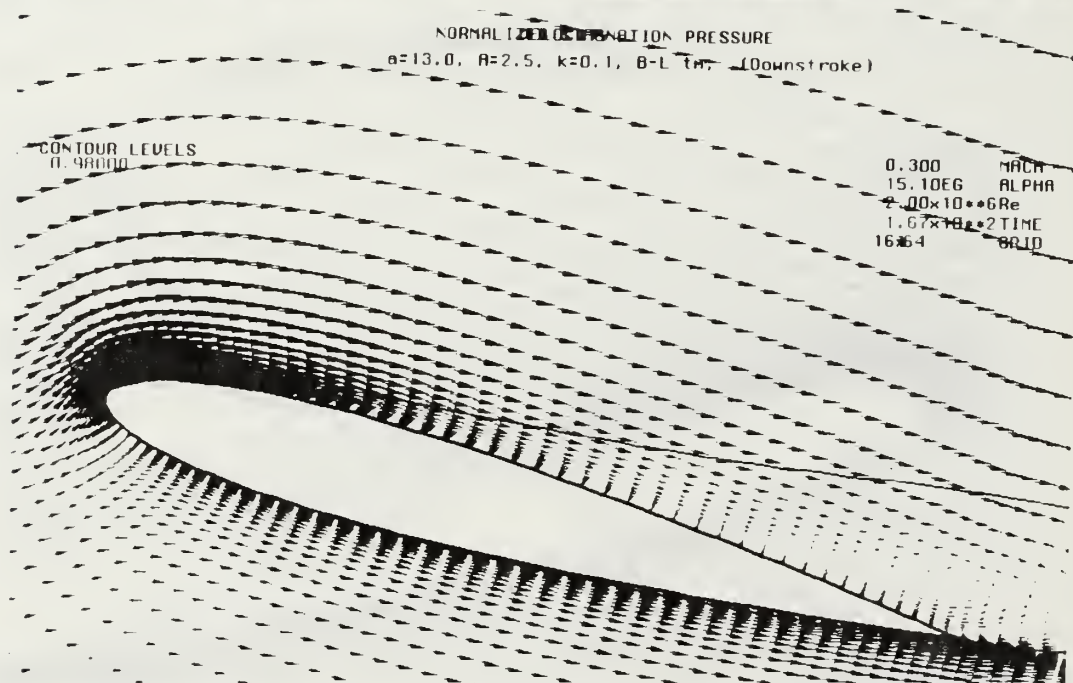
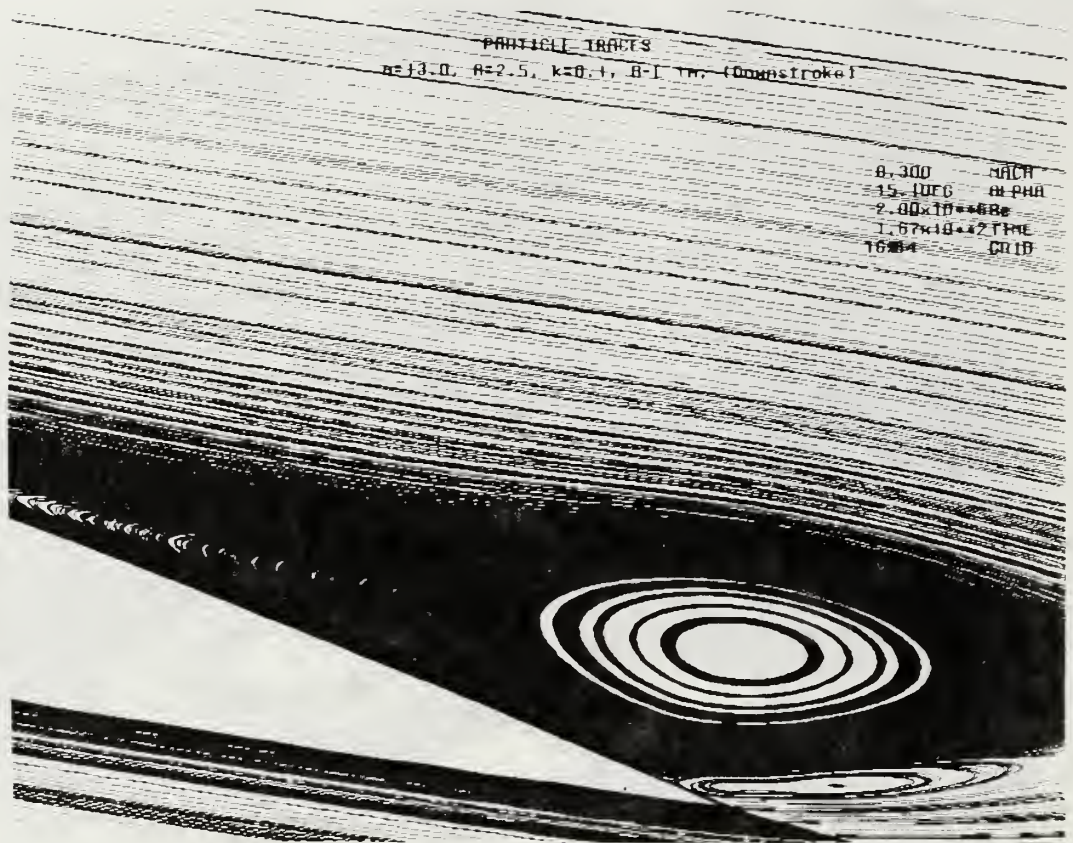


Figure 73. Instantaneous Particle Trace and Velocity Field, Oscillatory Motion, $M=0.3$, $\alpha=15.1^\circ$ (Downstroke), $\alpha(t)=13^\circ \pm 2.5^\circ \sin(\omega t)$, $k=0.10$, $Re=2 \times 10^6$

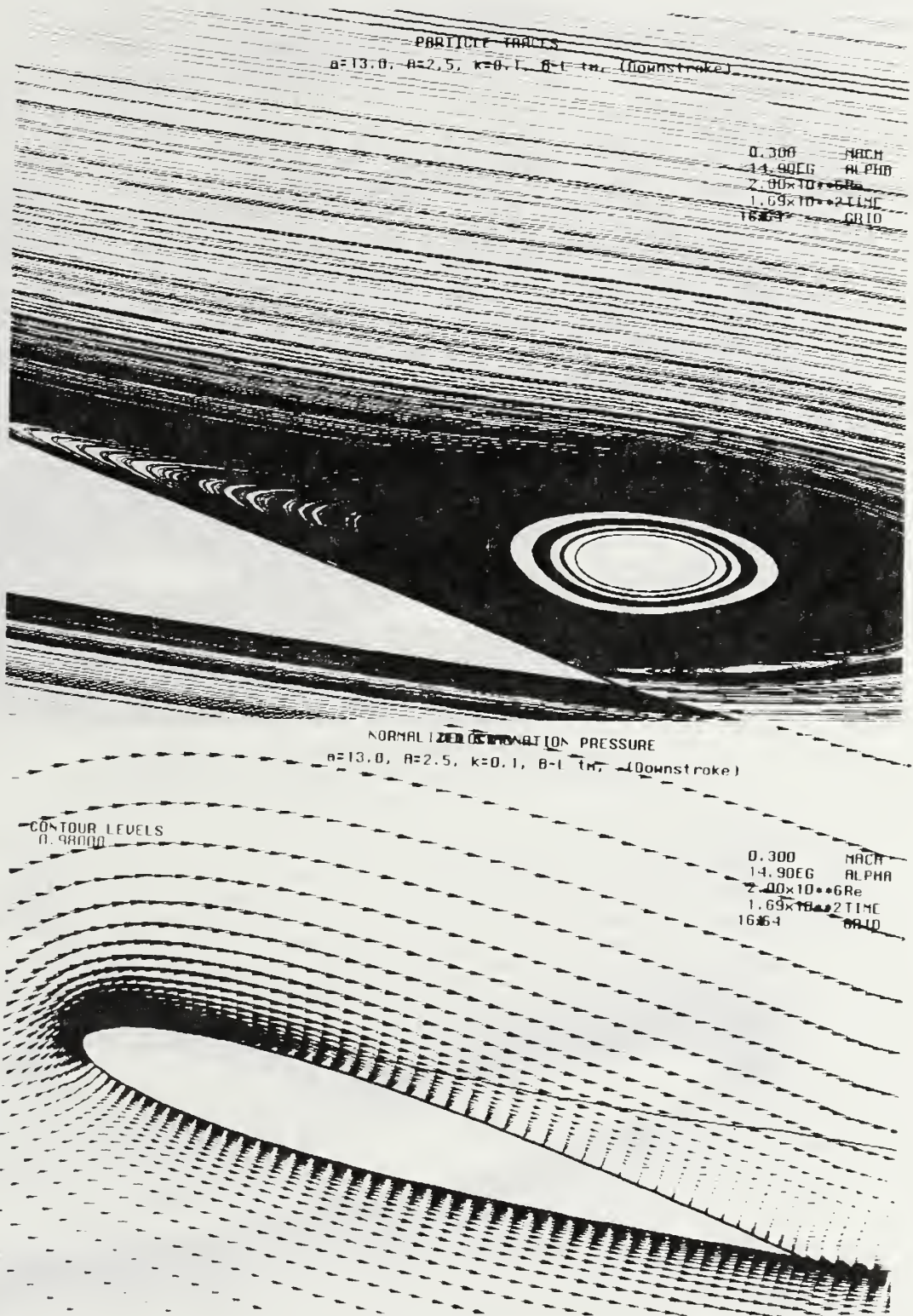


Figure 74. Instantaneous Particle Trace and Velocity Field, Oscillatory Motion, $M=0.3$, $\alpha=14.9^\circ$ (Downstroke), $\alpha(t)=13^\circ \pm 2.5^\circ \sin(\omega t)$, $k=0.10$, $Re=2 \times 10^6$

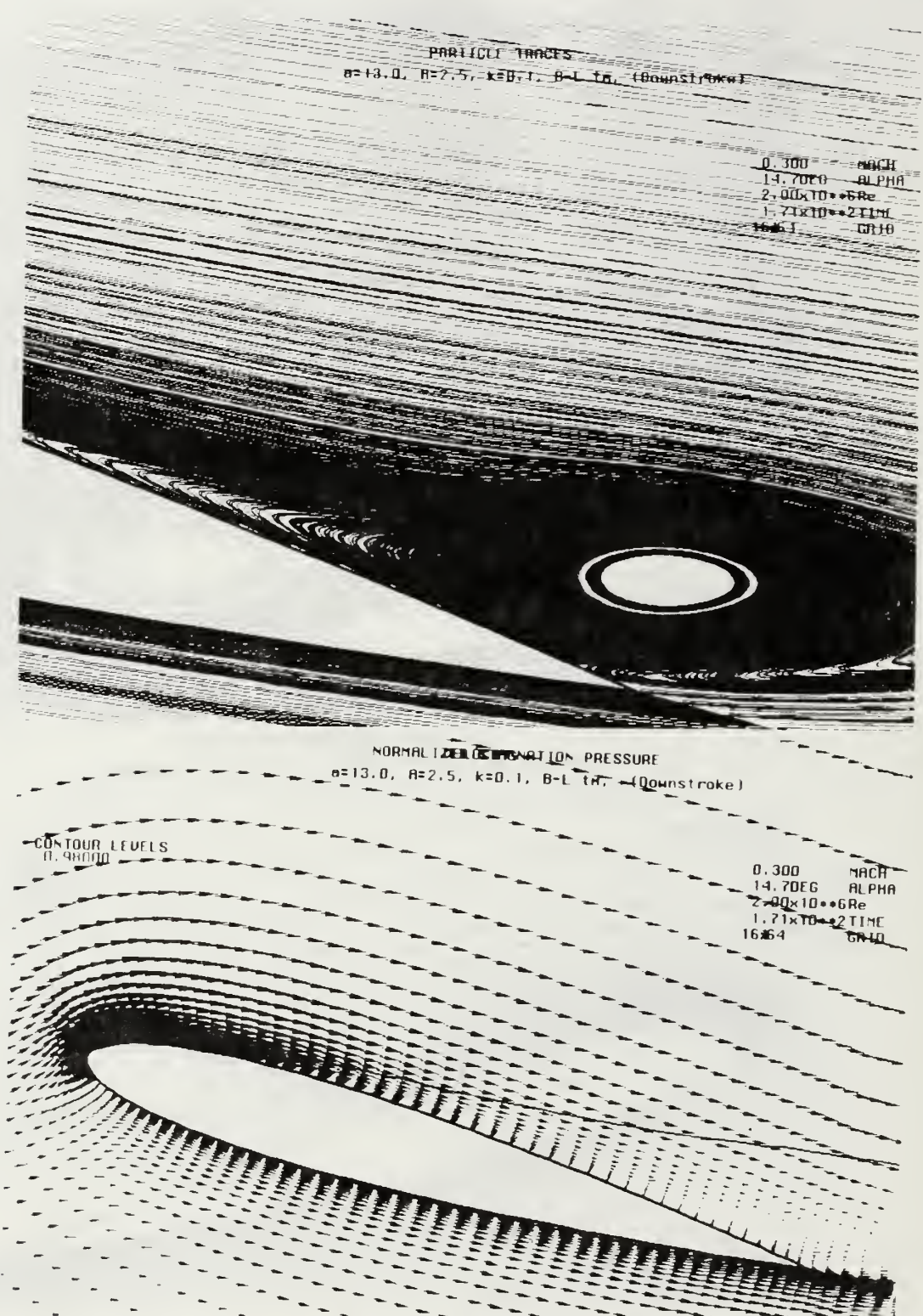


Figure 75. Instantaneous Particle Trace and Velocity Field, Oscillatory Motion, $M=0.3$, $\alpha=14.7^\circ$ (Downstroke), $\alpha(t)=13^\circ \pm 2.5^\circ \sin(\omega t)$, $k=0.10$, $Re=2 \times 10^6$

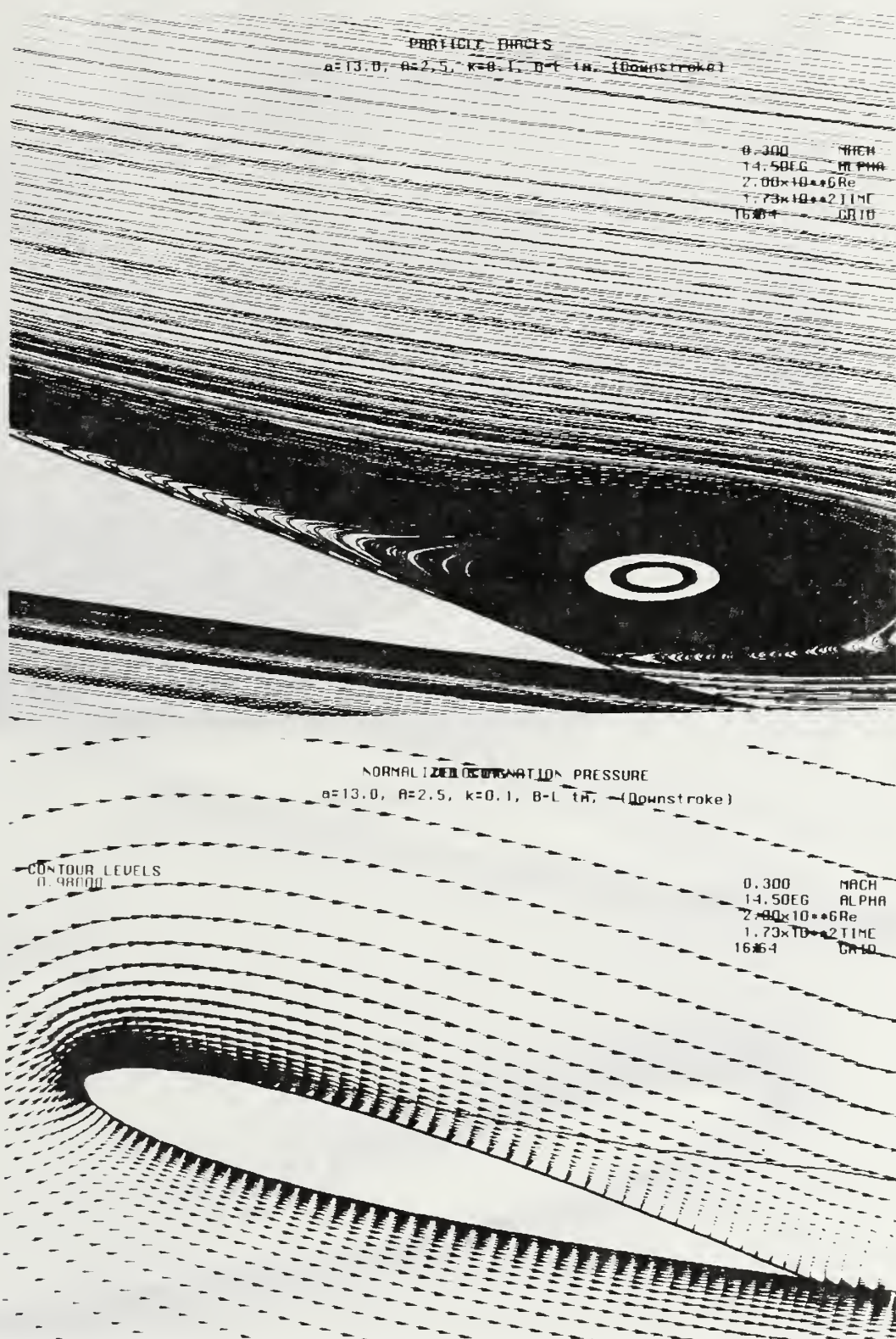


Figure 76. Instantaneous Particle Trace and Velocity Field, Oscillatory Motion, $M=0.3$, $\alpha=14.5^\circ$ (Downstroke), $\alpha(t)=13^\circ \pm 2.5^\circ \sin(\omega t)$, $k=0.10$, $Re=2 \times 10^6$

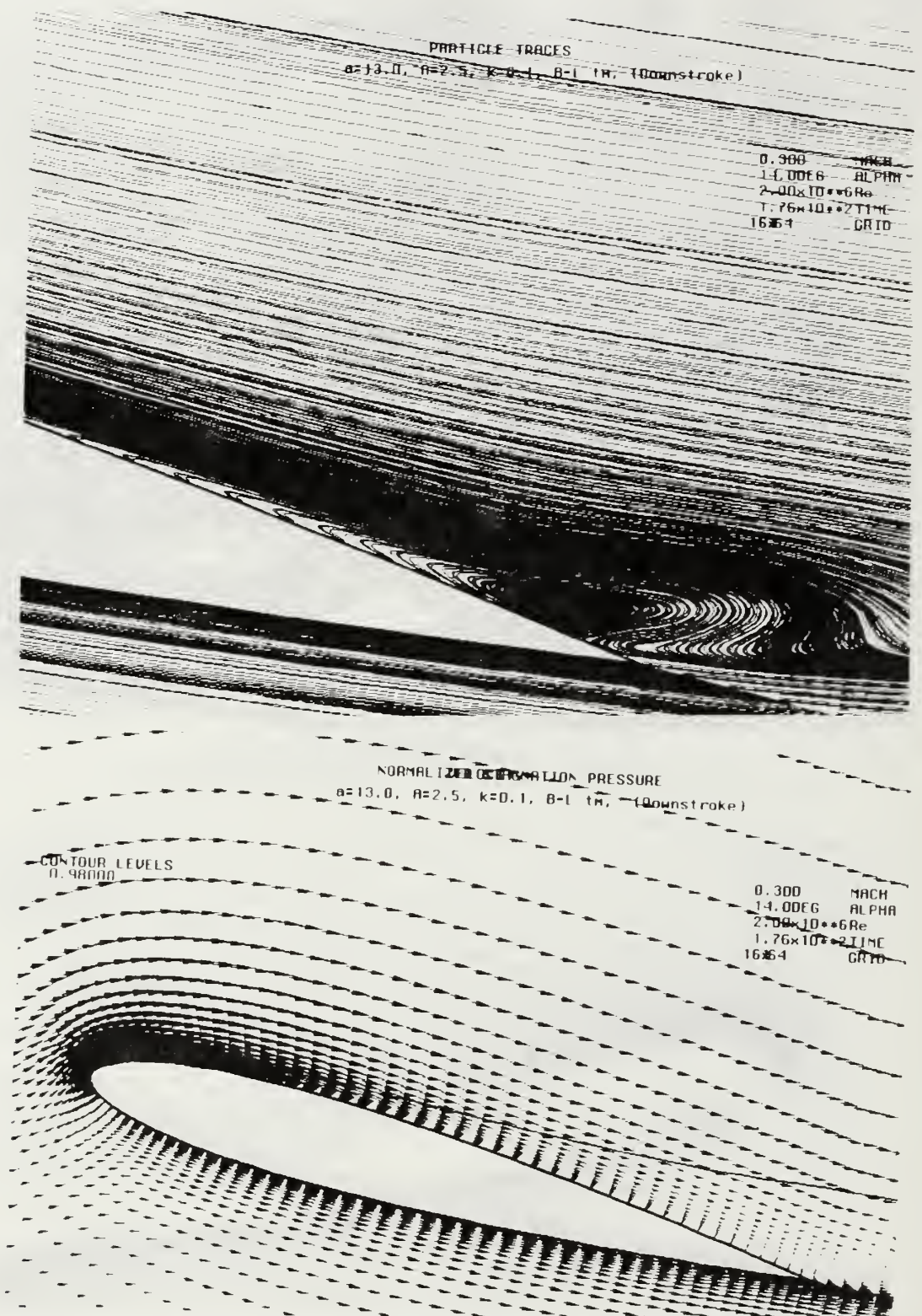


Figure 77. Instantaneous Particle Trace and Velocity Field, Oscillatory Motion, $M=0.3$, $\alpha=14^\circ$ (Downstroke), $\alpha(t)=13^\circ \pm 2.5^\circ \sin(\omega t)$, $k=0.10$, $Re=2 \times 10^6$

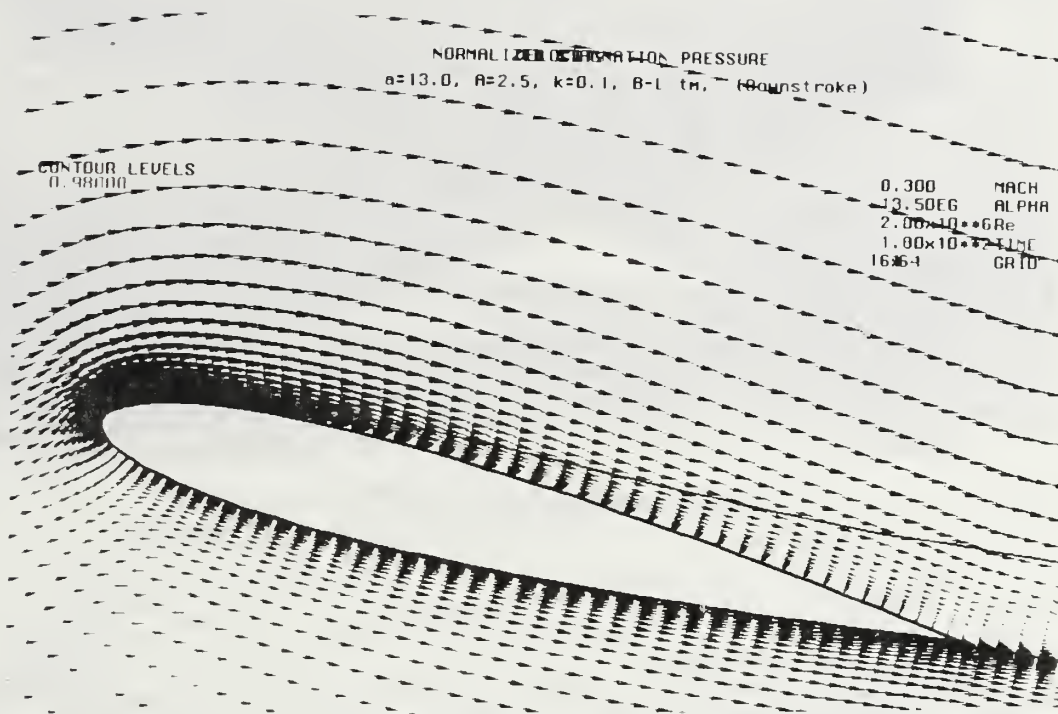


Figure 78. Velocity Field, Oscillatory Motion, $M=0.3$, $\alpha=13.5^\circ$
 (Downstroke), $\alpha(t)=13^\circ \pm 2.5^\circ \sin(\omega t)$, $k=0.10$, $Re=2 \times 10^6$

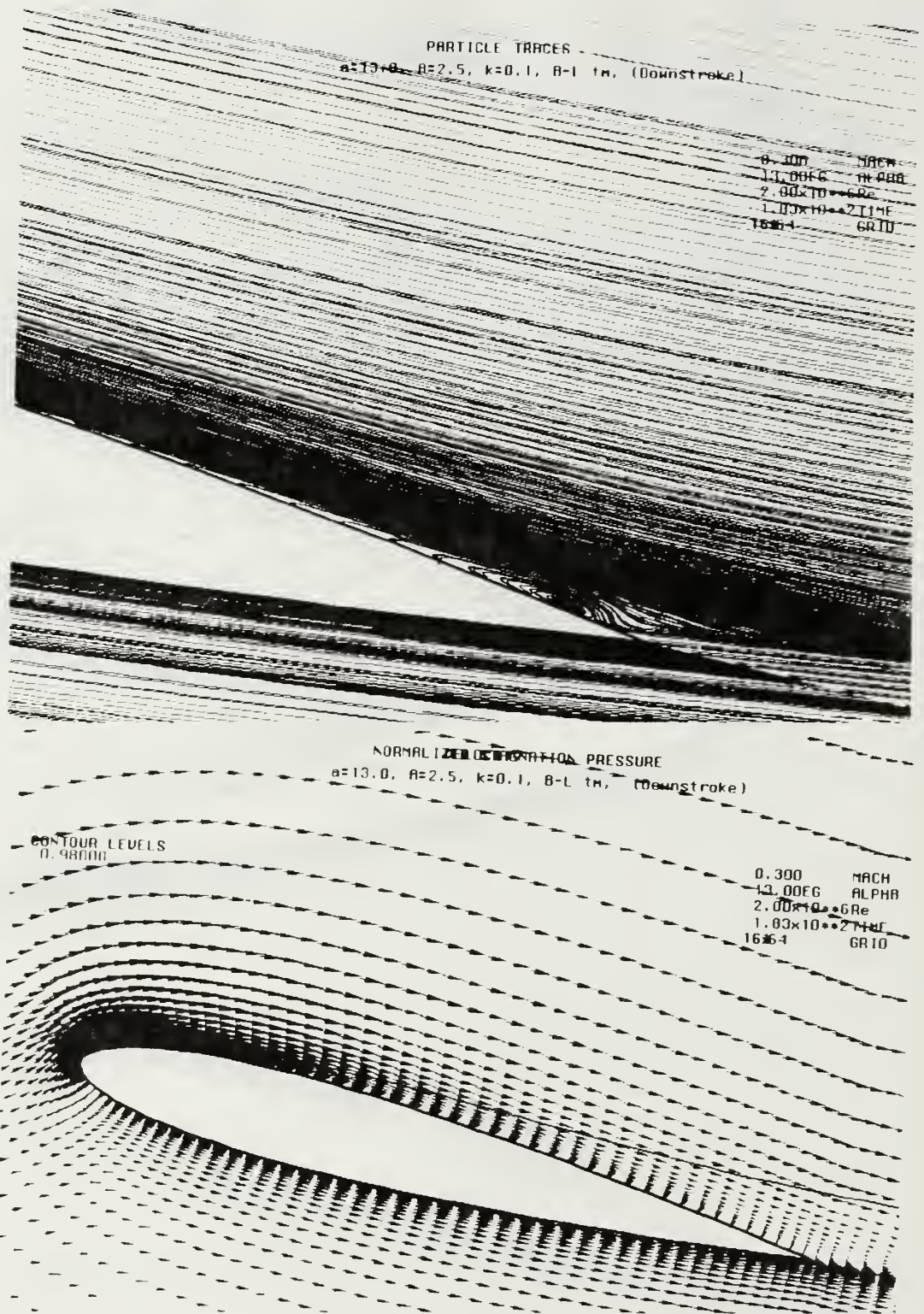


Figure 79. Instantaneous Particle Trace and Velocity Field,
Oscillatory Motion, $M=0.3$, $\alpha=13^\circ$ (Downstroke),
 $\alpha(t)=13^\circ \pm 2.5^\circ \sin(\omega t)$, $k=0.10$, $Re=2 \times 10^6$

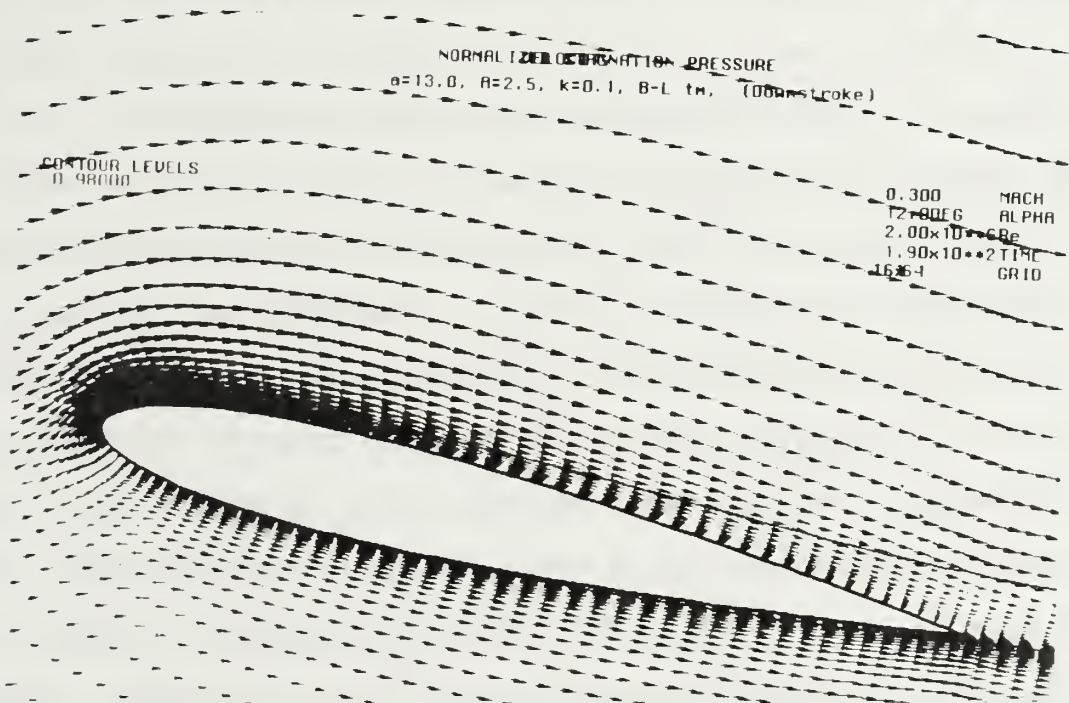


Figure 80. Instantaneous Particle Trace and Velocity Field, Oscillatory Motion, $M=0.3$, $\alpha=12^\circ$ (Downstroke), $\alpha(t)=13^\circ\pm 2.5^\circ\sin(\omega t)$, $k=0.10$, $Re=2\times 10^6$

4. Effect of Turbulence Modeling

a. Case 9. $\alpha(t)=9^\circ\pm5^\circ\sin(\omega t)$, $k=0.2$, $Re=4\times10^6$

Figures 81 and 82 show a comparison of the lift and moment hysteresis loops using the Baldwin-Lomax turbulence model for an oscillation of 5 degrees amplitude about a mean angle of attack of 9.0 degrees with McCroskey's experimental data for a Mach number of 0.3, a Reynolds number of four million, and a reduced frequency $k=0.2$. It is seen that there is a substantial difference between the computed and the experimental lift hysteresis loops. This difference becomes even more pronounced when the computed and experimental moment hysteresis loops are compared with each other. In an effort to understand the failure of Ns2.f to predict the experimental pitching moment hysteresis loop, the pressure distributions for several upstroke and downstroke angles of attack were compared to measured data from Reference 1. Figures 83 through 87 show pressure distributions for $\alpha=11.9^\circ$ on the upstroke portion of the cycle; and $\alpha=13.7^\circ$, $\alpha=13.0^\circ$, $\alpha=10.5^\circ$, and $\alpha=8.9^\circ$ on the down stroke cycle. U2diif.f overpredicts the suction peak at $\alpha=11.9^\circ$ on the upstroke and Ns2.f underpredicts the peak. Even though the values are off, the general shape of the distribution is well predicted. However, on the downstroke at $\alpha=13.7^\circ$, a significant difference between the computed and the measured distributions is observed. The measured pressure distribution shows a lower suction near the leading edge but higher suction near the trailing edge. Neither of these changes are predicted by Ns2.f. As the oscillation continues on the downstroke the measured distribution tends to flatten out creating a "plateau". Just after $\alpha=8.9^\circ$ on the downstroke, the flow begins to reattach and the positive pressure difference at the trailing edge becomes smaller. The failure of Ns2.f to

predict the experimental loop results from the inability of Ns2.f to accurately compute the pressure distributions. Since the pitching moment is an integrated quantity, the size of the area under the pressure distribution aft of the quarter chord must be greater than the area forward of the quarter chord to compute a negative or downward pitching moment. Ns2.f clearly does not predict the experimental pressure distributions during the downstroke.

Oscil. Motion: $M=0.3$, $A_0=9$, $A_1=5$, $k=2$, $Re=4 \times 10^6$

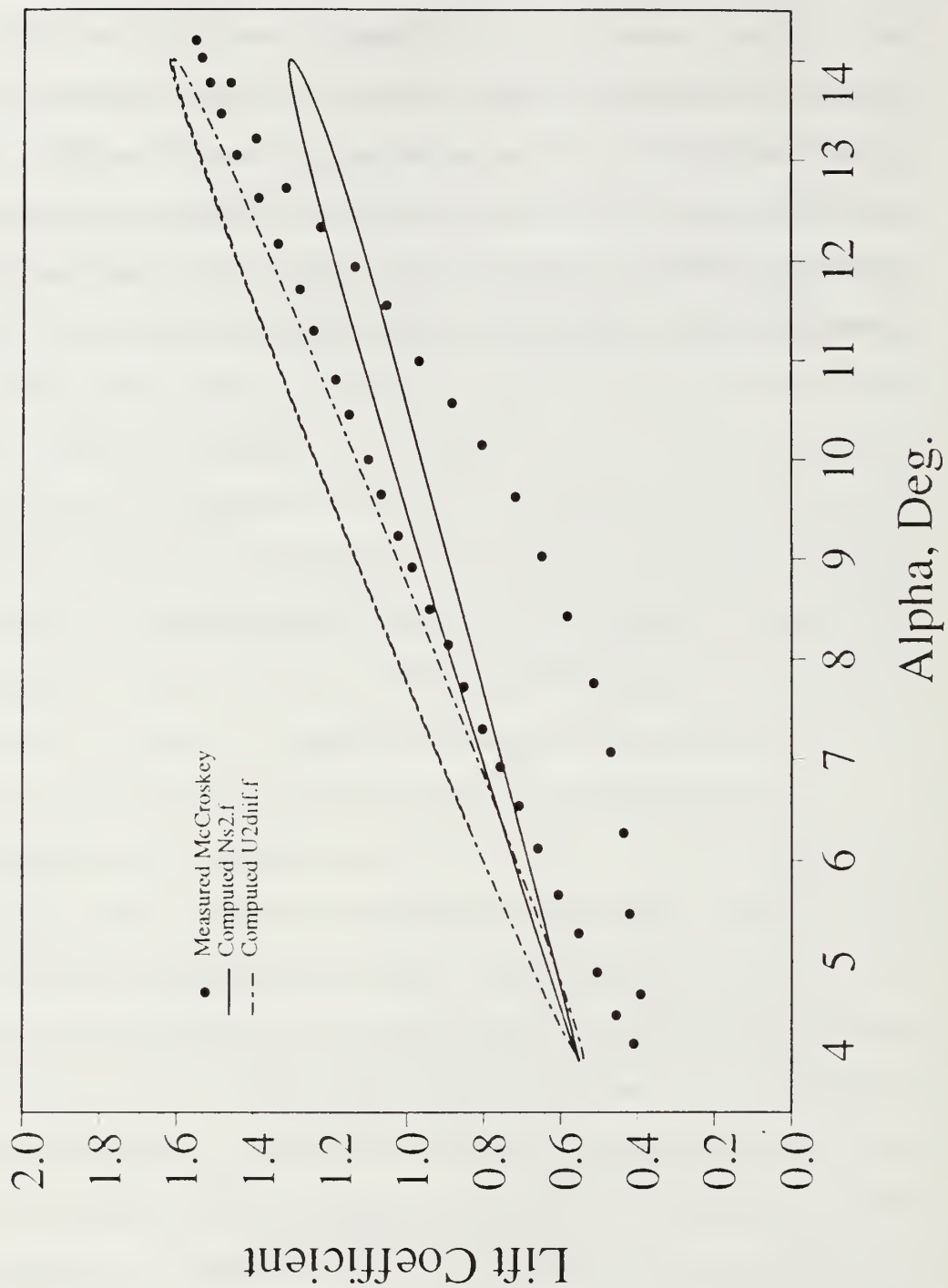


Figure 81. C_l vs α , Oscillatory Motion, $M=0.3$, $\alpha(t)=9^\circ \pm 5^\circ \sin(\omega t)$, $k=0.2$, $Re=4 \times 10^6$

Oscil. Motion: $M=0.3$, $A_0=9$, $A_1=5$, $k=.2$, $Re=4 \times 10^6$

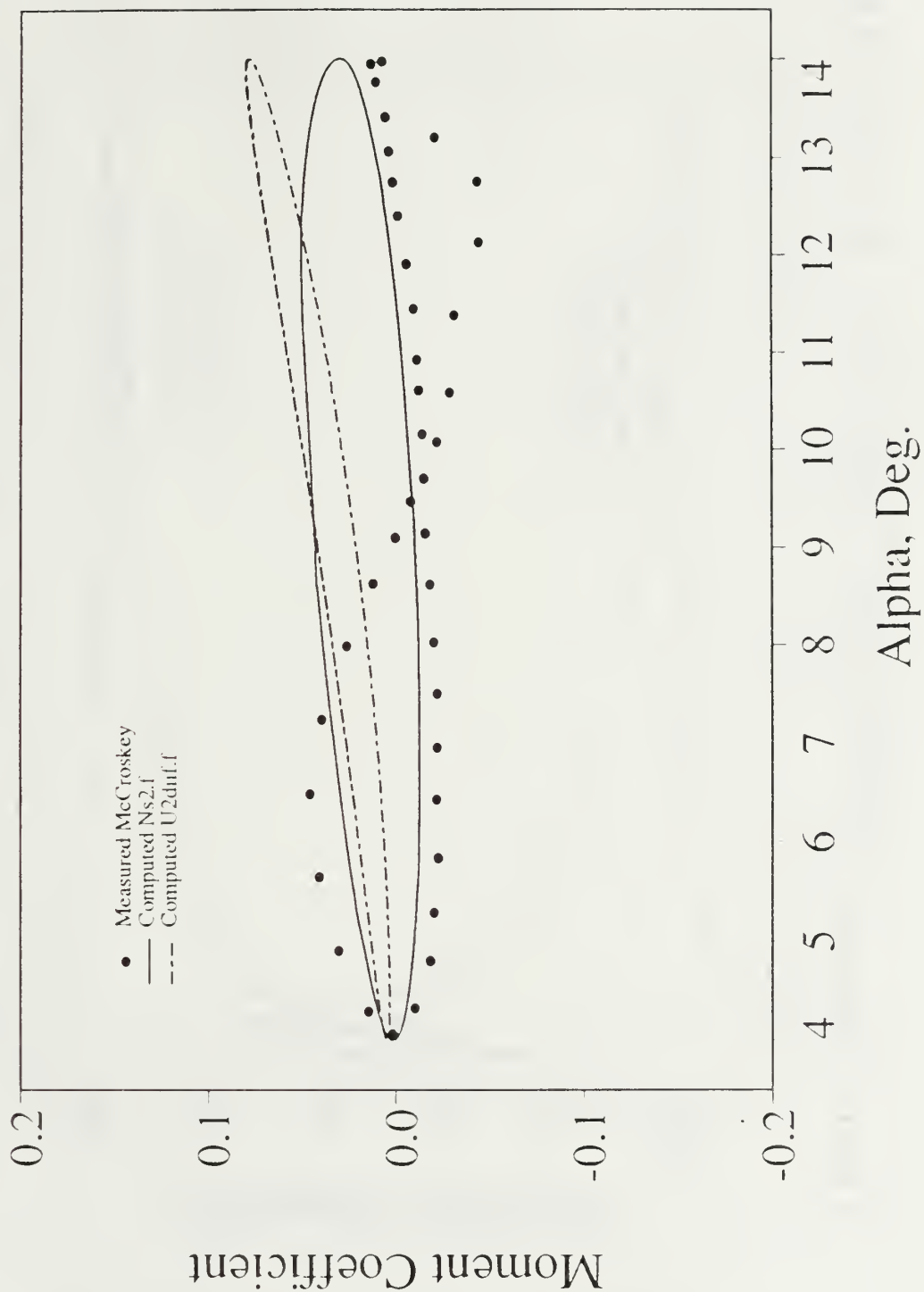


Figure 82. C_m vs α , Oscillatory Motion, $M=0.3$, $\alpha(t)=9^\circ \pm 5^\circ \sin(\omega t)$, $k=0.2$, $Re=4 \times 10^6$

Oscil. Motion: $M=0.3$, $A_0=9$, $A_1=5$, $k=0.2$, $Re=4 \times 10^6$

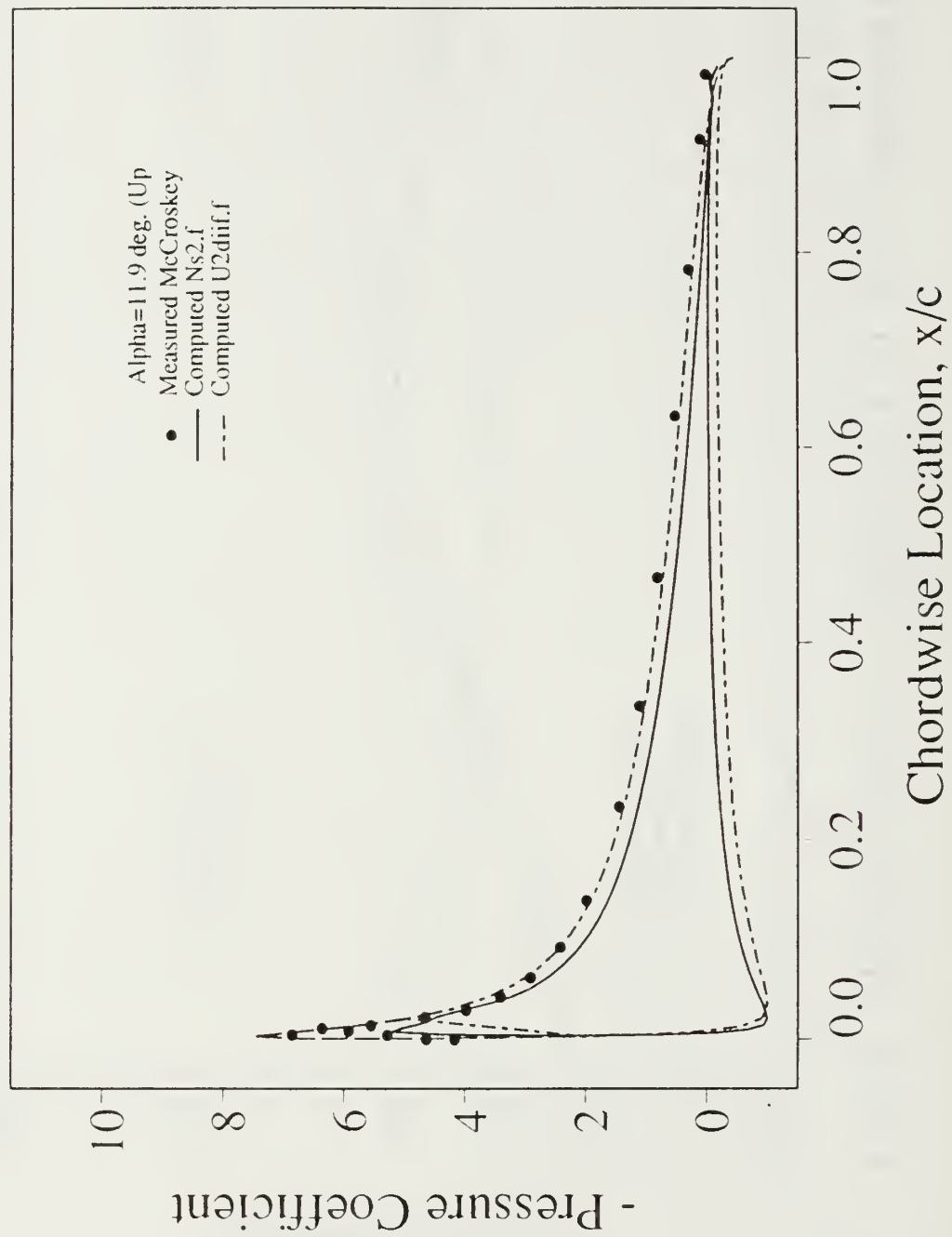


Figure 83. Pressure Distribution, Oscillatory Motion, $M=0.3$, $\alpha=11.9^\circ$ (Upstroke), $\alpha(t)=9^\circ \pm 5^\circ \sin(\omega t)$, $k=0.2$ $Re=4 \times 10^6$

Oscil. Motion: $M=0.3$, $A_0=9$, $A_1=5$, $k=2$, $Re=4 \times 10^6$

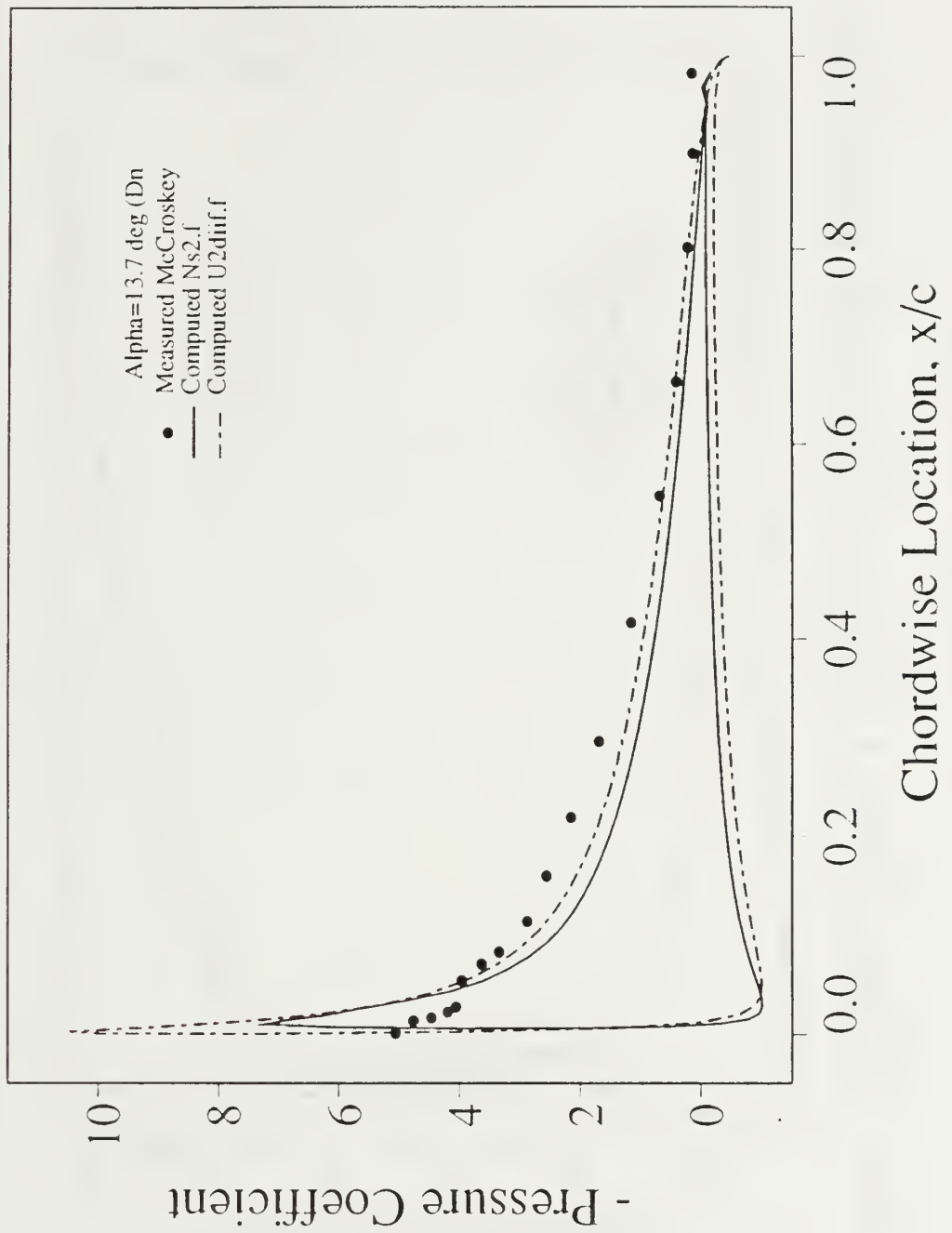


Figure 84. Pressure Distribution, Oscillatory Motion, $M=0.3$, $\alpha=13.7^\circ$ (Downstroke), $\alpha(t)=9^\circ \pm 5^\circ \sin(\omega t)$, $k=0.2$, $Re=4 \times 10^6$

Oscil. Motion: $M=0.3$, $A_0=9$, $A_1=5$, $k=0.2$, $Re=4 \times 10^6$

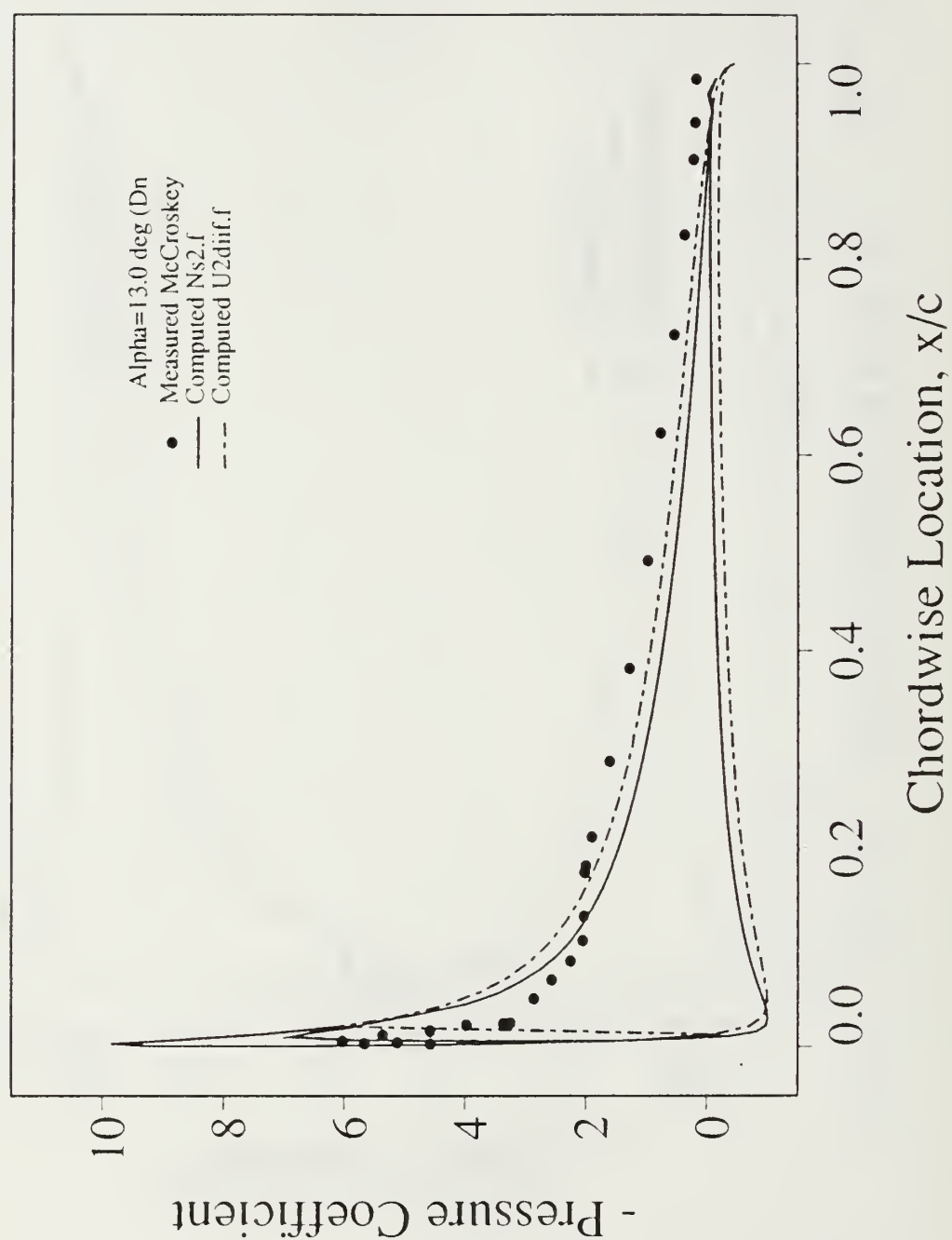


Figure 85. Pressure Distribution, Oscillatory Motion, $M=0.3$, $\alpha=13.0^\circ$ (Downstroke), $\alpha(t)=9^\circ \pm 5^\circ \sin(\omega t)$, $k=0.2$, $Re=4 \times 10^6$

Oscil. Motion: $M=0.3$, $A_0=9$, $A_1=5$, $k=0.2$, $Re=4 \times 10^6$

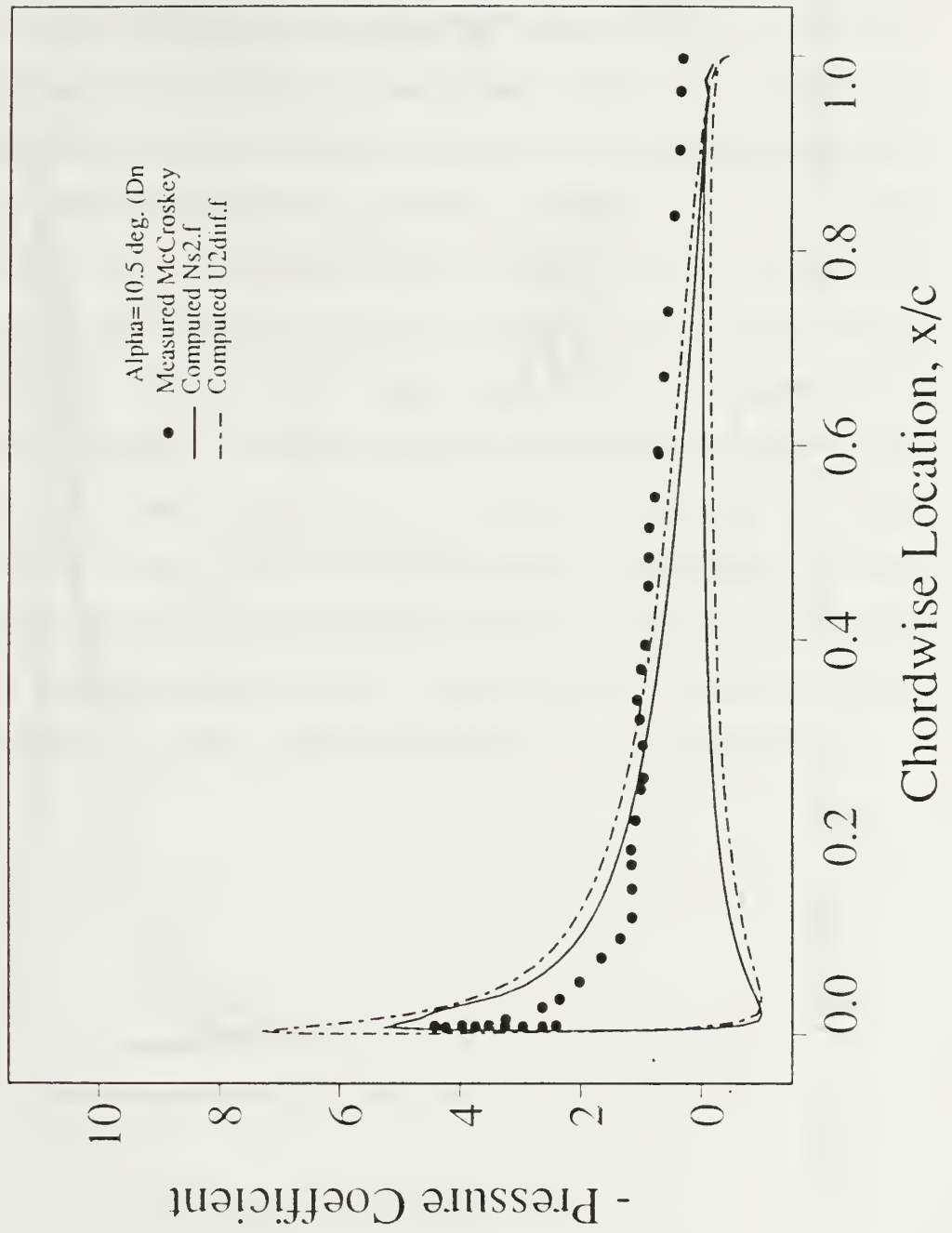


Figure 86. Pressure Distribution, Oscillatory Motion, $M=0.3$, $\alpha=10.5^\circ$ (Downstroke), $\alpha(t)=9^\circ \pm 5^\circ \sin(\omega t)$, $k=0.2$, $Re=4 \times 10^6$

Oscil. Motion: $M=0.3$, $A_0=9$, $A_1=5$, $k=.2$, $Re=4 \times 10^6$

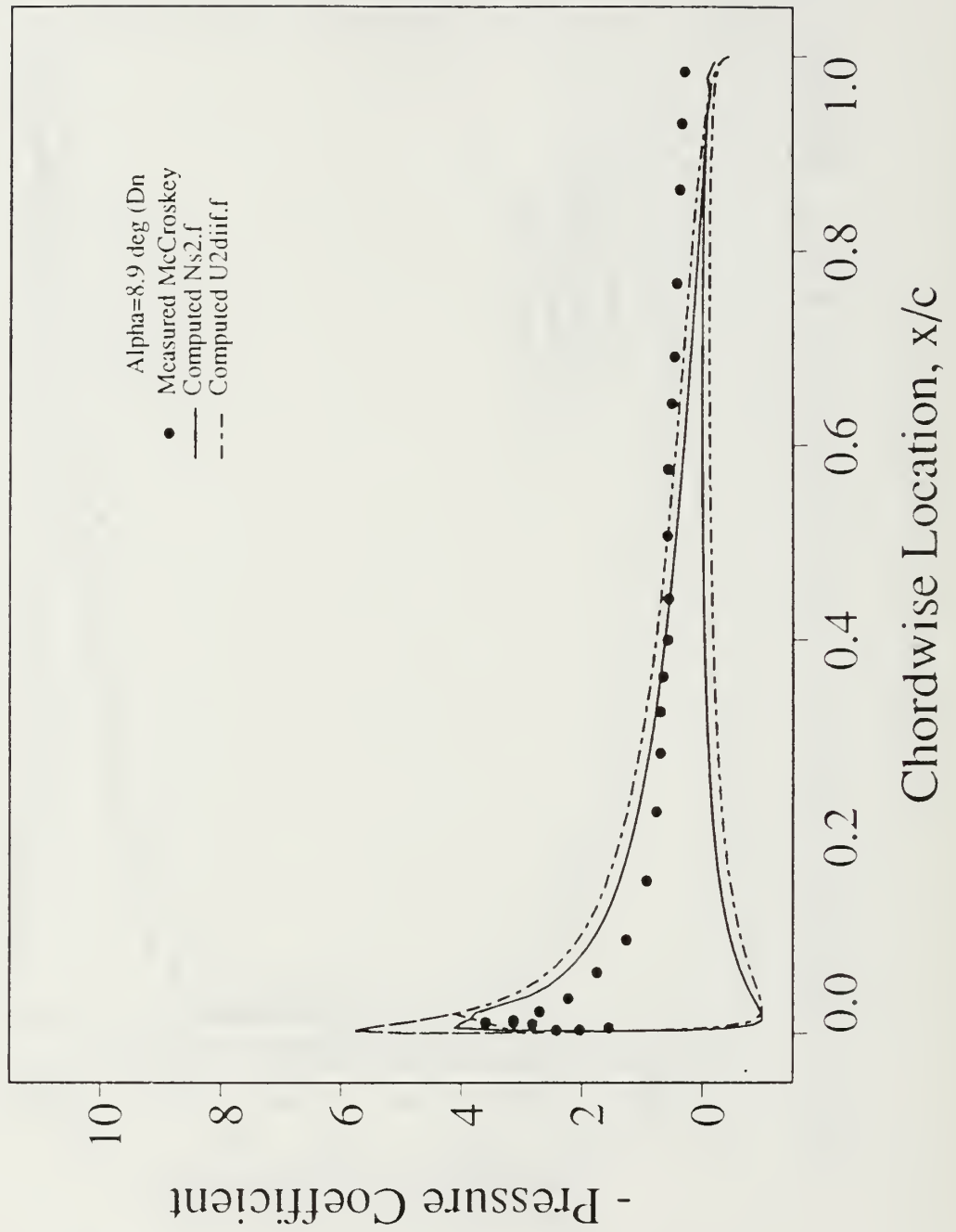


Figure 87. Pressure Distribution, Oscillatory Motion, $M=0.3$, $\alpha=8.9^\circ$ (Downstroke), $\alpha(t)=9^\circ \pm 5^\circ \sin(\omega t)$, $k=0.2$, $Re=4 \times 10^6$

b. Case 10. $\alpha(t)=10^\circ\pm5.5^\circ\sin(\omega t)$, $k=0.1$, $Re=4\times10^6$

The measured loop consists of two subloops, a clockwise “unstable” subloop and a counterclockwise “stable” subloop. It is seen that the Navier-Stokes calculations in combination with the Baldwin-Lomax turbulence model fails to predict the destabilizing clockwise pitching moment loop. For this reason the sensitivity of the computed loops to different turbulence models was studied next. Figures 88 and 89 show the computed lift and pitching moment loops for oscillation about a slightly higher mean angle of 10 degrees at an amplitude of 5.5 degrees. The Mach and Reynolds numbers are again 0.3 and four million, and k was decreased to 0.1 to minimize the effects of reduced frequency. It can be seen that the Baldwin-Lomax, Johnson-King, and the RNG turbulence models produce significantly different hysteresis loops. The RNG model produces relatively good agreement with the measured lift hysteresis loop but fails again to predict the destabilizing moment subloop.

EFFECT OF TURBULENCE MODELING ON THE UNSTEADY LIFT

$M_\infty = 0.3$, $\alpha(t) = 10^\circ + 5.5^\circ \sin(\omega t)$, $k = 0.1$, $Re = 4 \times 10^6$

Experiment: McCroskey

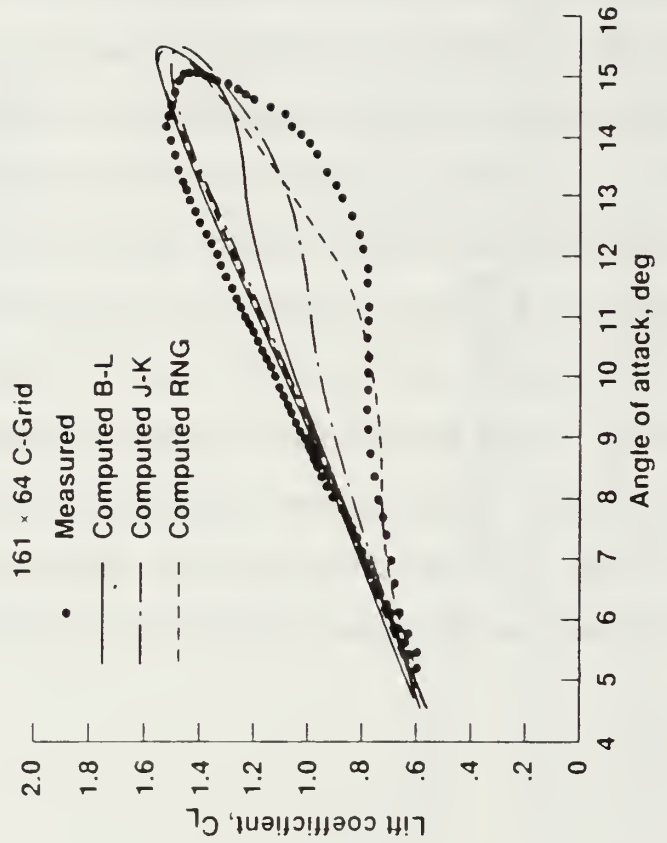


Figure 88. C_L vs α , Oscillatory Motion, $M=0.3$, $\alpha(t)=10^\circ \pm 5.5^\circ \sin(\omega t)$, $k=0.10$, $Re=4 \times 10^6$

EFFECT OF TURBULENCE MODELING ON UNSTEADY PITCHING MOMENT

$M_\infty = 0.3$, $\alpha(t) = 10^\circ + 5.5^\circ \sin(\omega t)$, $k = 0.1$, $Re = 4 \times 10^6$

Experiment: McCroskey

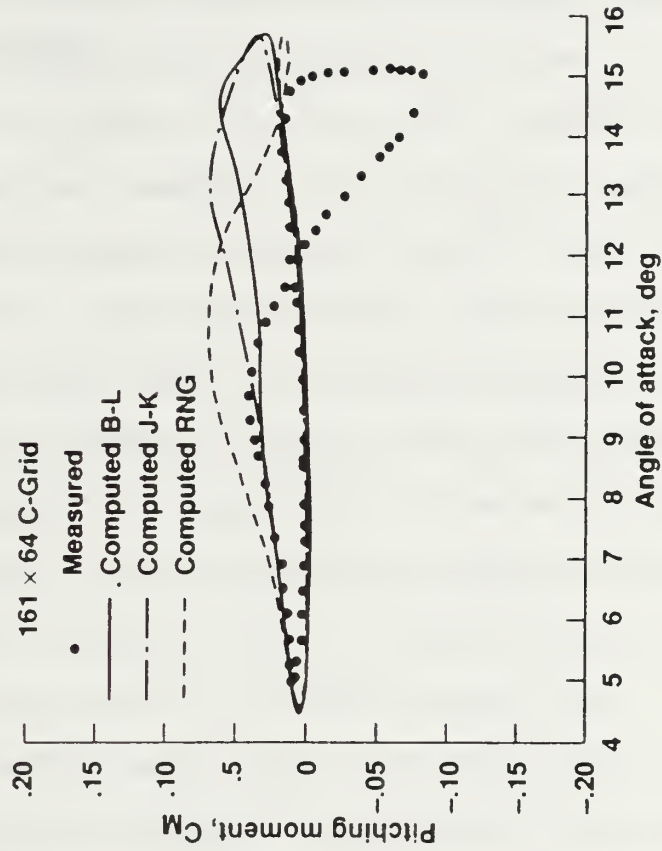


Figure 89. C_m vs α , Oscillatory Motion, $M=0.3$,
 $\alpha(t)=10^\circ \pm 5.5^\circ \sin(\omega t)$, $k=0.10$, $Re=4 \times 10^6$

c. Case 11. $\alpha(t)=11^\circ\pm5^\circ\sin(\omega t)$, $k=0.1$, $Re=4\times10^6$

A solution was also computed for oscillations about a mean angle of 11 degrees at an amplitude of 5 degrees, the other parameters left unchanged. Figures 90 and 91 show the computed lift and moment hysteresis loops. As before, the calculations fail to predict the expected destabilizing moment subloop. The reason for this failure can be better appreciated by visualizing the separated flow structures computed with these turbulence models. Figures 92 and 93 show the computed flowfield with particle traces and the velocity field. Figure 92 corresponds to the instant when the airfoil oscillates through an incidence of 15 degrees during the downstroke. Different turbulence models produce substantially different recirculatory flow patterns on the upper surface near the trailing edge. The Baldwin-Lomax model produced the smallest recirculatory region while the RNG model produced the largest. In addition, Figure 93 ($\alpha=15^\circ$) shows the relative magnitudes of the velocity vectors. Note, near the surface at the trailing edge, the magnitude of the velocity vectors in the reverse flow region calculated by the Baldwin-Lomax model are much smaller than the region calculated by the Johnson-King model or RNG model. As the cycle continues, Figures 94 and 95 ($\alpha=14^\circ$) show the recirculation region to shrink slightly and loose intensity for the Baldwin-Lomax model, while the regions as calculated by the Johnson-King and RNG continue to expand and intensify. As noted in Case 8 the recirculatory flow region grows and then vanishes again during the course of the oscillation. Even though the structure at the trailing edge resembles a vortex it does not shed from the trailing edge. The occurrence of the destabilizing moment loop appears to be closely associated with the vortex shedding from the trailing

edge, an event which occurs soon after the static angle is substantially exceeded during part of the cycle. Although the static stall angle is significantly exceeded in the present calculations the numerical procedure along with the turbulence modeling used in the calculations appears to be unable to produce the anticipated shedding process.

EFFECT OF TURBULENCE MODELING ON UNSTEADY LIFT

$M_\infty = 0.3$, $\alpha(t) = 11^\circ + 5^\circ \sin(\omega t)$, $k = 0.1$, $Re = 4 \times 10^6$

Experiment: McCroskey

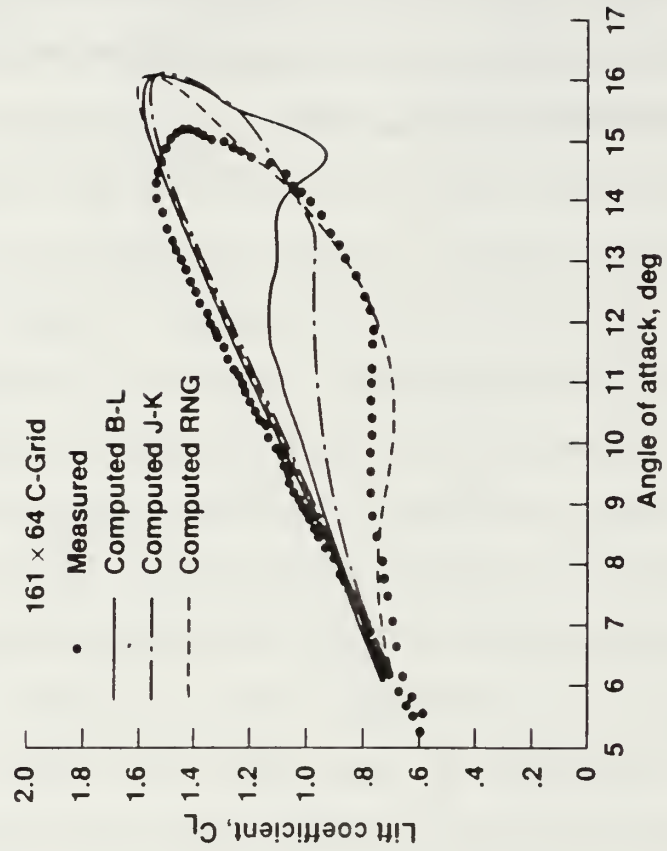


Figure 90. C_L vs α , Oscillatory Motion, $M=0.3$, $\alpha(t)=11^\circ \pm 5^\circ \sin(\omega t)$, $k=0.10$, $Re=4 \times 10^6$

EFFECT OF TURBULENCE MODELING ON UNSTEADY PITCHING MOMENT

$M_\infty = 0.3$, $\alpha(t) = 11^\circ + 5^\circ \sin(\omega t)$, $k = 0.1$, $Re = 4 \times 10^6$

Experiment: McCroskey

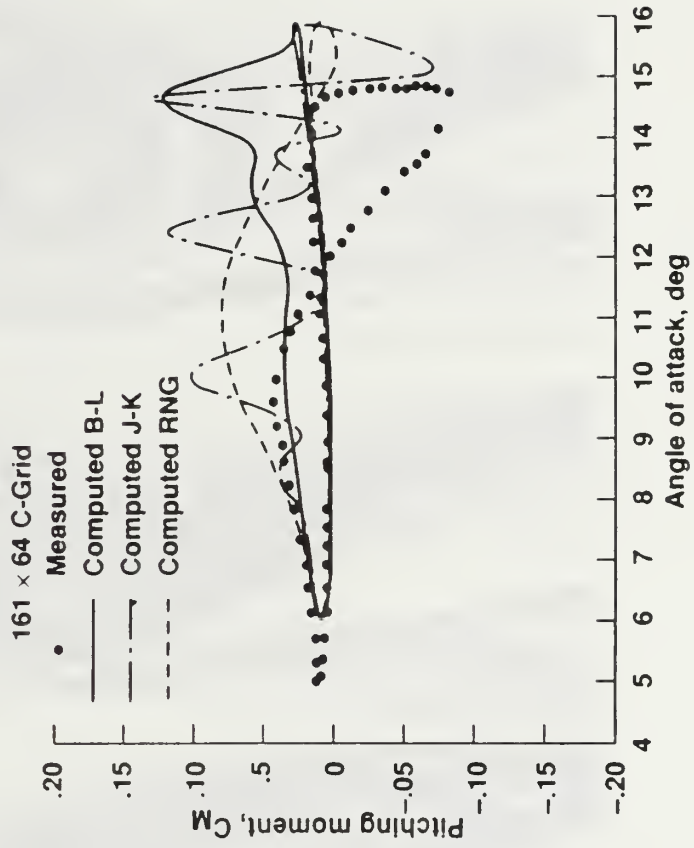
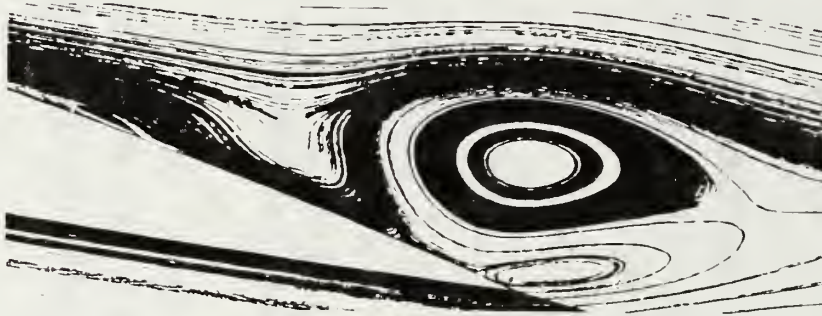


Figure 91. C_m vs α , Oscillatory Motion, $M=0.3$, $\alpha(t)=11^\circ \pm 5^\circ \sin(\omega t)$, $k=0.10$, $Re=4 \times 10^6$

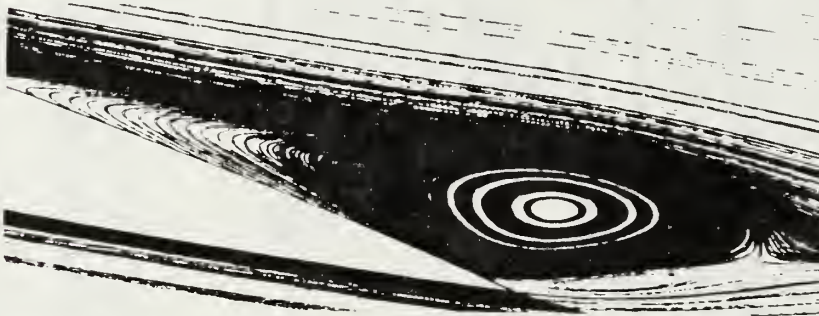
EFFECT OF TURBULENCE MODELING ON THE COMPUTED TRAILING EDGE FLOWFIELD

$M_\infty = 0.3$, $\alpha(t) = 11^\circ + 5^\circ \sin(\omega t)$, $k = 0.1$, $Re = 4 \times 10^6$

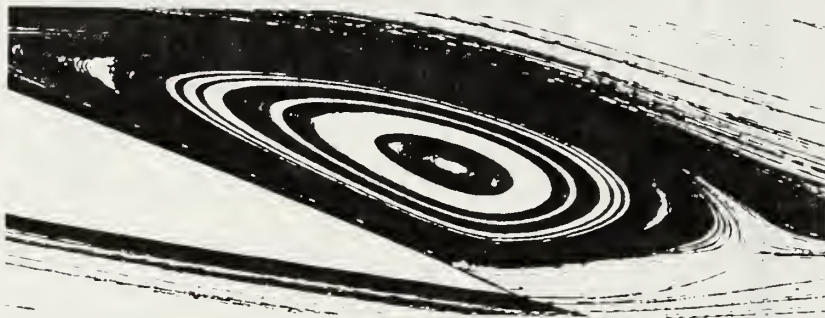
$\alpha = 15^\circ$ DOWNSTROKE



(a) Baldwin-Lomax



(b) Johnson-King



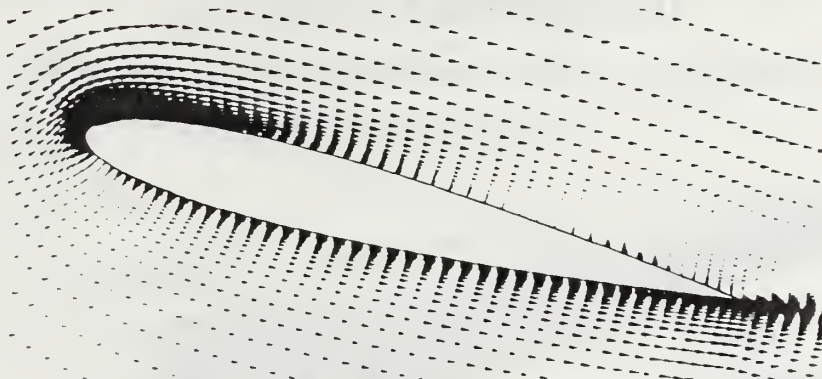
(c) RNG

Figure 92. Instantaneous Particle Trace, Oscillatory Motion, $M=0.3$, $\alpha=15^\circ$ (Downstroke), $\alpha(t)=11^\circ \pm 5^\circ \sin(\omega t)$, $k=0.10$, $Re=4 \times 10^6$

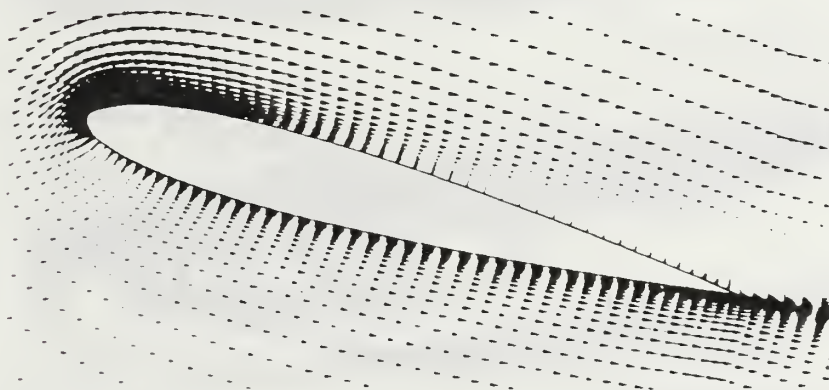
EFFECT OF TURBULENCE MODELING ON THE COMPUTED TRAILING EDGE FLOWFIELD

$$M_{\infty} = 0.3, \alpha(t) = 11^{\circ} + 5^{\circ} \sin(\omega t), k = 0.1, Re = 4 \times 10^6$$

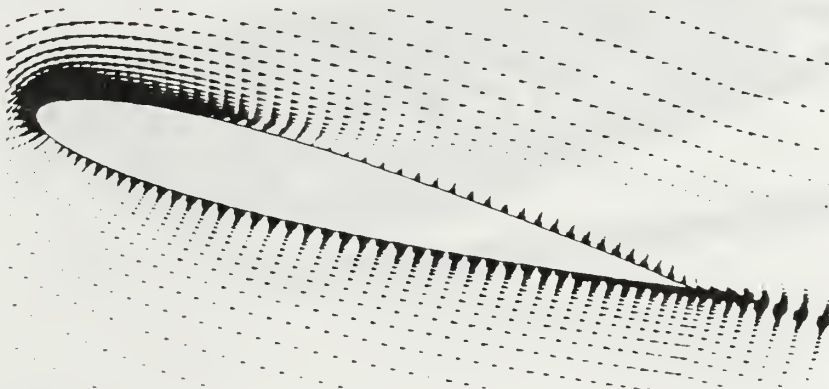
$$\alpha = 15^{\circ} \text{ DOWNSTROKE}$$



(a) Baldwin-Lomax



(b) Johnson-King



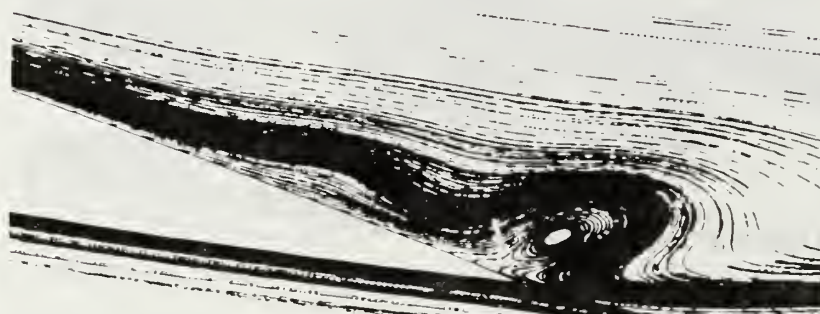
(c) RNG

Figure 93. Velocity Field, Oscillatory Motion, $M=0.3$, $\alpha=15^{\circ}$ (Downstroke), $\alpha(t)=11^{\circ}\pm 5^{\circ}\sin(\omega t)$, $k=0.10$, $Re=4\times 10^6$

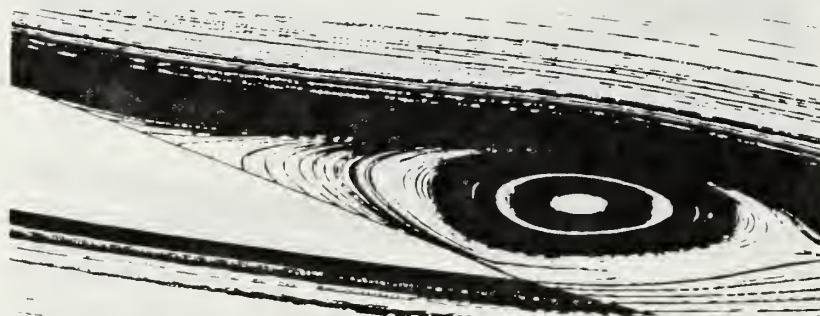
EFFECT OF TURBULENCE MODELING ON THE COMPUTED TRAILING EDGE FLOWFIELD

$$M = 0.3, \alpha(t) = 11^\circ + 5^\circ \sin(\omega t), k = 0.1, Re = 4 \times 10^6$$

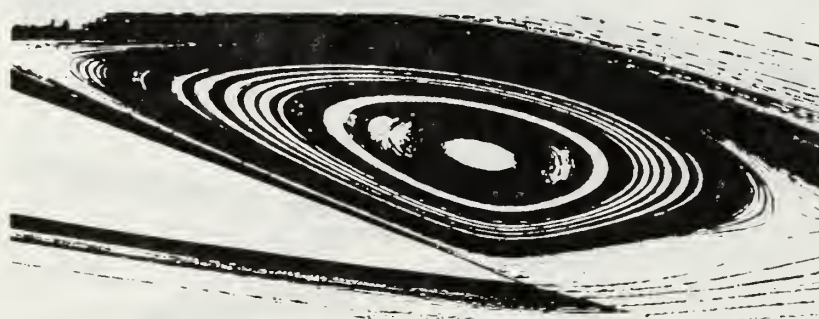
$\alpha = 14^\circ$ DOWNSTROKE



(a) Baldwin-Lomax



(b) Johnson-King



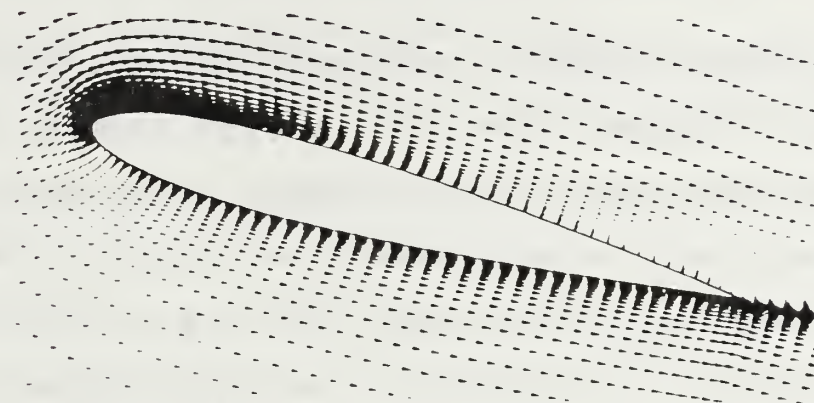
(c) RNG

Figure 94. Instantaneous Particle Trace, Oscillatory Motion, $M=0.3$, $\alpha=14^\circ$ (Downstroke), $\alpha(t)=11^\circ \pm 5^\circ \sin(\omega t)$, $k=0.10$, $Re=4 \times 10^6$

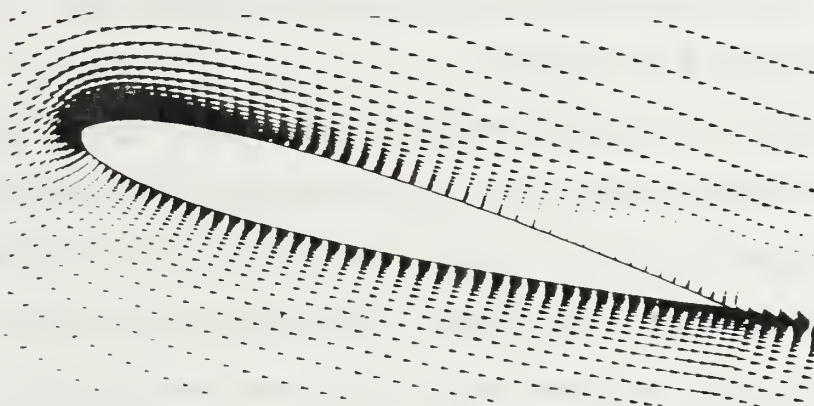
EFFECT OF TURBULENCE MODELING ON THE COMPUTED TRAILING EDGE FLOWFIELD

$$M = 0.3, \alpha(t) = 11^\circ + 5^\circ \sin(\omega t), k = 0.1, Re = 4 \times 10^6$$

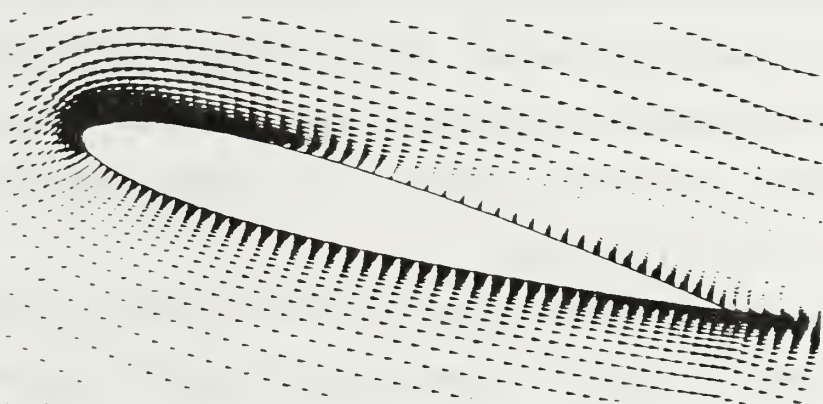
$$\alpha = 14^\circ \text{ DOWNSTROKE}$$



(a) Baldwin-Lomax



(b) Johnson-King



(c) RNG

Figure 95. Velocity Field, Oscillatory Motion, $M=0.3$, $\alpha=14^\circ$ (Downstroke), $\alpha(t)=11^\circ \pm 5^\circ \sin(\omega t)$, $k=0.10$, $Re=4 \times 10^6$

V. CONCLUSIONS AND RECOMMENDATIONS

In the preceding investigation a computationally efficient, fully factorized, two-dimensional Navier-Stokes flow solver was utilized to predict steady and unsteady flow solutions about a NACA 0012 airfoil. Comparisons between a steady viscous/inviscid interaction method code using the Cebeci-Smith turbulence model and the Navier-Stokes code using the Baldwin-Lomax turbulence model show close agreement up to just prior to the static stall angle of attack. After this point, the viscous/inviscid interaction method code fails to accurately model the flow separation.

When applied to the unsteady problem of airfoil stall flutter in compressible flow, the Navier-Stokes code shows that the modeling of the recirculatory flow region with current turbulence models fails to capture the essential physics which governs the onset of stall flutter. Comparisons of the computed results with available experimental data indicates that even though the lift response is fairly well predicted, the computation of the pitching moment hysteresis loops is very sensitive to turbulence modeling. Results computed with several current models are in good agreement whenever the steady stall angle is exceeded only slightly. However, they fail to capture a vortex shedding process that may contribute to the onset of stall flutter.

Therefore, further detailed studies of improved numerical schemes and turbulence models as well as viscous/inviscid interaction approaches are required to improve the prediction of the unsteady flow separation and vortex shedding phenomenon. Further computational work with the full Navier-Stokes equations instead of applying the thin-layer approximation is recommended. In

addition, local grid refinement studies that focus on the the leading and trailing edge upper surface may lead to the accurate prediction of the extremely complex vortex development and shedding process.

LIST OF REFERENCES

1. McCroskey, W. J., and Pucci, S L. W., *Viscous-Inviscid Interaction on Oscillating Airfoils in Subsonic Flow*, AIAA Journal, Vol. 20, No. 2, pp.167-174, 1982.
2. Lorber, P. F., and, Carta, F. O., *Airfoil Dynamic Stall at Constant Pitch Rate and High Reynolds Number*, Journal of Aircraft, pp. 548-556, June 1988.
3. Carta, F. O., and Lorber, P. F., *Experimental Study of the Aerodynamics of Incipient Torsional Flutter*, Journal of Propulsion, Vol. 3, No. 2, pp. 164-170, 1987.
4. Carta, F. O., and Niebanck, C. F., *Prediction of Rotor Instability at High Forward Speeds*, USAAVLABS Technical Report 68-18C, February 1969.
5. Beam, R., and Warming, R. F., *An Implicit Finite-Difference Algorithm for Hyperbolic Systems in Conservation Law Form*, Journal of Computational Physics, Vol. 22, pp.87-110, 1976.
6. Anderson J. D., *Fundamentals of Aerodynamics*, McGraw-Hill Publishing Company, 1984.
7. Teng, N. G., *The Development of a Computer Code (U2DIIF) for the Numerical Solution of Unsteady, Inviscid, and Incompressible Flow over an Airfoil*, Master's Thesis, Naval Postgraduate School, Monterey, California, June, 1987.
8. Krainer, A., *A Numerical Method for Computing Unsteady 2-D Boundary Layer Flow*, NASA Contractor Report 4198, December 1988.
9. Cebeci, T., and Bradshaw, P., *Momentum Transfer in Boundary Layers*, McGraw-Hill Publishing Company, 1977.
10. Snir, Z., *Investigation of Incompressible Cascade Flows Using a Viscous/Inviscid Interactive Code*, Master's Thesis, Naval Postgraduate School, Monterey, California, December, 1988.
11. Cebeci, T., and Smith A. M. O., *Analysis of Turbulent Boundary Layers*, Academic Press, New York, 1974.

12. Baldwin, B. S., and Lomax, H., *Thin Layer Approximation and Algebraic Model for Separated Turbulent Flows*, AIAA 16th Aerospace Science Meeting Report No. 78-257, January 1978.
13. Johnson, D. A., and King, L. S., *A Mathematically Simple Turbulence Closure Model for Attached and Separated Turbulent Boundary Layers*, AIAA Journal, Vol. 23, No. 11, November 1985.
14. Yakhot, V., and Orszag, S. A., *Renormalization Group Analysis of Turbulence. I Basic Theory*, Journal of Scientific Computing, Vl. 1, 1986.
15. Martinelli, L., and Yakhot, V., *RNG-Based Turbulence Transport Approximations with Applications to Transonic Flows*, AIAA Paper 89-1950, 1989.
16. Harris, C. D., *Two-Dimensional Aerodynamic Characteristics of the NACA 0012 Airfoil in the 8 Foot Transonic Pressure Tunnel*, NASA TM 81927, 1981.
17. McCroskey, W. J., McAlister, K. W., Carr, L. W., Pucci, S. L., and Lambert, D., *An Experimental Study of Dynamic Stall on Advanced Airfoil Sections*, USA AVRADCOM TR 82-A-8, 1982.
18. Landon, R. H., *NACA 0012 Oscillating and Transient Pitching*, AGARD Report No. 702, December 1982.
19. Grohsmeyer, S. P., *Numerical Investigation of the Effect of Leading Edge Geometry on Dynamic Stall of Airfoils*, Engineer's Thesis, Naval Postgraduate School, Monterey, California, September 1990.

APPENDIX A - FLUX JACOBIAN MATRIX

The Jacobian matrices $\hat{A} = \partial \hat{E} / \partial \hat{q}$ and $\hat{B} = \partial \hat{F} / \partial \hat{q}$ are given by \hat{A} or $\hat{B} = k_0 I + k_1 A + k_2 B$, where $A = \partial E / \partial q$ and $B = \partial F / \partial q$ are the usual Jacobian matrices of the Cartesian flux vectors. The \hat{A} or \hat{B} matrix is

$$\hat{A} = \frac{\partial \hat{E}}{\partial \hat{q}} = \begin{bmatrix} k_0 & k_1 & k_2 & 0 \\ -u(k_1 u + k_2 v) + k_1 \phi^2 & -(\gamma - 2)k_1 u + k_0 + k_1 u + k_2 v & -(\gamma - 1)k_1 v + k_2 u & (\gamma - 1)k_1 \\ -v(k_1 u + k_2 v) + k_2 \phi^2 & k_1 v - (\gamma - 1)k_2 u & -(\gamma - 2)k_2 v + k_0 + k_1 u + k_2 v & (\gamma - 1)k_2 \\ (k_1 u + k_2 v)^* & [\gamma(e / \rho) - \phi^2]k_1 - [-\gamma(e / \rho) + 2\phi^2] & [\gamma(e / \rho) - \phi^2]k_2 - (\gamma - 1)(k_1 u + k_2 v)u & \gamma(k_1 u + k_2 v)v + k_0 \end{bmatrix}$$

where $\phi^2 = 0.5(\gamma - 1)(u^2 + v^2)$, $k_0 = \xi_t$, $k_1 = \xi_x$, $k_2 = \xi_z$ for \hat{A} , and $k_0 = \zeta_t$, $k_1 = \zeta_x$, $k_2 = \zeta_z$ for \hat{B} .

APPENDIX B - PITCHING MOMENT DERIVATION

Figure 96 shows the nomenclature for the integration of the pressure and shear stress distributions over a two dimensional body surface as generated by the Navier-Stokes code Ns2.f. For unsteady motion the airfoil is rotated with respect to a fixed inertial frame of reference (x,z : Laboratory frame of Reference). Note, for unsteady motion, as the airfoil rotates through an angle of attack, all grid ($i=1...I_{\max}$, $k=1...K_{\max}$) are rotated about the desired pivot point with respect to the fixed x,z coordinate system. As the solution is advanced in time the flow quantities for this new grid location are updated for each point.

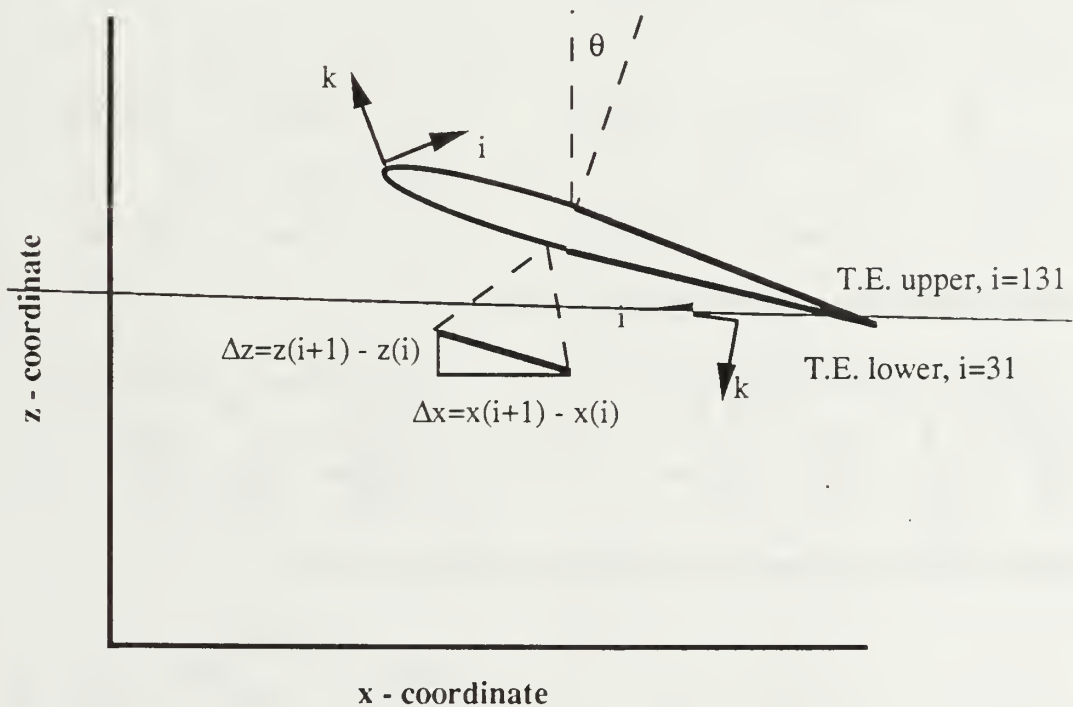


Figure 96. Pitching Moment Derivation

PITCHING MOMENT DERIVATION GENERATED BY MATHCAD

1. Read tabulated data generated from Ns2.f. Data computed at $\alpha=0^\circ$ and a $Re=4 \times 10^{**6}$.

```

Data_u := READPRN(up)      Data_l := READPRN(low)      i := 1 .. 50

      <0>
x_u := Data_u
      <1>
z_u := Data_u
      <2>
cp_u := Data_u
      <3>
tau_u := Data_u

      <0>
x_l := Data_l
      <1>
z_l := Data_l
      <2>
cp_l := Data_l
      <3>
tau_l := Data_l
    
```

2. Compute Δx and Δz for upper and lower surface.

```

Delta_x_u := x_u - x_u
              i      i      i-1

Delta_x_l := x_l - x_l
              i      i      (i-1)

Delta_z_u := z_u - z_u
              i      i      i-1

Delta_z_l := z_l - z_l
              i      i      (i-1)
    
```

3. Compute segment length Δs for upper and lower surface.

```

Delta_s_u := sqrt([Delta_x_u]^2 + [Delta_z_u]^2)
              i      i      i

Delta_s_l := sqrt([Delta_x_l]^2 + [Delta_z_l]^2)
              i      i      i
    
```

4. Compute angle, θ , relative to perpendicular for upper and lower surface.

```

theta_u := 0 * [pi / 180] + atan([Delta_z_u] / [Delta_x_u])
              i      i      i      i

theta_l := 0 * [pi / 180] + atan([Delta_z_l] / [Delta_x_l])
              i      i      i      i
    
```


Computed the x and z moment arms for the upper and lower surface.

$$xx_u := \frac{x_u^i + x_u^{i-1}}{2} \quad zz_u := \frac{z_u^i + z_u^{i-1}}{2}$$

$$xx_l := \frac{x_l^i + x_l^{i-1}}{2} \quad zz_l := \frac{z_l^i + z_l^{i-1}}{2}$$

Compute pitching moment coefficient about quarter chord by applying equation 1.11 from [Ref. p. 17].

$$Cm_{25} := \sum_i \left[\begin{aligned} & \left[\left[-cp_u^i \cdot \cos[\theta_u^i] + \tau_u^i \cdot \sin[\theta_u^i] \right] \cdot xx_u^i \dots \right] \cdot \Delta s_u^i \\ & + \left[cp_u^i \cdot \sin[\theta_u^i] + \tau_u^i \cdot \cos[\theta_u^i] \cdot zz_u^i \right] \dots \\ & + \left[\left[cp_l^i \cdot \cos[\theta_l^i] + \tau_l^i \cdot \sin[\theta_l^i] \right] \cdot xx_l^i \dots \right] \cdot \Delta s_l^i \\ & + \left[-cp_l^i \cdot \sin[\theta_l^i] + \tau_l^i \cdot \cos[\theta_l^i] \cdot zz_l^i \right] \dots \end{aligned} \right]$$

$$Cm_{25} = 0.005$$

The computed pitching moment coefficient from Ns2d.f (Computed on a Cray Super-Computer) was $Cm=0.0006$, as compared to the calculations made on a Macintosh SE/30 where $Cm=0.005$.

Upper Surface Data:

x	z	-Cp	Tau
-2.5e-1	-1.6e-3	-1.0319e+0	3e-3
-2.497e-1	3e-3	-9.841e-1	-7.4e-3
-2.479e-1	7.6e-3	-6.798e-1	-1.5e-2
-2.447e-1	1.2e-2	-4.091e-1	-1.64e-2
-2.404e-1	1.65e-2	-1.766e-1	-1.54e-2
-2.346e-1	2.09e-2	9.93e-2	-1.19e-2
-2.273e-1	2.49e-2	2.286e-1	-8.4e-3
-2.187e-1	2.88e-2	2.769e-1	-6.3e-3
-2.088e-1	3.26e-2	3.316e-1	-4.9e-3
-1.975e-1	3.61e-2	3.715e-1	-3.8e-3
-1.85e-1	3.94e-2	3.951e-1	-3e-3
-1.713e-1	4.26e-2	4.105e-1	-2.4e-3
-1.564e-1	4.55e-2	4.199e-1	-1.9e-3
-1.403e-1	4.81e-2	4.245e-1	-1.5e-3
-1.23e-1	5.05e-2	4.248e-1	-1.2e-3
-1.047e-1	5.26e-2	4.221e-1	-1e-3
-8.54e-2	5.44e-2	4.168e-1	-7e-4
-6.51e-2	5.6e-2	4.094e-1	-6e-4
-4.38e-2	5.73e-2	3.996e-1	-4e-4
-2.17e-2	5.82e-2	3.904e-1	-3e-4
1.3e-3	5.89e-2	3.778e-1	-2e-4
2.5e-2	5.93e-2	3.628e-1	-1e-4
4.95e-2	5.94e-2	3.494e-1	0e+0
7.45e-2	5.92e-2	3.343e-1	1e-4
1.002e-1	5.88e-2	3.184e-1	1e-4
1.264e-1	5.81e-2	3.031e-1	2e-4
1.53e-1	5.72e-2	2.875e-1	2e-4
1.8e-1	5.6e-2	2.71e-1	2e-4
2.073e-1	5.46e-2	2.544e-1	3e-4
2.348e-1	5.3e-2	2.378e-1	3e-4
2.626e-1	5.13e-2	2.211e-1	3e-4
2.904e-1	4.93e-2	2.045e-1	3e-4
3.182e-1	4.72e-2	1.884e-1	3e-4
3.461e-1	4.5e-2	1.716e-1	4e-4
3.738e-1	4.27e-2	1.559e-1	4e-4
4.014e-1	4.02e-2	1.421e-1	4e-4
4.287e-1	3.77e-2	1.252e-1	4e-4
4.557e-1	3.5e-2	1.067e-1	4e-4
4.823e-1	3.23e-2	9.05e-2	4e-4
5.085e-1	2.96e-2	7.46e-2	4e-4
5.342e-1	2.68e-2	5.68e-2	4e-4
5.593e-1	2.4e-2	3.86e-2	4e-4
5.838e-1	2.12e-2	2.06e-2	4e-4
6.076e-1	1.84e-2	1.3e-3	3e-4
6.306e-1	1.56e-2	-2.05e-2	3e-4
6.528e-1	1.29e-2	-4.42e-2	3e-4
6.742e-1	1.01e-2	-7.02e-2	3e-4
6.946e-1	7.4e-3	-9.2e-2	2e-4
7.141e-1	4.7e-3	-1.441e-1	1e-4
7.325e-1	2.2e-3	-1.088e-1	0e+0
7.499e-1	0e+0	-2.34e-1	0e+0

Lower Surface Data:

x	z	-Cp	Tau
-2.5e-1	-1.6e-3	-1.0319e+0	3e-3
-2.486e-1	-6.2e-3	-7.832e-1	4.9e-3
-2.458e-1	-1.06e-2	-4.815e-1	2.3e-3
-2.419e-1	-1.51e-2	-2.554e-1	-2e-4
-2.366e-1	-1.96e-2	2.4e-2	-2.2e-3
-2.298e-1	-2.37e-2	2.063e-1	-2.8e-3
-2.215e-1	-2.76e-2	2.624e-1	-2.7e-3
-2.12e-1	-3.14e-2	3.142e-1	-2.5e-3
-2.012e-1	-3.5e-2	3.619e-1	-2.2e-3
-1.891e-1	-3.84e-2	3.892e-1	-1.9e-3
-1.758e-1	-4.16e-2	4.067e-1	-1.7e-3
-1.613e-1	-4.45e-2	4.178e-1	-1.4e-3
-1.456e-1	-4.73e-2	4.239e-1	-1.2e-3
-1.288e-1	-4.97e-2	4.256e-1	-1e-3
-1.109e-1	-5.19e-2	4.237e-1	-8e-4
-9.19e-2	-5.39e-2	4.191e-1	-7e-4
-7.2e-2	-5.55e-2	4.126e-1	-5e-4
-5.11e-2	-5.69e-2	4.035e-1	-4e-4
-2.94e-2	-5.79e-2	3.932e-1	-3e-4
-6.8e-3	-5.87e-2	3.84e-1	-2e-4
1.66e-2	-5.92e-2	3.681e-1	-1e-4
4.06e-2	-5.94e-2	3.527e-1	0e+0
6.53e-2	-5.93e-2	3.419e-1	1e-4
9.06e-2	-5.9e-2	3.249e-1	1e-4
1.164e-1	-5.84e-2	3.084e-1	2e-4
1.427e-1	-5.76e-2	2.941e-1	2e-4
1.694e-1	-5.65e-2	2.777e-1	3e-4
1.963e-1	-5.52e-2	2.612e-1	3e-4
2.236e-1	-5.37e-2	2.448e-1	3e-4
2.51e-1	-5.2e-2	2.283e-1	4e-4
2.785e-1	-5.02e-2	2.118e-1	4e-4
3.061e-1	-4.82e-2	1.957e-1	4e-4
3.336e-1	-4.6e-2	1.794e-1	4e-4
3.61e-1	-4.38e-2	1.631e-1	4e-4
3.883e-1	-4.14e-2	1.49e-1	4e-4
4.154e-1	-3.89e-2	1.342e-1	4e-4
4.421e-1	-3.64e-2	1.16e-1	4e-4
4.685e-1	-3.37e-2	9.88e-2	5e-4
4.945e-1	-3.11e-2	8.37e-2	5e-4
5.199e-1	-2.84e-2	6.73e-2	5e-4
5.448e-1	-2.57e-2	4.95e-2	5e-4
5.69e-1	-2.29e-2	3.18e-2	4e-4
5.926e-1	-2.02e-2	1.43e-2	4e-4
6.155e-1	-1.75e-2	-5.3e-3	4e-4
6.375e-1	-1.48e-2	-2.69e-2	4e-4
6.587e-1	-1.21e-2	-5.06e-2	4e-4
6.789e-1	-9.5e-3	-7.47e-2	4e-4
6.982e-1	-6.9e-3	-9.64e-2	3e-4
7.165e-1	-4.4e-3	-1.491e-1	2e-4
7.338e-1	-2.1e-3	-1.101e-1	1e-4
7.499e-1	0e+0	-2.34e-1	0e+0

APPENDIX C - USING THE PROGRAMS

A. DIRECTIONS FOR THE EXECUTION OF NS2.F

1. Steady State Case

In order to generate a C_p , C_l , or C_m plot from `Ns2.f` there are many steps, using six different programs that must be taken: (1.) **grape** (grid generation program), (2.) **rotgr** (grid rotation program), (3.) **Ns2.f** (Navier-Stokes code), (4.) **vi** (editor), (5.) **plot3d** (flow visualization program), and (6.) **xyplot** (a simple x-y plot program).

A.) `Ns2.f` is a fortran code and will take hours to run even on the Stardent mini-super computer. To run this code, an executable file (`ns2`), an input file `ns2.in` (actual name of input file is users choice) and a grid file `FOR011.DAT` (Stardent) or `fort.11` (on other computers) must be in the directory.

B.) To obtain a grid, a grid generation program such as **grape** must first be used. **Grape** output places the leading edge of the grid at the reference axis at 0.0° AOA. Now, the grid must be rotated to the desired AOA by using the program **rotgr**. The input file (output from **grape**) for **rotgr** must be `FOR001.DAT` and the output is `FOR002.DAT`. The output from **rotgr** (`FOR002.DAT`) must be renamed to `FOR011.DAT` for use in `ns2`.

C.) Next edit the input file to reflect the desired flow conditions. Any editor will do, however **vi** is perhaps the most common editor and it is found on most unix based machines. Enter Mach No. and AOA, check smoothing factors, set time step, Courant No. and initial no. of iterations (small value- for first run). Check restart false for first run and make sure No. point of your grid match input values.

D.) The code is executed as follows: `ns2 <ns2.in> ns2.out`

The first ten iterations should take 1-10 minutes, depending on the type of computer used. Several output files will be generated:

TABLE 3. NS2.F OUPUT

OUTPUT	COMMENTS
<code>ns2.out:</code>	convergence data
<code>FOR004.DAT:</code>	C_l data
<code>FOR007.DAT:</code>	residuals
<code>FOR008.DAT:</code>	C_l , C_d , C_m data
<code>FOR009.DAT:</code>	C_p data (to be used with xyplot)
<code>FOR031.DAT:</code>	Flow data (to be used with plot3d)

E.) Re-run the code for a greater number of iterations to achieve a converged solution. When the change in the max residual (`FOR007.DAT`) has dropped 10^{-2} , the solution has converged. Ensure restart is set to **true**. The CFL can also be adjusted to obtain a converged solution more rapidly.

a. Sample Input to Ns2.f

```

MACH,  ALFA0,  ALFA1,  ALFARE,  REDFRE,  REYNOLDS
0.300,  0.00,  0.0,   0.00,   0.00,   2.70
ED2X,   ED2Y,   ED4X,   ED4Y,   ED
0.00,   0.00,  0.030,  0.030,   2.0
DT,     COUR,   NITER,   NEWTIT
0.0020, 2100,   50,     2
RSTRT,  OSCIL,  RAMP,    NPER,   TSHIFT
true,   false, false,   10000,  -0.5
TIMEAC, IMPLBC, EXPLBC,  CIRCOR
1,      false,  true,   false
VISC,   BLTM,   JKTM,   RNGTM
true,   true,   false,  false
ITEL,   ITEU
31,     131
IA1, IA2, IA3, IA4, IA5, IA6, IA7, IA8, IA9, IA10
1250,1350,1450,1550,1570,1590,1610,1630,1630, 1805
false

```

UNSTST (If true Time = 0., Set TRUE only when unsteady motion starts from steady steady state, TRUE for steady-state ok, but for unsteady restarts must be FALSE for proper recording of unsteady motion)

```

Mach      :   Free stream Mach number
Alfa0     :   Angle of attack, also mean angle of attack for unsteady
Alfa1     :   Amplitude of Oscillatory motion
Alfare    :   Reference angle
Redfre    :   Reduced frequency  $k = \omega * c / 2U$ 
Reynolds  :   Reynolds number  $Re = cU/\nu$ 

ED2x      :   X-direction 2nd order explicit smoothing ( e2x = 0.00 subsonic,
                                                         0.25 < e2x < 0.50 transonic)
ED2z      :   Z-direction 2nd order explicit smoothing ( e2z = 0.00 subsonic,
                                                         0.10 < e2z < 0.20 transonic)
ED4x      :   X-direction 4nd order explicit smoothing ( e4x = 0.03 subsonic,
                                                         e4x = 0.05 transonic)
ED4z      :   Z-direction 4nd order explicit smoothing ( e4z = 0.03 subsonic,
                                                         e4z = 0.05 transonic)
ED        :   Scaling of Implicit smoothing
ISPEC     :   Spectral radius parameter

Dt        :   Time step
Cour      :   Courant number  $Cu = dt * L_{max}$ 
Niter     :   Number of Iteration in this run
Newtit    :   Newton subiteration within each timestep

RSTRT     :   Restart
OSCIL     :   Oscillatory motion  $A(t) = A0 + A1 * \sin ( k * M * t )$ 
RAMP      :   Ramp motion
NPER      :   Number of time steps in one period of oscillation,  $dt=T/Nper$ 
TSHIFT    :   Time shift in radians to start oscilation for any a(t)

TIMEAC    :   Time accurate Tacc=1 and for Jacobian Scaled Dt, Tacc=0
IMPLBC    :   Implicit wall BC Treatment
EXPLBC    :   Explicit wall BC Treatment

```


VISC : Only laminar viscosity
TURBL : Baldwin-Lomax eddy viscosity
JKTM : Johnson-King eddy viscosity
RNGTM : RNG eddy viscosity

ITEL, ITEU : Lower and Upper trailing edge I locations
IAI etc. : Write out (IAN/100) angles of attack in units
61 - 70

Read grid from unit fort.11 and the flow from unit fort.31

b. Sample Output from Ns2.f

Grid dimensions : 161x64

Mach = 0.30000

Ao = 0.00000 A1 = 0.00000 k = 0.01272

Re = 0.2700E+07 Dt = 0.00200 Cu=2100.00000

Dimpl = 2.00000

D2x = 0.00000 D2z = 0.00000

D4x = 0.03000 D4z = 0.03000

Restart = T

Oscil = F

Ramp = F

Itel = 31 Iteu = 131 Ile = 81

Timeac = T

BC impl = F

BC expl = T

.

Cour = 2100.

L_max = 232096.4825513

Dt = 0.00904796

	It	drmax	dumax	dvmax	demax	ir	kr
	3000	0.573103E-07	0.371716E-07	0.563395E-07	0.129865E-06	140	63
Ni=	1	0.903247E-08	0.711341E-08	0.803250E-08	0.219128E-07		

Alfa(t) = 0.000 Cl = 0.007196 Cd = 0.003260 Cm = -0.000692

2. Unsteady Case

The execution of an unsteady case is essentially the same as for the steady-state case.

A. First, a well converged steady-state solution must be obtained. This solution then becomes the starting point for the unsteady solution.

B. The restart is left set to **true**, however, to reset the time counter to time=0, the UNSTST variable must be set to **true** for several iterations and then back to **false** for normal time counting.

C. As the unsteady motion begins to march in time Flow data and Grid position data may be stored at user determined angles of attack. To store flow data at $\alpha=12.5^\circ$, $\alpha=13.5^\circ$, $\alpha=14.5^\circ$, etc... enter the data shown in Table 4. into the input file.

TABLE 4. ANGLE OF ATTACK INPUT

IA1	IA2	IA3	IA4	IA5	IA6	IA7	IA8	IA9	IA10
1250	1350	1450	1550	1570	1590	1610	1630	1630	1805

D. The Flow data and the Grid data at each α will be stored in data files FOR021.DAT through FOR030.DAT. The Grid and Flow data can be separated using a simple fortran code that reads the data and then writes the data to two separate files. Splgf.f inputs the desired file ID and outputs a Grid file and Flow file.

a. Sample Input to Ns2.f

```

MACH,   ALFA0,   ALFA1,   ALFARE,   REDFRE,   REYNOLDS
0.300,   0.00,   15.54,   0.00,   0.01272,   2.70
ED2X,   ED2Y,   ED4X,   ED4Y,   ED
0.00,   0.00,   0.030,   0.030,   2.0
DT,     COUR,   NITER,   NEWTIT
0.0020,  2100,   50,     1
RSTRT,   OSCIL,   RAMP,   NPER,   TSHIFT
true,    false,   true,   3000,   -0.5
TIMEAC,  IMPLBC,  EXPLBC,  CIRCOR
1,       false,   true,   false
VISC,    BLTM,    JKTM,    RNGTM
true,    true,    false,   false
ITEL,    ITEU
31,     131
IA1, IA2, IA3, IA4, IA5, IA6, IA7, IA8, IA9, IA10
1250,1350,1450,1550,1570,1590,1610,1630,1630, 1805
false

```

UNSTST (If true Time = 0., Set TRUE only when unsteady motion starts from steady state, TRUE for steady-state ok, but for unsteady restarts must be FALSE for proper recording of unsteady motion)

```

Mach      :   Free stream Mach number
Alfa0     :   Angle of attack, also mean angle of attack for unsteady
Alfa1     :   Amplitude of Oscillatory motion
Alfare    :   Reference angle
Redfre    :   Reduced frequency  $k = \omega * c / 2U$ 
Reynolds  :   Reynolds number  $Re = cU/\nu$ 

ED2x      :   X-direction 2nd order explicit smoothing ( e2x = 0.00 subsonic,
                                                         0.25 < e2x < 0.50 transonic)
ED2z      :   Z-direction 2nd order explicit smoothing ( e2z = 0.00 subsonic,
                                                         0.10 < e2z < 0.20 transonic)
ED4x      :   X-direction 4nd order explicit smoothing ( e4x = 0.03 subsonic,
                                                         e4x = 0.05 transonic)
ED4z      :   Z-direction 4nd order explicit smoothing ( e4z = 0.03 subsonic,
ED         :   Scaling of Implicit smoothing
ISPEC     :   Spectral radius parameter

Dt         :   Time step
Cour       :   Courant number  $Cu = dt * L_{max}$ 
Niter      :   Number of Iteration in this run
Newtit     :   Newton subiteration within each timestep

RSTRT     :   Restart
OSCIL     :   Oscillatory motion  $A(t) = A0 + A1 * \sin ( k * M * t )$ 
RAMP       :   Ramp motion
NPER       :   Number of time steps in one period of oscillation,  $dt=T/Nper$ 
TSHIFT     :   Time shift in radians to start oscillation for any a(t)

TIMEAC     :   Time accurate Tacc=1 and for Jacobian Scaled Dt, Tacc=0
IMPLBC     :   Implicit wall BC Treatment
EXPLBC     :   Explicit wall BC Treatment

```

VISC : Only laminar viscosity
TURBL : Baldwin-Lomax eddy viscosity
JKTM : Johnson-King eddy viscosity
RNGTM : RNG eddy viscosity

ITEL, ITEU : Lower and Upper trailing edge I locations
IA1 etc. : Write out (IAN/100) angles of attack in units
61 - 70

Read grid from unit fort.11 and the flow from unit fort.31

b. Sample Output from Ns2.f

Grid dimensions : 161x64

Mach = 0.30000
 Ao = 0.00000 A1 = 16.00000 k = 0.01272
 Re = 0.2700E+07 Dt = 0.01829 Cu = 15.00000

Dimpl = 2.00000
 D2x = 0.00000 D2z = 0.00000
 D4x = 0.03000 D4z = 0.03000

Restart = T
 Oscil = F
 Ramp = T

Itel = 31 Iteu = 131 Ile = 81

Timeac = T
 BC impl = F
 BC expl = T

Cour = 4289.735274387
 L_max = 234539.9275225
 Dt = 0.01829000

	It	drmax	dumax	dvmax	demax	ir	kr
	1950	0.849290E-06	0.107934E-05	0.190543E-05	0.174200E-05	119	63
Ni=	1	0.113997E-06	0.302620E-06	0.448250E-06	0.196797E-06		

it = 1950 Time = 35.665500 omega = 0.007632 phase = 0.043322
 Alfa(t) = 15.596 Cl = 1.425268 Cd = 0.137214 Cm = 0.003384

	2000	0.778403E-06	0.107038E-05	0.191827E-05	0.158330E-05	118	63
Ni=	1	0.113176E-06	0.297453E-06	0.450476E-06	0.197668E-06		

it = 2000 Time = 36.580000 omega = 0.007632 phase = 0.044433
 Alfa(t) = 15.996 Cl = 1.453050 Cd = 0.146989 Cm = 0.001525

B. DIRECTIONS FOR THE EXECUTION OF U2DIIF.F

1. Unsteady Case

A. A complete description of the input and output parameters can be found in Teng.

TABLE 5. U2DIIF.F INPUTS/OUTPUTS

FILE	COMMENTS
FOR001.DAT	Input
U2diif.out	Output

B.) For a unix based machine the code is executed as follows:

U2diif > U2diif.out

Note: The original Fortran code can be modified to store desired output in separate data files by inserting a WRITE (9,*) statement inside the required do-loop. (Example: Cp vs x/c data could be stored in a data file FOR009.DAT). This requires some knowledge of Fortran programming.

a. Sample Input to U2diif

4

```
*****
AIRFOIL TYPE : NACA 0012 AIRFOIL
NLOWER = 50 , NUPPER = 50
*****
0, 50, 50
12
0.00, 15.54, 10.67, 0.00, 0.25, 0.00, 0.00
0.00, 0.00, 0.00
11.00, 0.010, 0.0001, 0.00
108, 294, 487, 584, 802, 891, 1006, 1007, 1283, 1554
ITITLE
INPUT TITLE (ITITLE = NO. LINE)
IFLAG NLOWER NUPPER
AIRFOIL TYPE
ALPI DALP TCON FREQ PIVOT UGUST VGUST
DELHX DELHY PHASE
TF DTS TOL TADK
ia1 ia2 ia3 ia4 ia5 ia6 ia7 ia8 ia9 ia10
```

b. Sample Output to U2diif.f

DATA FROM fort.1: (IRIS) OR FOR001.DAT: (STARDENT)

```
*****
AIRFOIL TYPE : NACA 0012 AIRFOIL
NLOWER = 50 , NUPPER = 50
*****
```

```
=====
IFLAG      (0:NACA, 1:INPUT)      =      0
NO. PANELS UPPER SURFACE          =     50
NO. PANELS LOWER SURFACE          =     50
=====
INITIAL ANGLE OF ATTACK            =      0.0000
FINAL   ANGLE OF ATTACK            =     15.5400
RISE TIME                          =     10.6700
REDUCED FREQ. FOR OSCIL            =      0.0000
PIVOT POINT                       =      0.2500
STREAMWISE GUST VELOCITY           =      0.0000
PERPENDICULAR GUST VELOCITY        =      0.0000
=====
X AMPLITUDE OF TRANS OSCILL. =      0.0000
Y AMPLITUDE OF TRANS OSCILL. =      0.0000
PHASE      OF TRANS OSCILL. =      0.0000
=====
FINAL TIME                        =     11.0000
INITIAL TIME STEP FOR S.S.       =      0.0100
TOLERANCE FOR CONVERGENCE        =      0.0001
FACTOR BY WHICH DTS ADJUSTED    =      0.0000
=====
```

COORDINATES OF AIRFOIL NODES

```
      X/C      Y/C
1.000000  0.000000
0.999013 -0.000141
0.996057 -0.000562
      .
      .
      .
0.984292  0.002222
0.991144  0.001258
0.996057  0.000562
0.999013  0.000141
1.000000  0.000000
```

AIRFOIL PERIMETER LENGTH = 2.039290

STEADY FLOW SOLUTION AT ALPHA = 0.000000

J	X(J)	Q(J)	GAMMA	CP(J)	V(J)
---	------	------	-------	-------	------

90	0.894883	-0.131445	0.000000	0.035461	0.982110
91	0.913336	-0.132561	0.000000	0.056813	0.971178
92	0.930159	-0.133333	0.000000	0.079566	0.959393
93	0.945283	-0.133704	0.000000	0.104048	0.946547
94	0.958651	-0.133607	0.000000	0.130706	0.932359
95	0.970208	-0.132956	0.000000	0.160183	0.916415
96	0.979910	-0.131634	0.000000	0.193471	0.898070
97	0.987718	-0.129461	0.000000	0.232226	0.876227
98	0.993600	-0.126109	0.000000	0.279518	0.848812
99	0.997535	-0.120869	0.000000	0.341902	0.811232
100	0.999507	-0.112063	0.000000	0.433845	0.752433

```
GAMMA FROM KUTTA CONDITION: -0.00000024
GAMMA FROM CONTOUR INTEGR (TRAIL EDGE): -0.00000025
GAMMA FROM CONTOUR INTEGR (MIDPOINTS): -0.00000025
GAMMA FROM BOX INTEGR (OFF THE CONTOUR): -0.00000024
GAMMA FROM PRECISE CONTOUR INTEG (6 PT): -0.00000024
```


J	X(J)	Q(J)	GAMMA	CP(J)	V(J)	PREV PHI(J)	CURR PHI(J)
1	0.999507	-0.107774	0.000004	0.432728	-0.753023	0.032660	0.032661
2	0.997535	-0.117297	0.000004	0.341094	-0.811709	0.033045	0.033045
3	0.993600	-0.123077	0.000004	0.279152	-0.849194	0.033663	0.033661
4	0.987718	-0.126843	0.000004	0.232351	-0.876535	0.034408	0.034404
5	0.979910	-0.129345	0.000004	0.194095	-0.898321	0.035211	0.035205
6	0.970208	-0.130932	0.000004	0.161293	-0.916622	0.036018	0.036011
7	0.958651	-0.131801	0.000004	0.132278	-0.932531	0.036785	0.036776
8	0.945283	-0.132080	0.000004	0.106051	-0.946691	0.037475	0.037463
9	0.930159	-0.131864	0.000004	0.081967	-0.959514	0.038055	0.038041
10	0.913336	-0.131225	0.000004	0.059576	-0.971280	0.038497	0.038482

.

90	0.894883	-0.132662	0.000004	0.032373	0.982025	0.038778	0.038794
91	0.913336	-0.133893	0.000004	0.054048	0.971077	0.038497	0.038511
92	0.930159	-0.134798	0.000004	0.077163	0.959272	0.038054	0.038067
93	0.945283	-0.135322	0.000004	0.102044	0.946404	0.037474	0.037486
94	0.958651	-0.135406	0.000004	0.129134	0.932188	0.036785	0.036794
95	0.970208	-0.134972	0.000004	0.159071	0.916209	0.036018	0.036025
96	0.979910	-0.133914	0.000004	0.192844	0.897820	0.035210	0.035216
97	0.987718	-0.132066	0.000004	0.232097	0.875921	0.034407	0.034411
98	0.993600	-0.129123	0.000004	0.279879	0.848433	0.033662	0.033664
99	0.997535	-0.124414	0.000004	0.342703	0.810760	0.033045	0.033044
100	0.999507	-0.116362	0.000004	0.434960	0.751843	0.032659	0.032658

===== C O M P A R I S O N O F G A M M A S

GAMMA FROM KUTTA CONDITION: 0.00000411

GAMMA FROM CONTOUR INTEGR (TRAIL EDGE): -0.00000165

GAMMA FROM CONTOUR INTEGR (MIDPOINTS): -0.00000137

GAMMA FROM BOX INTEGR (OFF THE CONTOUR): 0.00000462

GAMMA FROM PRECISE CONTOUR INTEG (6 PT): 0.00000385

=====

CD = 0.000324 CL = 0.005136 CM = -0.003050

TRAILING VORTICES DATA

M	X(M)	Y(M)	CIRC
1	1.004137	0.000001	-0.000009

TIME STEP TK = 0.020000 TK - TKM1 = 0.010000

ALPHA(T) = 0.000164 OMEGA(T) = -0.000285

U(T) = 0.000000 V(T) = -0.000071

NITR	VXW	VYW	WAKE	THETA	GAMMA
0	0.827452	0.000256	0.008275	0.000309	0.411158E-05

CONVERGED SOLUTION OBTAINED AFTER NITR = 0

J	X(J)	Q(J)	GAMMA	CP(J)	V(J)	PREV PHI(J)	CURR PHI(J)
1	0.999507	-0.104926	0.000011	0.432928	-0.753413	0.032661	0.032658
2	0.997535	-0.114799	0.000011	0.341275	-0.812045	0.033045	0.033042
			.				
			.				
20	0.669285	-0.109493	0.000011	-0.121525	-1.061102	0.031441	0.031419
21	0.639427	-0.105975	0.000011	-0.138604	-1.069082	0.029361	0.029339
22	0.609018	-0.102029	0.000011	-0.155875	-1.077078	0.027013	0.026992
23	0.578179	-0.097571	0.000011	-0.173377	-1.085108	0.024398	0.024378

C. DIRECTIONS FOR THE EXECUTION OF INCOMPBL.F

1. Steady State Case

A. Execution of Incompbl.f is straight forward. First edit the input files, FOR001.DAT and incompbl.dat, and set the desired flow conditions.

TABLE 6. INCOMPBL.F INPUTS

INPUT	COMMENTS
incompbl.dat	IWAKE-Flag Wake Calulation NXT NW-No. of point in wake ITREND-No. of Iterations ITR(1)-Transition Flag Upper Surface ITR(2)-Transition Flag Upper Surface ISWPMX RL-Reynolds Number XCTR(1)-Transition Location Upper Surface IP-Print flag
FOR001.DAT	Input AOA, pivot point and Airfoil Coordinates, and No. of Panels

B.) For a unix based machine the code is executed as follows:

incompbl <incompbl.dat> incompbl.out.

TABLE 7. INCOMPBL.F OUPUT

OUTPUT	COMMENTS
incompbl.out	Flow data

Note: The original Fortran code can be modified to store desired output in separate data files by inserting a WRITE (24,*) statement inside the required do-loop. (Example: Cp vs x/c data could be stored in a data file FOR024.DAT). This requires some knowledge of Fortran Programming.

a. Sample Input to Incompbl.f
File Named fort.1 of FOR001.DAT

3

C
C NACA 0012 AIRFOIL
C

ALPI	PIVOT
4.000000	0.250000
NLOWER	NUPPER
50	50

X/C

1.00000	0.98000	0.96000	0.94000	0.92000	0.90000
0.88000	0.86000	0.84000	0.82000	0.80000	0.78000
0.76000	0.74000	0.72000	0.70000	0.68000	0.66000
0.64000	0.62000	0.60000	0.58000	0.56000	0.54000
0.52000	0.50000	0.48000	0.46000	0.44000	0.42000
0.40000	0.38000	0.36000	0.34000	0.32000	0.30000
0.28000	0.26000	0.24000	0.22000	0.20000	0.18000
0.16000	0.14000	0.12000	0.10000	0.08000	0.06000
0.04000	0.02000	0.00000	0.02000	0.04000	0.06000
0.08000	0.10000	0.12000	0.14000	0.16000	0.18000
0.20000	0.22000	0.24000	0.26000	0.28000	0.30000
0.32000	0.34000	0.36000	0.38000	0.40000	0.42000
0.44000	0.46000	0.48000	0.50000	0.52000	0.54000
0.56000	0.58000	0.60000	0.62000	0.64000	0.66000
0.68000	0.70000	0.72000	0.74000	0.76000	0.78000
0.80000	0.82000	0.84000	0.86000	0.88000	0.90000
0.92000	0.94000	0.96000	0.98000	1.00000	

Y/C

-0.00126	-0.00403	-0.00674	-0.00938	-0.01196	-0.01448
-0.01694	-0.01935	-0.02170	-0.02399	-0.02623	-0.02842
-0.03056	-0.03264	-0.03467	-0.03664	-0.03856	-0.04042
-0.04222	-0.04396	-0.04563	-0.04723	-0.04878	-0.05026
-0.05165	-0.05294	-0.05415	-0.05530	-0.05634	-0.05726
-0.05803	-0.05868	-0.05923	-0.05966	-0.05995	-0.06006
-0.05997	-0.05966	-0.05911	-0.05838	-0.05737	-0.05607
-0.05444	-0.05236	-0.04990	-0.04683	-0.04309	-0.03842
-0.03231	-0.02382	0.00000	0.02382	0.03231	0.03842
0.04309	0.04683	0.04990	0.05236	0.05444	0.05607
0.05737	0.05838	0.05911	0.05966	0.05997	0.06006
0.05995	0.05966	0.05923	0.05868	0.05803	0.05726
0.05634	0.05530	0.05415	0.05294	0.05165	0.05026
0.04878	0.04723	0.04563	0.04396	0.04222	0.04042
0.03856	0.03664	0.03467	0.03264	0.03056	0.02842
0.02623	0.02399	0.02170	0.01935	0.01694	0.01448
0.01196	0.00938	0.00674	0.00403	0.00126	

File named incompbl.dat

IWAKE	NXT	NW	ITREND	
0	161	37	40	
ITR(1)	ITR(2)	ISWPMX	RL	XCTR(1)
0	0	1	3000000.0	0.10000
IP				
1				

b. Sample Output from Incompbl.f

C
C
C

NACA 0012 AIRFOIL

INPUT DATA FOR INVISCID-FLOW CALCULATIONS

ALPI= 4.0000 PIVOT= 0.2500
NLOWER= 50 NUPPER= 50

COORDINATES OF THE BODY

X/C

1.000000	0.980000	0.960000	0.940000	0.920000	0.900000
0.880000	0.860000	0.840000	0.820000	0.800000	0.780000
0.760000	0.740000	0.720000	0.700000	0.680000	0.660000
0.640000	0.620000	0.600000	0.580000	0.560000	0.540000
0.520000	0.500000	0.480000	0.460000	0.440000	0.420000
0.400000	0.380000	0.360000	0.340000	0.320000	0.300000
0.280000	0.260000	0.240000	0.220000	0.200000	0.180000
0.160000	0.140000	0.120000	0.100000	0.080000	0.060000
0.040000	0.020000	0.000000	0.020000	0.040000	0.060000
0.080000	0.100000	0.120000	0.140000	0.160000	0.180000
0.200000	0.220000	0.240000	0.260000	0.280000	0.300000
0.320000	0.340000	0.360000	0.380000	0.400000	0.420000
0.440000	0.460000	0.480000	0.500000	0.520000	0.540000
0.560000	0.580000	0.600000	0.620000	0.640000	0.660000
0.680000	0.700000	0.720000	0.740000	0.760000	0.780000
0.800000	0.820000	0.840000	0.860000	0.880000	0.900000
0.920000	0.940000	0.960000	0.980000	1.000000	

Y/C

-0.001260	-0.004030	-0.006740	-0.009380	-0.011960	-0.014480
-0.016940	-0.019350	-0.021700	-0.023990	-0.026230	-0.028420
-0.030560	-0.032640	-0.034670	-0.036640	-0.038560	-0.040420
-0.042220	-0.043960	-0.045630	-0.047230	-0.048780	-0.050260
-0.051650	-0.052940	-0.054150	-0.055300	-0.056340	-0.057260
-0.058030	-0.058680	-0.059230	-0.059660	-0.059950	-0.060060
-0.059970	-0.059660	-0.059110	-0.058380	-0.057370	-0.056070
-0.054440	-0.052360	-0.049900	-0.046830	-0.043090	-0.038420
-0.032310	-0.023820	0.000000	0.023820	0.032310	0.038420
0.043090	0.046830	0.049900	0.052360	0.054440	0.056070
0.057370	0.058380	0.059110	0.059660	0.059970	0.060060
0.059950	0.059660	0.059230	0.058680	0.058030	0.057260
0.056340	0.055300	0.054150	0.052940	0.051650	0.050260
0.048780	0.047230	0.045630	0.043960	0.042220	0.040420
0.038560	0.036640	0.034670	0.032640	0.030560	0.028420
0.026230	0.023990	0.021700	0.019350	0.016940	0.014480
0.011960	0.009380	0.006740	0.004030	0.001260	

1

INVISCID FLOW RESULTS

PANEL	XP	YP	CP
1	0.99000E+00	-0.14950E-02	0.25519E+00
2	0.97000E+00	-0.44813E-02	0.17805E+00

3	0.95000E+00	-0.74415E-02	0.13179E+00
4	0.93000E+00	-0.10321E-01	0.97803E-01
5	0.91000E+00	-0.13061E-01	0.74658E-01
6	0.89000E+00	-0.15646E-01	0.60117E-01
7	0.87000E+00	-0.18113E-01	0.49465E-01
8	0.85000E+00	-0.20502E-01	0.39706E-01
9	0.83000E+00	-0.22829E-01	0.30916E-01
10	0.81000E+00	-0.25104E-01	0.21877E-01

.

90	0.79000E+00	0.27319E-01	-0.12424E+00
91	0.81000E+00	0.25096E-01	-0.10630E+00
92	0.83000E+00	0.22823E-01	-0.88121E-01
93	0.85000E+00	0.20492E-01	-0.69791E-01
94	0.87000E+00	0.18084E-01	-0.49935E-01
95	0.89000E+00	0.15564E-01	-0.24583E-01
96	0.91000E+00	0.12899E-01	0.93575E-02
97	0.93000E+00	0.10105E-01	0.51153E-01
98	0.95000E+00	0.72366E-02	0.99432E-01
99	0.97000E+00	0.43440E-02	0.15874E+00
100	0.99000E+00	0.14480E-02	0.25519E+00

1 INVISCID WAKE RESULTS

PANEL	XP	YP	CP
101	0.10033E+01	0.26712E-04	0.34783E+00
102	0.10110E+01	0.93657E-04	0.26481E+00
103	0.10209E+01	0.19595E-03	0.21845E+00
104	0.10340E+01	0.35320E-03	0.18376E+00
105	0.10510E+01	0.59334E-03	0.15510E+00
106	0.10732E+01	0.95766E-03	0.13035E+00
107	0.11023E+01	0.15069E-02	0.10857E+00
108	0.11402E+01	0.23302E-02	0.89285E-01
109	0.11897E+01	0.35565E-02	0.72269E-01
110	0.12543E+01	0.53713E-02	0.57416E-01
111	0.13387E+01	0.80381E-02	0.44666E-01
112	0.14489E+01	0.11926E-01	0.33948E-01
113	0.15928E+01	0.17545E-01	0.25162E-01
114	0.17806E+01	0.25591E-01	0.18168E-01
115	0.20259E+01	0.36999E-01	0.12767E-01
116	0.23462E+01	0.53013E-01	0.87308E-02
117	0.27643E+01	0.75273E-01	0.58084E-02
118	0.33103E+01	0.10592E+00	0.37624E-02
119	0.38079E+01	0.13479E+00	0.26992E-02

CL = 0.47937E+00

INPUT DATA FOR BOUNDARY-LAYER CALCULATIONS

IWAKE	NXT	NW	ITREND	
0	161	37	40	
ITR(1)	ITR(2)	ISWPMX	10**-6*RL	XCTR(1)
0	0	1	3.00	0.10
IP				
1				

***** CYCLE 40 *****

SUMMARY OF THE DRAG, LIFT AND PITCHING MOMENT
COEFFICIENTS WITH THE CYCLE

CD,CL AND CM ARE EVALUATED FROM THE INTEGRATION OF CP

CYCLE	CD	CL	CM
1	0.001978	0.001684	0.427162
2	0.003184	0.001730	0.427756
3	0.002734	0.001684	0.427162
4	0.002422	0.001730	0.427770
5	0.002227	0.001684	0.427157
.	.	.	.
35	0.001684	0.427157	0.004733
36	0.001731	0.427790	0.004494
37	0.001684	0.427165	0.004731
38	0.001731	0.427807	0.004491
39	0.001684	0.427167	0.004731
40	0.001731	0.427822	0.004488

BOUNDARY_LAYER PROPERTIES FOR THE LAST CYCLE

----- UPPER SURFACE -----

XCTR= 0.134E+00

	NX	XC	XS	CF	DLS	UE	CP	IT
76	0.00294	0.003411	0.06394	0.00005	0.15840	0.97491	0.97491	3
77	0.00140	0.006562	0.03670	0.00005	0.33362	0.88870	0.88870	2
78	0.00056	0.009021	0.02384	0.00005	0.48286	0.76685	0.76685	2
79	0.00018	0.010828	0.01910	0.00005	0.59624	0.64450	0.64450	2
.
158	0.98712	1.018435	0.00046	0.00711	0.87987	0.22583	0.22583	5
159	0.99209	1.023461	0.00035	0.00749	0.87320	0.23751	0.23751	4
160	0.99639	1.027802	0.00025	0.00785	0.86751	0.24742	0.24742	5
161	1.00000	1.031453	0.00019	0.00818	0.86283	0.25553	0.25553	5

----- LOWER SURFACE -----

XCTR= 0.677E+00

	NX	XC	XS	CF	DLS	UE	CP	IT
87	0.00540	0.000436	0.47509	0.00006	0.02025	0.99959	0.99959	2

88	0.00888	0.004971	0.15459	0.00006	0.18949	0.96409	2
89	0.01333	0.010187	0.02621	0.00007	0.36027	0.87021	2
90	0.01841	0.016077	0.01498	0.00007	0.53294	0.71597	3
			.				
			.				
			.				
158	0.98713	0.992288	0.00204	0.00181	0.89064	0.20676	2
159	0.99210	0.997313	0.00186	0.00191	0.88051	0.22471	2
160	0.99639	1.001654	0.00171	0.00202	0.87121	0.24100	2
161	1.00000	1.005305	0.00159	0.00212	0.86310	0.25505	2

INITIAL DISTRIBUTION LIST

	No. Copies
1. Defense Technical Information Center Cameron Station Alexandria, Virginia 22304-6145	2
2. Library, Code 52 Naval Postgraduate School Monterey, California 93943-5100	2
3. Dr. M.F. Platzer Dept. of Aeronautics and Astronautics, Code AA/PL Naval Postgraduate School Monterey, California 93943-5002	5
4. Dr. J. A. Ekaterinaris NASA Ames Research Center (M.S. 258-1) Moffet Field, California 94035	5
5. Lt Jeffrey D. Clarkson 226 Orange Ave. #102 Coronado, California 92118	1

Thesis

C5017 Clarkson

c.1 A computational investigation of airfoil stall flutter.

Thesis

C5017 Clarkson

c.1 A computational investigation of airfoil stall flutter.

DUDLEY KNOX LIBRARY



3 2768 00033065 8